Theoretische Modellierung aktiver Zentren von molybdänabhängigen Enzymen

INAUGURAL – DISSERTATION

zur

Erlangung der Doktorwürde

der

Naturwissenschaftlich-Mathematischen Gesamtfakultät

der

Ruprecht-Karls-Universität Heidelberg

Vorgelegt von

M.Phil. Uzma Habib

aus: Wah Cantt, Pakistan

Thema

Theoretische Modellierung aktiver Zentren von molybdänabhängigen Enzymen

Gutachter:

Tag der mündlichen Prüfung: . .2012

Erklärung

Erklärung gemäß § 8 (3) b) und c) der Promotionsordnung:

a) Ich erkläre hiermit an Eides statt, dass ich die vorgelegte Dissertation selbst verfasst und mich keiner anderen als der von mir ausdrücklich bezeichneten Quellen und Hilfen bedient habe.

b) Ich erkläre hiermit an Eides statt, dass ich an keiner anderen Stelle ein Prüfungsverfahren

beantragt bzw. die Dissertation in dieser oder anderer Form bereits anderweitig als Prüfungsarbeit verwendet oder einer anderen Fakultät als Dissertation vorgelegt habe.

Heidelberg, den . . 2012 _____

Uzma Habib

Dedication

To my family especially my parents,

the SKY of my life.

"میرے پیارے امی ابو کے نام"

Message for life

Plan more than what you think you could do, then try to accomplish it all. Build your castle in the clouds. Then build a ship to take you there.

Aim high, even if you don't make

it to the sun, you will at least

land among the

STARS.

ACKNOWLEDGEMENT

I like to thank ALLAH almighty for HIS blessings throughout our lives.

I am enormously indebted to PD. Dr. Matthias Hofmann, for offering me a doctoral position under his supervision. I am grateful to him for providing me the motivation and encouragement during my doctoral studies. I am indebted to him for sharing his vast knowledge of chemistry and providing excellent training of handling and presenting scientific projects. I am also thankful to him for providing financial support and very nice company over the years.

I express my sincere gratitude to Prof. Dr. Roland Krämer for giving me place in his group and for his kind formal supervision. I express my gratitude to all the present and past members of AK Krämer during my PhD time, especially Dr. Andriy Mokhir, Larisa, Helga, Katharina, Susanne, Annemarie, Birgit, Claudia, Ute, Helen, Uli, Armin, Gerrit, Paul, Subrata, Michael, Ulrich and Volker.

I am grateful to Prof. Dr. Peter Comba for providing an excellent additional education through the program of the Graduate College-850. I am also thankful to all members of "Graduate College-850, Modeling of Molecular Properties" especially Bodo Martin, for his help during seminars and conferences.

I am very much grateful to the administrative staff including Frau Jeannette Grosse, Frau Claudia Aßfalg, Frau Silke Dussel, Frau Karin Stelzer and Frau Marlies Schilli. I am also thankful to the official and technical staff of Anorganisch Institüt for their help in completing my research.

My sincere gratitude to Dr. M. Rasul Jan and Dr. Jasmin Shah, Chemistry Department, Peshawar University, Pakistan. A source of inspiration that induce in me a thirst of acquiring knowledge, whose ever encouraging and

valuable guidance always persisted me to work hard and to come up with task accomplished. For me they are a source of admiration Thanks to them for all they did for me and for their kind consideration and care which is continued uptil now and hope will forever, Inshallah.

I like to say especial thanks to Rabia, Zarghoona, Rashda, Saba, Faiza, Shanthi, Sajjad Bhai, Farooq bhai and Awais. Words cannot express the nature and extent of my deepest appreciation for them. They were always there in the hour of need. I want to thank them for their kind behaviour, valuable advices, timely suggestions and constant encouragement all the time.

My love and especial thanks to most precious Ischal, Shees and Shaeel, for their unconditional love as during my stay in Germany I always get energy after spending lovely time with them.

Acknowledgements are also due to my friends, Anashua, Kiran, Lubna, Maryum, Tanuja and Avik, for their kindly cooperation, valuable suggestions and encouragement throughout my stay.

Finally I wish to thank my parents for their moral support and their encouragement to come so far from my home to achieve the goal. I would also like to thank to my brothers and sisters and their beloved partners and their precious kids for their love and support. Without their prayers I couldn't have put my best in the research and I am grateful for that.

Uzma

Summary

Chapter 1: Introduction

Summary

Molybdenum and tungsten active site model complexes, derived from the protein X-ray crystal structure of the first W-containing nitrate reductase isolated from *Pyrobaculum aerophilum*, were computed for nitrate reduction at the COSMO-B3LYP/SDDp//B3LYP/Lanl2DZ(p) level of density functional theory (DFT). The molybdenum containing active site model complex has a considerably larger activation energy (34.4 kcal/mol) for the oxygen atom transfer from the nitrate to the metal center as compared to the tungsten containing active site model complex (12.0 kcal/mol). Oxidation of the educt complex is close to thermoneutral (-1.9 kcal/mol) for the Mo active site model complex but strongly exothermic (-34.7 kcal/mol) for the W containing active site model complex. The low relative energy for the oxidized W metal complex makes the regeneration of the +IV oxidation state much more difficult as compared to the Mo metal complex. The M^{VI} to M^{IV} reduction requires much more reductive power (more negative redox potential) when the metal center M is a tungsten rather than a molybdenum atom. So, although the reduction of nitrate is stimulated when W replaces Mo in the active site of Nar the catalytic cycle breaks after the reduction of nitrate to nitrite when the biochemical reducer is not strong enough to reduce the metal center.

Ethylbenzene dehydrogenase (EBDH) is an enzyme that catalyzes the oxygen-independent, stereospecific hydroxylation of ethylbenzene to (*S*)-1-phenylethanol. EBDH active site models, derived from protein X-ray crystal structure, were computed at the COSMO-B3LYP/SDDp//B3LYP/Lanl2DZ(p) energy level of DFT in order to investigate most probable mechanism, ionic or radical pathway. In addition, different protonation states and participation of amino acid residues near to the Mo center were considered. Models with protonation of His_{192}, Lys_{450}, Asp_{223} and model without protonation were investigated for comparison. Computed relative energies indicate that the overall lowest energy barrier pathway results when ionic and radical pathways are mixed. This mechanism of ethylbenzene hydroxylation starts with a homolytic C_1-H_s bond cleavage (**TS1ô**) resulting in the formation of a radical type intermediate (**Iô**) and then in order to continue the reaction by the easier O_1H_s anion transfer, an electron needs to be transferred from the substrate to the Mo-OH moiety to transform the di-radical to the zwitter ionic intermediate. Then the transfer of O_1H_s anion from the Mo to the cationic substrate (**TS2**) results in the formation of product bound complex (**P**). Among those the protonated Lys site corresponds to the energetically best pathway for the hydroxylation of ethylbenzene by EBDH.

Acetylene hydratase (AH) of *Pelobacter acetylenicus* is a tungsten (W) containing iron-sulfur enzyme that catalyzes the transformation of acetylene to acetaldehyde. DFT studies were performed on the model complexes derived from the native protein X-ray crystal structure of AH. Based on the computational results we proposed the most likely nucleophilic mechanism for the hydration of acetylene by the acetylene hydratase (AH) enzyme. In this mechanism, the water (Wat_{1424}) molecule is coordinated to the W center and Asp_{13} is assumed to be in anionic form. The Wat_{1424} molecule is activated by W and then donates one of its proton to the anionic Asp_{13} forming the W-bound hydroxide and protonated Asp_{13}. The W-bound hydroxide then attacks the C_1 atom of acetylene together with the transfer of proton from the Asp_{13} to its C_2 atom, resulting in the formation of a vinyl alcohol intermediate complex. The energy barrier associated with this step is 14.4 kcal/mol. The final, rate limiting, step corresponds to the tautomerization of the vinyl alcohol intermediate to acetaldehyde via intermolecular assistance of two water molecules, associated with the energy barrier of 18.9 kcal/mol. An alternative, electrophilc pathway, was also considered but the energy barriers are found to be higher than for the nucleophilic pathway described here.

Sulfite oxidase (SO), selenate reductase (SeR) and nitrate reductases (NRs) are among the mononuclear molybdenum enzymes involved in the catalysis of metabolic redox reactions. The active site composition of SO has one molybdopterin (MPT) ligand and it *oxidizes* the sulfite to sulfate, SeR has two MPT ligands and it *reduces* the selenate to selenite, while NRs reduces nitrate to nitrite by either one or with two MPT's at the active site. Is the active site itself special in some way for the oxidation/reduction of one or the other substrate? Or do the different active sites behave essentially the same way and it is the role of the protein to make it specific. To clarify these, DFT studies were performed on the computational model complex, $[Mo^{VI}O_2(S_2C_2Me_2)SMe]^-$ (**A**, derived from the X-ray crystal structure of native SO), and on the experimental model complex $[Mo^{VI}O_2(mnt)_2]^{2-}$ (**B**, coordination mode similar to the active site of SeR) for the oxidation of selenite and sulfite. For the oxidation of sulfite model **A** which resembles the SO active site is clearly the best choice (lowest barrier, minor exothermicity). For the reduction of selenate a smaller activation is computed for model **A**, but the reaction is less exothermic with model **B**, which resembles the SeR active site.

DFT computations were also carried out on simple active site model complexes of SeR to investigate different ways of binding the substrate and the OAT reaction. Unfortunately, the results are little conclusive. Larger models might be needed to obtain more meaningful computational results.

Zusammenfassung

Ausgehend von der Protein-Röntgenbeugungs-Kristallstruktur der ersten wolframhaltigen Nitratreduktase, die aus *Pyrobaculum aerophilum* isoliert wurde, wurden molybdän- und wolframhaltige Modellkomplexe für das aktive Zentrum auf dem COSMO-B3LYP/SDDp// B3LYP/Lanl2DZ(p) Dichtefunktionaltheorie(DFT)-Niveau hinsichtlich der Reduktion von Nitrat berechnet. Der Mo-haltige Modellkomplex besitzt eine wesentlich größere Aktivierungsenergie (34.4 kcal/mol) für den Sauerstoffatomtransfer (OAT) von Nitrat auf das Metallzentrum als das W-Analogon (12.0 kcal/mol). Die Oxidation des Eduktkomplexes ist nahezu thermoneutral (-1.9 kcal/mol) für den molybdänhaltigen Modellkomplexes, aber deutlich exotherm (-34.7 kcal/mol) im Falle des Wolframkomplexes. Die vergleichsweise niedrige relative Energie des oxidierten Wolframkomplexes erschwert die Regeneration der Oxidationsstufe +IV deutlich im Vergleich zum Molybdänkomplex. Die Reduktion von M^{VI} zu M^{IV} erfordert also eine höhere Reduktionskraft (negativeres Redoxpotenzial), wenn das Metallzentrum M aus einem Wolfram- statt einem Molybdänatom besteht. Obwohl die Reduktion von Nitrat gefördert wird, wenn W das Mo im aktiven Zentrum ersetzt, wird der katalytische Zyklus nach der ersten Reduktion eines Nitrations unterbrochen, wenn das biochemische Reduktionsmittel nicht stark genug ist, das Metallzentrum zu reduzieren.

Das Enzym Ethylbenzoldehydrogenase (EBDH) katalysiert die sauerstoffunabhängige stereospezifische Hydroxylierung von Ethylbenzol zu (S)-1-Phenylethanol. Modellkomplexe für das aktive Zentrum von EBDH, abgeleitet aus der Protein-Röntgenbeugungs-Kristallstruktur, wurden mit dem COSMO-B3LYP/SDDp//B3LYP/Lanl2DZ(p) DFT-Niveau berechnet um den wahrscheinlichsten Mechanismus aufzufinden. Sowohl ionische als auch radikalische Reaktionspfade wurden in Betracht gezogen und zwar für verschiedene Protonierungszustände von Aminosäureresten, die wegen ihrer räumlichen Nähe zum Molybdänzentrum an der Reaktion teilhaben könnten. Modelle mit protonierten Aminosäureresten von His_{192}, Lys_{450} und Asp_{223} sowie ein Modell ohne Protonierung wurden vergleichend untersucht. Die berechneten relativen Energien weisen darauf hin, dass der Reaktionspfad mit den insgesamt geringsten Barrieren aus einer Mischung von ionischen und radikalischen Reaktionsschritten resultiert. Dabei wird die Hydroxylierung von Ethylbenzol durch einen homolytischen C_1-H_s Bindungsbruch (**TS1ó**) eingeleitet, was zu einem diradikalischen Intermediat (**Ió**) führt. Um dann den leichteren Transfer eines OH Anions zu ermöglichen, müsste zunächst ein Elektron vom Substrat auf die Mo-OH Einheit übertragen werden, was aus dem diradikalischen das zwitterionische Intermediat werden lässt. Die

Übertragung des O_1H_s Anions vom Molybdän auf das kationische Substrat (**TS2**) lässt den Produktkomplex (**P**) entstehen. Der energetisch günstigste Reaktionspfad für die Hydroxylierung von Ethylbenzol durch EBDH ergibt sich dabei für die protonierte Lysinseitenkette.

Acetylenhydratase (AH) aus *Pelobacter acetylenicus* ist ein wolframhaltiges Eisen-Schwefel-Enzym, das die Umsetzung von Acetylen zu Acetaldehyd katalysiert. Modellkomplexe, die aus der nativen AH-Proteinkristallstruktur abgeleitet wurden, wurden mit DFT-Methoden untersucht. Basierend auf den Rechenergebnissen wird ein nukleophiler Mechanismus als der wahrscheinlichste für die Hydratisierung von Acetylen durch AH vorgeschlagen. Gemäß diesem Mechanismus ist ein Wassermolekül (Wat_{1424}) an das W-Zentrum koordiniert und Asp_{13} wird als ionisiert angenommen. Das Wassermolekül Wat_{1424} ist durch das W aktiviert und gibt so ein Proton an die anionische Gruppe Asp_{13} ab, was zu einem W-gebundenen Hydroxid und protoniertem Asp_{13} führt. Das W-gebundene Hydroxid greift das C_1-Atom des Acetylens an und damit gekoppelt erfolgt der Protonentransfer von Asp_{13} auf das C_2-Atom. Dadurch bildet sich ein intermediärer Vinylalkohol-Komplex. Die Energiebarriere für diesen Schritt beträgt 14.4 kcal/mol. Den abschließenden, geschwindigkeitsbestimmenden Schritt stellt die Tautomerisierung des Vinylalkohols zu Acetaldehyd dar. Dafür wird unter Einbeziehung von zwei Wassermolekülen eine Barriere von 18.9 kcal/mol berechnet. Für einen alternativen, elektrophilen Reaktionspfad wurden höhere Barrieren als für den hier beschriebenen nukleophilen berechnet.

Sulfit Oxidase (SO), Selenat Reduktase (SeR) und Nitrat Reduktasen (NRs) gehören zu den mononuklearen Molybdoenzymen, die metabolische Redoxreaktionen katalysieren. Das SO aktive Zentrum besitzt einen Molybdopterinliganden (MPT) und *oxidiert* Sulfit zu Sulfat; SeR mit zwei MPT *reduziert* Selenat zu Selenit; NRs schließlich können Nitrat zu Nitrit reduzieren und besitzen entweder einen oder zweit MPT-Liganden im aktiven Zentrum. Ist das aktive Zentrum in irgendeiner Art spezifisch für die Oxidation bzw. die Reduktion des einen oder anderen Substrates? Oder verhalten sich die verschiedenartigen Aktiven Zentren im Wesentlichen gleich und erst das Protein schafft Spezifität? Zur Klärung dieser Fragen wurde die Selenit- und die Sulfitoxidation durch Modellkomplexe mit DFT rechnerisch untersucht: $[Mo^{VI}O_2(S_2C_2Me_2)SMe]^-$ (**A**, abgeleitet von der Röntgenkristallstruktur der nativen SO) und der auch experimentell untersuchte Modellkomplex $[Mo^{IV}O(mnt)_2]^{2-}$ (**B**, mit einem der SeR ähnlichen Koordinationsmuster). Für die Oxidation von Sulfit stellt Modell **A** tatsächlich die beste Wahl dar (geringste Barriere, geringfügig exotherme Reaktionsenergie).

Für die Reduktion von Selenat hingegen wird zwar mit Modell **A** eine geringere Barriere berechnet, aber die Reaktion verläuft mit Modell **B** weniger stark exotherm.

Weitere DFT Rechnungen wurden an einfachen Modellkomplexen zum aktiven Zentrum der SeR unternommen, um verschiedene Bindungsmodi des Substrats und die Sauerstoffübertragung zu untersuchen. Die Ergebnisse sind leider wenig aufschlussreich. Größere Modelle dürften nötig sein um sinnvollere Rechenergebnisse zu erhalten.

Introduction

1) Enzymes

Almost all processes in the biological cell need enzymes to occur at significant rates.

$$E + S \overset{\text{Substrate binding}}{\rightleftharpoons} ES \xrightarrow{\text{Catalytic Step}} \acute{E} + P \quad (1.1)$$

Eq. 1.1: Simple mechanism for the enzyme (**E**) substrate (**S**) reaction, **É** = reduced enzyme, **P** = product.

Enzymes are proteins that catalyze chemical reactions. Metals occur as natural constituents of these proteins. Enzymes vary in their size and properties. Most enzymes are much larger than the substrates they act on, and only a small portion of the enzyme (around 3–4 amino acids) is directly involved in catalysis. Approximately one-third of all proteins and enzymes purified to apparent homogeneity require metal ions as cofactors for biological function. They are called metalloproteins. Metalloproteins when perform catalytic function are called metalloenzymes and metal ions in these enzymes are usually part of the active sites. Active site is the region that is involved in catalysis contains the catalytic residues, binds the substrate, and then carries out the reaction.[1,2]

2) Chemical properties of Molybdenum and Tungsten

Molybdenum and tungsten are the only 4d (Mo) and 5d (W) transition metals (of group 6) that are involved in the metabolism of biological systems. The atomic radii and electron affinity for molybdenum and tungsten are almost the same because of the lanthanide contraction. The coordination chemistry of both the elements is comparable. Both form complexes in oxidation state ranges from –II to +VI, of which +IV, +V, and +VI oxidation states are relevant in biological systems (Table 1.1).[3]

Despite of their chemical properties, their geochemistry in the Earth´s crust is quite different. Molybdenum occurs as molybdenite, MoS_2, whereas tungsten occurs as scheelite, $CaWO_4$, and wolframite, $(Fe, Mn)WO_4$ in the Earth´s crust. The reduced tungstenite (WS_2) is very rare because WS_2 is readily solubilized.[4]

$$WS_2 + 4H_2O \rightleftharpoons WO_4^{2-} + 2H_2S + 4H^+ + 2e^- \quad (1.2)$$

Primary mechanism for the uptake and transport of both molybdenum and tungsten involves the binding of $[MO_4]^{2-}$ tetrahedral anions in a cavity of suitable size by hydrogen bonds from

the polypeptide chain. Because of the same size of $[MoO_4]^{2-}$ and $[WO_4]^{2-}$, the transport proteins do not discriminate significantly between the two $[MO_4]^{2-}$ anions.[5,6]

Table 1.1: Physical and Chemical properties of molybdenum and tungsten.

Properties	**Molybdenum (Mo)**	**Tungsten (W)**
Atomic number	42	74
Average atomic weight	95.94	183.85
Electronic configuration of outer shell	$4d^5\ 5s^1$	$4f^{14}\ 5d^4\ 6s^2$
Atomic radii (Å)	1.40	1.40
Ionic radii for +IV oxidation state (Å)	0.65	0.66
Ionic radii for +V oxidation state (Å)	0.61	0.62
Ionic radii for +VI oxidation state (Å)	0.59	0.60
Electronegativity	1.8	1.7
pKa of Oxo acid (MO_4^{2-}/HMO_4^-)	3.87	4.60
Concentration in sea water	~100 nM	~ 1 pM
Concentration in fresh water	~ 5-50 nM	~ 500 pM
M=O bond length (Å)	1.76	1.76

3) Biological distribution of Molybdenum and Tungsten enzymes

Enzymes containing molybdenum or tungsten at their active sites appear to be present in all forms of life, from ancient archaea to man. These enzymes catalyze a wide range of reactions in carbon, sulfur, and nitrogen metabolism.[7,8,9] In general, these enzymes utilize water as the ultimate source or sink of oxygen in the overall catalytic reaction. The reactions are coupled to electron transfer between substrate X/XO, a Fe-S center, heme, or flavin.

$$X + H_2O \rightleftharpoons XO + 2H^+ + 2e^- \quad (1.3)$$

The enzymes are referred to as ***oxotransferases*** when the substrate is transformed by primary oxygen atom transfer and as ***hydroxylases*** when bound or unbound water or hydroxide is directly involved in the substrate transformation reaction.[10]

3.1 Molybdenum Enzymes

Molybdenum enzymes have been known for more than 75 years and are found in all types of living systems.[9,11,12] Molybdenum is widely available to biological systems due to the

solubility of its high-valent oxides in water. It is found in two basic forms: as an integral component of the multinuclear M center of nitrogenases[13,14] and as the mononuclear active sites of a much more diverse group of enzymes that in general function catalytically to transfer an oxygen atom either to or from a physiological acceptor/donor molecule. It is on the basis of this commonly encountered aspect of catalysis that these enzymes are frequently referred to as oxotransferases.[10] These enzymes catalyze a variety of important reactions in the metabolism of nitrogen and sulfur containing compounds and also of various carbonyl compounds (e.g., aldehydes, formate, CO and CO_2). In plants, e.g., nitrate reductases catalyze the first and rate-limiting step in the assimilation of nitrate from the soil,[15] and an indole-3-acetaldehyde oxidase is responsible for the final step in the biosynthesis of the hormone indole-3-acetate.[16] In bacteria and archaea, these enzymes catalyze the hydroxylation of a carbon center as the first step in the breakdown of these compounds.[17,18,19,20] In addition, fish bacterial enzymes, such as trimethylamine-N-oxide (TMAO) reductase and dimethylsulfoxide (DMSO) reductase from algae catalyze terminal oxidation reactions under a variety of conditions.[21] In humans, xanthine oxidoreductase catalyzes the final two steps in purine metabolism: sequential hydroxylation of hypoxanthine to xanthine and then uric acid.[22] The closely related mammalian aldehyde oxidases are important in the metabolism of a variety of aldehyde compounds and have implications specifically in the biosynthesis of retinoic acid, both in the retina and in the developing nervous system.[23] Finally, sulfite oxidase is responsible for the final step of sulfur metabolism in humans: oxidation of sulfite to sulfate.[24]

3.2 Tungsten Enzymes

In contrast to molybdenum, evidence for the involvement of tungsten in biological systems has been obtained not more than 25 years ago.[25,26] Initial studies showed that the production and activity of formate dehydrogenase, which catalyzes the first step in the reduction of CO_2 to acetate, was significantly higher in acetogens if the bacteria were grown in the presence of $[WO_4]^{2-}$ rather than $[MoO_4]^{2-}$.[27,28] The first tungsten containing enzyme was purified and characterized, from an acetogen, a bacterium that grows by producing acetate.[29] Tungsten is important for the metabolism of hyperthermophilic archaea that live in volcanic vents on the sea bed at > 100°C.[30] Although more than a dozen tungstoenzymes have been isolated and characterized from bacteria and archaea, it has yet to be isolated from higher organism.

4) Pyranopterin cofactor

An organic pterin cofactor, commonly called Moco, is present in all mononuclear molybdenum and tungsten enzymes. In the literature it is referred to as molybdopterin for molybdenum enzymes and pyranopterin for tungsten enzymes. This cofactor does not participate directly in catalysis but it appears to be involved in electron transfer from the metal center once it has been reduced by a substrate.

The pterin structure of Moco is unique in nature and has probably been evolved in order to control and maintain the special redox properties of Mo. The task of cofactor is to position the catalytic metal, Mo, correctly within the active site, to control its redox behavior and to participate with its pterin ring system in the electron transfer to or from the Mo atom. The pterin with its several possible reduction states as well as different structural conformations could also be important for channeling electrons to other prosthetic groups.[31,32] X-ray crystallographic analyses of Mo-enzymes revealed that the cofactor is not located on the surface of the protein, but it is buried deeply within the interior of the enzyme and a tunnel-like structure makes it accessible to the appropriate substrates.[31,32,33]

Moco containing enzymes can be distinguished according to their amino acid sequences, spectroscopic properties, active site structures and catalyzed reactions. Eukaryotic molybdenum enzymes usually contain only one pterin as cofactor, whereas prokaryotic enzymes can contain different cofactors consisting of one or two pterins and a nucleotide covalently linked to the pterin (Fig 1.1). It coordinates to the metal via the ene-di-thiolate moiety.[7]

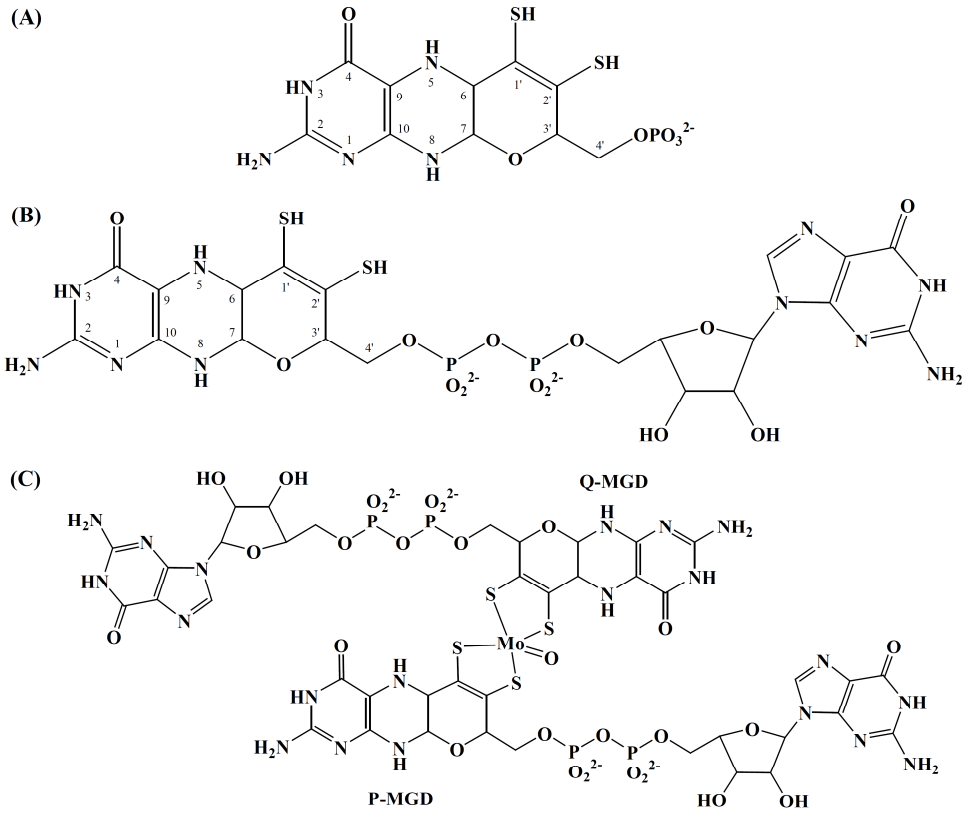

Fig. 1.1: Cofactors of molybdenum and tungsten enzymes, (**A**) Molybdenum cofactor called molybdopterin (Moco)[34], (**B**) Molybdopterin guanosine dinucleotide (MGD)[35], (**C**) Extended molybdenum cofactor (bis-MGD)[36]

5) Classification and structure of the Molybdenum enzymes

According to the molybdenum cofactors, molybdenum enzymes are classified into three families (Fig. 1.2), named

5.1 The Molybdenum Hydroxylases (Xanthine Oxidase family)

5.2 The Eukaryotic Oxotransferases (Sulfite Oxidase family)

5.3 The Prokaryotic Oxotransferases (DMSO Reductase family)

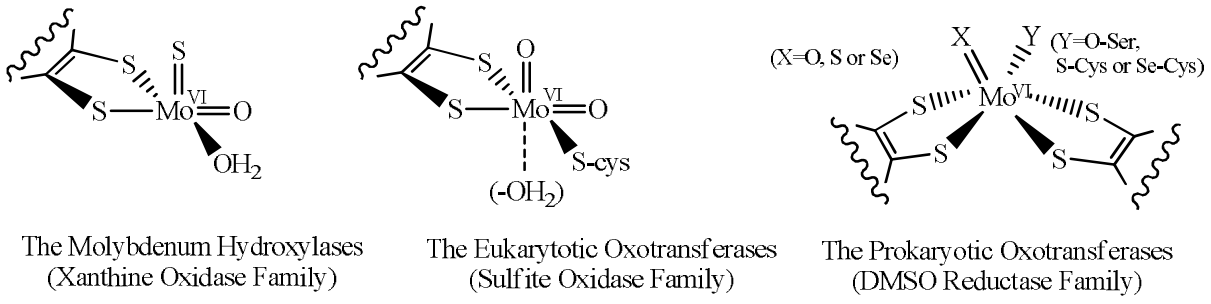

Fig. 1.2: Active site composition of major families of mononuclear molybdenum enzymes

5.1 The Molybdenum hydroxylases

The molybdenum hydroxylases constitute the largest group of mononuclear molybdenum enzymes. More than 20 enzymes have been characterized to varying degree ranging from the xanthine and aldehyde oxidoreductases from higher organisms to bacterial enzymes responsible for the hydroxylation of a diverse range of aromatic heterocycles.[9]

These enzymes contain the molybdenum cofactor, Moco, in which molybdenum is associated with a pterin derivative, called molybdopterin. The active sites of these enzymes contain a molybdenum atom coordinated with two dithiolene sulfur atoms of the molybdopterin unit, terminal oxygen, sulfur atom and terminal hydroxide/water molecule (Fig. 1.2).[37] These Moco containing enzymes participate in hydroxylation and oxo-transfer reactions that are two electron transfer processes occurring at the Moco site. Water is the ultimate source of the oxygen atom incorporated into the substrate, and reducing equivalents are generated in this process.[38] Moco enzymes usually contain additional redox-active cofactors, such as iron-sulphur clusters, flavins or haem centers, which mediate electron transfer from Moco to the final electron acceptor.[39]

The properties of these enzymes are closely related.[40,41,42] They play important roles in the metabolism of exogenous compounds. These flavoenzymes generally catalyze nucleophilic oxidation of *N*-heterocycles, resulting in metabolites different from those obtained via electrophilic oxidation by the cytochrome P_{450} system. However, the substrate specification among these enzymes differs.[43]

5.1.1. Aldehyde Oxidase
5.1.2. Xanthine Oxidase / Dehydrogenase

5.1.1. Aldehyde Oxidase

Aldehyde oxidase belongs to a large family of molybdenum enzymes whose members catalyze the oxidative hydroxylation of a diverse range of aldehydes and nitrogen-containing aromatic heterocycles, isoxazole, and isothiazole in reactions that necessarily involve the cleavage of a C-H bond. These enzymes are properly considered hydroxylases,[44] although product tautomerization in reactions involving heterocyclic substrates usually results in the keto rather than enol form predominating in aqueous solution.

$$RCHO + H_2O \rightarrow RCOOH + 2H^+ + 2e^- \quad (1.4)$$

The aldehyde oxidoreductase from *Desulfovibrio gigas* was the first mononuclear enzyme for which an X-ray crystal structure was reported, at 2.25 Å resolution[45] (later refined to 1.8 Å resolution[46]). The pterin cofactor in this enzyme is a molybdopterin cytosine dinucleotide. It has pair of 2Fe-2S centers but lacks the flavin domain. This crystal structure indicates the presence of a glycine residue, Gly_{623}, in the molybdenum-binding portion of the protein that is conserved among the hydroxylase family of mononuclear molybdenum enzymes.[45]

5.1.2. Xanthine Oxidase or Xanthine Dehydrogenase

Xanthine oxidase and xanthine dehydrogenase are two forms of the same enzyme, differing in the co-substrate for the reaction: xanthine oxidase utilizes molecular oxygen whereas xanthine dehydrogenase utilizes NAD^+. These enzymes play an important role in the catabolism of purines in some species, including humans.[42, 47]

Xanthine oxidase is a homodimer that possesses FAD (flavin adenine dinucleotide) in addition to the molybdenum cofactor, Moco and as additional redox center a pair of 2Fe-2S centers. Members of the xanthine oxidase family generally catalyze hydroxylation reactions of the type

$$RH + H_2O \rightarrow ROH + 2H^+ + 2e^- \quad (1.5)$$

This stoichiometry is unique among biological systems catalyzing hydroxylation reactions as reducing equivalents are generated rather than consumed in the course of the reaction, and water[48] rather than dioxygen is utilized as the ultimate source of the oxygen atom incorporated into the substrate. The overall reaction mechanism of these and related enzymes is typically broken down into reductive and oxidative half-reactions of the catalytic cycle, defined from the standpoint of the enzyme. It is the reductive half-reaction in which the molybdenum center participates, with the metal becoming reduced from Mo (VI) to Mo (IV).[9] Re-oxidation of the molybdenum center takes place via simple electron transfer to the other redox-active centers of the enzyme, ultimately to the FAD where electrons are removed from the enzyme by reaction with dioxygen.[49,50,51,52]

5.2 The Eukaryotic Oxotransferases

These enzymes also contain the molybdenum cofactor, Moco. The active sites of these enzymes are composed of a molybdenum atom coordinated with two dithiolene sulfur atoms of the molybdopterin unit, a sulfur atom of cysteinate and two terminal oxygen atoms. These

enzymes catalyze oxygen atom transfer reactions to or from an available electron lone pair of substrate and can itself be subdivided into two families.

5.2.1. Sulfite Oxidase

5.2.2. Assimilatory nitrate reductase

5.2.1. Sulfite Oxidase

Sulfite oxidase possesses another redox-active center in addition to the molybdenum: a *b*-type cytochrome. It catalyzes the oxidation of sulfite to sulfate[53,54] which is the terminal reaction in the oxidative degradation of the sulfur-containing amino acids cysteine and methionine.

$$SO_3^{2-} + H_2O \rightarrow SO_4^{2-} + 2H^+ + 2e^- \quad (1.6)$$

Oxidation of sulfite by the enzyme is efficient even at very low concentration of substrate and occurs in the presence of electron acceptors other than oxygen.[55] The conversion of sulfite to sulfate is a two-electron oxidation, whereas cytochrome *c*, the physiological electron acceptor for sulfite oxidase, is a one electron acceptor. Sulfite oxidation occurs at the molybdenum center and cytochrome *c* reduction at the heme site.

The enzyme also plays an important role in detoxifying exogenously supplied sulfite and sulfur dioxide. In humans, the deficiency of sulfite oxidase may lead to neurological problems, mental retardation, and dislocation of the ocular lens.

5.2.2. Assimilatory Nitrate Reductase

Assimilatory nitrate reductases also possess redox-active centers in addition to the molybdenum: a *b*-type cytochrome and FAD. These enzymes have been isolated from fungi, algae, and higher plants. They catalyzes a redox reaction involving an electron transport chain at the two active sites, i) the cytochrome *b* reductase fragment contains the active site where NAD(P)H transfer electrons to FAD and these electrons are transferred to the Mo-MPT by the internal cytochrome *b*, ii) the nitrate reductase, Mo-MPT active site, to reduce nitrate to nitrite.[56,57] The overall reaction is

$$NO_3^- + NADH \rightarrow NO_2^- + NAD^+ + OH^- \quad (1.7)$$

This is the first and the rate-limiting step in nitrogen assimilation in higher plants, the uptake of nitrate, a light dependent phenomenon. This metabolic role is different from that of the dissimilatory nitrate reductase of bacteria.[58]

5.3 The Prokaryotic Oxotransferases

The prokaryotic oxo-transferases family, also called DMSO reductase family, is a diverse group of enzymes that catalyzes either oxygen atom transfer or other redox reactions. The active site of these enzymes consists of a molybdenum atom coordinated by a pair of dithiolene ligands, a terminal oxygen atom and one amino acid ligand (oxygen atom of serinate or oxygen atom of aspartate or sulfur atom of cysteine or selenium atom of cysteine or hydroxide, depending on the surrounding polypeptide chains). These enzymes are found as integral components of multisubunit membrane-bound proteins that possess additional redox-active centers in other subunits. They are particularly important in the anaerobic respiration including the dissimilatory reduction of certain toxic oxo-anions.[59]

Members of this family so far have been divided into:

5.3.1. DMSO Reductase (DMSOR)
5.3.2. Trimethylamine *N*-Oxide Reductase (TMAOR)
5.3.3. Nitrate Reductase (NR)
5.3.4. Formate Dehydrogenase (FDH)
5.3.5. Pyrogallol-phloroglucinol transhydroxylase (TH)
5.3.6. Arsenite Oxidase (AO)

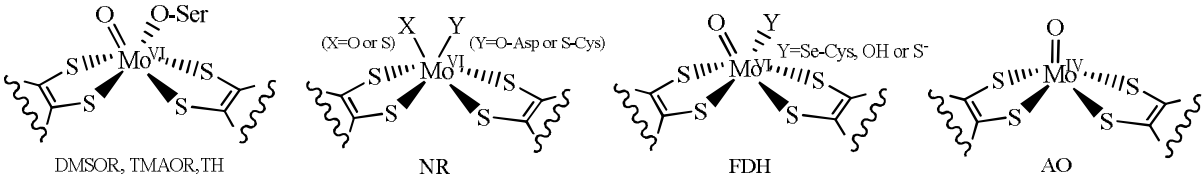

Fig. 1.3: Active site composition of the members of prokaryotic oxotransferases.

5.3.1. DMSO Reductase (DMSOR)

DMSO reductase, isolated from *Rhodobacter* species, is linked to the respiratory chain of the organism. The sixth coordination site of molybdenum is occupied by the oxygen of a serinate from the polypeptide (Fig. 1.3). This enzyme has no other redox-active center other than molybdenum while the DMSO reductase from *E.coli* is a multi-subunit protein.[21] Other than molybdenum subunit it possesses four 4Fe/4S iron-sulfur clusters, and a membrane anchor which lacks redox-active centers but has a quinol binding site.[60]

DMSO reductase is an oxotransferase that catalyzes the reductive deoxygenation of dimethyl sulfoxide (DMSO) to dimethyl sulfide (DMS) in a two stage reaction. In the first stage, DMSO binds to reduced (Mo^{IV}) enzyme, which is oxidized to Mo^{VI} with an extra oxygen ligand and DMS is released. In the second stage, the reduced enzyme is regenerated by transfer of two electrons from a specific cytochrome, resulting in the release of oxygen as a water molecule.[61] The overall reaction is:

$$Me_2SO + 2e^- + 2H^+ \rightleftharpoons Me_2S + H_2O \quad (1.8)$$

5.3.2. Trimethylamine *N*-Oxide Reductase (TMAO)

Trimethylamine *N*-oxide, from *E.coli*, is a periplasmic molybdoenzyme that catalyzes the reduction of trimethylamine *N*-oxide (TMAO) to trimethylamine (TMA) during an anaerobic respiratory process.

$$(CH_3)_3NO + 2H^+ + 2e^- \rightarrow (CH_3)_3N + H_2O \quad (1.9)$$

The properties of TMAO reductases have been studied in several organisms. The active site structure is very similar to the DMSO reductase. Based on their substrate specificity, these enzymes can be divided into two groups, the TMAO reductases which have high substrate specificity and DMSO/TMAO reductases which can reduce a broad range of *N* and *S*-oxide substrates. The TMAO reductase from *E.coli, Shewanelly putrefaciens* and *Roseobacter denitrificans* are unable to reduce *S*-oxide compounds and belongs to the first group. In the second group, the constitutive DMSO from *E.coli* and *Proteus vulgari*s and the DMSO reductases from *Rhodobacter capsulatus* or *R. sphaeroides* can reduce TMAO as well as other *N* and *S*-oxides. Except the constitutive DMSO reductases from *E. coli* and *P. vulgaris* which are membrane bound all these molybdoenzymes are located in the periplasm and induced by TMAO.[62]

TMAOR, from *Escherichia coli, Shewanelly massilia, Salmonella typhimurium* and *Roseobacter denitrificans*, possess oxygen atom of serine at the sixth coordination site of molybdenum (Fig. 1.3). It also possesses *b*-type cytochrome as a redox-active center.[62]

5.3.3. Nitrate Reductase (NR)

Nitrate reductases, molybdo-iron-flavoproteins, are playing key roles in the first step of ammonification, denitrification and dissimilatory ammonification. They catalyze the reduction of nitrate to nitrite, by transferring an oxygen atom from nitrate to molybdenum. Two electrons and two protons are consumed in the process, and in the end a water molecule

is produced. Electrons are transferred to the active site of NR by the *b*-type cytochrome and an iron-sulfur containing subunit of the nitrate reductase.

$$NO_3^- + 2H^+ + 2e^- \rightarrow NO_2^- + H_2O \quad (1.10)$$

This reduction of nitrate is performed by the organisms for three principle reasons: to incorporate nitrogen into biomolecules, to generate energy for cellular function, and to dissipate extra energy by respiration.[63,64] Although the chemical reaction is always the reduction of nitrate to nitrite, the prokaryotic nitrate reductases have been classified into three groups, assimilatory nitrate reductase (NAS), respiratory nitrate reductase (NAR) and periplasmic nitrate reductase (NAP). NAR and NAP are linked to respiratory electron transport systems and are located in the membrane and periplasm, respectively. NAS is located in the cytoplasm.[65]

These nitrate reductases from a variety of bacterial and archaeal sources are more closely related to DMSO reductase. In the NAP, dissimilatory nitrate reductase from *Desulfovibrio desulfuricans* (*Dd*NapA), the sixth coordination site is occupied by a sulfur atom of cysteine (Fig 1.4). It possesses a 4Fe/4S iron-sulfur cluster as a redox-active center in addition to molybdenum in the same polypeptide chain. For NAR, respiratory nitrate reductase from *E.coli* (*Ec* NarGHI, *Ec* NarGH), two structures were reported (Fig 1.4), where NarG represents the molybdenum catalytic active site of the protein. The sixth coordination site of molybdenum is occupied by an oxygen atom of aspartate (Asp_{222}). In the NarGHI, Asp_{222} acts as a bidentate ligand, but in NarGH, where an additional oxo group is attached with molybdenum, it acts as a monodentate ligand.[66] The two *E.coli* nitrate reductases (NAR) also possess further redox-active sites, three 4Fe-4S, one 3Fe-4S and the membrane anchor subunit a pair of *b*-type cytochromes.[67] Unlike eukaryotic nitrate reductase, no heme or flavin adenine dinucleotide (FAD) is present in the active subunit of NAS.[68]

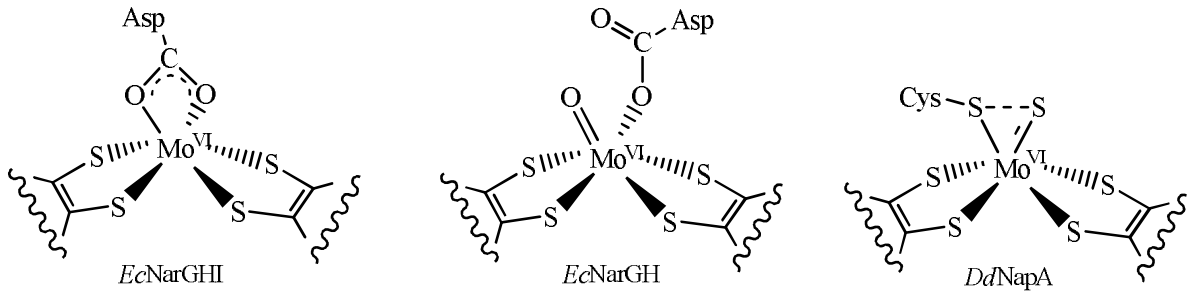

Fig. 1.4: Active site composition of nitrate reductases.

5.3.4. Formate Dehydrogenase (FDH)

Formate dehydrogenase, a membrane bound enzyme, catalyzes the oxidation of formate to carbon dioxide as the first step in acetogenic glucose fermentation.[69]

$$HCOO^- \rightarrow CO_2 + H^+ + 2e^- \quad (1.11)$$

There are two molybdenum containing FDH from *Escherichia coli*, the FDH-H which is one of the components of the formate hydrogen lyase complex in *E.coli*[70] and FDH-N, a membrane bound protein, which is supposed to participate in the redox loop of the proton motive force generation across the membrane cell.[71] FDH from *Desulfovibrio desulfuricans* is also a molybdenum containing enzyme.[72,73] *Desulfovibrio alaskensis* has been shown to produce two active isoforms, W-FDH and Mo-FDH, each containing either tungsten or molybdenum as an active metal. The two isoforms have similar molecular properties and cannot be chromatographically separated, which suggests they have the same isoelectronic point.[74]

Selenocysteinate is present as the sixth ligand attached to the molybdenum in most of the FDHs but there is an exception where, instead of selenocysteinate, one hydroxyl or sulfide ligand is present (Fig 1.3).[69]

Instead of oxygen atom transfer from the molybdenum to the substrate, the current proposed mechanism for these enzymes suggests a replacement of the hydroxyl group bound to the molybdenum by one of the oxygen atoms from formate, resulting in the reduction of Mo^{VI} to Mo^{IV} and the cleavage of C-H bond.[70]

5.3.5. Pyrogallol-phloroglucinol Transhydroxylase (TH)

The Mo containing transhydroxylase from the anaerobic microorganism *Pelobacter acidigallici* is a cytoplasmic enzyme. It catalyzes the conversion of pyrogallol to phloroglucinol by the transfer of hydroxyl group in the absence of oxygen.

$$C_6H_6O_3 \text{ (1, 2, 3-trihydroxybenzene)} \rightarrow C_6H_6O_3 \text{ (1, 3, 5-trihydroxybenzene)} \quad (1.12)$$

It is a non-redox reaction. The active site structure is similar to the DMSO reductase (Fig 1.3). Although there are additional three iron-sulfur redox-active centers, [4Fe-4S], their role is still not clear.[75]

5.3.6. Arsenite Oxidase

Arsenite Oxidase from *Alcaligenes faecalis*, a molybdo-iron enzyme, is involved in the detoxification of arsenic. It catalyzes the oxidation of arsenite to arsenate.

$$As^{III}O_2^- + 2H_2O \rightarrow As^{V}O_4^{3-} + 4H^+ + 2e^- \quad (1.13)$$

Like for the other subgroups of the prokaryotic oxidoreductase family, the molybdenum atom in *A. faecalis* arsenite oxidase is not coordinated by the side chain of a serine, cysteine, or selenocysteine residue (Fig 1.3). The corresponding residue is Alanine199 (Ala_{199}) but there is no covalent linkage between the molybdenum atom and the polypeptide chain. As a consequence, the loop containing this residue is folded away from the Mo site and the active site is significantly more exposed than in the other subgroups. It also possesses two redox active sites, iron-sulfur containing [3Fe-4S] and [2Fe-2S] and azurin or cytochrome *c*.[76]

6) Classification and structure of Tungsten enzymes

Tungstoproteins are usually found in thermophilic organisms that grow in extreme environments.[77,78] Tungstoenymes are involved in the low redox potential reactions. They can be classified into three functionally and phylogenetically distinct families:

6.1 The Aldehyde Ferredoxin Oxidoreductase Family (AOR)

6.2 The Formate/ Formyl Methanofuran Dehydrogenase Family (F(M)DH)

6.3 The Acetylene Hydratase Family (AH)

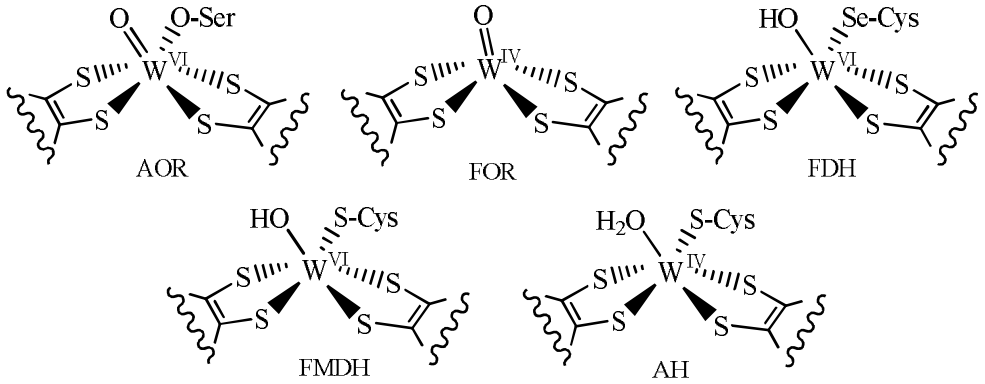

Fig. 1.5: Active site composition of tungsten containing enzymes.

6.1 The Aldehyde Ferredoxin Oxidoreductase Family (AOR)

The majority of the known tungstoenzymes belong to this family. The enzymes in this family are related phylogenetically and display high sequence similarity at the amino acid level. However, none of the enzyme of this family shows any sequence similarity to any known molybdoenzyme. These enzymes catalyze the oxidation of various types of aldehydes to the corresponding acids and use ferredoxin as redox active site.

$$RCHO + H_2O + 2Fd_{(ox)} \rightarrow RCOOH + 2H^+ + 2Fd_{(red)} \quad (1.14)$$

Where, RCHO represents the substrate with the aldehyde functional group and Fd represents the electron acceptor ferredoxin.

Enzymes of this family are generally oxygen sensitive and have broad range of substrate specificities. In these enzymes the tungsten atom coordinates to *bis*-pterin cofactors, to a terminal oxygen atom and an amino acid ligand depending on the surrounding polypeptide chain. It also possesses an electron transferring [4Fe-4S] cluster.[79,80]

Members of this family have been divided into:

6.1.1. Aldehyde Ferredoxin Oxidoreductase (AOR)
6.1.2. Formaldehyde Ferredoxin Oxidoreductase (FOR)
6.1.3. Glyceraldehyde-3-Phosphate Ferredoxin Oxidoreductase (GAPOR)
6.1.4. Carboxylic Acid Reductase (CAR)
6.1.5. Aldehyde Dehydrogenase (ADH)

6.1.1. Aldehyde Ferredoxin Oxidoreductase (AOR)

Aldehyde ferredoxin oxidoreductase (AOR) is purified from hyperthermophilic archaeon *Pyrococcus furiosus*[81], *Pyrococcus* strain ES4[82] and *Thermococcus* strain ES1.[83] The enzyme is extremely sensitive to oxygen. It oxidizes a broad range of both aliphatic and aromatic aldehydes to their corresponding acids. It catalyzes the reversible oxidation of aldehydes to their corresponding carboxylic acids with the accompanying reduction of the redox protein ferredoxin, the proposed physiological electron acceptor, Fd (eq. 1.14).
The Fd of *P. furiosus* contains a single [4Fe-4S] cluster and it undergoes a one-electron redox reaction. So one catalytic turnover per subunit requires the reduction of two molecules of Fd. In the active site tungsten is coordinated by two diothiolene side chains from two pterin cofactors, linked to each other via Mg^{2+} ion through their terminal phosphate groups. No protein ligand is coordinated with the tungsten. The [4Fe-4S] cluster is only at a distance of 10Å from the tungsten. It is coordinated by the protein via four cysteine ligands. One of these cysteine forms a hydrogen bond with a pterin ring nitrogen atom, which indicates that pterin might have an active role in the redox chemistry of this enzyme.[84,85]

6.1.2. Formaldehyde Ferredoxin Oxidoreductase (FOR)

Formate ferredoxin oxidoreductase (FOR) is purified from *Thermococcus litoralis*[86] and *Pyrococcus furious.*[87] It not only oxidizes formaldehyde (as the name indicates) but it can also use other short chain (C_1-C_4) aldehydes as substrates. Although, its activity is lost with the long chain aldehydes but it can oxidize C_4-C_6 acid substituted aldehydes and dialdehydes.[88]

$$CH_2O + H_2O + 2Fd_{(ox)} \rightarrow HCOOH + 2H^+ + 2Fd_{(red)} \quad (1.15)$$

Structurally FOR is similar to AOR, i.e. it contains a tungsto-*bis*-pterin cofactor, an [4Fe-4S] cluster and a Mg^{2+} ion bridging the two pterins but it also contains a Ca atom per subunit. The function of Ca, however, is still not known.[87]

6.1.3. Glyceraldehyde-3-Phosphate Ferredoxin Oxidoreductase (GAPOR)

Glyceraldehyde-3-Phosphate Ferredoxin Oxidoreductase (GAPOR) is purified from *Pyrococcus furiosus*[89]. It catalyzes the oxidation of glyceraldehyde-3-phosphate (GAP) to 3-phosphoglycerate. It is absolutely specific for its substrate and so far GAP is its only substrate. It cannot oxidize non-phosphorylated aldehydes such as formaldehyde, acetaldehyde, benzaldehyde, nor related compounds like glucose-6-phosphate or glycerol 3-phosphate[3].

$$\text{Glyceraldehyde-3-phosphate} + H_2O + 2Fd_{(ox)} \rightarrow \text{3-phosphoglycerate} + 2H^+ + 2Fd_{(red)} \quad (1.16)$$

This enzyme plays a key role in the glycolytic pathway during carbohydrate (maltose) metabolism in *P. furiosus*, where it converts the GAP dehydrogenase and phosphoglycerate kinase (PGK) to 3-phosphoglycerate. Like AOR and FOR, it contains a tungsto-*bis*-pterin cofactor, an [4Fe-4S] cluster and two Zn atoms per subunit. The function of Zn is still not known[90].

6.1.4. Carboxylic Acid Reductase (CAR)

Carboxylic acid reductase (CAR) is isolated from moderately thermophilic acetogenic bacteria, *Clostridium formicoaceticum*. It catalyzes the reduction of a wide range of aliphatic and aromatic non-activated carboxylic acids to aldehydes at the expense of reduced viologens (toxic bipyridinium derivatives of 4, 4'-bipyridyl).

$$RCOOH + 2H^+ + 2\text{“}e^-\text{”} \rightarrow RCHO + H_2O \quad (1.17)$$

However, neither its physiological electron carrier nor its function inside the cell is known. CAR in *Clostridium thermoaceticum* seems to be present in two forms. One of them contains a flavin (FAD) group. Compared with the other enzymes in the AOR family these two CAR enzymes are more complex, with multiple subunits and a much higher Fe content.[91,92]

6.1.5. Aldehyde Dehydrogenase (ADH)

Aldehyde dehydrogenase (ADH) is purified from sulfate reducing *Desulfovibrio gigas*[93]and *Desulfovibrio simplex.*[94] ADH from *D.gigas* catalyzes the oxidation of wide variety of

aldehyde substrates. It sufficiently oxidizes the C_3-C_4 aldehydes like acetaldehyde and propionaldehyde. It contains a tungsto-*bis*-pterin cofactor and one [4Fe-4S] cluster. The physiological electron carrier inside the cell is not known. ADH from *D. simplex* oxidizes both aliphatic and aromatic aldehydes and can use flavins (FMN or FAD) as electron carriers.

When *D. gigas* is grown in the absence of tungsten it produces a Mo-containing aldehyde-oxidizing enzyme termed aldehyde oxidoreductase (AOX).[92]

6.2 The Formate/ Formyl Methanofuran Dehydrogenase Family (F(M)DH)

The enzymes of this family are extremely sensitive to oxygen inactivation, which makes them difficult to isolate and characterize. They use carbon dioxide as a substrate. Members of this family are:

6.2.1. Formate Dehydrogenase (FDH)

6.2.2. Formyl Methanofuran Dehydrogenase (FMDH)

6.2.1. Formate Dehydrogenase (FDH)

Formate dehydrogenase (FDH), a tungsten-selenium-iron-sulfur protein, is purified from thermophilic acetogenic bacterium *Clostridium thermaceticum*[95] and *Desulfovibrio gigas*[96]. It catalyzes the reduction of CO_2 to formate and is the first reaction of an autotroph CO_2-fixation pathway occurring in many anaerobic bacteria.[95]

$$CO_2 + NADPH \rightarrow HCOO^- + NADP^+ \quad (1.18)$$

FDH from *C. thermaceticum* has tungsten atom coordinated to the two pterin cofactors. It also possesses FeS centers and unusual amino acid selenocysteine. It is extremely oxygen sensitive and uses NADP as the electron acceptor[3,79]. FDH from *D. gigas* was isolated in the presence of oxygen, although the activity could be only measured under strictly anoxic conditions. This FDH has mononuclear tungsten atom coordinated by two pterin cofactors, which are of the dinucleotide form (MGD). It also possesses two [4Fe-4S] clusters as redox active sites. No selenium atom is found in this enzyme. FDH from *D. gigas* is more related to the Mo containing FDHs as compared to AOR.[96]

6.2.2. Formyl Methanofuran Dehydrogenase (FMDH)

N-Formylmethanofuran (formyl-MFR) is purified from hyperthermophilic sulfate reducing archaeon, *Archaeoglobus fulgidus.*[97] FMDH is involved in the first step of the conversion of CO_2 to methane. It catalyzes the reductive addition of CO_2 to the organic cofactor

methanofuran (MFR) in a two-electron reaction. The physiological electron donor for this reaction is not known.

$$CO_2 + MFR + 2H^+ + 2\text{“}e^-\text{”} \rightarrow CHO\text{-}MFR + H_2O \quad (1.19)$$

FDMH has a mononuclear tungsten atom coordinated by two pterin cofactors (MGD). It also possesses Fe/S clusters but no selenium atom is found.[84]

6.3 The Acetylene Hydratase Family (AH)

This family has only one member characterized so far named Acelylene hydratase (AH). It is a tungsten-iron-sulfur protein and is purified from mesophilic anaerobe *Pelobacter acetylenicus*.[98,99] It is extremely oxygen sensitive and its activity is lost upon exposure to air. It catalyzes the hydration of acetylene to acetaldehyde, a net hydration reaction rather than a redox reaction.

$$C_2H_2 + H_2O \rightarrow CH_3CHO \quad (1.20)$$

AH contains a mononuclear tungsten atom coordinated by pterin cofactors (MGD), sulfur atom of cysteine and a terminal oxygen atom. It also possesses a [4Fe-4S] cluster which is not far from the tungsten center. It is a distinct class besides other tungstoenzymes as its reaction does not involve electron transfer. Also, the oxidation state of tungsten does not change during the reaction.[84,100]

7) Tungsten-substituted Molybdenum enzymes

Historically, Tungsten (W) has been regarded as an antagonist of the biological function of molybdenum. Early attempts to substitute W into active sites of molybdoenzymes resulted in inactive metal-free enzymes or W-substituted enzymes with little or no activity.[30] This failure could be because of the organism incapable of growing on the tungstate-containing medium or due to the pathway used for growth. Once the alternative growth medium and suitable pathway were established, growth was achieved and the effect of tungsten on the activity of enzyme could be examined. The successful tungsten substituted molybdenum enzymes are:

7.1 Xanthine Oxidase and Sulfite Oxidase

7.2 Trimethyamine Oxide Reductase

7.3 Dimethylsulfoxide Reductase

7.4 Nitrate Reductase

7.1 Xanthine Oxidase and Sulfite Oxidase

The activity of the molybdenum enzymes, xanthine oxidase and sulfite oxidase, in rats has been shown to be lowered by addition of tungstate $[WO_4]^{2-}$ to the drinking water of rats on a molybdenum dependent diet.[101]

7.2 Trimethylamine Oxide Reductase (TMAOR)

Tungsten substituted periplasmic TMAO reductase from *E.Coli* has been purified, characterized and shown to be enzymatically active. W-TMAOR is capable of catalyzing the reduction of TMAO to TMA as well as the reduction of DMSO to DMS at high redox potential while Mo-TMAOR can catalyze the reduction of various *N*-oxides but not *S*-oxides. W-TMAOR is more stable to high temperatures than Mo-TMAOR. However, the specific activity of the W-substituted enzyme is half than that of Mo-TMAOR.[102]

7.3 Dimethylsulfoxide Reductase (DMSOR)

Tungsten was substituted and characterized successfully for DMSO reductase from *R.capsulatus*. W-DMSOR reduces DMSO about 17 times faster than Mo-DMSOR[103]. This result is consistent with the previous observation that oxygen atom transfer from the substrate to the reduced metal center is faster for tungsten than molybdenum.[104] However, in contrast to Mo-DMSOR, W-DMSOR does not catalyze the oxidation of DMS.

7.4 Nitrate Reductases (NRs)

Tungsten substituted membrane bound respiratory nitrate reductase (Nar) was purified from *Pyrobaculum aerophilum* grown in the presence of tungstate $[WO_4]^{2-}$ and in the absence of molybdate, $[MoO_4]^{2-}$.[105] W-Nar is an active enzyme; however, it gradually lost activity. Also, the nitrate reductase activity is decreased when the tungstate concentration in the environment is increased.[106]

8) Molybdenum-substituted Tungsten enzyme, Acetylene Hydratase (AH)

Acetylene hydratase (AH) from *Pelobacter acetylenicus* has been characterized as an iron-sulfur, tungsten enzyme. Fully active molybdenum containing AH has been purified from cells grown in the absence of tungsten and exhibits different redox properties from those of the tungsten enzyme.[107] This Mo-AH is inactive under the strongly reducing conditions necessary for activity of the tungsten enzyme. However, the molybdenum enzyme was shown to have some activity upon careful reduction, which was lost upon further reduction.

Tungsten - Nitrate Reductase

1. Introduction

Nitrate reductases (NRs) play key roles in the first step of biological nitrogen cycles[108,109,110] i.e., assimilatory ammonification (to incorporate nitrogen into biomolecules), denitrification (to generate energy for cellular function) and dissimilatory ammonification (to dissipate extra energy by respiration). They always catalyze the reduction of nitrate to nitrite, and have been classified into three groups, assimilatory nitrate reductases (Nas), respiratory nitrate reductases (Nar) and periplasmic nitrate reductases (Nap). Nas belongs to the sulfite oxidase family and is located in the cytoplasm.[111] It is the first enzyme of a reduction sequence for nitrogen incorporation into the biomass that maintains the bioavailability of nitrate to plants, algae, fungi, archaea and bacteria.[112,113] Dissimilatory nitrate reductases, Nar and Nap belong to the DMSO reductase family of mononuclear MPT containing molybdo-enzymes. They are linked to respiratory electron transport systems and are located in the membrane and periplasm, respectively. They catalyze the first step of the catabolic, anaerobic respiration pathway in bacteria and archaea.[115]

Nitrate reduction, catalyzed by membrane bound respiratory nitrate reductase (Nar), is an important step of the denitrification in the anaerobic respiratory pathways employed by a diverse group of bacteria and archaea.[114] Nar was found to contain a Mo cofactor in all microbes from which it was isolated and belongs to the DMSO reductase family.[115] In general, Nar becomes inactive by the addition of tungstate (WO_4^{2-}) to the growth medium,[116] although due to similar chemical properties W can replace Mo as the active site metal and cannot only retain but increase its catalytic activity in *E. coli* TMAO reductase,[102] the *Desulfovibrio alaskensis* formate dehydrogenase[117] and the *Rhodobacter capsulatus* DMSO reductase.[118] However, recently the nitrate reductase (Nar) from the hyperthermophilic denitrifying archaeon *Pyrobaculum aerophilum* has been shown to retain its activity even at a tungsten rich environment.[105]

P. aerophilum, a hyperthermophilic archaeon, is naturally exposed to high levels of tungsten, a heavy metal that is abundant in high temperature environments. Tungsten was reported to stimulate the growth of several mesophilc methanogens and some mesophilic and thermophilic bacteria.[115] The growth of *P. aerophilum* also depends on the presence of tungstate in the growth medium which suggests the involvement of tungstoenzymes in essential metabolic pathways.[119]

P. aerophilum is the only hyperthermophilic archaeon isolated that reduces nitrate via a membrane bound respiratory nitrate reductase (Nar).[119] Nar purified from *P. aerophilum* grown in the absence of added molybdate (MoO_4^{2-}) and with 4.5μM tungstate (WO_4^{2-}) is a tungsten containing enzyme, which is identical to Mo-Nar[106] (previously isolated from *P. aerophilum*), indicating that either metal can serve as the active site ion. The crystal structure is similar to the previously reported Nar from *E. coli*,[120] a heterodimeric enzyme termed as NarGH where NarG hosts the metal (Mo or W) catalytic site. The metal is coordinated by two metallopterin guanine dinucleotide (*bis*-MGD) ligands, a carboxyl group of Asp_{222} and a water molecule. The NarH component possesses an iron-sulfur (FeS) redox active subunit.[105]

NarGH reduces nitrate to nitrite, changing the oxidation state of metal from +IV to +VI. Two electrons and two protons are required for the reductive half reaction, resulting in the formation of a water molecule and a nitrite ion (eq. 2.1).

$$NO_3^- + 2H^+ + 2e^- \rightleftharpoons NO_2^- + H_2O \quad (2.1)$$

An experimental study was carried out on small model complexes; an analogue of the active site of dissimilatory nitrate reductase (*Desulfovibrio desulfuricans*) which is in the reduced state contains a Mo atom bound by two metalopterindithiolene ligands and a cysteinate residue. This study demonstrates that nitrate reduction by primary (direct) oxo transfer[121] is a feasible reaction pathway (Fig. 2.1).[122]

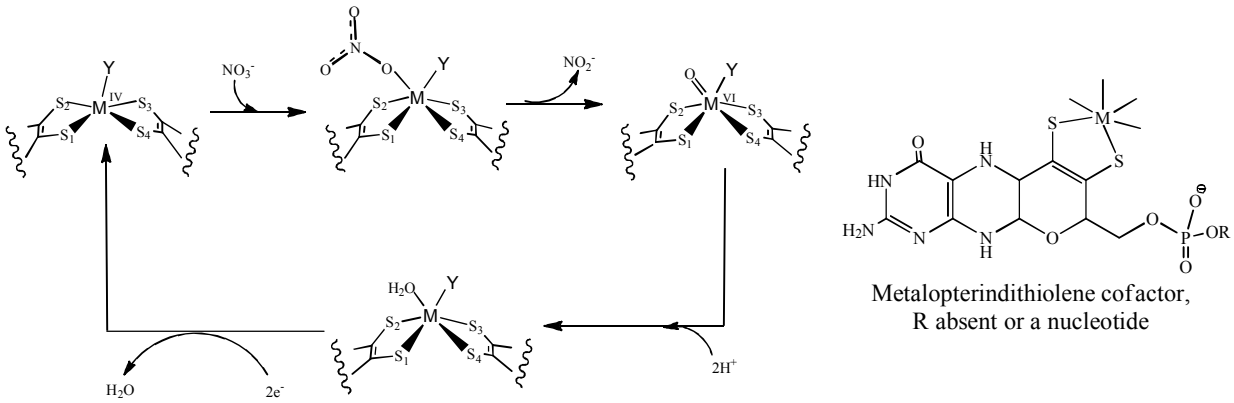

Fig. 2.1: Schematic description of the proposed mechansim[122] for the nitrate reduction, where M=Mo and Y= S-Cys. Also the metalopterindinucleotide cofactor is shown.

Here we have presented the density functional theory (DFT) study on chosen model complexes derived from the protein X-ray crystal structure of *P.aerophilum*[105] nitrate reductase (Nar). The purpose of the study was to investigate (i) The effect on the reduction of

nitrate when W replaces the Mo at the active site. (ii) The energy barriers on the potential energy surface. (iii) The reason for the activity loss of Nars (respiratory nitrate reductase) in the presence of W.

2. Computational Details

All the geometries were optimized using Gaussian 09 with the hybrid density functional B3LYP[123] and the LANL2DZ basis set[124,125,126,127] augmented by polarization functions on sulfur atoms (ζ = 0.421).[128] The starting nitrate complex geometries for transition state searches were generated by shortening and lengthening of forming and breaking bonds, respectively. Frequency calculations proved transition states to have exactly one imaginary frequency with the correct transition vector. Single point energies were computed with the B3LYP functional and the Stuttgart-Dresden effective core potential basis set (SDD)[129,130] augmented by polarization functions for all atoms except Mo, W and H (ζ = 0.600, 1.154, 0.864, and 0.421 for C, O, N, and S, respectively).[128] Self-consistent reaction field (SCRF) computations were performed on the optimized geometries to model the protein surrounding the active site by a conductor like polarizable continuum method (CPCM)[131] as implemented in Gaussian 09.[132,133] Default Gaussian 03 parameters were used for the evaluation of solute-solvent dispersion and repulsion interaction energies,[134,135] and solute cavitation energy variations.[136] The molecular cavity was specified using a minimum radius (RMin) of 0.5Å and an overlap index (OFac) of 0.8.[137]

3. Active Site Models

Two types of active site models were designed on the basis of the protein X-ray crystal structure of *Pyrobaculum aerophilum* (PDB ID 1R27)[105] only differing in the metal center, **a** containing Mo and **b** containing W at the active site. These active site models include the metal center coordinated by two enedithiolene moieties of the pterin molecules, by Asp_{222} and by H_2O_{8538}. His_{546}, Asn_{52}, Tyr_{220}, Gly_{549} and Val_{578} residues were also included in the model complexes as they may influence the catalytic reaction due to their proximity to the metal center. Hydrogen atoms were added manually. His_{546} and Gly_{549} residues form hydrogen bonds to the ionized Asp_{222} preventing it to rotate and become a bidentate ligand which then would block the substrate binding site. Asn_{52} was included as its distance of 3.9Å from the metal center suggests that it is suitable for substrate coordination.[105] During the optimizations, alpha (α) carbon atoms and nitrogen atoms attached to the beta (β) carbon atoms of His_{546}, Asn_{52}, Tyr_{220} and Asp_{222} were kept fixed to their crystal structure positions to mimic the steric

constraints by the protein matrix. Carbon atom C_7 and the nitrogen atom attached to carbon atom C_5 were kept fixed for residue Gly_{549}. The MPT ligands were truncated at the pyran rings and oxygen atoms of these pyran rings were also kept fixed (Fig.2.2).

First, hydrogen atoms were geometry optimized applying one negative overall charge (assuming Mo/W at the +VI oxidation state), keeping all heavy-atoms fixed at their positions. The resulting geometries served to generate the different starting geometries needed for computing the mechanism for nitrate reduction.

The starting geometries for the substrate and product complexes are generated by slight distortion of M-O and O-NO_2 in the optimized transition state geometries, **5a** and **5b**. Geometries with slightly elongated M-O distance and reduced O-NO_2 distance are considered as the starting geometries for the optimization of **4a** and **4b** educt-substrate complexes whereas reduced M-O distance and elongated O-NO_2 distance are considered as the starting geometries for the optimization of **6a** and **6b** product complexes. The geometry optimizations of these distorted geometries directly lead to complexes, **4a**/**4b** and **6a**/**6b**.

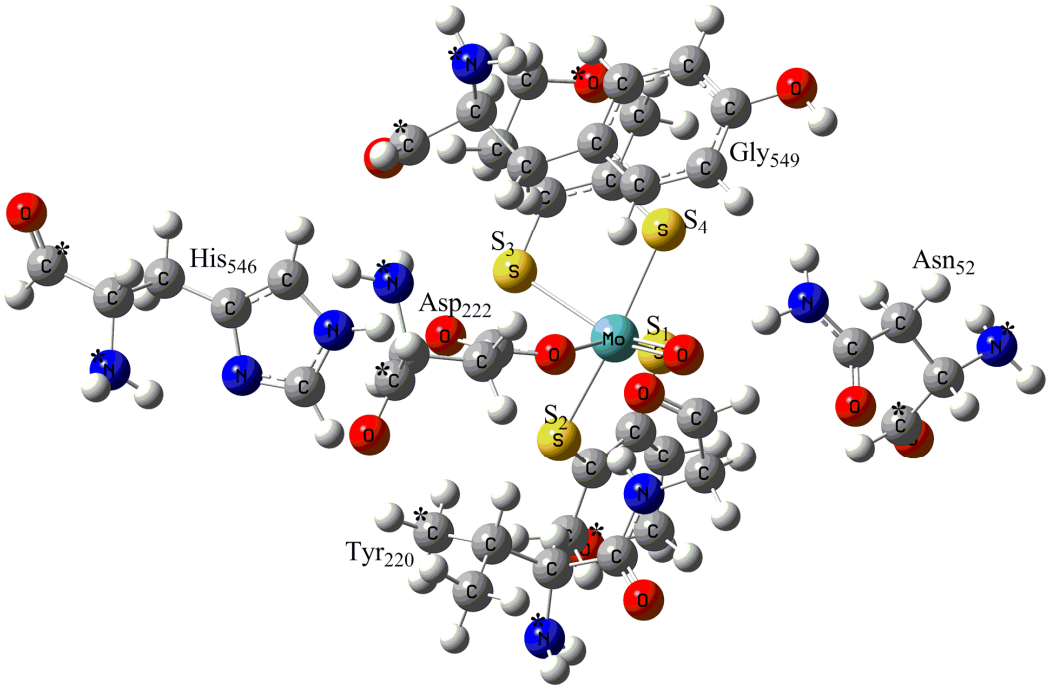

Fig. 2.2: Optimized oxidized active site model of Mo-Nar.

Atoms labeled (*) were kept fixed at their X-ray crystal structure positions.

4. Results

- *Optimized active site model complexes*, **1a, 1b, 2a** and **2b**:

The protein X-ray crystal structure of *P.aerophilum* Nar from the PDB data base (PDB ID: 1R27)[105] shows that at the active site the metal is coordinated by two metallopterin guanine dinucleotide (*bis*-MGD) ligands, a carboxyl group of Asp_{222} and a water molecule.[105] However, the distance of the oxygen atom (O_{wat}) of this coordinated water molecule from the metal center is 1.87 Å which neither falls in the range expected for metal oxide (1.71 - 1.75 Å),[138,139] nor for water (2.0 - 2.3 Å)[140] ligands. Also, the distance between O_{wat} and oxygen of Asp_{222} (O_{Asp}) is 1.59 Å, which is only 0.1 Å longer than the typical peroxo O-O$^-$ bond length (1.49 Å).

We have optimized two active site model complexes to clarify the nature of this oxo species; **1** (oxidation state of Mo/W is +IV, overall charge is -1) contains a water molecule and **2** (oxidation state of Mo/W is +VI, overall charge is -1) contains an oxide (O_1) group attached to the metal (Fig. 2.3). Geometry optimizations of active site model complexes **1** and **2** result in distinctively different geometrical parameters of the metal coordination site relative to the protein X-ray crystal structure geometry of NarGH.[105] Optimized geometry data for the model complexes **1a** with M=Mo (**1b**, M=W) show that the dithiolenes are twisted less against each other as the S_1-S_2-S_3-S_4 dihedral angle decreases from -18.3˚ to -6.4˚ for **1a** (-2.5˚ for **1b**) i.e., the coordination geometries are nearly trigonal prismatic. Bond distances between the metal center, M and the dithiolene sulfur atoms, S decreases from ~2.455 Å to ~2.393 Å (~2.384 Å) when comparison is made with the protein X-ray crystal structure (Tables 2.2 and 2.3). Elongated bond distances for M-O_{wat} (from 1.874 Å to 2.335 Å (2.286 Å)) and M-O_{Asp} (from 1.97 Å to 2.142 Å (2.122 Å)) are computed. But the main difference lies in the Mo-S_2 bond distance (from 2.537 Å to 2.387 Å (2.377 Å)), in the bond angles between the O_{Asp}, M and O_{wat} (from 49˚ to 66˚ (66˚)), and in the distance between the two oxygen atoms, O_{Asp}-O_{wat} (from 1.596 Å to 2.428 Å (2.392Å)).

Distorted octahedral coordination geometries result from geometry optimizations of oxidized model complexes **2a** (**2b**). Optimized data shows increase in the S_1-S_2-S_3-S_4 dihedral angles (from -18.3˚ to -43.7˚ (-42.1˚)) and in the M-S bond distances (from ~ 2.455 Å to ~2.474 Å (~2.461 Å)). There is one longer M-S bond relative to other three M-S bonds in the optimized oxidized model complexes and the protein X-ray crystal structure. However, it is M-S_2 bond (2.537 Å) in the X-ray structure while M-S_3 bond (2.591 Å (2.549 Å)) in the optimized oxidized model complexes. These sulfur atoms (S_2 in the X-ray crystal structure while S_3 in

the optimized oxidized model complexes) are at the trans position to the M=O ligand and oxo is a trans- influencing ligand which causes the stretching of M-S bonds to which they are trans.

Elongated bond angles between the O_{Asp}, M and O_1 (from 49˚ to 88˚ (88˚)), and distances between the two oxygen atoms, O_{Asp}-O_1 (from 1.596 Å to 2.684 Å (2.647Å)) are computed. Slightly elongated M-O_{Asp} distances (from 1.970 Å to 2.083 Å (2.040 Å)) and shortened M-O_1 distances (from 1.874 Å to 1.755 Å (1.764Å)) are also observed (Tables 2.2 and 2.3).

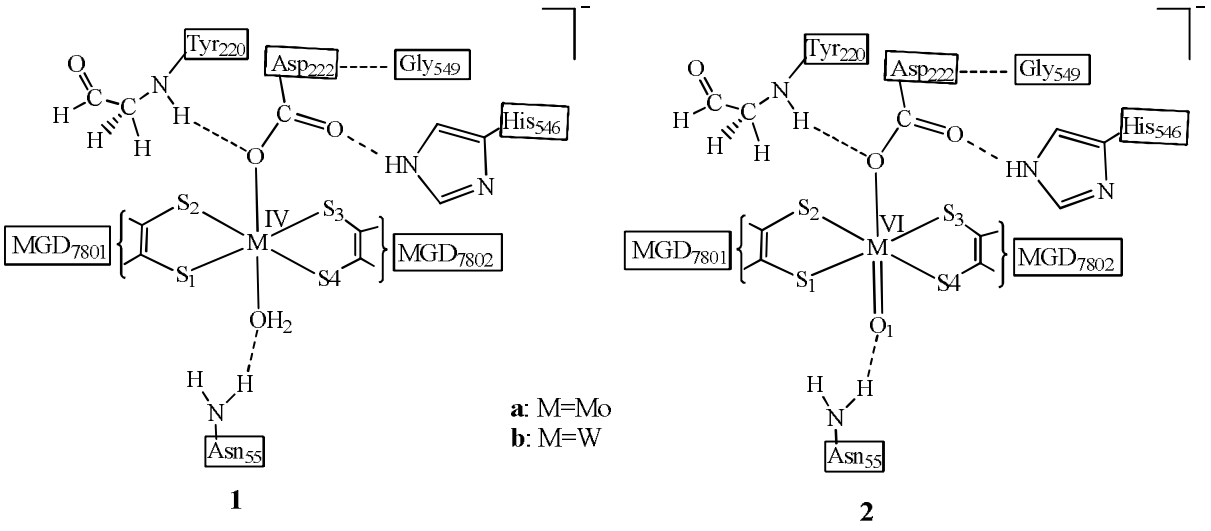

Fig. 2.3: The chemical structure of the active site model complexes **1** and **2** derived from the protein X-ray crystal structure of Nar (PDB ID 1R27)[105]

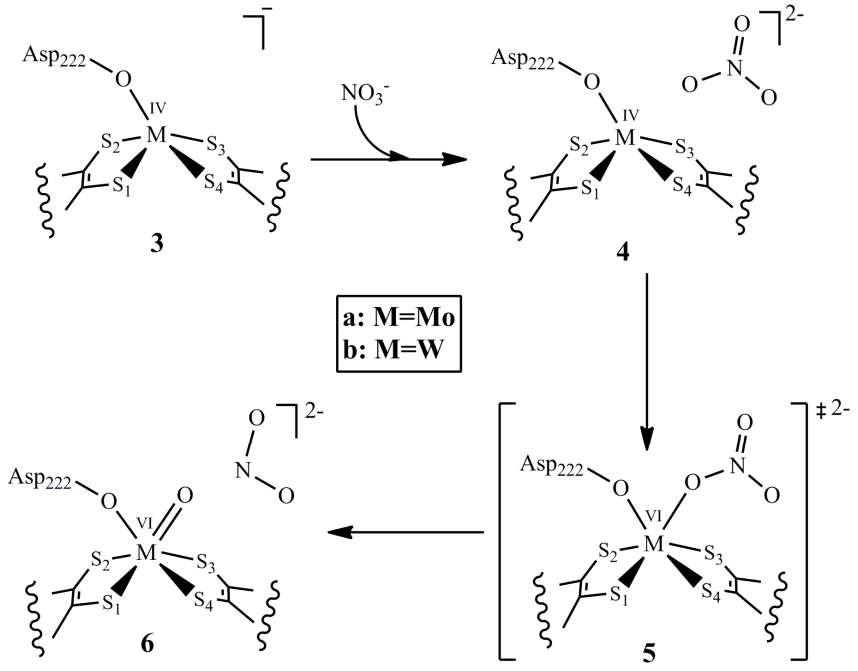

Fig. 2.4: Schematic description of the mechanism for nitrate reduction at the NR active site.

- *Optimized reduced complexes*, **3a** and **3b**:

The reaction catalyzed by nitrate reductase is an oxo-transfer reaction, in which an oxygen atom is transferred from nitrate to the reduced metal. As a consequence of the metal reduction from M^{VI} to M^{IV}, the oxo group of the oxidized M^{VI} is lost as hydroxo/water after proton uptake. Optimizations of the reduced active site model complexes **3a** (**3b**) without any additional ligand, i.e. fivefold coordinate metal center give S_1-S_2-S_3-S_4 dihedral angles of -0.2˚ (1.3˚), resulting in nearly tetragonal pyramidal geometries. The bond distances between the metal center M and S of the dithiolenes are ~2.362 Å (~2.353Å) (Table 2.2 and 2.3). The M-O_{Asp} distance is 2.017 Å (1.980Å).

- *Optimized substrate complexes*, **4a** and **4b**:

First, nitrate gets loosely bound in the active site pocket by weak interactions with the active site residues Asn_{52} and Gly_{549} resulting in the substrate complexes **4a** (**4b**) (Fig. 2.4 and Fig. 2.5). The computed reaction energies for the substrate complex formation are exothermic, -9.6 kcal/mol (-7.6 kcal/mol) in the gas phase and -4.6 kcal/mol (0.2 kcal/mol) for the polarizable continuum model relative to the separate substrate and educt complexes **3a** (**3b**) (Table 2.1). There is no significant change in geometrical parameters of the active site relative to the reduced complexes **3a** (**3b**) (Tables 2.2 and 2.3).

- *Optimized transition state complexes*, **5a** and **5b**:

Reduction of nitrate is a single step reaction in which the transfer of an oxygen atom proceeds through transition state **5a** (**5b**). The energy barrier computed for **5a**, 34.4 kcal/mol in the gas phase and 32.1 kcal/mol in the continuum is almost three times as large as compared to that of **5b**, 12.0 kcal/mol in the gas phase and 11.0 kcal/mol in the continuum (Table 2.1). There is also a remarkable difference in the geometries.

The Mo containing transition state (**5a**) has a distorted octahedral geometry. The optimized data shows an increase in the S_1-S_2-S_3-S_4 dihedral angle from 2.0˚ to 30.5˚ and in the Mo-S bond lengths from ~ 2.37 Å to ~2.45Å (Table 2.2) when comparison is made with the optimized **4a** geometry. The Mo-O and O-NO_2 distances are 1.918 Å and 1.723 Å, respectively. The Mo-O_{Asp} bond distance is elongated from 2.029 Å to 2.102 Å.

The W containing transition state (**5b**) on the other hand has a distorted trigonal prismatic geometry where the optimized data shows an increase in the S_1-S_2-S_3-S_4 dihedral angle from 1.2˚ to 7.6˚ and in the W-S bond lengths from ~ 2.37 Å to ~2.45Å (Table 2.3) as compared to

the optimized **4b** geometry. The W-O and O-NO_2 bond distances are 1.942 Å and 1.638 Å, respectively i.e., **5b** can be considered to be an earlier transition state than **5a**. The W-O_{Asp} distance is elongated from 1.986Å to 2.079Å.

In the optimized geometries **5a** and **5b**, NO_3^- is coordinated to the metal at the active center and also forms a hydrogen bond to the Asn_{55}.

- *Optimized product complexes*, **6a** and **6b**:

The nitrate reduction results in metal oxo product complexes **6a** (**6b**), having distorted octahedral geometries. In the optimized geometries, **6a** and **6b**, NO_2^- is loosely bound in the active site pocket and makes hydrogen bonds with the active site residues Asn_{52} and Gly_{549}. Oxygen atom transfer is computed to be a slightly exothermic step for M=Mo where the product complex (**6a**) has a relative energy of -7.6 kcal/mol in the gas phase and -1.9 kcal/mol in the continuum (Table 2.1). The Mo-O bond distance is reduced from 1.918 Å to 1.737 Å while the O-NO_2^- bond is broken (4.444 Å) when comparison is made with the optimized **5a** geometry (Table 2.2). The S_1-S_2-S_3-S_4 dihedral angle is further increased from 30.5˚ to 54.5˚ while the Mo-S bond distances are increased from ~2.438 Å to ~2.629 Å (Table 2.2). The Mo-O_{Asp} bond distance is increased from 2.102 Å to 2.133 Å.

On the contrary, the W containing product complex (**6b**) is highly exothermic, with computed relative energies of -43.3 kcal/mol in the gas phase and -34.7 kcal/mol in the continuum. The W-O bond distance is reduced from 1.942 Å to 1.757 Å while the O-NO_2^- bond is broken (5.133 Å) relative to the optimized **5b** geometry (Table 2.3). The S_1-S_2-S_3-S_4 dihedral angle of the dithiolenes is changed from 7.6 ˚to -42.4˚, whereas the W-S bond distances are increased from ~2.472 Å to ~2.562Å (Table 2.3). There is no significant change in the W-O_{Asp} bond distance (2.079 Å instead of 2.076 Å).

5. Discussion

To date, few archaeal Nars have been characterized from *P. aerophilum*,[106] *Haloarcula marimortui* [141,142] and *Haloferax mediterranei*.[143] These archaeal Nars contain Mo cofactors at their active sites. It is not clear how these microbes maintain their ability to respire with nitrate using Mo-containing Nar in a high temperature environment that is naturally enriched with W but depleted of molybdate (MoO_4^{2-}).[144] Early attempts to substitute tungsten for molybdenum in molybdo-enzymes failed because the organism was incapable of growing on the tungstate-containing medium.[145] However, the hyperthermophile *P. aerophilum* is a

denitrifying archaeon requiring tungstate (WO_4^{2-}) for growth although its Nar is a Mo cofactor containing enzyme.[119] Afshar et al. demonstrated that the external tungstate concentration affects the denitrification pathway efficiency of this archaeon, resulting in the complete denitrification only at high tungstate concentration.[119]

Recently, Nar purified from *P. aerophilum* grown in the absence of added molybdate and with 4.5μM tungstate has been reported[114] which is a W containing enzyme. *P. aerophilum* Nar is the first active nitrate reductase that contains a W cofactor. The presence of a W cofactor may be reflective of high concentrations of this metal at high temperatures.[3] As previously described this enzyme can also accommodate Mo as the active site metal.[106] To compare the properties of Mo and W cofactors containing enzymes, DFT calculations were performed on the active site model complexes derived from the protein X-ray crystal structure of *P. aerophilum.*[105]

The computed energy barrier for the oxygen atom transfer from the nitrate to the metal center is 34.4 kcal/mol for the Mo active site model complex, about triple the energy barrier of the W active site model complex (12.0 kcal/mol) (Table 2.1). Thus, as compared to Mo-Nar, W-Nar should be more active, which is in contrast to experimental findings,[146] but is similar to the *R. Capsulatus* DMSO reductase;[102,106,147] the W-substituted DMSO reductase was 17 times more active in the reduction of DMSO than the Mo-substituted enzyme. However, the W-substituted DMSO reductase was inactive for the oxidation of dimethysulfide (DMS).[147]

Oxidation of the educt complex is close to thermoneutral for the Mo active site model complex (-1.9 kcal/mol) but strongly exothermic for the W containing active site model complex (-34.7 kcal/mol) (Table 2.1). The low relative energy for the oxidized W metal complex makes the regeneration of the +IV oxidation state much more difficult as compared to the Mo metal complex. The M^{VI} to M^{IV} reduction requires much more reductive power with M=W then with M=Mo.

So, although the reduction of nitrate is stimulated when W replaces Mo in the active site of Nar the catalytic cycle breaks after the reduction of nitrate to nitrite when the biochemical reducer is not strong enough. It is similar/in agreement with the experimental findings which suggest that Nar from cells grown at high WO_4^{2-} concentrations appeared to be more labile than the previously isolated Mo-Nar; i.e., the enzyme gradually lost activity.[106] Also, the nitrate reductase activity is decreased with the increase in tungstate concentration in the

environment.[106] In conclusion, the Nar isolated from *P. aerophilum* is a molybdenum containing enzyme.

Table 2.1: Computed energies (kcal/mol) relative to the educt-substrate complex for the nitrate reduction.

	Educt Complex	Substrate Complex	Transition State Complex	Product Complex	
M=Mo	0.0	-9.7	30.2	-11.6	//B3LYP[a)]
	0.0	-9.6	34.4	-7.6	SDD[b)]
	0.0	-4.6	32.1	-1.9	COSMO[c)]
M=W	0.0	-7.8	7.0	-52.6	//B3LYP[a)]
	0.0	-7.6	12.0	-43.3	SDD[b)]
	0.0	0.2	11.0	-34.7	COSMO[c)]

Where, a) B3LYP/Lanl2DZ(p), b) B3LYP/SDDp//B3LYP/Lanl2DZ (p),
c) COSMO-B3LYP/SDDp//B3LYP/Lanl2DZ(p) (see Computational details)

Scheme 2.1: Plot of computed reaction energies (kcal/mol) relative to separate substrate and educt complex vs steps involved in the reaction mechanism.

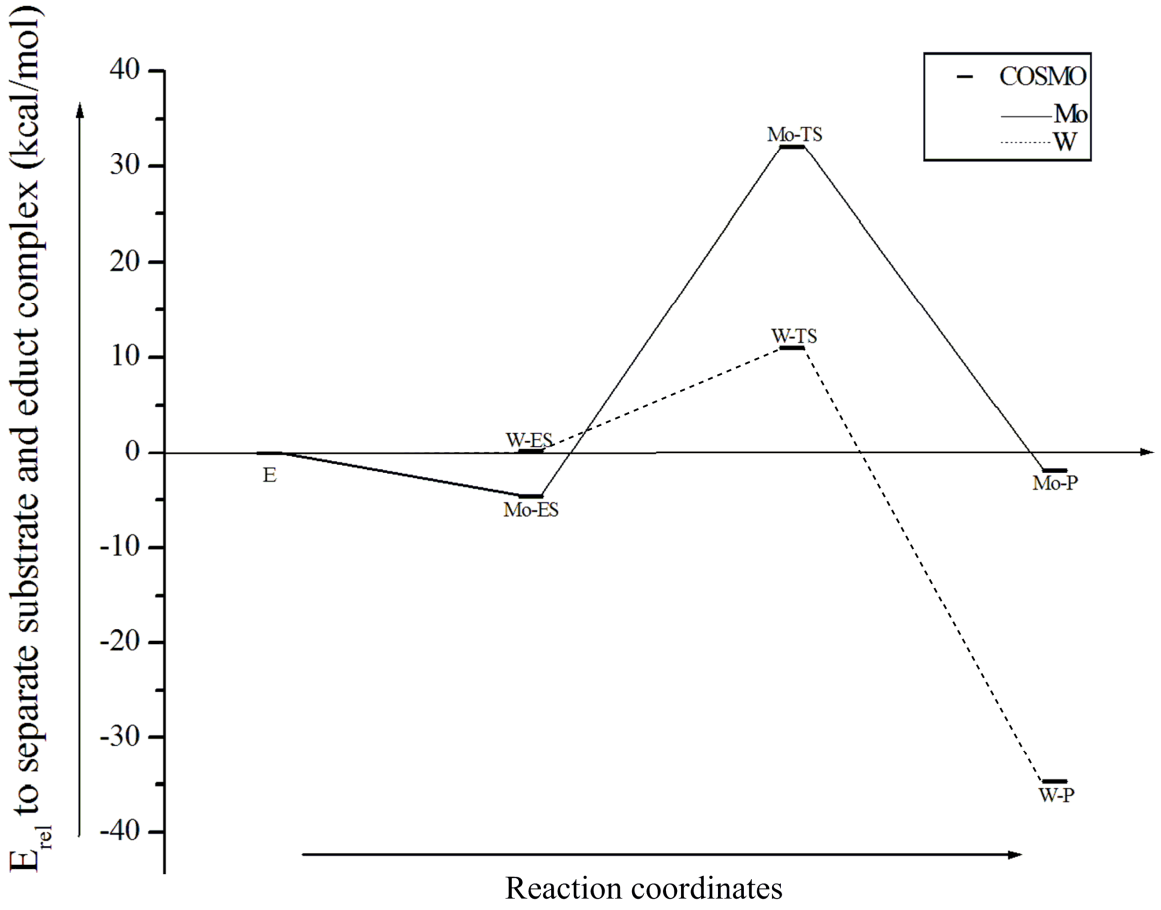

Where, **E** = educt complex, **ES** = educt-substrate complex, **TS** = transition state, **P** = product complex.

Table 2.2: Geometrical features of the optimized model complexes of the reaction mechanism for the molybdenum containing nitrate reductase

	Crystal Structure	Reduced Complex[1] 1a	Oxidized Complex[2] 2a	Reduced Complex 3a	Educt Complex 4a	Transition State 5a	Product Complex 6a
Mo-S_1 (Å)	2.405	2.409	2.446	2.379	2.370	2.420	2.430
Mo-S_2 (Å)	2.537	2.387	2.418	2.347	2.348	2.452	2.629
Mo-S_3 (Å)	2.395	2.380	2.591	2.345	2.349	2.422	2.421
Mo-S_4 (Å)	2.484	2.394	2.441	2.375	2.371	2.457	2.475
Mo-O_{Asp} (Å)	1.97	2.142	2.083	2.017	2.029	2.102	2.133
Mo-O_{wat} (Å)	1.874	2.335	-	-	-	-	-
Mo-O_1 (Å)	-	-	1.755	-	-	-	-
Mo-O (Å)	-	-	-	-	-	1.918	1.737
O-NO_2^- (Å)	-	-	-	-	1.310	1.723	-
O_{Asp}-$O_{wat/1}$ (Å)	1.596	2.428	2.684	-	-	-	2.786
O_{Asp}-Mo- $O_{wat/1}$(°)	49.0	65.5	88.3	-	-	-	91.5
S_1-S_2-S_3-S_4(°)	-18.3	-6.4	-43.7	-0.2	2.0	30.5	54.5

Where, [1] = Water containing reduced complex, [2] = Oxygen containing oxidized complex

Table 2.3: Geometrical features of the optimized model complexes of the reaction mechanism for the tungsten containing nitrate reductase

	Crystal Structure	Reduced Complex[1] 1b	Oxidized Complex[2] 2b	Reduced Complex 3b	Educt Complex 4b	Transition State 5b	Product Complex 6b
W-S_1 (Å)	2.405	2.397	2.439	2.369	2.363	2.428	2.455
W-S_2 (Å)	2.537	2.377	2.432	2.334	2.335	2.419	2.442
W-S_3 (Å)	2.395	2.373	2.549	2.337	2.337	2.424	2.562
W-S_4 (Å)	2.484	2.388	2.424	2.371	2.369	2.457	2.428
W-O_{Asp} (Å)	1.97	2.122	2.040	1.980	1.986	2.079	2.076
W-O_{wat} (Å)	1.874	2.286	-	-	-	-	-
W-O_1 (Å)	-	-	1.764	-	-	-	-
W-O (Å)	-	-	-	-	-	1.942	1.757
O-NO_2^- (Å)	-	-	-	-	1.310	1.638	-
O_{Asp}-$O_{wat/1}$ (Å)	1.596	2.392	2.647	-	-	-	2.747
O_{Asp}-W-$O_{wat/1}$(°)	49.0	65.6	87.9	-	-	-	91.2
S_1-S_2-S_3-S_4(°)	-18.3	-6.3	-42.1	1.3	1.2	7.6	-42.4

Where, [1] = Water containing reduced complex, [2] = Oxygen containing oxidized complex

Fig.2.5: Optimized geometries for the Mo (**a**) and W (**b**) containing active site model complexes **1-6**.

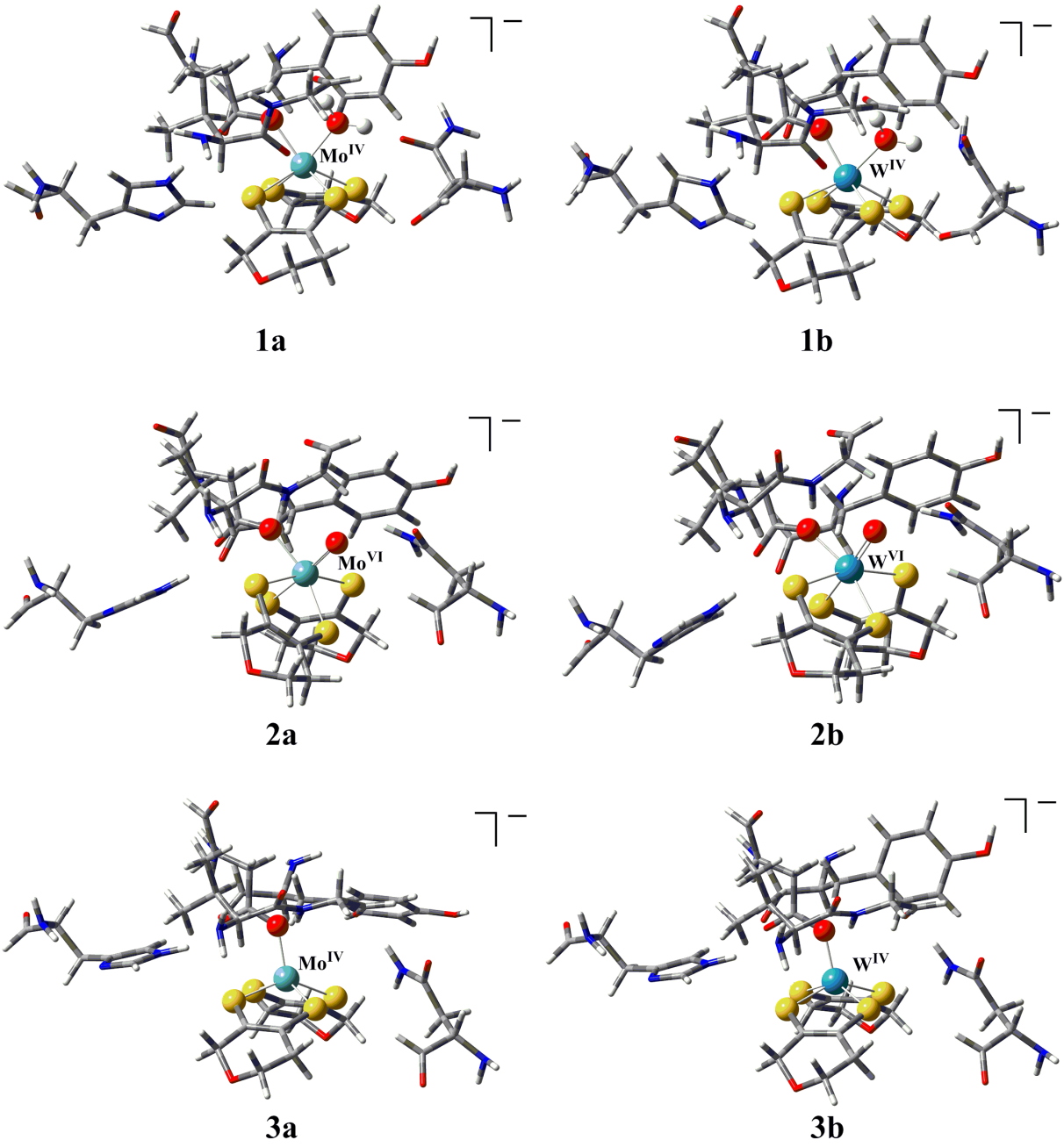

Fig. 2.5: Continued…

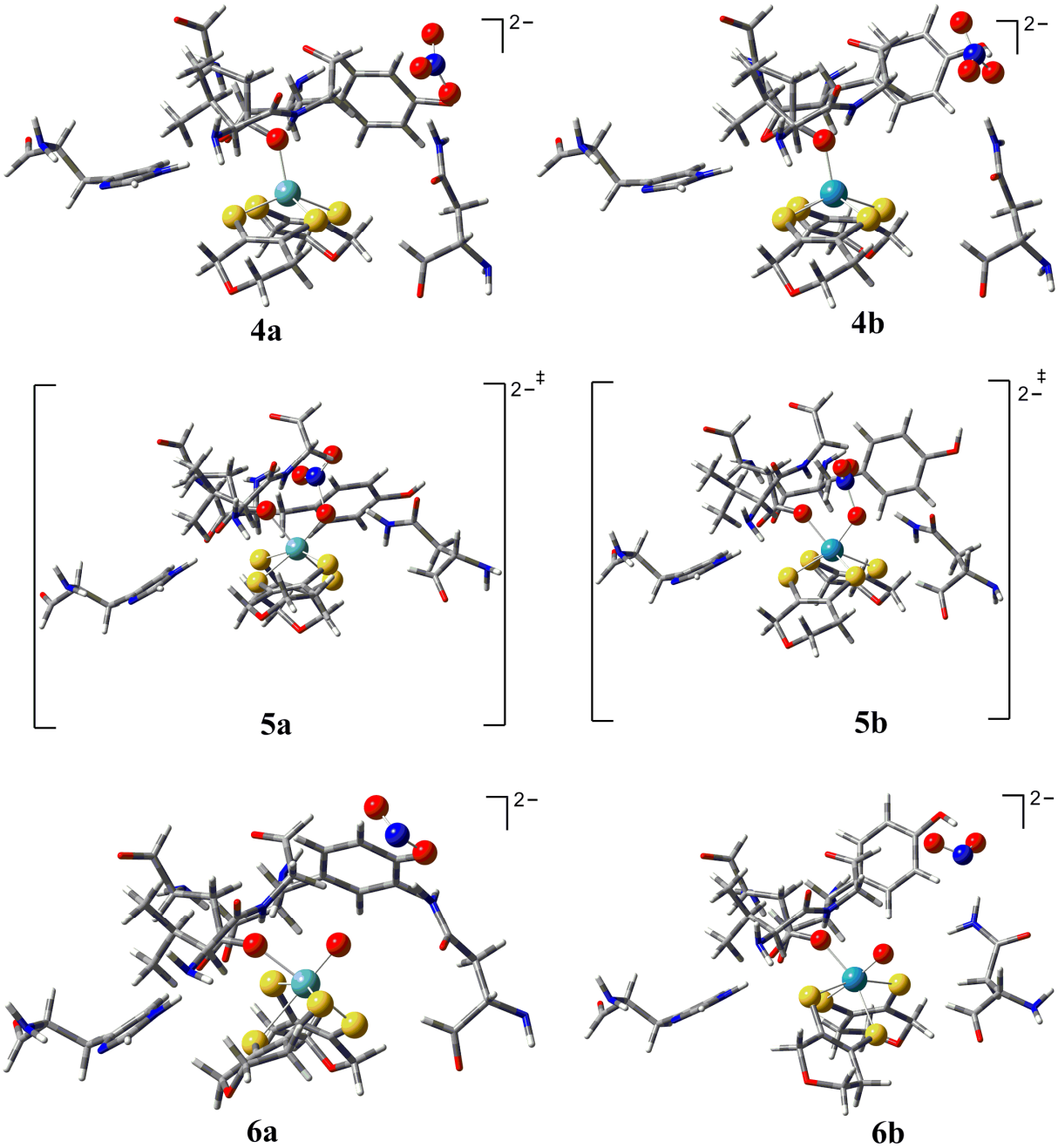

Ethylbenzene Dehydrogenase

1. Introduction

Ethylbenzene dehydrogenase (EBDH) is a soluble periplasmic molybdoenzyme. It catalyzes the oxygen independent stereospecific hydroxylation of ethylbenzene to (*S*)-1-phenylethanol as the initial step of anaerobic ethylbenzene degradation. It is the first known example of direct anaerobic oxidation of a non-activated hydrocarbon.[148]

$$\text{Ethylbenzene} \rightarrow \text{(S)-1-phenylethanol} \quad (3.1)$$

EBDH belongs to the prokaryotic oxotransferase (DMSO) family of mononuclear molybdenum enzymes and exhibits the highest sequence similarities to selenate reductase of *Thauera selenatis*,[149] dimethylsulfide dehydrogenase of *Rhodovulum sulfidophilum*,[150] perchlorate and chlorate reductases of *Dechloromonas* sp., and membrane bound nitrate reductases from archaebacteria and eubacteria.[151,152]

In contrast to the oxidized state, this enzyme is inactivated by exposure to air in the reduced state, possibly due to generation of reactive oxygen species at the reduced heme cofactor.[153] Elucidation of the detailed role of EBDH in bio-mineralization of ethylbenzene, a major component of crude oil, will help to improve the recovery of polluted ecosystems. EBDH promises potential applications in chemical and pharmaceutical industry, as pure enantiomers of alcohols are valuable as building blocks for physiologically active compounds; e.g.1-phenylethanol itself is used as food and drinking flavoring agent and additive of cosmetics. Also the enzyme seems to react with a relatively wide range of alkylaromatic and alkylheterocyclic substrates.[153,154] However, ethylbenzene is the native substrate of the enzyme. The high affinity for ethylbenzene may result from the presence of hydrophobic amino acid residues at the walls of a tunnel leading to the active center, which may facilitate substrate transport into the enzyme interior and discrimination of other compounds. The unsual catalytic versatility of EBDH may arise from a rather large active center cavity, which seems not to pose significant steric constraints for para- and meta- substituents.[155]

Three bacterial species capable of anaerobic degradation of the aromatic hydrocarbon ethylbenzene are known to date. All of these are denitrifying bacteria that belong to the genus *Azoarcus* of the β-proteobacteria. For one of these strains, *Azoarcus* sp. EB-1, ethylbenzene is the only known hydrocarbon utilized as growth substrate.[156] The other two strains utilize

either ethylbenzene or an alternative hydrocarbon compound, namely toluene (strain EbN1) or *n*-propylbenzene (strain PbN1).[157]

The X-ray protein structure of EBDH (PDB 2IVF),[155] isolated from *Aromatoleum aromaticum* strain EbN1 (formerly named *Azoarcus* sp.), is a heterotrimer. The first subunit contains the molybdenum active site and one Fe-S cluster, while the second subunit carries several Fe-S clusters and its third subunit binds a heme *b* (Fe-protoporphyrin IX).[155] At the active site, Mo^{IV} is coordinated with two metalopterin guanine dinucleotide (*bis*MGD) ligands, one oxygen atom of Asp_{223} and one oxygen atom of an acetate bound at the sixth coordination site. The two MGD molecules differ from each other: one has a closed pyran ring, while the other assumes an open form (Fig. 3.1).

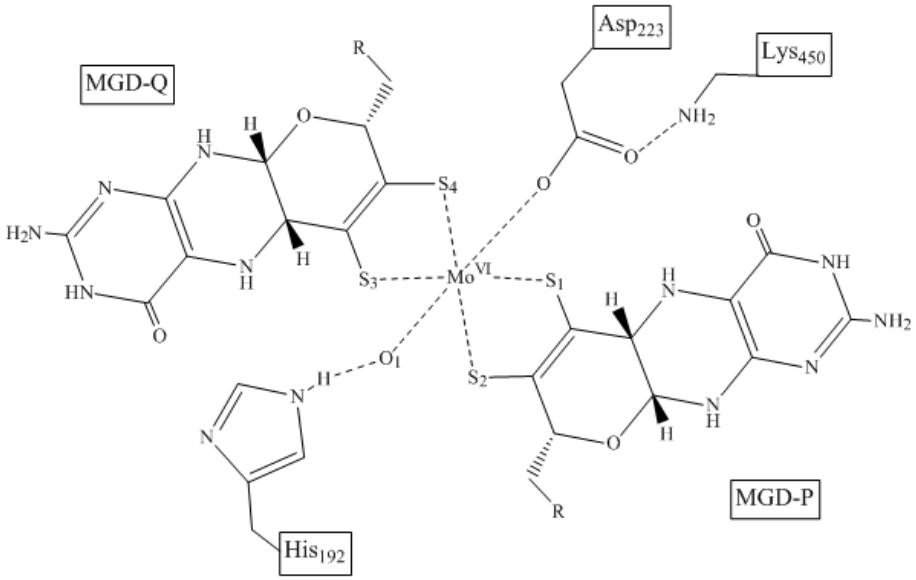

Fig. 3.1: The chemical structure of the active site of EBDH. Numbering follows the relevant literature.[158] MGD-P with an open pyran ring, MGD-Q with a closed pyran ring. R is (P_2O_7)-ribose-guanine nucleotide[155]

The proposed reaction sequence starts with an oxidation of the Mo^{IV} ion to the Mo^{VI} state by the removal of two electrons via the electron transport chain to the heme. Mo^{IV} binds a water molecule releasing two protons via nearest His_{192} to the bulk solvent resulting in the formation of a Mo-oxo group.[155] This oxidized active site is the active species for the hydroxylation of ethylbenzene (Fig. 3.2). Asp_{223}, Lys_{450} and His_{192} seem to be in the best position to take part in the hydrocarbon activation, together with the molybdenum oxo ligand in the oxidized form of EBDH (Fig. 3.2).

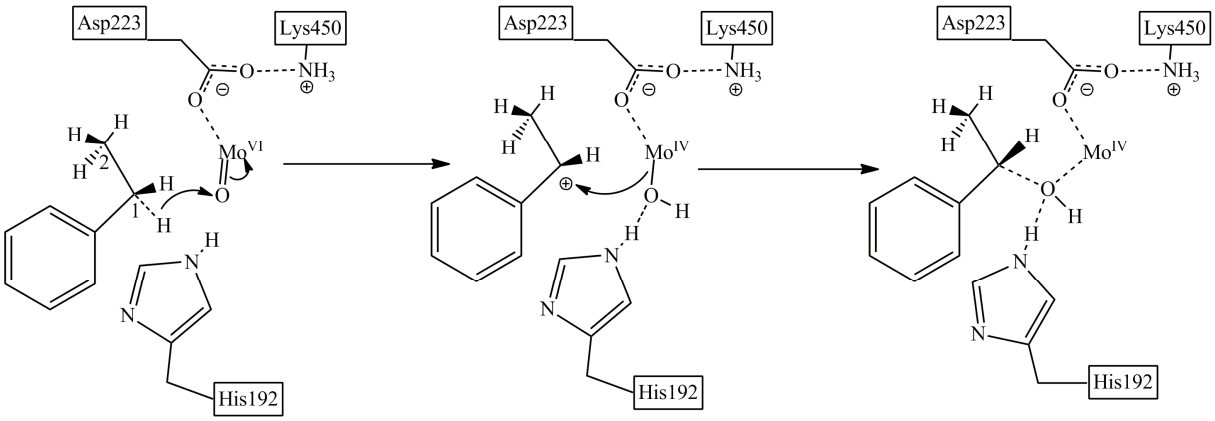

Fig. 3.2: Sketch of the catalytic reaction starting from an oxo group attached to the Mo(VI).[155]

On the basis of the analysis of kinetic data,[148] quantitative structure activity relationship (QSAR) studies[159] and X-ray crystal structure of the EBDH,[155] a reaction mechanism was proposed (Fig. 3.3) which explains the stereospecificity of EBDH in oxidation of ethylbenzene. The reaction retains the stereochemistry, i.e., the *pro-S* hydrogen of C_1 of ethylbenzene is removed and replaced by the OH group to yield (*S*)-1-phenylethanol.[148]

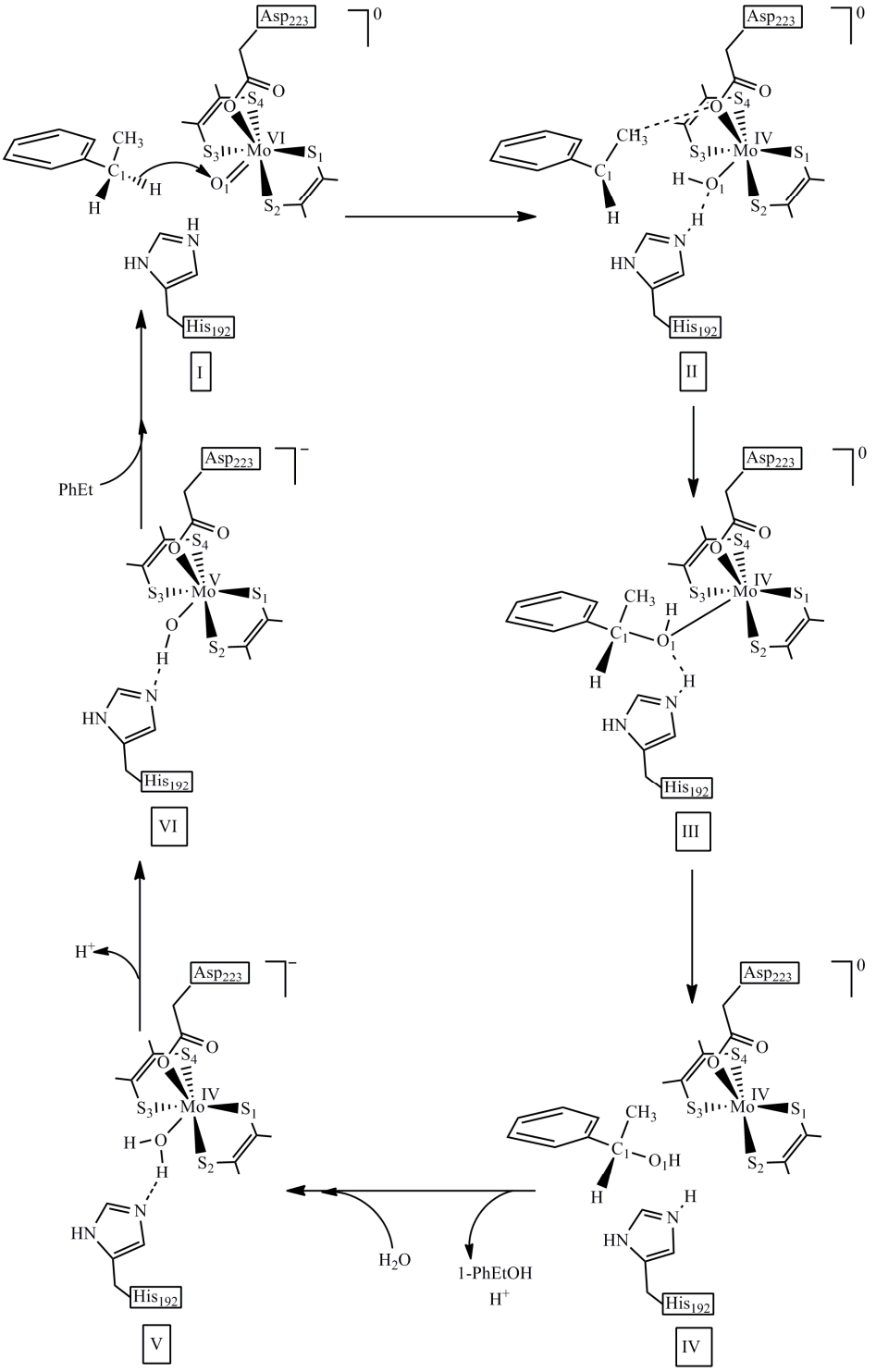

Fig. 3.3: Hypothetical mechanism of ethylbenzene oxidation by EBDH.[148]

The mechanism of ethylbenzene hydroxylation at the molybdenum cofactor of EBDH essentially involves the cleavage of a C-H bond (rate-limiting process) of the methylene group in order to activate the hydrocarbon by a two electron transfer step or two one electron transfer steps i.e. heterolytic cleavage and homolytic cleavage of the C-H bond, respectively. These options result in the formation of a carbocation or a hydrocarbon radical intermediate,

respectively, together with a hydroxide coordinated to molybdenum (Fig.3.4). Subsequently, this OH ligand must be shuttled back towards the activated (radical or carbocation) hydrocarbon intermediate. This transition state would therefore constitute either a reaction of two radicals (hydroxyl and alkyl) or a reaction of negatively charged OH^- and a carbocation. Finally, the oxidative half cycle of the reaction is followed by a series of electron transfers toward the external electron acceptor reoxidizing the enzyme active center.

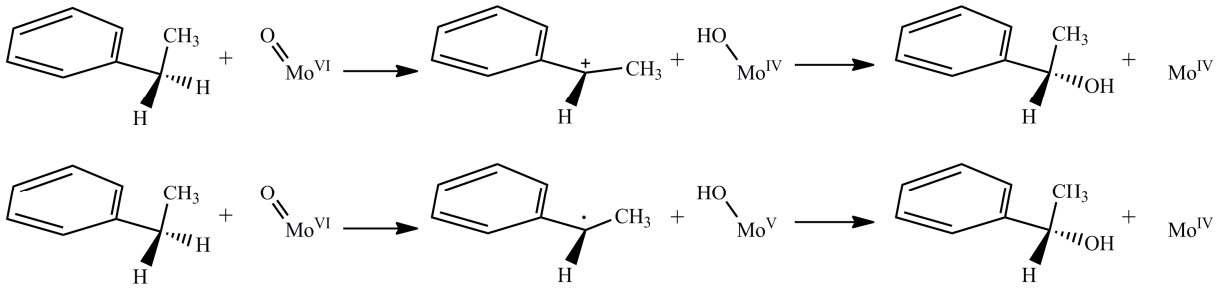

Fig. 3.4: Hypothetical variants of reaction mechanisms catalyzed by EBDH.
a) heterocyclic C-H cleavage, b) homolytic C-H cleavage.[159]

Small model complexes were computed by Dmitriy Bykov. Results for small model complexes derived from a protein crystal structure, where some atoms are fixed, are compared with free complexes with and without imidazole to estimate geometrical and chemical influences on the reactivity of the active site (Table. 3.1). The computed relative energies indicate that the intermediate and product formation is more favourable in the presence of the protein´s geometrical constraints. On the other hand there is no big difference (~3 kcal/mol) among the model complexes with and without imidazole where all the atoms are free to move.

Table 3.1: Computed energy barriers [kcal/mol] relative to the educt substrate complex for hydroxylation of ethyl benzene by small models of EBDH.

Small model complexes	**SCRF[a]**	**SCRF[b]**	**SCRF[c]**
Educt-substrate complex	0.0	0.0	0.0
Intermediate complex	34.0	47.9	44.4
Product complex	-7.7	13.4	16.4

Where, a = constraint containing complexes derived from the protein X-ray crystal structure, b = Free complexes without imidazole, c = Free complexes containing imidazole.

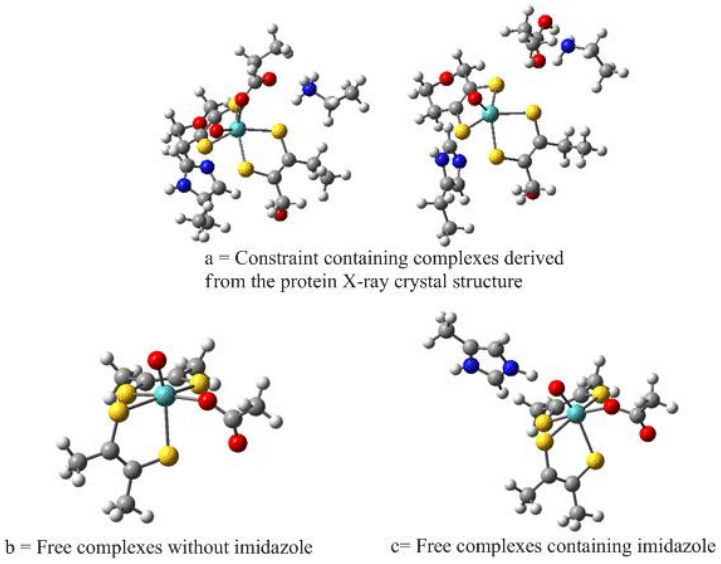

Fig. 3.5: Optimized geometries of small model complexes for the EBDH mechanism.

In the following a detailed density functional theory (DFT) study of the reaction mechanism for the hydroxylation of ethylbenzene is presented. Active site model complexes are derived from the protein X-ray crystal structure (PDB 2IVF).[155] Amino acid residues which may take part in the mechanism are included. For comparison models with protonation of His_{192}, Lys_{450}, Asp_{223} and a model without protonation are considered.

2. Computational Details

All the active site model geometries were optimized using Gaussian 09 with the hybrid density functional B3LYP[123] and the LANL2DZ basis set[124,125,126,127] augmented by polarization functions on sulfur atoms (ζ = 0.421).[128] The self-consistent field (SCF)[160] method was used with IntRep for the SCF procedure to account for integral symmetry and NoVaracc for full integral accuracy. Whenever there was an SCF convergence problem the QC[161] option was used which involves linear searches when far from convergence. The starting geometries for transition state (**TS**) searches were generated by shortening and lengthening of forming and breaking bonds, respectively. These geometries were then pre-optimized freezing the atoms that dominate the **TS** vector. Frequency calculations were performed on these pre-optimized geometries to obtain accurate internal force constants. For the frequency calculations #P was specified in the route section to produce some additional output. IOP (7/33=1) was used to get the internal force constants which were then helpful for the **TS** search. The optimized **TS** geometries were then slightly modified to generate the starting geometries for the geometry optimization of educt substrate complexes and intermediate complexes (from **TS1**) or intermediate complexes and product complexes (from

TS2). Single point energies were computed with the B3LYP functional and the Stuttgart-Dresden effective core potential basis set (SDD)[129,130] augmented by polarization functions for all atoms except Mo, W and H (ζ =0.600, 1.154, 0.864, and 0.421 for C, O, N, and S, respectively).[128] Self-consistent reaction field (SCRF) computations were performed on the optimized geometries to model the protein surrounding the active site by a conductor like polarizable continuum method (CPCM)[131] as implemented in Gaussian 09.[132,133] Default Gaussian 03 parameters were used for the evaluation of solute-solvent dispersion and repulsion interaction energies,[134,135] and solute cavitation energy variations.[136] The molecular cavity was specified using a minimum radius (RMin) of 0.5Å and an overlap index (OFac) of 0.8.[137]

3. Active Site Models

Active site model complexes were derived from the protein X-ray crystal structure (PDB 2IVF).[155] For the model complexes, the active site Mo coordinated with the two metallopterin ligands (*bis*MGD), Asp_{223}, Act_{1978} (acetate) group and nearby His_{192} were considered. Active site residues, Trp_{87}, Cys_{86}, Pro_{88}, Pro_{191}, Val_{193}, Gly_{222}, Thr_{224}, Phe_{446}, Gly_{445}, Ser_{447}, Lys_{450}, Ala_{449}, Ser_{151} were also considered as they may influence the catalytic reaction due to their proximity to the metal center. MGD ligands were truncated at the pyrazine ring, Act_{1978} to oxygen while Cys_{86}, Pro_{191}, Val_{193}, Gly_{222}, Thr_{224}, Phe_{446}, Gly_{445}, Ser_{447}, Ala_{449}, Ser_{151} were truncated at the alpha (α) carbon atoms. Pro_{88} was also truncated at the alpha (α) carbon atom but its ring was left intact. Hydrogen atoms were added manually. During all the calculations, alpha (α) carbon atoms of Cys_{86}, Pro_{88}, Pro_{191}, Val_{193}, Gly_{222}, Thr_{224}, Gly_{445}, Ser_{447}, Ala_{449}, and Ser_{151} were kept fixed at their crystal structure position to mimic the steric constraints by the protein matrix. The carbon atoms bonded with the dithiolene moieties of MGD ligands were also kept fixed.

First, hydrogen atoms were optimized applying one negative overall charge (assuming Mo at the +VI oxidation state), keeping all heavy-atoms fixed at their positions. The resulting geometries served as starting geometries for the generation of input geometries for relevant structures for computing the mechanism for hydroxylation of ethylbenzene.

4. Results

The reaction for the hydroxylation of ethylbenzene by EBDH starts with the oxidized (Mo^{VI}) enzyme. The EBDH active site center contains nearby residues, His_{192}, Lys_{450} and Asp_{223}, which seems to be in the best position to involve in the hydroxylation of ethylbenzene. For comparison, the active site centers are modeled in several forms; a non-protonated model and models having protonation at His_{192}, Lys_{450} or Asp_{223}.

In all the optimized geometries for the non-protonated, protonated His_{192}, protonated Lys_{450} and protonated Asp_{223} model complexes, hydrogen bonds are formed between Lys_{450}, Asp_{223} and Gly_{222} as well as between His_{192} and the O_1 atom of the oxo group ligated to the Mo atom (Fig 3.6). These hydrogen bonds help in the stabilization of the active site center and the hydroxylation of ethylbenzene. In the optimized geometries of non-protonated, protonated His_{192} and protonated Lys_{450} model EBDH reaction mechanisms, hydrogen atoms of terminal nitrogen atom of Lys_{450} form hydrogen bonds with the oxygen atom attached to the α carbon atom of Gly_{222} and with the oxygen atom of Asp_{223} as well as between His_{192} and the O_1 atom. These hydrogen bonds are present in all the optimized complex geometries except the optimized product complexes (**P** and **L-P**) where His_{192}-O_1 hydrogen bonds are missing (Fig. 3.7, 3.8 and 3.9).

In the optimized geometries of protonated Asp_{223} model EBDH reaction mechanism, one carbonyl oxygen atom of Gly_{222} forms hydrogen bonds with a NH_2 proton of Lys_{450} and the proton of Asp_{223} while the His_{192}-O_1 hydrogen bond is present in all the optimized geometries except **A-E**, **A-ES**, **A-TS2ô** and **A-P** (Fig. 3.10).

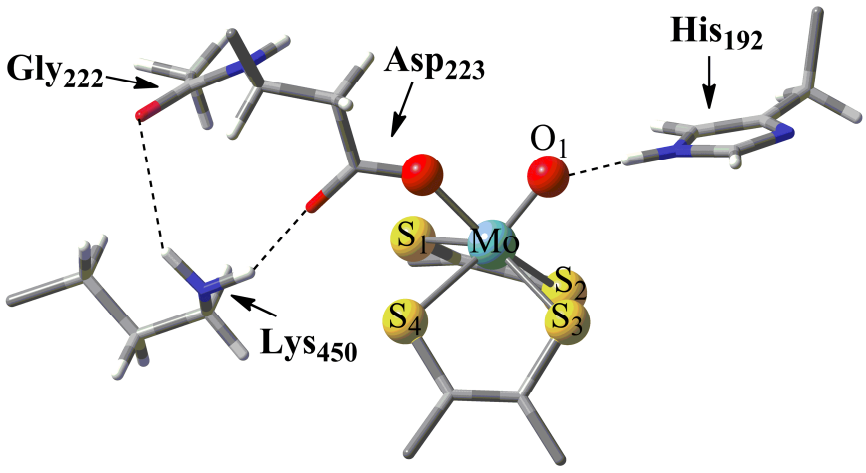

Fig. 3.6: The part of the active site of optimized model EBDH geometries chosen for the graphical representation of optimized complex geometries.

1. Non-protonated Complexes:

- *Optimized oxidized active site model complex* **E**:

The oxidized active site model complex (**E**) of EBDH was geometry optimized where the oxidation state of molybdenum is VI and the overall charge is -1. The optimized geometry is distinctively different in geometrical parameters of the coordination site of the metal center in comparison to the protein X-ray crystal structure of EBDH[154]. Optimized data show that the dithiolenes are twisted more against each other as the S_1-S_2-S_3-S_4 dihedral angle changes from -4.9˚ to 18.7˚ (Table 3.2), i.e. the coordination geometry is distorted trigonal prismatic. Bond distances between Mo and dithiolene sulfurs, S are also increased from ~2.370 Å to ~2.451 Å (Table 3.2).

- *Optimized educt-substrate complex* **ES**:

Geometry optimization of the educt-substrate model complex **ES** shows that the ethylbenzene is loosely bound to the active site center where the methylene group of the substrate molecule is facing the oxo ligand of the metal. The computed reaction energy for the **ES** complex formation is exothermic for the gas phase model, -3.7 kcal/mol, while it is endothermic for the continuum model, 12.0 kcal/mol with respect to separate substrate and educt complex **E** (Table 3.6). Optimized data shows that there is no considerable change in geometrical parameters of the active site relative to the oxidized active site model complex (**E**). Slight decrease in the S_1-S_2-S_3-S_4 dihedral angle (from 18.7˚ to 18.0˚) and in the Mo-S distances (from ~2.451 Å to ~2.448 Å) are observed.

In the optimized **ES** complex, *pro-S*-hydrogen (H_s) of C_1 of ethylbenzene substrate is at a distance of 2.525 Å from the metal bound oxygen (O_1) at the active site. The C_1-H_s bond distance is 1.099 Å and the dihedral angle between the ethyl group and the benzene ring of ethylbenzene is 68.9˚ (Table 3.2).

Hydroxylation of ethylbenzene is a two-step process; in the first step (**TS1**) the C_1-H_s bond of ethylbenzene breaks resulting in the formation of an intermediate having a metal bound hydroxide and a carbocation or radical substrate. The second step (**TS2**) involves the rebound of hydroxide from the metal center to the substrate intermediate resulting in the reduction of Mo and the formation of (*S*)-1-phenylethanol (hydroxylized substrate).

- *Optimized H-transfer transition state complexes* **TS1** *and* **TS1ô**

For the hydroxylation of ethylbenzene, the cleavage of the C_1-H_s bond is essential which could be by a two electron transfer step or two one electron transfer steps, i.e. heterolytic (singlet) or homolytic (triplet) cleavage of C_1-H_s bond, respectively. The activation of ethylbenzene appears to be possible when the substrate molecule approaches the oxo ligand with its methylene group. Two model complexes were optimized for the H-transfer transition state considering these two types of cleavages.

Geometrical optimization of transition state model complex **TS1** for heterolytic C_1-H_s bond cleavage shows a decrease in the S_1-S_2-S_3-S_4 dihedral angle (from 18.0˚ to 11.3˚) and in the Mo-S bond distances (from ~2.448 Å to ~2.430 Å) relative to the optimized **ES** geometry (Table 3.2). Elongated bond distances are observed for the Mo-O_1 (from 1.767 Å to 1.911 Å) and the C_1-H_s bond of ethylbenzene (from 1.099 Å to 1.492 Å). The O_1 and H_s distance is reduced from 2.525 Å to 1.120 Å. The dihedral angle between the ethyl group and the benzene ring of ethylbenzene is reduced from 68.9˚ to 9.5˚. The energy barrier for the heterolytic C_1-H_s bond cleavage and H-transfer from the ethylbenzene to the O_1 atom is 28.5 kcal/mol in the gas phase and 46.9 kcal/mol in the continuum (Table 3.6). It is the rate limiting step in the ethylbenzene hydroxylation.

In the optimized transition state model complex **TS1ô** for the homolytic C_1-H_s bond cleavage similar changes are observed in the S_1-S_2-S_3-S_4 dihedral angle (from 18.0˚ to 10.3˚) and in the Mo-S bond distances (~2.448 Å to ~2.426 Å). Elongated Mo-O_1 (from 1.767 Å to 1.912 Å) and C_1-H_s (from 1.099 Å to 1.508 Å) bonds are computed. The distance between O_1 and H_s is reduced from 2.525 Å to 1.116 Å when comparison is made to the optimized **ES** geometry. The dihedral angle between the ethyl group and the benzene ring of ethylbenzene is reduced from 68.9˚ to 8.8˚ (Table 3.2). The energy barrier for the homolytic C_1-H_s bond cleavage and H-transfer from the ethylbenzene to the O_1 atom is 27.1 kcal/mol in the gas phase and 42.3 kcal/mol in the continuum (Table 3.6). This makes the homolytic C_1-H_s bond cleavage somewhat (~4 kcal/mol) more favorable as compared to heterolytic C_1-H_s bond cleavage.

The educt substrate complex (**ES**) and the intermediate complex (**I** and **Iô**) starting geometries for geometry optimization were generated from these optimized transition state geometries. Slight reduction of Mo-O_1 and C_1-H_s bonds together with an elongation of the O_1-H_s distance gave the starting geometry for the **ES** complex. On the other hand a slight elongation of the

Mo-O_1 and C_1-H_s bonds and reduction of the O_1-H_s distance were performed to generate the starting geometry for the intermediate complexes **I** and **Iô**.

- *Optimized intermediate complexes* **I** *and* **Iô**:

The heterolytic C_1-H_s bond cleavage results in the formation of carbocation intermediate **I** while the homolytic C_1-H_s bond cleavage results in the formation of bi-radical type intermediate **Iô**.

The computed reaction energy for the formation of carbocation intermediate complex **I** is endothermic with respect to separate substrate and educt (**E**) complex, 26.8 kcal/mol in gas phase and 43.5 kcal/mol in the continuum (Table 3.6). Geometry optimization of **I** shows a decrease in the S_1-S_2-S_3-S_4 dihedral angle (from 11.3˚ to 5.5˚) and in the Mo-S bond distances (from ~2.43 Å to ~2.407 Å). The Mo-O_1 and C_1-H_s distances are elongated from 1.911 Å to 2.029 Å and 1.492 Å to 3.60 Å, respectively when comparison is made to the optimized **TS1** geometry. The O_1-H_s bond is reduced from 1.120 Å to 0.983 Å. The dihedral angle between the ethyl group and the benzene ring of ethylbenzene is reduced from 9.5˚ to 4.5˚ (Table 3.2).

The computed reaction energy for the formation of radical intermediate, **Iô** as a result of homolytic C_1-H_s bond cleavage, is also endothermic (10.6 kcal/mol in the gas phase and 23.3 kcal/mol in the continuum (Table 3.6)) but less endothermic as compared to the energy for the heterolytic C_1-H_s bond cleavage. Optimized data shows the decrease in S_1-S_2-S_3-S_4 dihedral angle (from 10.3˚ to 7.7˚) and in the Mo-S distances (from ~2.426 Å to ~2.407 Å), elongated Mo-O_1 (from 1.912 Å to 2.014 Å) and C_1-H_s (1.508 Å to 3.677 Å) distances with respect to optimized **TS1ô** geometry. The O_1-H_s bond is reduced from 1.116 Å to 0.983 Å. The dihedral angle between the ethyl group and the benzene ring of ethylbenzene is reduced from 8.8˚ to 0.0˚ (Table 3.2). The formation of the bi-radical type intermediate is (~20 kcal/mol) more favorable as compared to the carbocation intermediate.

In order to generate starting geometries for the OH-transfer transition state complexes (**TS2** and **TS2ô**) O_1-H_s was slightly reoriented, to facilitate the transfer of hydroxide from the metal to the C_1 of radical or carbocation type substrate intermediate, and the O_1-C_1 distance was reduced in the optimized intermediate complex (**I** and **Iô**).

- *Optimized OH-transfer transition state complexes* **TS2** *and* **TS2ô**:

The second step of the ethylbenzene hydroxylation involves the rebound of hydroxide from the metal center to the carbocation or radical intermediate substrate resulting in the reduction

of Mo from oxidation state VI to IV and the formation of (*S*)-1-phenylethanol (hydroxylized substrate).

The energy barrier for the transition state **TS2** where an O_1H_s anion is transferred from Mo to the C_1 of the carbocation intermediate is 32.0 kcal/mol in the gas phase and 45.1 kcal/mol in the continuum with respect to separate substrate and educt (**E**) complex (Table 3.6). Geometry optimization data shows a further decrease in the S_1-S_2-S_3-S_4 dihedral angle from 5.5˚ to -0.1˚ relative to optimized **I** geometry. Slight changes are found in the Mo-S and O_1-H_s bond distances. The Mo-O_1H_s bond is elongated from 2.029 Å to 2.102 Å. The distance between the C_1 and O_1H_s is decreased from 3.60 Å to 2.415 Å. The dihedral angle between the ethyl group and the benzene ring of ethylbenzene is increased from 4.5˚ to 18.0˚ (Table 3.2).

The energy barrier for the transition state **TS2ô** where O_1H_s is transferred from Mo to C_1 of the radical type intermediate is 35.1 kcal/mol in the gas phase and 54.6 kcal/mol in the continuum (Table 3.6). Optimized data shows a change in the S_1-S_2-S_3-S_4 dihedral angle (from 7.7˚ to -18.3˚) and in the Mo-S distances (from ~2.407 Å to 2.453 Å) when compared with optimized **Iô** geometry. The Mo-O_1H_s bond is elongated from 2.014 Å to 2.181 Å. A slight change is found in the O_1-H_s bond distance. The distance between the C_1 and O_1H_s is decreased from 3.677 Å to 2.290 Å. The dihedral angle between the ethyl group and the benzene ring of ethylbenzene is increased from 0.0˚ to 5.6˚ (Table 3.2).

Comparison between the energy barriers for the transition states **TS2** and **TS2ô** shows that **TS2** is more favorable. So, the second step may involve the abstraction of a second electron from the radical type intermediate (converting it to a carbocation intermediate) and then the rebound of the hydroxide (O_1H_s) group from the Mo to the carbocation intermediate resulting in the formation of (*S*)-1-phenylethanol.

The starting geometry for the geometry optimization of product complex **P** was generated by the slight modification in the optimized **TS2** geometry, i.e. slight elongation of the Mo-O_1H_s and reduction of the C_1-O_1H_s distances.

- *Optimized product complex* **P:**

The final step in the hydroxylation of ethylbenzene is the transfer of O_1H_s from the Mo to the C_1 of carbocation intermediate resulting in the formation of (*S*)-1-phenylethanol. The computed reaction energy for the product bound complex **P** is slightly exothermic, -1.2 kcal/mol in the gas phase and endothermic in the continuum, 17.5 kcal/mol (Table 3.6)

relative to separate substrate and educt complex **E**. Geometry optimization shows a slight change in the S_1-S_2-S_3-S_4 dihedral angle (from -0.1˚ to -1.7˚) and in the Mo-S distances (from ~2.403 Å to ~2.395 Å) when comparison is made with the optimized **TS2** geometry. The Mo-O_1H_s distance is increased from 2.102 Å to 2.242 Å while the C_1-O_1H_s distance is reduced from 2.415 Å to 1.506 Å. The dihedral angle between the ethyl group and the benzene ring of hydroxyl-ethylbenzene is reduced from 18.0˚ to -10.8˚ (Table 3.2).

Table 3.2: Geometrical parameters of the optimized model complexes of the reaction mechanism for the non-protonated EBDH model.

Non-prot	**Heterolytic Cleavage/Singlet**							**Homolytic Cleavage/Triplet**		
	X	**E**	**ES**	**TS1**	**I**	**TS2**	**P**	**TS1ô**	**Iô**	**TS2ô**
Mo-S_1 (Ù)	2.369	2.432	2.431	2.416	2.395	2.383	2.367	2.401	2.389	2.413
Mo-S_2 (Ù)	2.427	2.439	2.437	2.446	2.430	2.408	2.423	2.443	2.434	2.467
Mo-S_3 (Ù)	2.291	2.411	2.413	2.42	2.397	2.399	2.394	2.414	2.402	2.452
Mo-S_4 (Ù)	2.391	2.520	2.511	2.438	2.407	2.423	2.397	2.444	2.404	2.479
Dihedral, S_1-S_2-S_3-S_4(è)	-4.7	18.7	18.0	11.3	5.5	-0.1	-1.7	10.3	7.7	-18.3
Mo-O_1 (Ù)	2.18	1.762	1.767	1.911	2.029	2.102	2.242	1.912	2.014	2.181
O_1é H_s (Ù)	-	-	2.525	1.120	0.983	0.984	0.977	1.116	0.983	0.985
C_1é H_s/C_1é O_1 (Ù)	-	-	1.099	1.492	3.60	2.415	1.506	1.508	3.677	2.290
Ethyl-benzene ring dihedral (è)	-	-	68.9	9.5	4.5	18.0	-10.8	8.8	0.0	5.6

Where, **X** = protein X-ray crystal structure data, **E** = educt complex, **ES** = educt-substrate complex, **TS1** = H-transfer transition state complex, **I** = intermediate complex, **TS2** = OH-transfer transition state, **P** = Product bound complex.

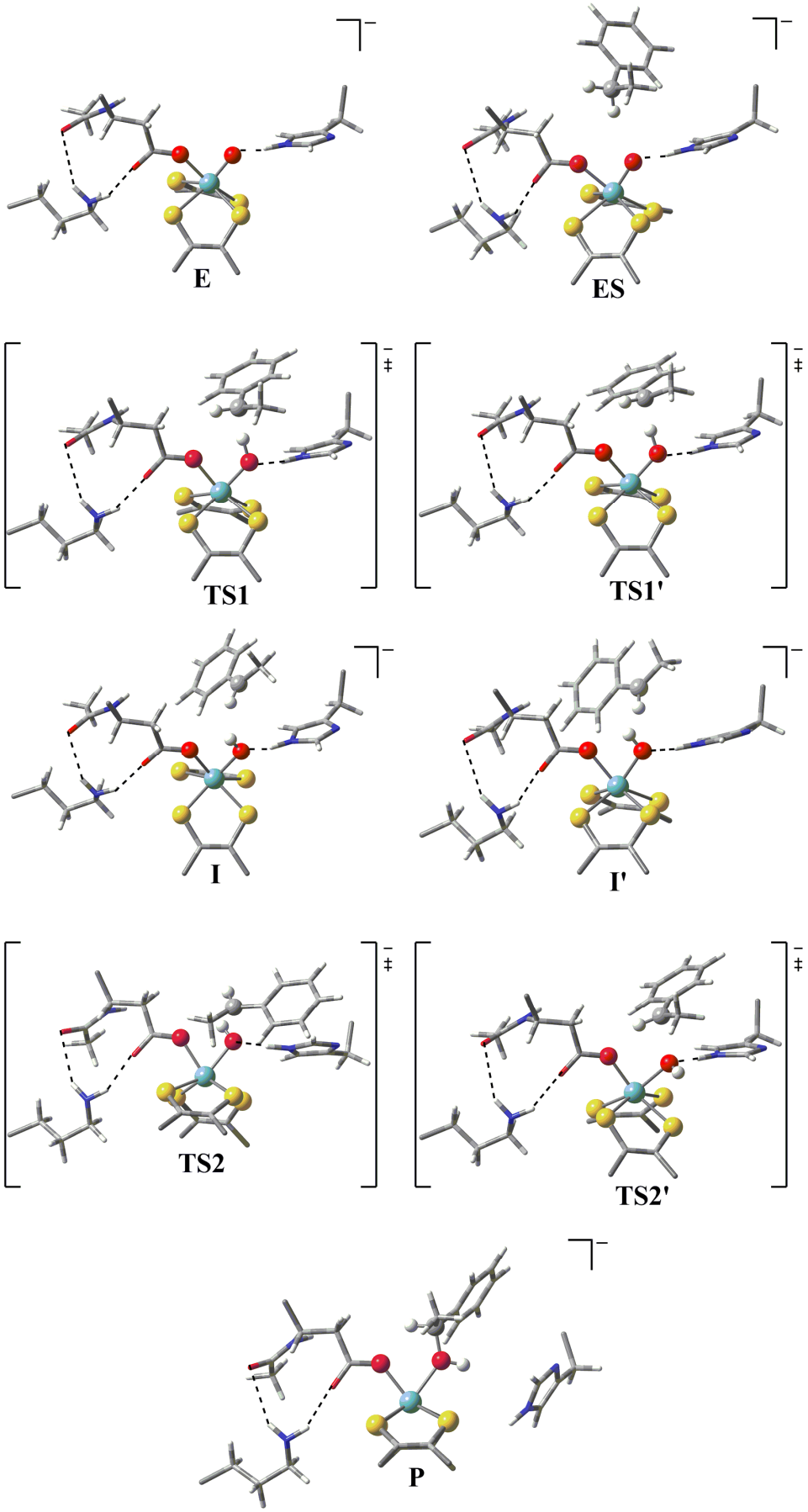

Fig. 3.7: Optimized geometries for the non-protonated EBDH reaction mechanism.

2. *Protonated His Complexes:*

- *Optimized oxidized model complex* **H-E**:

The oxidized active site model complex (**H-E**) of His_{192} protonated EBDH was geometry optimized where the oxidation state of molybdenum is VI and the overall complex is neutral. The optimized geometry is distinctively different in geometrical parameters of the metal coordination site, in the same way as the optimized non-protonated **E** geometry, when comparison is made to the protein X-ray crystal structure of EBDH.[154] Optimized data show that the dithiolenes are twisted more against each other as the S_1-S_2-S_3-S_4 dihedral angle changes from -4.9˚ to 17.3˚, i.e. the coordination geometry is distorted trigonal prismatic. Bond distances between Mo and dithiolene sulfurs, S are also increased from ~2.370 Å to ~2.441 Å (Table 3.3). The proton of protonated His_{192} (H_{His}) is making hydrogen bond (distance is 1.360 Å) with the O_1 attached to the Mo while the H_{His}-N_{His} bond distance is 1.124 Å (Fig 3.8).

- *Optimized educt-substrate complex* **H-ES**:

The computed reaction energy for the **H-ES** complex formation is exothermic for the gas phase model, -4.8 kcal/mol, while it is endothermic for the continuum model, 16.0 kcal/mol relative to separate substrate and educt (**H-E**) complex (Table 3.6). Optimized data shows that there is no considerable change in geometrical parameters of the active site relative to the oxidized active site model complex **H-E**. The S_1-S_2-S_3-S_4 dihedral angle is 16.8˚ and the Mo-S distance is ~2.439 Å (Table 3.3). The O_1-H_{His} (a hydrogen bond) and H_{His}-N_{His} bond distances are 1.408 Å and 1.103 Å, respectively.

In the optimized **H-ES** complex, *pro-S*-hydrogen (H_s) of C_1 of ethylbenzene substrate is at a distance of 2.375 Å from the metal bound oxygen (O_1) at the active site. The C_1-H_s bond distance is 1.098 Å and the dihedral angle between the ethyl group and the benzene ring of ethylbenzene is -13.2˚ (Table 3.3).

- *Optimized H-transfer transition state complexes* **H-TS1** *and* **H-TS1ô**:

Geometrical optimization of transition state model complex **H-TS1** for heterolytic C_1-H_s bond cleavage shows slight reductions in the S_1-S_2-S_3-S_4 dihedral angle (from 17.1˚ to 12.4˚) and in the Mo-S bond distances (from ~2.440 Å to ~2.420 Å). Elongated bond distances are observed for the Mo-O_1 (from 1.803 Å to 1.958 Å) and the C_1-H_s bond of ethylbenzene (from 1.098 Å to 1.493 Å). The O_1 and H_s distance is reduced from 3.623 Å to 1.134 Å. The

dihedral angle between the ethyl group and the benzene ring of ethylbenzene is reduced from 85.2˚ to 6.5˚ with respect to the optimized **H-ES** complex geometry (Table 3.3). The O_1-H_{His} (a hydrogen bond) distance is reduced from 1.408 Å to 1.308 Å while the H_{His}-N_{His} bond distance is increased from 1.103 Å to 1.169 Å. The energy barrier for the heterolytic C_1-H_s bond cleavage and H-transfer from the ethylbenzene to the O_1 atom is 24.3 kcal/mol in the gas phase and 46.1 kcal/mol in the continuum relative to separate substrate and educt (**H-E**) complex (Table 3.6). It is the rate limiting step in the ethylbenzene hydroxylation.

Optimized data for the transition state model complex **H-TS1ô** for homolytic C_1-H_s bond cleavage shows that, in contrast to the optimized **H-TS1** geometry, the proton (H_{His}) is transferred from the protonated His_{192} to the O_1 resulting in the formation of a water ligand coordinated to the Mo active site metal. As a result, the O_1-H_{His} distance is reduced from 1.408 Å to 1.073 Å while the H_{His}-N_{His} (a hydrogen bond) distance is increased from 1.103 Å to 1.467 Å. A decrease in the S_1-S_2-S_3-S_4 dihedral angle (from 17.1˚ to 8.7˚) and in the Mo-S bond distances (from ~2.440 Å to ~2.422 Å) is observed when comparison is made to the optimized **H-ES** geometry. Elongated Mo-O_1 (from 1.803 Å to 2.007 Å) and C_1-H_s (from 1.093 Å to 1.394 Å) bonds are computed. The distance between O_1 and H_s is reduced from 3.623 Å to 1.205 Å. The dihedral angle between the ethyl group and the benzene ring of ethylbenzene is reduced from 85.2˚ to 8.5˚ (Table 3.3). The energy barrier for the homolytic C_1-H_s bond cleavage and H-transfer from the ethylbenzene to the O_1 atom is 14.0 kcal/mol in the gas phase and 32.7 kcal/mol in the continuum relative to separate substrate and educt complex **H-E** (Table 3.6).

- *Optimized intermediate complexes* **H-I** *and* **H-Iô**:

The computed reaction energy for the formation of carbocation intermediate complex **H-I** is endothermic with respect to separate substrate and educt (**H-E**) complex, 21.0 kcal/mol in gas phase and 41.7 kcal/mol in the continuum (Table 3.6). Geometry optimization of the **H-I** complex shows that the proton (H_{His}) is transferred from the protonated His_{192} to the O_1 attached to Mo resulting in the formation of a Mo coordinated water molecule. As a result, the O_1-H_{His} distance is reduced from 1.308 Å to 1.092 Å while the H_{His}-N_{His} (a hydrogen bond) distance is increased from 1.169 Å to 1.399 Å. A decrease in the S_1-S_2-S_3-S_4 dihedral angle (from 12.4˚ to 3.5˚) and in the Mo-S bond distances (from ~2.420 Å to ~2.400 Å) are observed when compared to the optimized **H-TS1** geometry. The Mo-O_1 and C_1-H_s distances are elongated from 1.958 Å to 2.097 Å and 1.493 Å to 2.675 Å, respectively. The O_1-H_s bond

is reduced from 1.134 Å to 0.980 Å. The dihedral angle between the ethyl group and the benzene ring of ethylbenzene is reduced from 6.5˚ to 1.5˚ (Table 3.3).

The computed reaction energy for the formation of radical intermediate, **H-Iô** as a result of homolytic C_1-H_s bond cleavage, is also endothermic (2.8 kcal/mol in the gas phase and 20.0 kcal/mol for the polarizable continuum computation (Table 3.6) relative to the separate substrate and educt (**H-E**) complex) but less endothermic as compared to the computed energy for the heterolytic C_1-H_s bond cleavage. Optimized data shows a decrease in the S_1-S_2-S_3-S_4 dihedral angle (from 8.7˚ to 4.4˚) and in the Mo-S distances (from ~2.422 Å to ~2.400 Å), elongated Mo-O_1 (from 2.007 Å to 2.092 Å) and C_1-H_s (1.394 Å to 2.589 Å) distances with respect to optimized **H-TS1ô** geometry. The O_1-H_s bond is reduced from 1.205 Å to 0.980 Å. The dihedral angle between the ethyl group and the benzene ring of ethylbenzene is reduced from 8.5˚ to 1.9˚ (Table 3.3). The O_1-H_{His} distance is slightly increased from 1.073 Å to 1.090 Å while the H_{His}-N_{His} (a hydrogen bond) distance is reduced from 1.467 Å to 1.405 Å.

- *Optimized OH-transfer transition state complexes* **H-TS2** *and* **H-TS2ô**:

The optimized **H-I** and **H-Iô** geometries were slightly modified to generate the starting geometries for the optimization of OH-transfer transition state complexes, **H-TS2** and **H-TS2ô**. The O_1-H_{His} distance was slightly increased while the H_{His}-N_{His} distance was reduced. The O_1-H_s group was slightly reoriented and the O_1-C_1 distance was reduced to facilitate the transfer of hydroxide from the metal to the C_1 of the radical or carbocation type substrate in the optimized (**H-I** and **H-Iô**) intermediate geometries.

The energy barrier for the transition state (**H-TS2**) where an O_1H_s anion is transferred from Mo to the C_1 of the carbocation intermediate is 29.0 kcal/mol in the gas phase and 48.7 kcal/mol in the continuum (Table 3.6). Geometry optimization data shows no considerable change in the S_1-S_2-S_3-S_4 dihedral angle (from 3.5˚ to 3.2˚), in the Mo-S (from ~2.400 Å to ~2.395 Å) and in the O_1-H_s (from 0.980 Å to 0.981 Å) bond distances relative to the optimized **H-I** geometry. The Mo-O_1H_s bond is elongated from 2.097 Å to 2.230 Å. The distance between the C_1 and O_1H_s is decreased from 2.675 Å to 2.233 Å. The dihedral angle between the ethyl group and the benzene ring of ethylbenzene is slightly decreased from 1.5˚ to 0.4˚ (Table 3.3). The O_1-H_{His} (a hydrogen bond) distance is increased from 1.092 Å to 1.421 Å while the H_{His}-N_{His} bond distance is reduced from 1.399 Å to 1.119 Å.

The energy barrier for the transition state (**H-TS2ô**) where O_1H_s is transferred from Mo to C_1 of the radical type intermediate is 36.4 kcal/mol in the gas phase and 52.4 kcal/mol in the continuum (Table 3.6). Optimized data shows a change in the S_1-S_2-S_3-S_4 dihedral angle (from 4.4˚ to -3.8˚) and in the Mo-S distances (from ~2.400 Å to 2.430 Å) as compared to the optimized **H-Iô** geometry. The Mo-O_1H_s bond is elongated from 2.092 Å to 2.328 Å. No significant change is observed in the O_1-H_s (from 0.980 Å to 0.988 Å) bond distance. The distance between the C_1 and O_1H_s is decreased from 2.589 Å to 2.073 Å. The dihedral angle between the ethyl group and the benzene ring of ethylbenzene is increased from 1.9˚ to 19.7˚ (Table 3.3). The O_1-H_{His} (a hydrogen bond) distance is increased from 1.090 Å to 1.390 Å while the H_{His}-N_{His} bond distance is reduced from 1.405 Å to 1.132 Å.

- *Optimized product complex* **H-P***:*

The optimized **H-TS2** geometry is modified (the O_1-C_1 distance is slightly reduced) for the generation of starting geometry for geometry optimization of product bound complex **H-P**. The computed reaction energy for the product bound complex **H-P** is endothermic relative to separate substrate and educt (**H-E**) complex, 8.3 kcal/mol in the gas phase and 28.2 kcal/mol in the continuum (Table 3.6). Geometry optimization shows a change in the S_1-S_2-S_3-S_4 dihedral angle (from 3.2˚ to -4.6˚) and in the Mo-S distances (from ~2.395 Å to ~2.385 Å). The Mo-O_1H_s distance is increased from 2.230 Å to 2.669 Å while the C_1-O_1H_s distance is reduced from 2.233 Å to 1.518 Å when comparison is made with the optimized **H-TS2** geometry. The dihedral angle between the ethyl group and the benzene ring of hydroxy-ethylbenzene is 49.6˚ (Table 3.3). The O_1-H_{His} distance is increased from 1.421 Å to 1.595 Å while the H_{His}-N_{His} bond distance is reduced from 1.119 Å to 1.057 Å.

Table 3.3: Geometrical parameters of the optimized model complexes of the reaction mechanism for the His_{192} protonated EBDH.

Prot-His	Heterolytic Cleavage/Singlet							Homolytic Cleavage/Triplet		
	X	H-E	H-ES	H-TS1	H-I	H-TS2	H-P	H-TS1ô	H-Iô	H-TS2ô
Mo-S_1 (Ù)	2.369	2.429	2.431	2.407	2.383	2.384	2.329	2.418	2.390	2.386
Mo-S_2 (Ù)	2.427	2.435	2.431	2.439	2.439	2.416	2.422	2.465	2.452	2.459
Mo-S_3 (Ù)	2.291	2.409	2.408	2.412	2.390	2.392	2.421	2.399	2.382	2.441
Mo-S_4 (Ù)	2.391	2.491	2.486	2.421	2.386	2.388	2.369	2.407	2.379	2.432
Dihedral, S_1-S_2-S_3-S_4(è)	-4.9	17.3	16.8	12.4	3.5	3.2	-4.6	8.7	4.4	-3.8
Mo-O_1 (Ù)	2.18	1.807	1.805	1.958	2.097	2.230	2.669	2.007	2.092	2.328
O_1é H_s (Ù)	-	-	2.375	1.134	0.980	0.981	0.989	1.205	0.980	0.988
C_1é H_s/C_1é O_1 (Ù)	-	-	1.098	1.493	2.675	2.233	1.518	1.394	2.589	2.073
Ethyl-benzene ring dihedral (è)	-	-	-13.2	6.5	1.5	0.4	49.6	8.5	1.9	19.7
O_1-H_{His} (Ù)	-	1.360	1.408	1.308	1.092	1.421	1.595	1.073	1.090	1.390
H_{His}-N_{His} (Ù)	-	1.124	1.103	1.169	1.399	1.119	1.057	1.467	1.405	1.132

Where, **X** = protein X-ray crystal structure data, **H-E** = educt complex, **H-ES** = educt-substrate complex, **H-TS1** = H-transfer transition state complex, **H-I** = intermediate complex, **H-TS2** = OH-transfer transition state complex, **H-P** = Product bound complex.

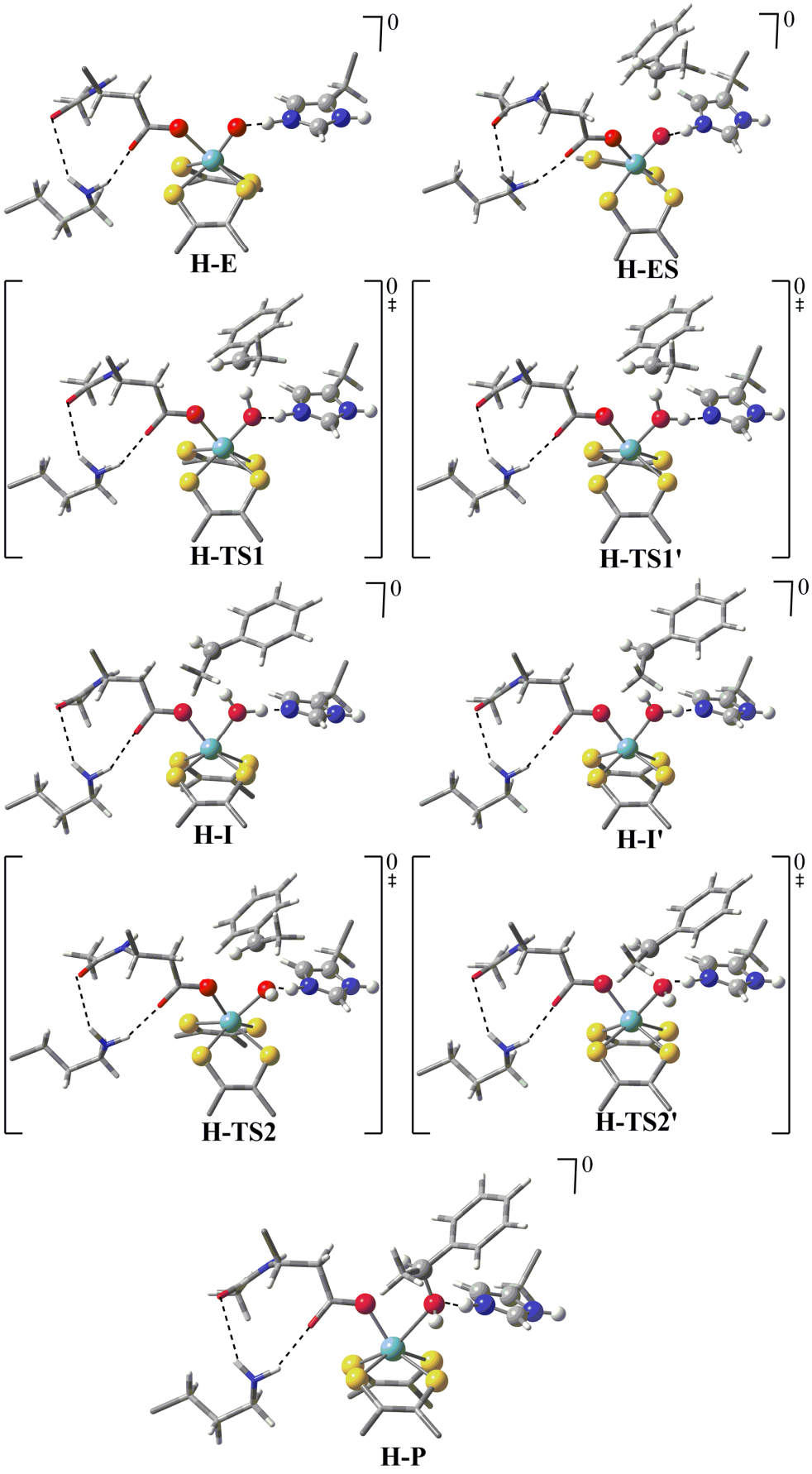

Fig. 3.8: Optimized geometries for the His_{192}-protonated EBDH reaction mechanism.

3. Protonated Lys Complexes:

- *Optimized oxidized model complex* **L-E**:

The oxidized active site model complex (**L-E**) of Lys_{450} protonated EBDH derived from the protein X-ray crystal structure was geometry optimized where the oxidation state of molybdenum is VI and the overall complex is neutral. The optimized geometry is distinctively different in geometrical parameters of the coordination site of the metal center in comparison to the protein X-ray crystal structure of EBDH[154] as well as to the optimized **E** and **H-E** geometries. The optimized data shows that the dithiolenes are twisted more against each other as the S_1-S_2-S_3-S_4 dihedral angle changes from -4.9˚ to 36.0˚. Bond distances between Mo and dithiolene sulfurs, S also increased from ~2.370 Å to ~2.461 Å (Table 3.4).

- *Optimized educt-substrate complex* **L-ES**:

The computed reaction energy for the **L-ES** complex formation is exothermic for the gas phase model, -8.1 kcal/mol, while it is endothermic for the continuum model, 12.4 kcal/mol relative to the separate substrate and educt (**L-E**) complex (Table 3.6). Optimized data shows that there is no considerable change in geometrical parameters of the active site relative to the oxidized active site model complex **L-E**. The S_1-S_2-S_3-S_4 dihedral angle is 35.1˚ and Mo-S distance is ~2.469 Å (Table 3.4).

In the optimized **L-ES** complex, *pro-S*-hydrogen (H_s) of C_1 of ethylbenzene substrate is at a distance of 2.502 Å from the metal bound oxygen (O_1) at the active site. The C_1-H_s bond distance is 1.098 Å and the dihedral angle between the ethyl group and the benzene ring of ethylbenzene is -12.7˚ (Table 3.4).

- *Optimized H-transfer transition state complexes* **L-TS1** *and* **L-TS1**

Geometrical optimization of transition state model complex **L-TS1** for heterolytic C_1-H_s bond cleavage shows reductions in the S_1-S_2-S_3-S_4 dihedral angle (from 35.1˚ to 14.2˚) and in the Mo-S bond distances (from ~2.469 Å to ~2.430 Å). Elongated bond distances are observed for the Mo-O_1 (from 1.753 Å to 1.899 Å) and the C_1-H_s bond of ethylbenzene (from 1.098 Å to 1.493 Å). The O_1 and H_s distance is reduced from 2.502 Å to 1.114 Å. The dihedral angle between the ethyl group and the benzene ring of ethylbenzene is increased from -12.7˚ to 11.8˚ relative to the optimized **L-ES** geometry (Table 3.4). The energy barrier for the heterolytic C_1-H_s bond cleavage and H-transfer from the ethylbenzene to the O_1 atom is 22.5

kcal/mol in the gas phase and 47.5 kcal/mol in the continuum with respect to the separate substrate and educt (**L-E**) complex (Table 3.6).

Optimized data for the transition state model complex **L-TS1ô** for homolytic C_1-H_s bond cleavage shows a decrease in the S_1-S_2-S_3-S_4 dihedral angle (from 35.1˚ to 7.4˚) and in the Mo-S bond distances (from ~2.469 Å to ~2.427 Å). Elongated Mo-O_1 (from 1.753 Å to 1.912 Å) and C_1-H_s (from 1.098 Å to 1.369 Å) bonds are computed. The distance between O_1 and H_s is reduced from 2.502 Å to 1.223 Å. The dihedral angle between the ethyl group and the benzene ring of ethylbenzene is increased from -12.7˚ to 16.0˚ as compared to the optimized **L-ES** geometry (Table 3.4). The energy barrier for the homolytic C_1-H_s bond cleavage and H-transfer from the ethylbenzene to the O_1 atom is 30.7 kcal/mol in the gas phase and 36.5 kcal/mol in the continuum (Table 3.6).

- *Optimized intermediate complexes* **L-I** *and* **L-Iô**:

The computed reaction energy for the formation of carbocation intermediate complex **L-I** is endothermic relative to the separate substrate and educt (**L-E**) complex, 26.1 kcal/mol in gas phase and 40.3 kcal/mol in the continuum (Table 3.6). Geometry optimization of **L-I** shows a decrease in the S_1-S_2-S_3-S_4 dihedral angle (from 14.2˚ to 6.3˚) and in the Mo-S bond distances (from ~2.430 Å to ~2.403 Å). The Mo-O_1 and C_1-H_s distances are elongated from 1.899 Å to 2.010 Å and 1.493 Å to 3.794 Å, respectively, as compared to the optimized **L-TS1** geometry. The O_1-H_s bond is reduced from 1.114 Å to 0.983 Å. The dihedral angle between the ethyl group and the benzene ring of ethylbenzene is reduced from 11.8˚ to 1.3˚ (Table 3.4).

The computed reaction energy for the formation of radical intermediate complex **L-Iô** as a result of homolytic C_1-H_s bond cleavage, is also endothermic (8.1 kcal/mol in the gas phase and 25.5 kcal/mol when a polarizable continuum model is included (Table 3.6)) but less endothermic as compared to the energy for the heterolytic C_1-H_s bond cleavage. Optimized data shows no significant change in the S_1-S_2-S_3-S_4 dihedral angle (from 7.4˚ to 8.0˚) and a decrease in the Mo-S distances (from ~2.427 Å to ~2.408 Å), elongated Mo-O_1 (from 1.912 Å to 1.981 Å) and C_1-H_s (1.369 Å to 4.532 Å) distances with respect to the optimized **L-TS1ô** geometry. The O_1-H_s bond distance is reduced from 1.223 Å to 0.982 Å. The dihedral angle between the ethyl group and the benzene ring of ethylbenzene is reduced from 16.0˚ to 3.5˚ (Table 3.4).

- *Optimized OH-transfer transition state complexes* **L-TS2** *and* **L-TS2ô**:

The energy barrier for the transition state **L-TS2** where an O_1H_s anion is transferred from Mo to the C_1 of the carbocation intermediate is 22.0 kcal/mol in the gas phase and 43.0 kcal/mol in the polarizable continuum model (Table 3.6). Geometry optimization data shows a further decrease in S_1-S_2-S_3-S_4 dihedral angle from 6.3˚ to 3.6˚ relative to the optimized **L-I** geometry. Slight changes are found in the Mo-S and O_1-H_s bond distances. The Mo-O_1H_s bond is elongated from 2.010 Å to 2.057 Å. The distance between the C_1 and O_1H_s is decreased from 3.794 Å to 2.701 Å. The dihedral angle between the ethyl group and the benzene ring of ethylbenzene is changed from 1.3˚ to -0.7˚ (Table 3.4).

The energy barrier for the transition state **L-TS2ô** where O_1H_s is transferred from Mo to C_1 of the radical type intermediate is 29.9 kcal/mol in the gas phase and 53.4 kcal/mol in the continuum (Table 3.6). Optimized data shows a change in the S_1-S_2-S_3-S_4 dihedral angle (from 8.0˚ to -17.7˚) and in the Mo-S distances (from ~2.408 Å to 2.446 Å). The Mo-O_1H_s bond is elongated from 1.981 Å to 2.155 Å. No significant change is found in the O_1-H_s (from 0.982 Å to 0.985 Å) bond distance. The distance between the C_1 and O_1H_s is decreased from 4.532 Å to 2.370 Å. No considerable change is observed in the dihedral angle between the ethyl group and the benzene ring of ethylbenzene (from 3.5˚ to 3.9˚) relative to the optimized **L-Iô** geometry (Table 3.4).

- *Optimized product complex* **L-P***:*

The optimized **L-TS2** geometry is modified (the O_1-C_1 distance is slightly reduced) for generating the starting geometry for geometry optimization of product bound complex **L-P**. The computed reaction energy for the product bound complex is exothermic in the gas phase, -8.7 kcal/mol and endothermic for the continuum model, 12.5 kcal/mol (Table 3.6) relative to separate substrate and educt (**L-E**) complex. Geometry optimization shows a slight change in the S_1-S_2-S_3-S_4 dihedral angle (from 3.6˚ to 4.3˚) and in the Mo-S distances (from ~2.399 Å to ~2.391 Å) when comparison is made with the optimized **L-TS2** geometry. The Mo-O_1H_s bond distance is increased from 2.057 Å to 2.248 Å while the C_1-O_1H_s distance is reduced from 2.701Å to 1.505 Å. The dihedral angle between the ethyl group and the benzene ring of hydroxy-ethylbenzene is increased from -0.7˚ to 60.4˚ (Table 3.4).

Table3.4: Geometrical parameters of the optimized model complexes of the reaction mechanism for the Lys_{450} protonated EBDH.

Prot-Lys	Heterolytic Cleavage/Singlet							Homolytic Cleavage/Triplet		
	X	L-E	L-ES	L-TS1	L-I	L-TS2	L-P	L-TS1ô	L-Iô	L-TS2ô
Mo-S_1 (Ù)	2.369	2.436	2.439	2.410	2.380	2.382	2.357	2.417	2.381	2.414
Mo-S_2 (Ù)	2.427	2.417	2.420	2.451	2.419	2.408	2.421	2.445	2.421	2.453
Mo-S_3 (Ù)	2.291	2.429	2.427	2.415	2.401	2.393	2.391	2.400	2.408	2.434
Mo-S_4 (Ù)	2.391	2.567	2.589	2.445	2.412	2.411	2.395	2.444	2.423	2.483
Dihedral, S_1-S_2-S_3-S_4(ę)	-4.9	36.0	35.1	14.2	6.3	3.6	4.3	7.4	8.0	-17.7
Mo-O_1 (Ù)	2.18	1.751	1.753	1.899	2.010	2.057	2.248	1.912	1.981	2.155
O_1é H_s (Ù)	-	-	2.502	1.114	0.983	0.980	0.979	1.223	0.982	0.985
C_1é H_s/C_1é O_1 (Ù)	-	-	1.098	1.493	3.794	2.701	1.505	1.369	4.532	2.370
Ethyl-benzene ring dihedral (ę)	-	-	-12.7	11.8	1.3	-0.7	60.4	16.0	3.5	3.9

Where, **X** = protein X-ray crystal structure data, **L-E** = educt complex, **L-ES** = educt-substrate complex, **L-TS1** = H-transfer transition state complex, **L-I** = intermediate complex, **L-TS2** = OH-transfer transition state, **L-P** = Product bound complex.

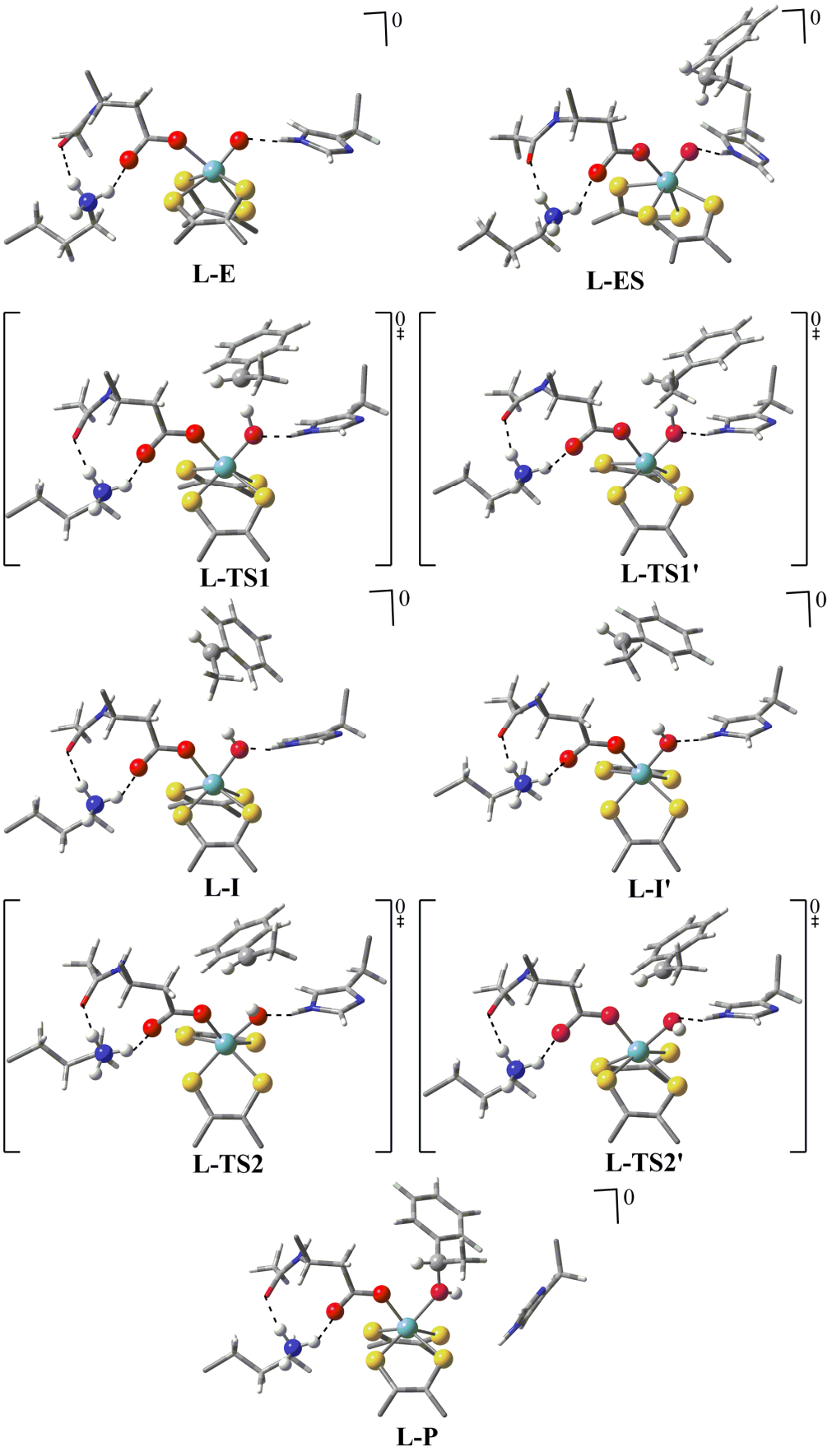

Fig. 3.9: Optimized geometries of Lys-protonated model structures relevant in the EBDH reaction mechanism.

4. Protonated Asp_{223} Complexes:

- *Optimized oxidized model complex* **A-E**:

The oxidized active site model complex (**A-E**) of Asp_{223} protonated EBDH derived from protein X-ray crystal structure is geometry optimized where the oxidation state of molybdenum is VI and the overall complex is neutral. Geometrical optimization shows that the Asp_{223} is detached from the Mo while the proton of Asp_{223} forms a hydrogen bond with the oxygen atom of Gly_{222} when comparison is made with the protein X-ray crystal structure of EBDH. The dithiolenes are not much twisted against each other as the S_1-S_2-S_3-S_4 dihedral angle changes from -4.9˚ to 1.9˚. Bond distances between Mo and dithiolene sulfurs, S are increased from ~2.370 Å to ~2.416 Å (Table 3.5). The Mo-O_1 bond distance is decreased from 2.18 Å to 1.728 Å.

- *Optimized educt-substrate complex* **A-ES**:

The computed reaction energy for the **A-ES** complex formation is exothermic for the gas phase model, -3.3 kcal/mol, while it is endothermic for the continuum model, 16.5 kcal/mol relative to the separate substrate and educt (**A-E**) complex (Table 3.6). Optimized data shows that there is no considerable change in Mo-S distances relative to the oxidized active site model complex **A-E**. The S_1-S_2-S_3-S_4 dihedral angle is slightly changed from 1.9˚ to 1.2˚ (Table 3.5).

In the optimized **A-ES** complex, *pro-S*-hydrogen (H_s) of C_1 of ethylbenzene substrate is at a distance of 3.478 Å from the metal bound oxygen (O_1) at the active site. The C_1-H_s bond distance is 1.100 Å and the dihedral angle between the ethyl group and the benzene ring of ethylbenzene is 84.0˚ (Table 3.5).

The oxidized model complex (**A-E**) starting geometry for geometry optimization was generated from the optimized educt-substrate complex **A-ES** geometry.

- *Optimized H-transfer transition state complexes* **A-TS1** *and* **A-TS1**

Geometrical optimization of transition state model complex **A-TS1** for heterolytic C_1-H_s bond cleavage shows increase in the S_1-S_2-S_3-S_4 dihedral angle from 1.2˚ to 11.8˚. No considerable change is observed for the Mo-S bond distances (from ~2.415 Å to ~2.413 Å). Elongated bond distances are observed for the Mo-O_1 (from 1.732 Å to 1.910 Å) and the C_1-H_s of ethylbenzene (from 1.100 Å to 1.5146 Å) as compared to the optimized **A-ES** geometry. The O_1 and H_s distance is reduced from 3.478 Å to 1.119 Å. The dihedral angle between the ethyl

group and the benzene ring of ethylbenzene is reduced from 84.0˚ to 10.9˚ (Table 3.5). The energy barrier for the heterolytic C_1-H_s bond cleavage and H-transfer from the ethylbenzene to the O_1 atom is 45.6 kcal/mol in the gas phase and 62.2 kcal/mol in the continuum relative to the separate substrate and educt (**A-E**) complex (Table 3.6).

Optimized data for the transition state model complex **A-TS1ô** for homolytic C_1-H_s bond cleavage shows an increase in the S_1-S_2-S_3-S_4 dihedral angle (from 1.2˚ to 10.5˚) and in the Mo-S bond distances (from ~2.415 Å to ~2.420 Å). Elongated Mo-O_1 (from 1.732 Å to 1.915 Å) and C_1-H_s (from 1.100 Å to 1.419 Å) bonds are computed. The distance between O_1-H_s is reduced from 3.478 Å to 1.179 Å as compared to the optimized **A-ES** geometry. The dihedral angle between the ethyl group and the benzene ring of ethylbenzene is reduced from 84.0˚ to 18.9˚ (Table 3.5). The energy barrier for the homolytic C_1-H_s bond cleavage and H-transfer from the ethylbenzene to O_1 atom is 36.7 kcal/mol in the gas phase and 47.6 kcal/mol in the continuum (Table 3.6).

The optimized **A-TS1** geometry was modified to generate the starting geometry for the geometry optimization of educt-substrate complex **A-ES** while the intermediate complexes, **A-I** and **A-Iô** starting geometries for geometry optimization were generated from the optimized transition state geometries, **A-TS1** and **A-TS1ô**.

- *Optimized intermediate complexes* **A-I** *and* **A-Iô**:

The computed reaction energy for the formation of carbocation intermediate complex **A-I** is endothermic relative to the separate substrate and educt (**A-E**) complex, 43.8 kcal/mol in gas phase and 53.6 kcal/mol in the continuum (Table 3.6). Geometry optimization of **A-I** shows a decrease in the S_1-S_2-S_3-S_4 dihedral angle (from 11.8˚ to 4.6˚) and in the Mo-S bond distances (from ~2.413 Å to ~2.399 Å). The Mo-O_1 and C_1-H_s distances are elongated from 1.910 Å to 2.020 Å and 1.504 Å to 4.060 Å, respectively as compared to the optimized **A-TS1** geometry. The O_1-H_s bond is reduced from 1.119 Å to 0.980 Å. The dihedral angle between the ethyl group and the benzene ring of ethylbenzene is reduced from 10.9˚ to 2.2˚ (Table 3.5).

The computed reaction energy for the formation of radical intermediate **A-Iô** as a result of homolytic C_1-H_s bond cleavage, is also endothermic (22.8 kcal/mol in the gas phase and 30.4 kcal/mol in the continuum (Table 3.6)). The optimized data shows a decrease in the S_1-S_2-S_3-S_4 dihedral angle (from 10.5˚ to 5.8˚) and in the Mo-S distances (from ~2.420 Å to ~2.399 Å), elongated Mo-O_1 (from 1.915 Å to 2.011 Å) and C_1-H_s (1.419 Å to 4.211 Å) distances relative to the optimized **A-TS1ô** geometry. The O_1-H_s bond is reduced from 1.179 Å to 0.980

Å. The dihedral angle between the ethyl group and the benzene ring of ethylbenzene is reduced from 18.9˚ to 3.8˚ (Table 3.5).

- *Optimized OH-transfer transition state complexes* **A-TS2** *and* **A-TS2ô**:

The energy barrier for the transition state **A-TS2** where an O_1H_s anion is transferred from Mo to the C_1 of carbocation intermediate is 47.5 kcal/mol in the gas phase and 64.6 kcal/mol in the continuum (Table 3.6). Geometry optimization data shows a decrease in S_1-S_2-S_3-S_4 dihedral angle (from 4.6˚ to 2.2˚) and in the Mo-S distances (from ~2.399 Å to ~2.389 Å). The Mo-O_1H_s bond is elongated from 2.020 Å to 2.128 Å as compared to the optimized **A-I** geometry. The distance between the C_1 and O_1H_s is decreased from 4.060 Å to 2.565 Å. The dihedral angle between the ethyl group and the benzene ring of ethylbenzene is slightly changed from 2.2˚ to 3.7˚ (Table 3.5).

The energy barrier for the transition state **A-TS2ô** where O_1H_s is transferred from Mo to C_1 of the radical type intermediate is 46.8 kcal/mol in the gas phase and 61.6 kcal/mol in the continuum (Table 3.6). Optimized data shows increase in the S_1-S_2-S_3-S_4 dihedral angle (from 5.8˚ to 17.2˚) and in the Mo-S distances (from ~2.399 Å to 2.462 Å) relative to the optimized **A-Iô** geometry. The Mo-O_1H_s bond is reduced from 2.011 Å to 1.998 Å. The distance between the C_1-O_1H_s is decreased from 4.211 Å to 2.277 Å. The dihedral angle between the ethyl group and the benzene ring of ethylbenzene is increased from 3.8˚ to 5.6˚ (Table 3.5).

- *Optimized product complex* **A-P***:*

The optimized **A-TS2** geometry is modified (the O_1-C_1 distance is slightly reduced) for generating the starting geometry for geometry optimization of product bound complex **A-P**. The computed reaction energy for the **A-P** complex is endothermic, 12.9 kcal/mol for the gas phase and 30.3 kcal/mol in the continuum relative to separate substrate and educt (**A-E**) complex (Table 3.6). Geometry optimization shows a slight change in the S_1-S_2-S_3-S_4 dihedral angle (from 2.2˚ to 1.9˚) and in the Mo-S distances (from ~2.389 Å to ~2.384 Å). The Mo-O_1H_s bond distance is increased from 2.128 Å to 2.261 Å while the C_1-O_1H_s distance is reduced from 2.565 Å to 1.506 Å. The dihedral angle between the ethyl group and the benzene ring of hydroxyl-ethylbenzene is 60.5˚ (Table 3.5).

Table 3.5: Geometrical parameters of the optimized model complexes of the reaction mechanism for the Asp_{223} protonated EBDH.

Prot-Asp	Heterolytic Cleavage/Singlet							Homolytic Cleavage/Triplet		
	X	A-E	A-ES	A-TS1	A-I	A-TS2	A-P	A-TS1ô	A-Iô	A-TS2ô
Mo-S_1 (Ù)	2.369	2.384	2.381	2.401	2.400	2.398	2.368	2.407	2.392	2.420
Mo-S_2 (Ù)	2.427	2.394	2.396	2.410	2.408	2.393	2.392	2.432	2.421	2.430
Mo-S_3 (Ù)	2.291	2.431	2.431	2.386	2.370	2.364	2.370	2.384	2.367	2.451
Mo-S_4 (Ù)	2.391	2.456	2.451	2.453	2.418	2.401	2.405	2.456	2.417	2.547
Dihedral, S_1-S_2-S_3-S_4(è)	-4.9	1.9	1.2	11.8	4.6	2.2	1.9	10.5	5.8	17.2
Mo-O_1 (Ù)	2.18	1.728	1.732	1.910	2.020	2.128	2.261	1.915	2.011	1.998
O_1é H_s (Ù)	-	-	3.478	1.119	0.980	0.979	0.979	1.179	0.980	0.980
C_1é H_s/C_1é O_1 (Ù)	-	-	1.100	1.504	4.060	2.565	1.506	1.419	4.211	2.277
Ethyl-benzene ring dihedral (è)	-	-	84.0	10.9	2.2	3.7	60.5	18.9	3.8	5.6

Where, **X** = protein X-ray crystal structure data, **A-E** = educt complex, **A-ES** = educt-substrate complex, **A-TS1** = H-transfer transition state complex, **A-I** = intermediate complex, **A-TS2** = OH-transfer transition state, **A-P** = Product bound complex.

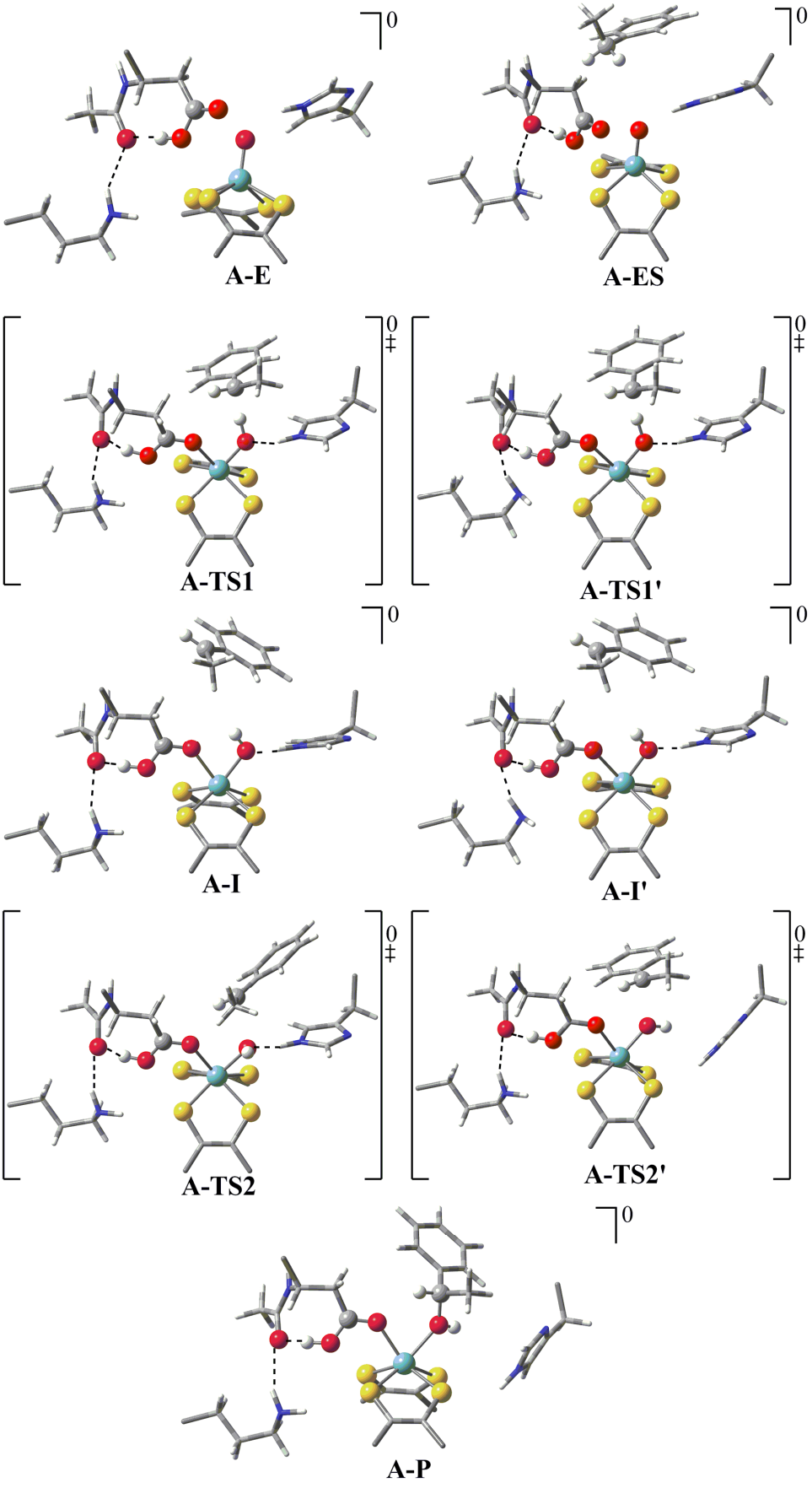

Fig 3.9: Optimized geometries for model structures with protonated Asp relevant for the EBDH reaction mechanism.

Table 3.6: Computed energy barriers [kcal/mol] relative to the separate substrate and edduct complex for hydroxylation of ethyl benzene by EBDH models.

Multiplicity	**Heterolytic Cleavage/Singlet**				**Homolytic Cleavage/Triplet**				
Protonation site	**none**	**His**	**Lys**	**Asp**	**none**	**His**	**Lys**	**Asp**	
E	0.0	0.0	0.0	0.0	-	-	-	-	//B3LYP[a] SDD[b] COSMO[c]
ES	-4.6 -3.7 12.0	-5.2 -4.8 16.0	-8.8 -8.1 12.4	-4.0 -3.3 16.5	-	-	-	-	//B3LYP[a] SDD[b] COSMO[c]
TS1	**21.5** **28.5** **46.9**	**18.2** **24.3** **46.1**	**18.0** **22.5** **47.5**	**37.8** **45.6** **62.2**	**19.1** **27.1** **42.3**	**10.2** **14.0** **32.7**	**20.7** **30.7** **36.5**	**26.6** **36.7** **47.6**	//B3LYP[a] SDD[b] COSMO[c]
I	16.8 26.8 43.5	15.1 21.0 41.7	18.1 26.1 40.3	35.0 43.8 58.6	1.8 10.6 23.3	-3.1 2.8 20.0	3.2 8.1 25.5	13.0 22.8 30.4	//B3LYP[a] SDD[b] COSMO[c]
TS2	**23.4** **32.0** **45.1**	**22.0** **29.0** **48.7**	**15.6** **22.0** **43.0**	**39.4** **47.5** **64.6**	**29.4** **35.1** **54.6**	**30.4** **36.4** **52.4**	**25.0** **29.9** **53.4**	**39.4** **46.8** **61.6**	//B3LYP[a] SDD[b] COSMO[c]
P	-8.3 -1.2 17.5	5.1 8.3 28.2	-11.8 -8.7 12.5	9.2 12.9 30.3	-	-	-	-	//B3LYP[a] SDD[b] COSMO[c]

Where, **none** = non-protonated EBDH, **His** = His_{192} protonated EBDH, **Lys** = Lys_{450} protonated EBDH, **Asp** = Asp_{223} protonated EBDH. **E** = educt complex, **ES** = educt-substrate complex, **TS1** = H-transfer transition state complex, **I** = intermediate complex, **TS2** = OH-transfer transition state complex, **P** = product complex. a) B3LYP/Lanl2DZ(p), b) B3LYP/SDDp//B3LYP/Lanl2DZ (p), c) COSMO-B3LYP/SDDp//B3LYP/Lanl2DZ(p) (see Computational details)

5. Discussion

The mechanism of ethylbenzene hydroxylation at the molybdenum cofactor of *Aromatoleum aromaticum* EBDH has been investigated by using density functional theory (DFT). The mechanism involves two transition states; **TS1** for the cleavage of the C_1-H_s bond of ethylbenzene and the transfer of H_s from the substrate to metal bound oxygen atom (O_1), and **TS2** for the rebound of O_1H_s from the metal to the C_1 of the substrate intermediate resulting in the formation of (S)-1-phenylethanol (a hydroxylized substrate) and reduced metal. Heterolytic and homolytic cleavages of C_1-H_s bond of ethylbenzene were considered. The heterolytic cleavage of the C_1-H_s bond (**TS1**) leads to the formation of a carbocation intermediate. The rebound of the O_1H_s (**TS2**) anion to the carbocation intermediate leads to the formation of the hydroxylized substrate. The homolytic cleavage of the C_1-H_s bond (**TS1ô**) leads to the formation of a radical type intermediate. The reaction is followed by the rebound of a O_1H_s (**TS2ô**) radical from the Mo to the radical substrate resulting in the formation of the hydroxylized substrate.

Scheme 3.1: Plot of computed reaction energies (kcal/mol) relative to educt complex vs steps involved in the different level of computations for the non-protonated EBDH reaction mechanism.
Where, **OPT** = geometry optimization, **SDD** = single point energy calculation in the gas phase, **COSMO** = single point energy calculation in the continuum.

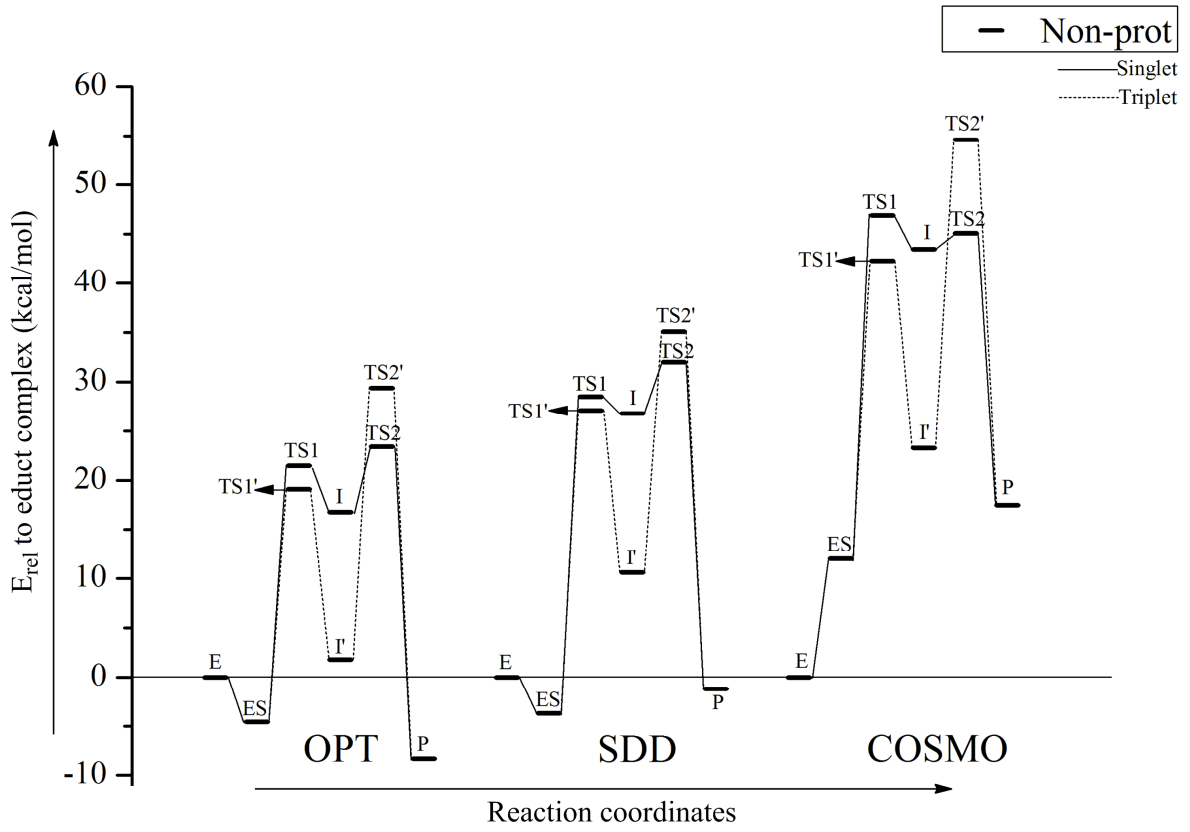

Three different levels of computation (**OPT**, **SDD** and **COSMO**) were considered for all the geometries involved in the mechanism. The graphical representation (Scheme 3.1) of different level of computations for the non-protonated EBDH pathway shows that the computed relative energies are increased with the level of computations. There is small energy change from the level of geometry optimization (**OPT**) to the single point energy calculations in the gas phase (**SDD**) but a major difference is evident between the **SDD** and the polarizable continuum (**COSMO**) results. For the **OPT** and **SDD**, the computed relative energies for the educt-substrate **ES** complex formation are exothermic relative to the separate substrate and educt (**E**) complex while it is endothermic for the **COSMO** (see Scheme 3.1 and Table 3.6). Most likely the interaction of the two separate entities, substrate and model complex, with a polarizable continuum is overestimated in comparison with the educt, where the active site complex is 'wrapped' around the substrate. In the **COSMO**, a solvent accessible surface is formed around the molecule, so both substrate and the educt (**E**) complex have their own solvent surfaces. Dispersion interactions between the substrate and the surrounding molecules

are underestimated with the DFT method used and in the substrate educt complex **ES** only the outer surface interacts with the polarizable continuum in the COSMO approach. Due to this reason the energy increases relative to the separate substrate and educt (**E**) complex from **SDD** to **COSMO** models and more reliable energy profile results from energies relative to the substrate educt complexes **ES**, as shown in Scheme 3.3 and Table 3.7.

Table 3.7: Computed energy barriers [kcal/mol] relative to the edduct substrate complex for hydroxylation of ethyl benzene by EBDH models.

Multiplicity	**Heterolytic Cleavage/Singlet**				**Homolytic Cleavage/Triplet**				
Protonation site	**none**	**His**	**Lys**	**Asp**	**none**	**His**	**Lys**	**Asp**	
ES	0.0	0.0	0.0	0.0	-	-	-	-	//B3LYP[a] SDD[b] COSMO[c]
TS1	**26.1** **32.2** **35.0**	**23.5** **29.1** **30.1**	**26.7** **30.6** **35.1**	**41.7** **48.9** **45.7**	**23.7** **30.9** **30.3**	**15.5** **18.9** **16.7**	**29.5** **38.8** **24.1**	**30.6** **40.0** **31.1**	//B3LYP[a] SDD[b] COSMO[c]
I	21.4 30.5 31.5	20.5 25.9 25.7	26.9 34.2 27.9	39.0 47.1 37.1	6.3 14.3 11.3	2.3 7.6 3.9	12.0 16.2 13.1	16.9 26.1 13.9	//B3LYP[a] SDD[b] COSMO[c]
TS2	**28.0** **35.7** **33.1**	**27.3** **33.8** **32.7**	**24.4** **30.1** **30.6**	**43.3** **50.8** **48.1**	**34.0** **38.8** **42.6**	**35.7** **41.2** **36.4**	**33.7** **38.0** **41.0**	**43.3** **50.2** **45.1**	//B3LYP[a] SDD[b] COSMO[c]
P	-3.7 2.6 5.5	10.5 13.2 12.2	-3.0 -0.6 0.1	13.2 16.2 13.8	-	-	-	-	//B3LYP[a] SDD[b] COSMO[c]

Where, **none** = non-protonated EBDH, **His** = His_{192} protonated EBDH, **Lys** = Lys_{450} protonated EBDH, **Asp** = Asp_{223} protonated EBDH. **ES** = educt-substrate complex, **TS1** = H-transfer transition state complex, **I** = intermediate complex, **TS2** = OH-transfer transition state complex, **P** = product complex. a) B3LYP/Lanl2DZ(p), b) B3LYP/SDDp//B3LYP/Lanl2DZ (p), c) COSMO-B3LYP/SDDp//B3LYP/Lanl2DZ(p) (see Computational details)

In the computed unprotonated EBDH pathway, the energy barrier for the heterolytic cleavage of C_1-H_s bond (**TS1**) is 35.0 kcal/mol in the polarizable continuum (the rate limiting step). This heterolytic cleavage leads to the formation of a carbocation intermediate (**I**) which is 3.4 kcal/mol lower in energy than the **TS1** complex. The energy barrier for the rebound of O_1H_s anion to the carbocation intermediate (**TS2**) is 33.1 kcal/mol in the polarizable continuum (Table 3.7). The energy barrier for the homolytic cleavage of C_1-H_s bond (**TS1ô**) is 30.3 kcal/mol in the polarizable continuum. This homolytic cleavage leads to the formation of a radical type intermediate (**Iô**) which is 19 kcal/mol lower in energy than **TS1ô**. The energy barrier for the rebound of O_1H_s radical from the Mo to the radical type intermediate substrate (**TS2ô**) is 42.6 kcal/mol in the polarizable continuum. This is the rate limiting step in the unprotonated EBDH pathway followed by homolytic cleavage of C_1-H_s bond. The energy required for the formation of hydroxylized substrate containing product complex **P** is 5.5

kcal/mol in the polarizable continuum relative to the educt substrate (**ES**) complex (Table 3.7).

In the computed protonated His_{192} EBDH pathway, the energy barrier for the heterolytic cleavage of the C_1-H_s bond (**H-TS1)** is 30.1 kcal/mol in the polarizable continuum relative to the educt substrate (**H-ES**) complex. The carbocation intermediate complex **H-I** is 4.4 kcal/mol lower in energy than the transition state **H-TS1** (Table 3.7). The energy barrier for the transition state **H-TS2** is 32.7 kcal/mol in the polarizable continuum, which corresponds to the rate limiting step. In the homolytic cleavage pathway, the energy barrier for the **H-TS1ô** is 16.7 kcal/mol in the polarizable continuum relative to the educt substrate (**H-ES**) complex. The radical type intermediate (**H-Iô**) is 12.8 kcal/mol lower in energy than the transition state **H-TS1ô**. The energy barrier associated with **H-TS2ô** for the rebound of O_1H_s radical from the Mo to the radical type intermediate substrate is 36.4 kcal/mol in the polarizable continuum, which is the rate limiting step. The formation of the hydroxylized substrate containing product complex **H-P** is endothermic, 12.2 kcal/mol in the polarizable continuum, relative to the educt substrate (**H-ES**) complex (Table 3.7).

To evaluate the effect of protonation and non-protonation of His_{192}, energy barriers are compared in Table 3.8, also with the data reported by Szaleniec et al.[162] According to our results the protonation of His_{192} is helpful for the hydrogen abstraction as it reduces the energy barrier for the radical type C_1-H_s bond cleavage from 30.3 kcal/mol (**TS1ô**) to 16.7 kcal/mol (**H-TS1ô**) in the presence of a polarizable continuum relative to the educt-substrate (**ES**) complexes. However, a small effect of His_{192} protonation is observed on the energy barriers associated with the heterolytic type C_1-H_s bond cleavage **TS1**= 35.0 kcal/mol and **H-TS1**=30.1 kcal/mol. Also, the energy barrier for the second step (**H-TS2**), which is rate determining, in the prot-His_{192} pathway is equal (prot-His_{192} is lower by 0.3 kcal/mol) to that of the non-prot (**TS2**) EBDH pathway (Table 3.8, Scheme 3.3).

According to the reported data,[162] the radical type C_1-H_s bond cleavage is energetically more favorable than the heterolytic cleavage in both non-prot and prot His_{192} pathways. The same effect is observed in our computational results, where **TS1ô** is ~5 kcal/mol lower in energy than **TS1** and **H-TS1ô** is ~13 kcal/mol lower in energy than **H-TS1**. However, comparing the computed energy barriers with the reported data, the computed energy barrier for **H-TS1ô** is ~14 kcal/mol lower than the energy barrier reported for the homolytic cleavage of C_1-H_s bond, while the energy barrier for **H-TS1** is ~6 kcal/mol lower than reported for the heterolytic C_1-H_s bond cleavage (see Table 3.8). According to Szaleniec et al.[162] for the non-protonated

EBDH, it was not possible to identify a transition state (**TS2**) associated with the O_1H_s rebound as the optimization of an intermediate species led directly to the product complex. However, we were able to localize this transition state (**TS2**) for the O_1H_s rebound to the carbocation intermediate. The energy barrier associated with it (**TS2**) is very similar to that of **H-TS2**, for the protonated His_{192} (Table 3.8).

Table 3.8: Computed and reported energy barriers [kcal/mol] relative to the educt substrate complex for hydroxylation of ethyl benzene by the non-protonated, protonated His_{192} and protonated Lys_{450} EBDH models.

Protonation site	Heterolytic Cleavage/Singlet					Homolytic Cleavage/Triplet					
	None		His		Lys	None		His		Lys	
	a	b	a	b	a	a	b	a	b	a	
TS1	26.1	-	23.5	-	26.7	23.7	-	15.5	-	29.5	//B3LYP
	32.2	33.2	29.1	31.1	30.6	30.9	29.7	18.9	26.1	38.8	SDD
	35.0	31.0	30.1	36.3	35.1	30.3	29.7	16.7	30.8	24.1	COSMO
TS2	28.0	-	27.3	-	24.4	34.0	-	35.7	-	33.7	//B3LYP
	35.7	-	33.8	31.7	30.1	38.8	27.8	41.2	31.5	38.0	SDD
	33.0	-	32.7	28.2	30.6	42.6	24.9	36.4	27.5	41.0	COSMO

Where, **a** = this work, **b** = data reported in Ref.162.

The protonated Lys_{450} EBDH pathway was also considered, as the Lys_{450} residue seems to be in a perfect position to take part in the hydroxylation of ethylbenzene. The protonation of Lys_{450} is 9.8 kcal/mol lower in energy (including a polarizable continuum model) as compared to the protonation of His_{192} (Scheme 3.2). The energy barrier for the heterolytic C_1-H_s bond cleavage (**L-TS1)** is 35.1 kcal/mol in the polarizable continuum (energy similar to the energy barriers associated with non-protonated transition state **TS1**), which is the rate limiting step. The heterolytic cleavage leads to the formation of a carbocation intermediate (**L-I**) which is 7.2 kcal/mol lower in energy than the **L-TS1** complex. The energy barrier associated with the **L-TS2** for the rebound of the O_1H_s anion to the carbocation intermediate is 30.6 kcal/mol in the polarizable continuum (Table 3.7). The energy barrier for the homolytic cleavage of C_1-H_s bond (**L-TS1ô**) is 24.1 kcal/mol in the polarizable continuum relative to the educt substrate (**L-ES**) complex. The radical type intermediate (**L-Iô**), formed as a result of homolytic C_1-H_s bond cleavage, is 11.0 kcal/mol lower in energy than the transition state **L-TS1ô** The energy barrier associated with **L-TS2ô** for the rebound of the O_1H_s radical from the Mo to the radical type intermediate substrate is 41.0 kcal/mol in the polarizable continuum, which is the rate limiting step. The formation of the hydroxylized substrate containing product complex **L-P** is thermoneutral, 0.1 kcal/mol in the polarizable continuum, relative to the educt substrate (**L-ES**) complex (Table 3.7).

Scheme 3.2: Plot of computed reaction energies (kcal/mol) relative to His_{192} protonated educt complex vs steps involved in the protonated EBDH reaction mechanism.

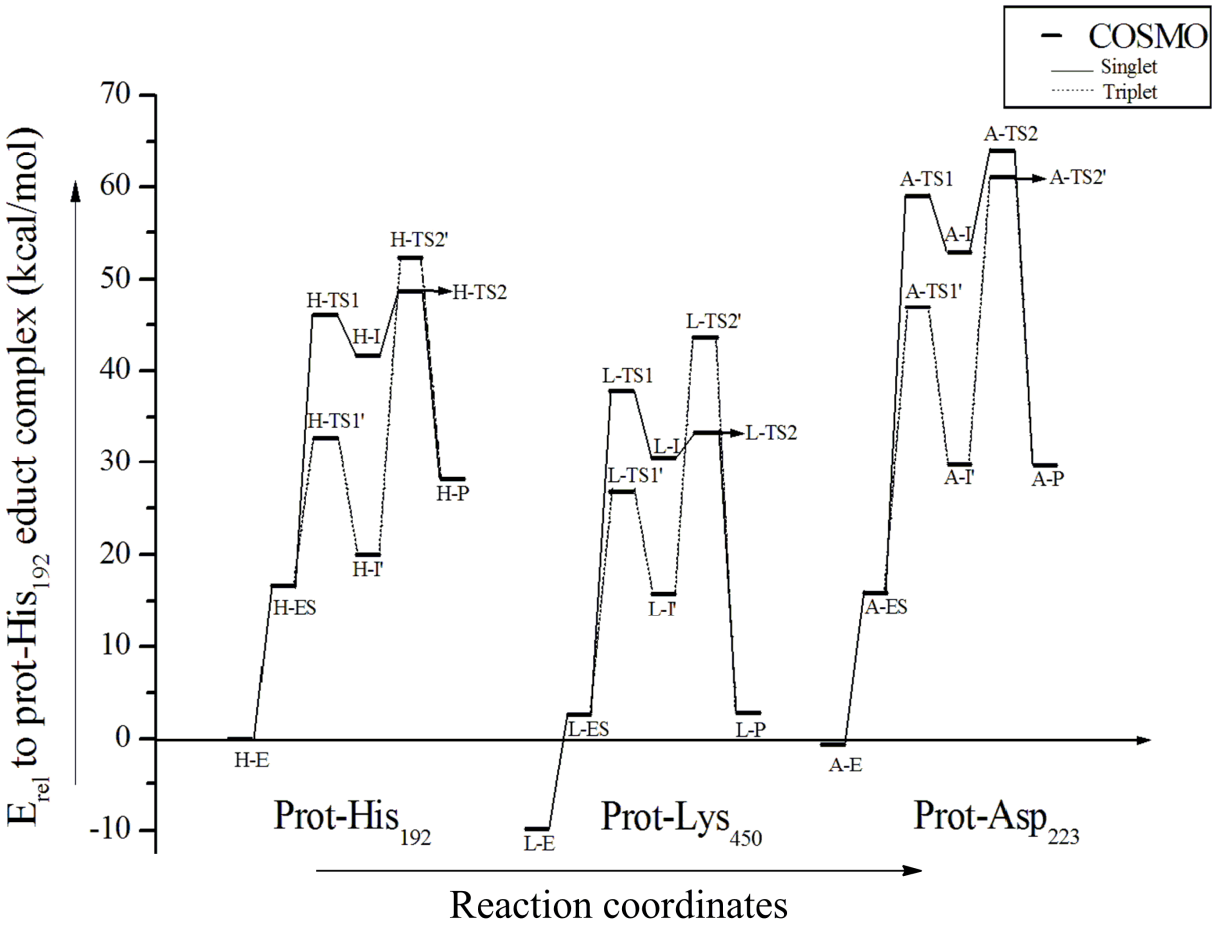

Although the energy barrier associated with **L-TS1ô** (i.e. the energy of **L-TS1ô** relative to **L-ES**) for the Lys_{450} protonated EBDH model is higher in energy than for the His_{192} protonated EBDH model (i.e. **H-TS1ô** vs **H-ES**), the Lys_{450} protonated EBDH pathway is more favorable. As shown in Scheme 3.2, **L-TS1ô** of protonated Lys_{450} is lower in energy than the **H-TS1ô** for protonated His_{192} and the **L-TS2** of prot-Lys_{450} is about the same energy as the **H-TS1ô** of prot-His_{192}. Also, among all the computed product complexes **P**, **H-P**, **L-P** and **A-P**, **L-P** is the only product complex which is thermoneutral (~0.1 kcal/mol) relative to the educt-substrate complex **L-ES** (Table 3.7, Scheme 3.2 and 3.3). In all other cases the product complex formation is considerably endothermic relative to the educt substrate complex (unprotonated: 5.5 kcal/mol, His_{192} protonated: 12.2 kcal/mol and Asp_{223} protonated: 13.8 kcal/mol).

Scheme 3.3: Plot of computed reaction energies (kcal/mol) relative to educt-substrate complex vs steps involved in the non-protonated, prot His and prot Lys EBDH reaction mechanism.

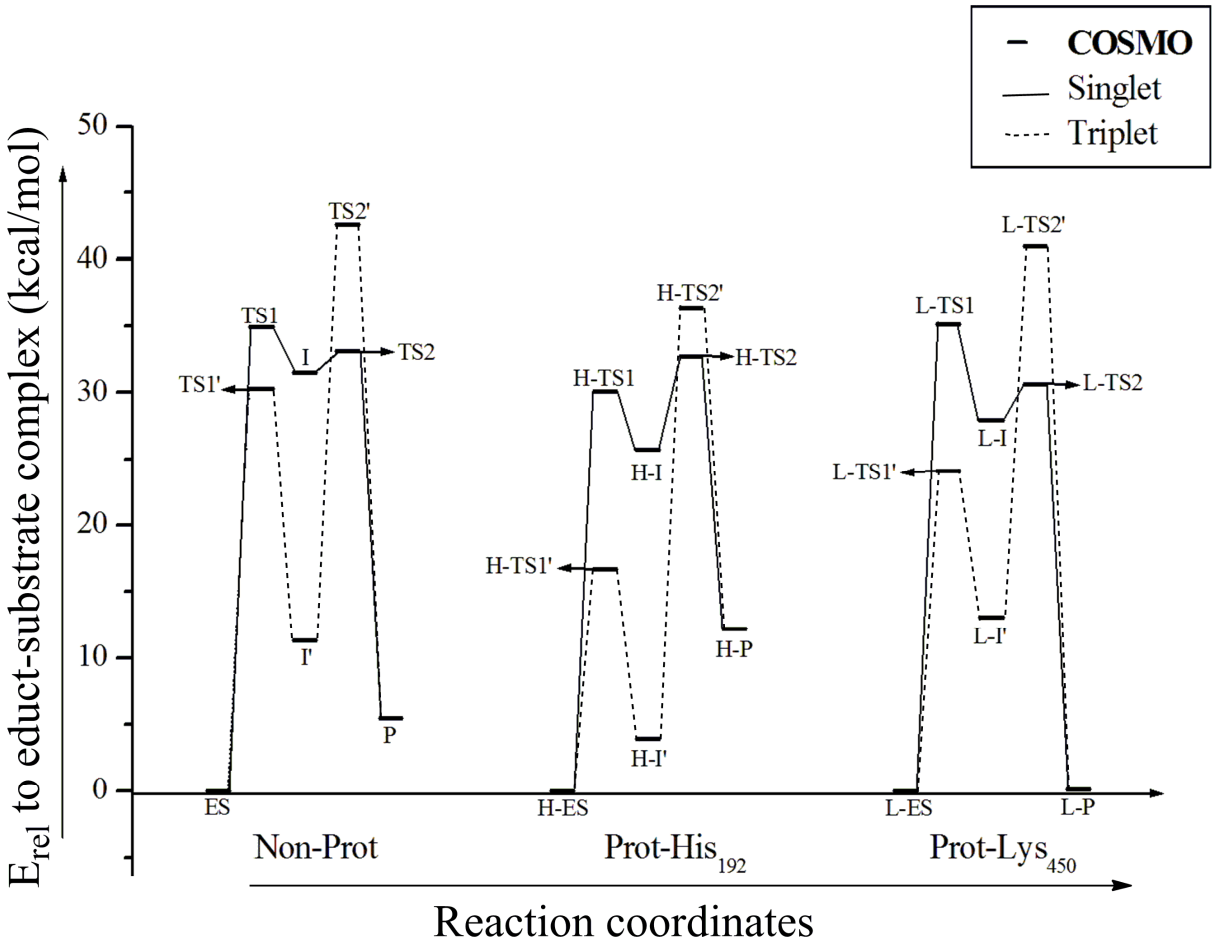

Like His_{192} and Lys_{450} residues, Asp_{223} residue also seems to be in a perfect position to take part in the hydroxylation of ethylbenzene. So, the protonated Asp_{223} EBDH pathway was also considered. The relative energy for the protonation of Asp_{223} is very close (~0.6 kcal/mol lower) to that for the His_{192} (Scheme 3.2). The energy barrier for the heterolytic C_1-H_s bond cleavage (**A-TS1)** is 45.7 kcal/mol in the polarizable continuum. This heterolytic cleavage leads to the formation of a carbocation intermediate (**A-I**) which is only 8.6 kcal/mol lower in energy than the **A-TS1** complex. The energy barrier associated with **A-TS2** for the rebound of O_1H_s anion to the carbocation intermediate is 48.1 kcal/mol in the polarizable continuum (Table 3.7). The energy barrier for the homolytic cleavage of C_1-H_s bond (**A-TS1ô**) is 31.1 kcal/mol in the polarizable continuum relative to the educt substrate (**A-ES**) complex. As a result of homolytic C_1-H_s bond cleavage, a radical type intermediate (**A-Iô**) is formed which is 17.2 kcal/mol lower in energy than the transition state **A-TS1ô**. The energy barrier associated with **A-TS2ô** for the rebound of O_1H_s radical from the Mo to the radical type intermediate substrate is 45.1 kcal/mol in the polarizable continuum, which makes it the rate limiting step

for this pathway. The formation of hydroxylized substrate containing product complex **A-P** is also endothermic, 13.8 kcal/mol in the polarizable continuum, relative to the educt substrate (**A-ES**) complex (Table 3.7).

Comparing the computed results of protonated Asp_{223} EBDH pathway with the other model EBDH pathways, the prot-Asp_{223} is the worst as the energy barrier for the C_1-H_s bond cleavage (**A-TS1ô**) is ~7-15 kcal/mol higher than the prot-His_{192} and prot-Lys_{450}. Also, the energy barrier for the second step (**A-TS2**) in the pathway of prot-Asp_{223} is higher (~3 kcal/mol) in energy than the **A-TS2ô** which is higher in case of non-prot, prot-His_{192} and prot-Lys_{450} EBDH pathways.

Comparing heterolytic and homolytic pathways, both **TS1ô** and **Iô** are energetically more favorable than **TS1** and **I**, respectively, for each protonation state (Scheme 3.1, 3.2 and 3.3). However, transition state **TS2** is lower in energy than transition state **TS2ô** in all except the Asp_{223} protonated model EBDH pathway. The **TS2** is also lower in energy than the **TS1** in the non-protonated and Lys_{450} protonated model pathways. For the His_{192} and Asp_{223} protonated model pathways the energy differences between transition state **TS1** and transition state **TS2** are also very small (~2.5 kcal/mol) but **TS2** is higher in energy than **TS1** (Table 3.7, Scheme 3.2).

6. Conclusion

Among the model EBDH pathways Lys_{450} protonated EBDH offers energetically the best pathway. The protonation of Lys_{450} is computed to be 9.8 kcal/mol lower in energy than the protonation of His_{192} (protonation of Asp_{223} is similar to His_{192}). **L-TS1** is the rate limiting step in the heterolytic pathway and it is lower in energy than the transition state **H-TS1** of prot-His_{192}. For the homolytic pathway, the rate limiting step is associated with transiton state **L-TS2ô** which is lower in energy than the rate limiting steps (**H-TS2** and **H-TS2ô**) of prot-His_{192} (Scheme 3.2). However, the overall lowest barrier pathway results when ionic and radical pathways are mixed. So, based on the computational results, the mechanism of ethylbenzene hydroxylation starts with a homolytic C_1-H_s bond cleavage (**L-TS1ô**) resulting in the formation of a radical type intermediate (**L-Iô**) and then in order to continue the reaction by the O_1H_s anion transfer, an electron needs to be transferred to transform the di-radical to the ionic intermediate. Then the transfer of O_1H_s anion from the Mo to the cationic substrate (**L-TS2**) results in the formation of product bound complex (**L-P**).

In the meantime a similar mechanism has been presented by Szaleniec et al.[162,163] where the hydroxylation of ethylbenzene, as well as different experimentally active substrates, by the EBDH enzyme has been investigated by quantum chemical methods. However, only the unprotonated and protonated His_{192} model complexes of EBDH were considered in these studies. The reported computational results point towards the radical type C-H cleavage as the initial reaction and the rate limiting step. It was also suggested that His_{192} residue of the active site is apparently involved in the reaction mechanism but it is most probably in the unprotonated state. So, non-protonated EBDH enzyme was favoured by Szaleniec et al.[162]

However, we have found a better possibility where Lys_{450} is in the protonated state. Comparing the Lys_{450} protonated EBDH and reported non-protonated EBDH pathways data, the transition state **L-TS1ô** is 5.6 kcal/mol lower in energy than the reported non-protonated transition state for the cleavage of C_1-H_s bond (Table 3.8). According to Szaleniec et al.[162] it was not possible to identify a transition state (**TS2**) associated with the O_1H_s rebound. However, we were able to localize this transition state (**L-TS2**) which is 30.6 kcal/mol in the polarizable continuum (0.4 kcal/mol lower in energy than **L-TS1** and 6.5 kcal/mol higher in energy than the **L-TS1ô**) (Table 3.8). So, according to our results, Lys_{450} protonated EBDH enzyme shows the energetically best pathway for the hydroxylation of ethylbenzene.

Acetylene Hydratase

1. Introduction

Acetylene hydratase (AH) of *Pelobacter acetylenicus* is a tungsten (W) containing iron-sulfur enzyme. It is the only member of the third class of W enzymes, the acetylene hydratase family besides the aldehyde oxidoreductase family and the formyl-methanofuran dehydrogenase family. It can also be grouped into the DMSO reductase family of mononuclear Mo/W enzymes on the basis of protein sequence homology and metal coordination. AH catalyzes a non-redox reaction, the hydration of acetylene to acetaldehyde as part of an anaerobic degradation pathway of unsaturated hydrocarbons.[98]

$$C_2H_2 + H_2O \rightarrow CH_3CHO \quad (23)$$

The oxidation state of W is unchanged throughout the catalytic cycle.[98] AH is the only enzyme capable of carrying out this reaction, although a nitrogenase can reduce acetylene to ethylene.[164,165]

Based on the studies of biomimetic complexes of AH[166] and redox titration,[167] it has been demonstrated that W^{IV} participates in the catalysis of acetylene hydration, whereas W^{VI} is inactive.[167] AH is extremely oxygen-sensitive and its activity is lost irreversibly upon exposure to air as its [4Fe-4S] cluster is converted to [3Fe-4S].[99] Interestingly, the enzyme needs to be activated by reduction of the W center from W^{VI} to W^{IV} and it requires a strong reductant for this activation. The [4Fe-4S] cluster is thought to facilitate this activation step.[168] Once the W is reduced, no further changes in the oxidation state of metal occur during catalytic activity. For the stability of the reduced tungstoprotein, bis(dithiolene) coordination through metallopterin cofactors is proposed to be an obligate requirement.[169] The role of the pterin part of AH may involve provision of structural stability through hydrogen bonding with the apoprotein and/or participation in the electron flow path between the tungsten and Fe-S centers during the necessary stages of activation or deactivation.[167]

The protein X-ray crystal structure of AH[100] from *Pelobacter acetylenicus* reveals a mononuclear W center in the active site and a nearby iron-sulfur [4Fe-4S] cluster.[166] In the active site W is coordinated by two metallopterin guanine dinucleotide cofactors (MGD), a sulfur atom of cysteine and an oxygen species, which was assigned to be a water molecule because of its distance (2.04 Å) from the W center. The location of the [4Fe-4S] cluster is not far from the W center.[100] (Fig. 4.1)

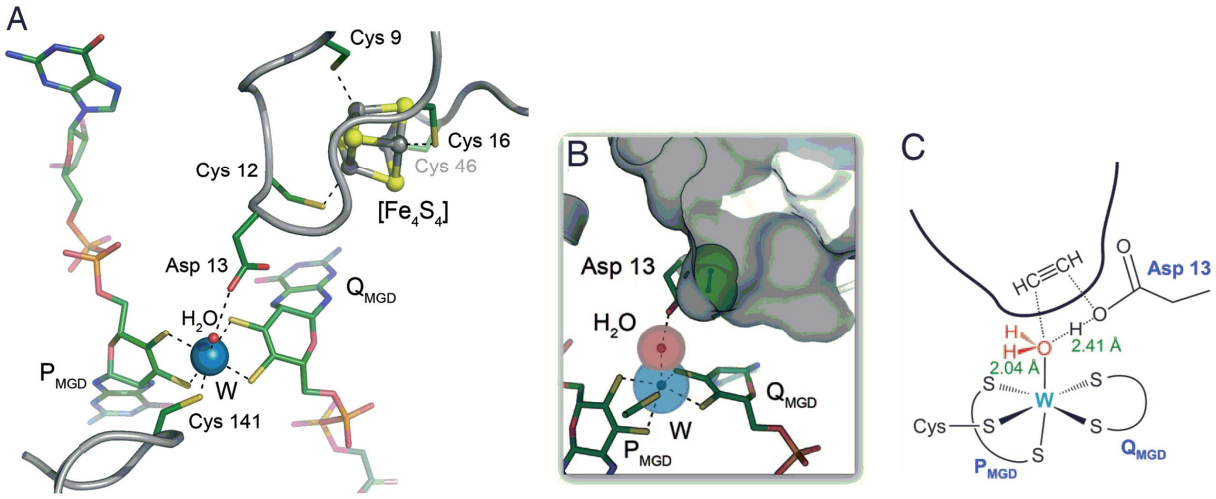

Fig. 4.1: Cofactors and active site of AH. (*A*) The tungsten atom (blue) is coordinated by the dithiolene groups of both MGD cofactors and the side chain of Cys-141. A water molecule completes the slightly distorted octahedral geometry. This water is also hydrogen-bonded to Asp-13, a residue adjacent to the [4Fe-4S] cluster ligand Cys-12. (*B*) The binding pocket positions an acetylene molecule directly above the water molecule and Asp-13. (*C*) Bond distances of 2.04 Å to W and 2.41 Å to the OH atom of Asp-13 indicate a highly activated water molecule positioned right below a binding pocket for acetylene. (Pictures taken from reference 100)

The proposed catalytic mechanism of AH depends on the nature of the oxygen ligand bound to the W. The distance of oxygen from the metal is 2.04 Å which falls in the range expected for both hydroxo ligands (1.9-2.1 Å) and coordinated water (2.0-2.3 Å). According to Seiffert et al.[100] the two possibilities lead to two different mechanisms that do not take place through organometallic intermediates. A hydroxo ligand would constitute a strong nucleophile and a water molecule would constitute an electrophile. In both these mechanisms, Asp_{13} is assumed to be protonated and to donate a hydrogen bond to the water/hydroxide molecule attached to the W.[166]

Seiffert et al.[100] suggest an electrophilic addition mechanism (Scheme 4.1) for the hydration of acetylene. As the bound water molecule gains a partial positive charge through protonated Asp_{13}, it directly attacks the triple bond of acetylene as an electrophile.

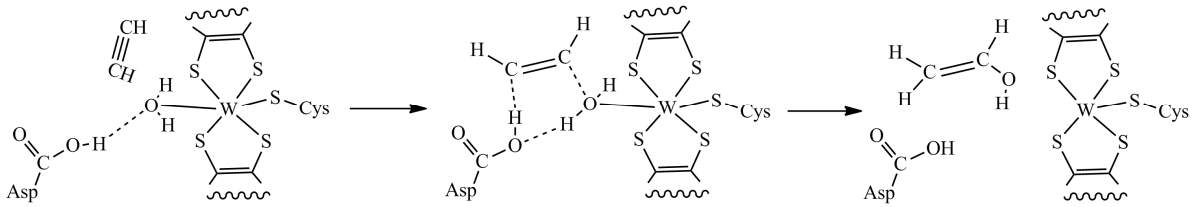

Scheme 4.1: Reaction mechanism of acetylene hydratase suggested by Seiffert et al.[100]

Density functional theory (DFT) calculations on small models of AH by Antony and Bayse[170] (Scheme 4.2) show that the displacement of a water molecule by an acetylene molecule is exothermic. Based on this result, they suggest the nucleophilic attack of a water molecule at the acetylene η^2 –bound to W to form vinyl alcohol assisted by protonated Asp_{13}.

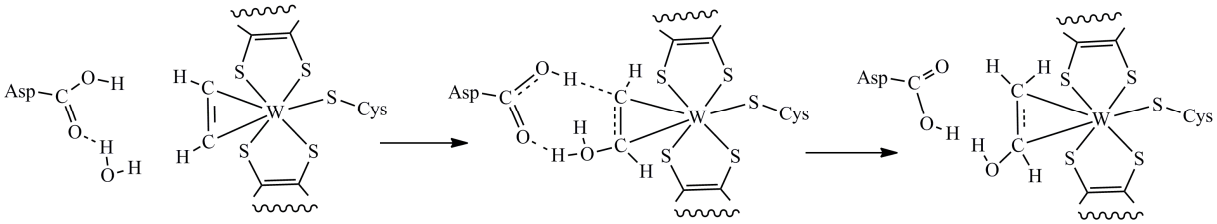

Scheme 4.2: Reaction mechanism of acetylene hydratase suggested by Antony and Bayse.[170]

Vincent et al.[171] computed high energy barriers (higher than 40 kcal/mol) for both the mechanisms with DFT methods and therefore ruled out both. Instead they speculated that the reaction starts with the displacement of the water molecule, by acetylene bound to the metal center in an η^2 fashion. The reaction proceeds through intermediate vinylidene ($W{=}C{=}CH_2$) and carbene ($W{=}C(OH)CH_3$) complexes (see Scheme 4.3). However, the energy barriers for the formation of these intermediates are also quite high (28 and 34 kcal/mol, respectively).[171]

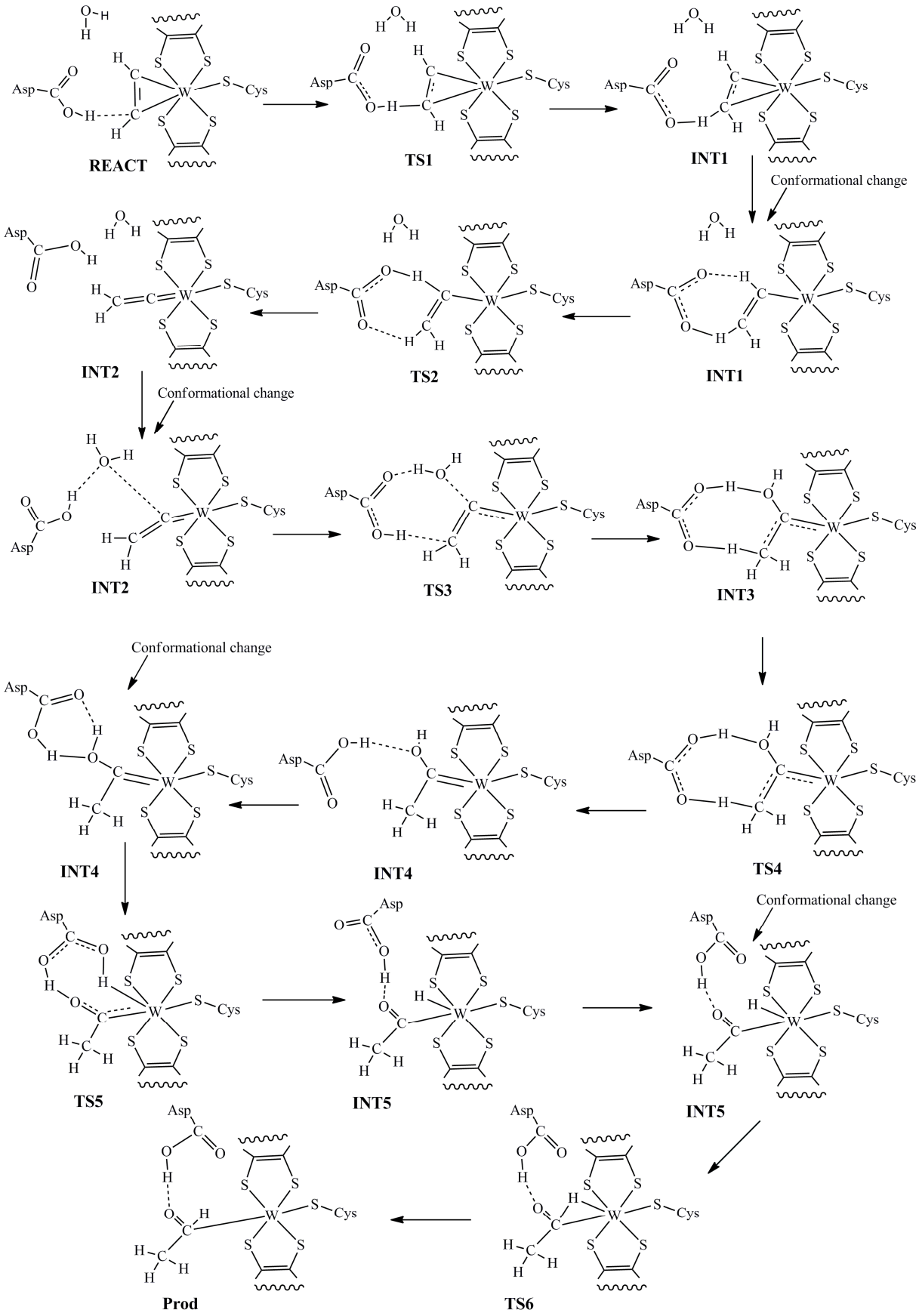

Scheme 4.3: Reaction mechanism of the acetylene hydratase suggested by Vincent et al.[171]

Recently, Himo et al[172] performed quantum chemical calculations on considerably larger models of the active site of AH derived from the protein X-ray crystal structure and proposed a five step mechanism. This mechanism starts with the displacement of the W^{IV}-bound water molecule with η^2-acetylene in an exothermic step (**REACT → INT1**). The water molecule, activated by the ionized Asp_{13}, performs nucleophilic attack on the acetylene resulting in the formation of a vinyl anion intermediate (**INT2**) which is stabilized by metal coordination. The protonated Asp_{13} then acts as an acid and donates a proton to the vinyl anion generating a vinyl alcohol intermediate (**INT3**). This is the rate limiting step (energy barrier of 23 kcal/mol). The two final steps involve tautomerization of vinyl alcohol to acetaldehyde (**PROD**) with the help of Asp_{13} and the W metal center (Scheme 4.4).[172]

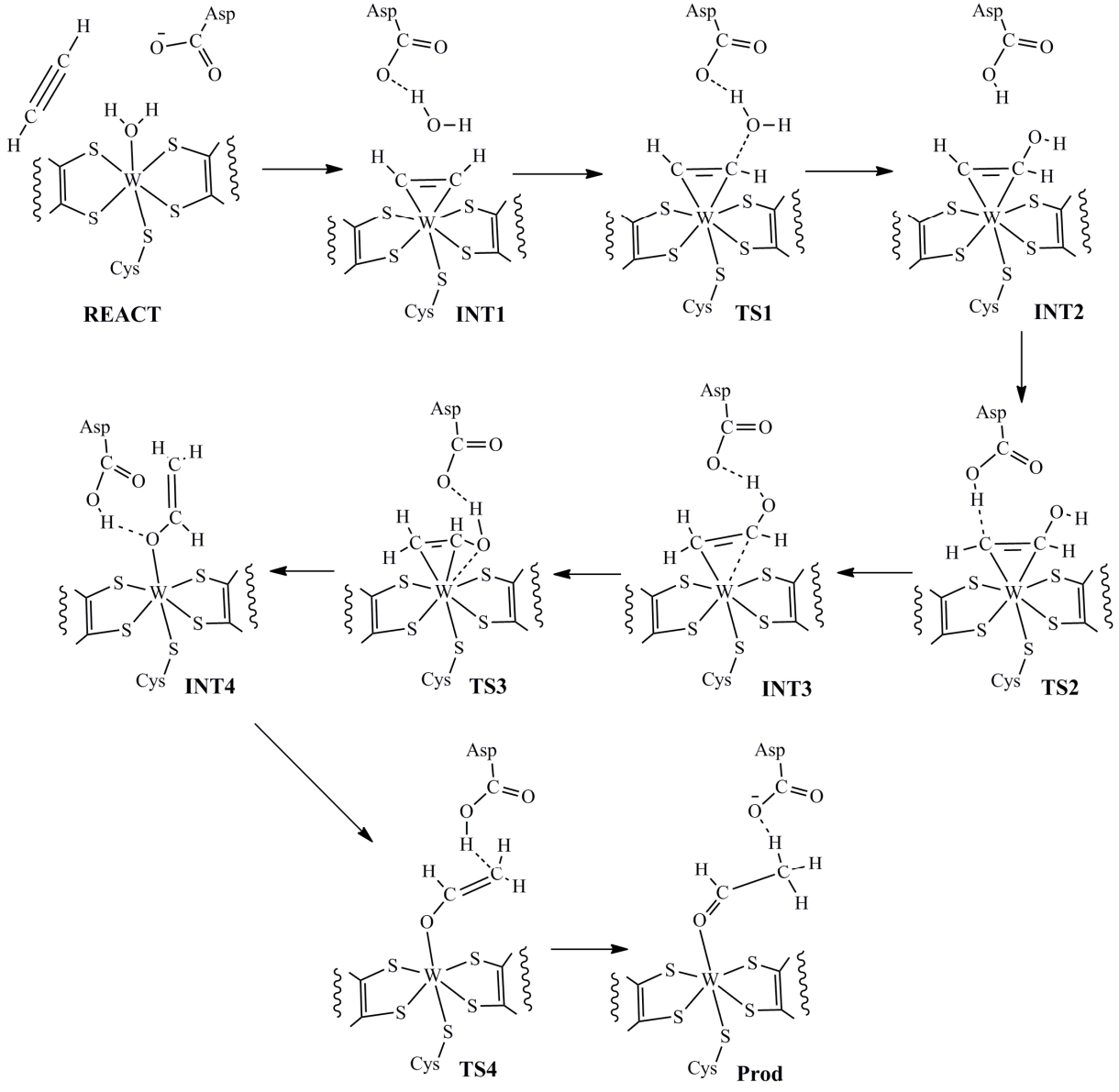

Scheme 4.4: Reaction mechanism of the acetylene hydratase suggested by Himo et al.[172]

Here, we have investigated the two mechanisms for catalysis, proposed by Seiffert et al.,[100] which do not take place through organometallic intermediates. The first proposed mechanism, favoured by Seiffert et al.,[100] involves electrophilic attack on acetylene by the water molecule activated by the nearby Asp_{13}. The OH group of Asp_{13} forms a hydrogen bond with the oxygen atom of the water molecule, leading to a partial positive charge at the oxygen atom that can then act as an electrophile. This water molecule may become sufficiently acidic to protonate the triple bond of acetylene generating a vinyl cation intermediate. The oxygen atom of nearby water molecule activated by some base then attacks the vinyl cation intermediate resulting in the formation of vinyl alcohol.

This vinyl alcohol then tautomerizes to acetaldehyde (Scheme 4.5). Suenobou et al.[173] computed the energy barrier for the tautomerization of vinyl alcohol to acetaldehyde with and without the assistance of a water molecule. He suggests that when the reaction is catalysed by a water molecule, the energy barrier decreases from 55.8 kcal/mol to 29.6 kcal/mol in the gas phase. Lledós et al.[174] suggests that the intervention of a chain of two water molecules further reduces the potential energy barrier to 21.8 kcal/mol.

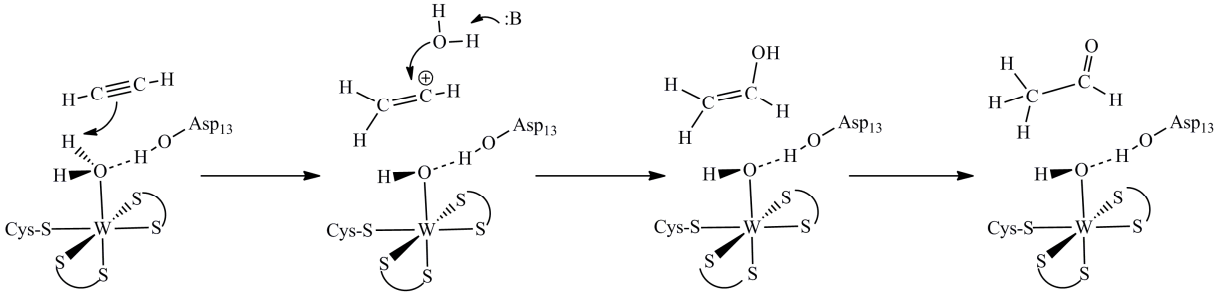

Scheme 4.5: Proposed electrophilic reaction mechanism suggested by Seiffert et al.[100]

In the second proposed mechanism, a metal bound water molecule is activated by the W center, which acts as a Lewis acid, generating a W-bound hydroxide ligand and protonated Asp_{13}. The nucleophilic attack of coordinated hydroxide at the acetylene results in the formation of vinyl alcohol which then tautomerized to acetaldehyde (Scheme 4.6).

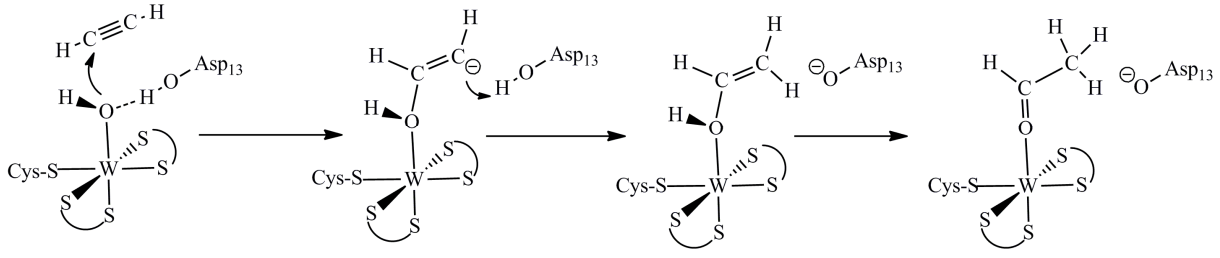

Scheme 4.6: Proposed nucleophilic reaction mechanism suggested by Seiffert et al.[100]

Considering the two proposed mechanisms, DFT calculations were performed on small and large model complexes of the AH active site designed on the basis of the protein X-ray crystal structure of AH.[100]

2. Computational Details

2.1. Small model complexes:

All the small model geometries were optimized using Gaussian 03[175] with the density functional BP86[176,177,178] and the LANL2DZ basis set.[124,125,126,127] The self-consistent field (SCF)[160] method was used with the IntRep option for the SCF procedure to account for integral symmetry and NoVaracc for full integral accuracy. Whenever there was an SCF convergence problem, the QC[161] option was used which involves linear searches when far from convergence. The starting geometries for transition state searches were generated by shortening and lengthening of forming and breaking bonds, respectively. Single point energies were computed with the B3LYP[123] functional and the Stuttgart-Dresden effective core potential basis set (SDD)[129,130] augmented by polarization functions for all atoms except W and H (ζ = 0.600, 1.154, 0.864, and 0.421 for C, O, N, and S, respectively).[128] In addition self-consistent reaction field (SCRF) computations were performed on the optimized geometries to model the protein surrounding the active site by a conductor like polarizable continuum method (CPCM)[131] with a dielectric constant of 4 and a solvent radius of 1.4 Å. The molecular cavity was specified using a minimum radius (RMin) of 0.5 Å and an overlap index (OFac) of 0.8.[137]

2.2. Large model complexes:

All the large model geometries were optimized using Gaussian 03[175] with the hybrid density functional B3LYP[123] and the LANL2DZ basis set[124,125,126,127] augmented by polarization function on sulfur atoms (ζ = 0.421).[128] The self-consistent field (SCF)[160] method was used with the same parameters as for the small model complexes. The starting geometries for transition state searches were generated by shortening and lengthening of forming and breaking bonds, respectively. Single point energies were computed with the same parameters as for the small model complexes.

2.3. Large model complexes with water molecules:

All the water containing large model geometries were optimized using Gaussian 09 with the hybrid density functional B3LYP[123] and the LANL2DZ basis set[124,125,126,127] augmented by

polarization function on sulfur atoms (ζ = 0.421).[128] The Self consistent field (SCF)[160] method was used with the same parameters as for the small and large model complexes. The starting geometries for transition state (**TS**) searches were generated by shortening and lengthening of forming and breaking bonds, respectively. These geometries were then pre-optimized freezing the crucial atoms dominating the transition vector. Frequency calculations were performed on these pre-optimized geometries to get the internal force constants. For the frequency calculations #P was specified in the route section to produce some additional output. IOP (7/33=1) was used to get the internal force constants which were then supplied as starting values in the TS search. Single point energies were computed with the B3LYP functional and the Stuttgart-Dresden effective core potential basis set (SDD)[129,130] augmented by polarization functions for all atoms except Mo, W and H (ζ =0.600, 1.154, 0.864, and 0.421 for C, O, N, and S, respectively).[128] Self-consistent reaction field (SCRF) computations were performed on the optimized geometries to model the effect of protein surrounding the active site by the conductor like polarizable continuum method (CPCM)[131] as implemented in Gaussian 09.[132,133] In order to make it consistent with the results of small and large model complexes, the default Gaussian 03 procedure and parameters were used with solute-solvent dispersion and repulsion interaction energies,[134,135] and solute cavitation energy variations.[136] The molecular cavity was specified using a minimum radius (RMin) of 0.5Å and overlap index (OFac) of 0.8.[137]

3. Active site Models

Active site model complexes were designed on the basis of the protein X-ray crystal structure of *Pelobacter acetylenicus* (PDB-ID: 2E7Z).[100]

3.1. Small model complexes:

Small active site models, designed on the basis of the protein crystal structure,[100] were considered to identify the most probable reaction mechanism. These models include the W metal center coordinated with two molybdopterin ligands (MGD), a metal bound water (Wat_{1862}) molecule, a cysteinate (Cys_{141}) ligand and an additional aspartate (Asp_{13}) residue. The water molecule (Wat_{1424}), nearby Asp_{13} and Wat_{1862}, were also considered in case of the electrophilic reaction mechanism (Scheme 4.7 A). Cys_{141} was truncated to a H_3CS^- group, Asp_{13} to acetate (CH_3COO^-) and MGD to 2, 3-dithiolato but-2-ene (enedithiolate). Hydrogen atoms were added manually. Beta (β) carbon atom of acetate and methyl carbon atoms of the

ene-dithiolato ligands were kept fixed during the calculations to their crystal structure positions to mimic the steric constraints of the protein matrix (Fig. 4.2).

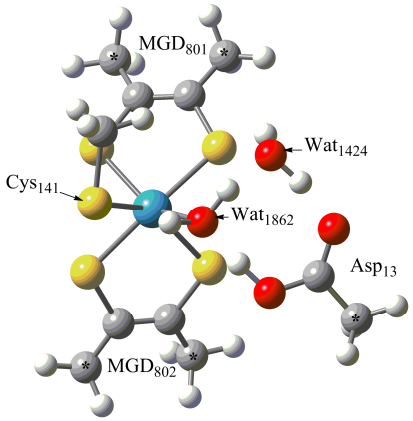

Fig. 4.2: Optimized reduced active site small model of AH.

Atoms labeled (*) were kept fixed at their X-ray crystal structure positions.

3.2. Large model complexes:

From the protein crystal structure,[100] it was deduced that Asp_{13} forms hydrogen bonds to the oxygen species attached to W as well as to the peptide bond of Cys_{12} and to the side chain of Trp_{179}. So, Trp_{179}, Trp_{293} and Trp_{472} were included for the large models to account for the effect of second shell ligands on the energy profile and reaction mechanism. Hydrogen atoms were added manually. During the optimizations, alpha (α) carbon atoms and nitrogen atoms attached to the beta (β) carbon atoms of Asp_{13}, Trp_{179}, Trp_{293} and Trp_{472} were kept fixed to their crystal structure positions to mimic the steric constraints by the protein matrix. Nitrogen attached to the beta (β) carbon atom of Cys_{141} was also kept fixed. The MGD ligands were truncated to pyran rings and the oxygen atoms of these pyran rings were kept fixed (Fig. 4.3).

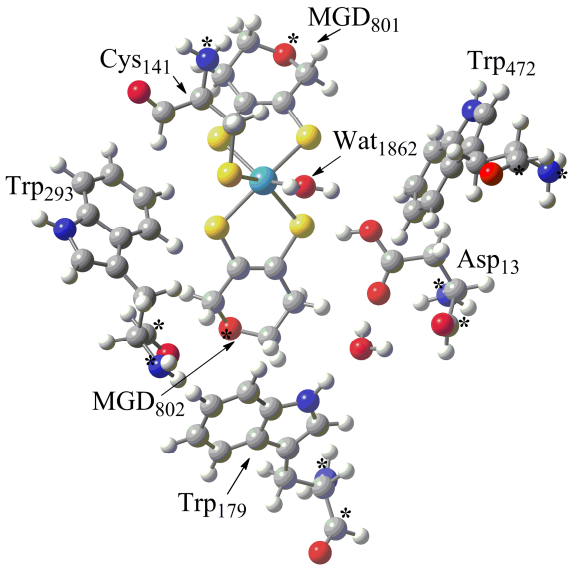

Fig. 4.3: Optimized reduced active site large model of AH.

Atoms labeled (*) were kept fixed at their X-ray crystal structure positions.

3.3. Large model complexes with water molecules:

The protein X-ray crystal structure[100] shows that there are at least 16 well defined water molecules in a vestibule directly adjacent to the active site and these molecules may help in the catalytic activity, the hydration of acetylene to acetaldehyde. So, Wat_{1209}, Wat_{1212}, and Wat_{1432} water molecules were considered in the large active site models. Ala_{137}, Met_{138}, Ile_{113}, Ile_{142}, and Phe_{611} were also considered to keep the water molecules at their locations as they form hydrogen bonds to these water molecules. Hydrogen atoms were added manually. Alpha (α) carbon atoms and nitrogen atoms attached to the β carbon atoms of Asp_{13}, Ile_{113}, Trp_{179}, Trp_{472}, Phe_{611}; β carbon atom of Ala_{137}, nitrogen atom attached to the β carbon atom of Cys_{141}, α carbon of Ile_{142}, α and β carbon atoms of Trp_{293}, C_4 of Met_{138}, the oxygen atoms of the pyran rings of dithiolenes were kept fixed to their crystal structure positions during optimizations to mimic the steric constraints by the protein matrix (Fig. 4.4).

For all the active site model complexes, first, the hydrogen atoms were optimized, applying two negative charges for the nucleophilic pathway (assuming W at the +IV oxidation state and Asp_{13} in the deprotonated form) while one negative charge for the electrophilic pathway (assuming W at the +IV oxidation state and Asp_{13} in the protonated form), keeping all the heavy-atom fixed at their positions. The resulting geometries served as starting geometries when generating input geometries for the study of the mechanism for acetylene hydratase (Fig. 4.4). The educt-substrate complexes (**ES**) and the alcohol product complexes (**EP1**)

starting geometries for geometry optimizations were generated from the optimized transition state (**TS**) geometries.

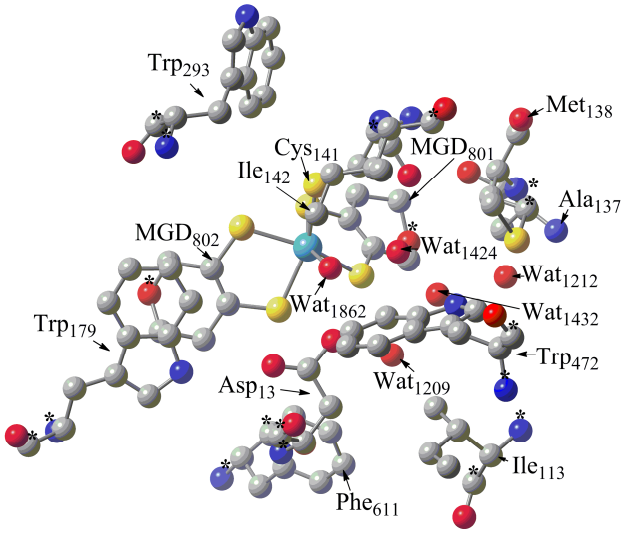

Fig. 4.4: Optimized reduced active site large model (water containing) complex of AH.

Atoms labeled (*) were kept fixed at their X-ray crystal structure positions. Hydrogen atoms were excluded to get the clear view of the selected active site model.

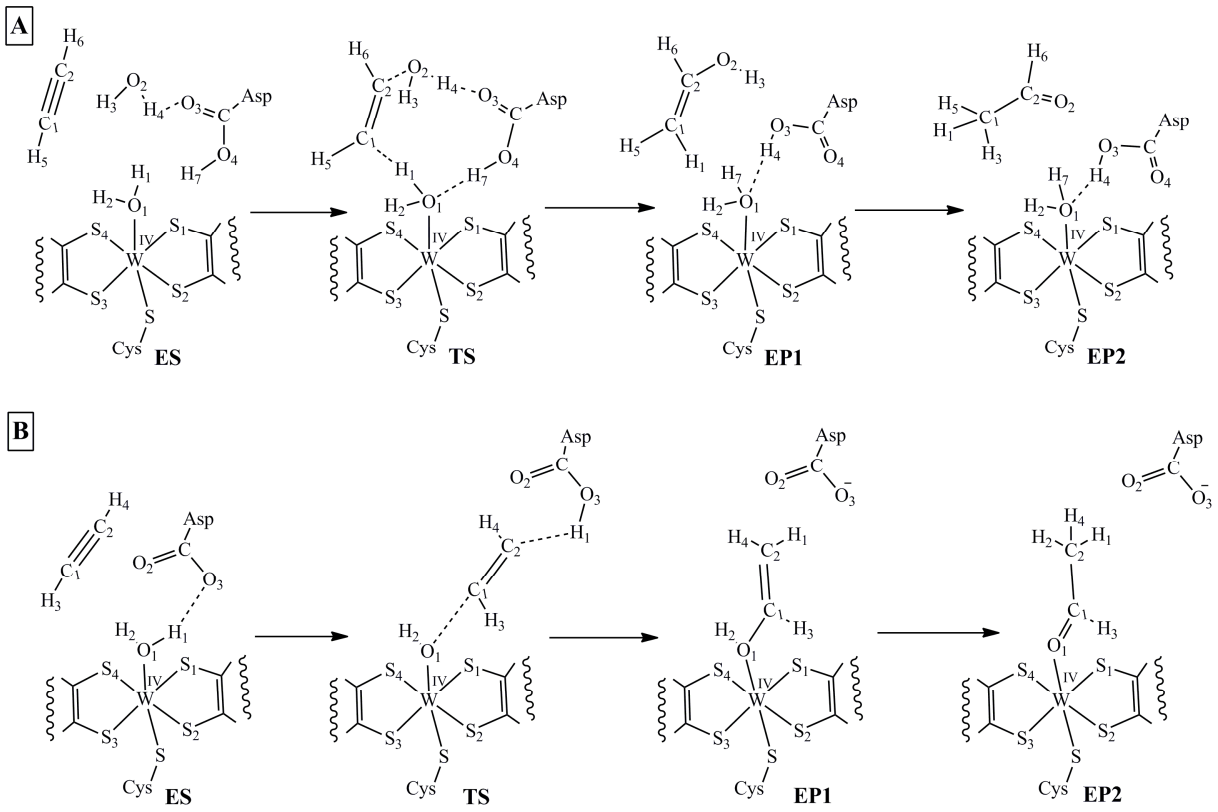

Scheme 4.7: Schematic description of the mechanism for the acetylene hydration at the Acetylene hydratase, where **A** = Electrophilic pathway, **B** = Nucleophilic pathway, **ES** =educt-substrate complex, **TS** = transition state, **EP1** = alcoholic product, **EP2** = tautomerized (to aldehyde) product.

4. Results

4.1. Small model complexes:

- ***Electrophilic pathway* (SE)*:***

We started our search for the hydration of acetylene on small model complexes derived from the protein X-ray crystal structure,[100] where Asp_{13} was considered to be protonated. The W-bound water molecule (Wat_{1862}) is activated by the nearby Asp_{13} residue and second water molecule (Wat_{1424}). This activated water molecule (Wat_{1862}) then attacks the acetylene substrate (Scheme 4.7A). Thus, starting with this activated Wat_{1862} molecule, transition state involves the electrophilic attack on the triple bond of acetylene with the simultaneous transfer of protons among Asp_{13}, Wat_{1862}, Wat_{1424} and acetylene. The proton from Asp_{13} residue (-COOH) is transferred to the Wat_{1862} molecule and one proton of Wat_{1862} molecule is transferred to the alpha carbon atom (Cα or C_1) of acetylene. From the Wat_{1424}, one proton is transferred to Asp_{13} while its electron donating part (-OH) is transferred to the second carbon atom (Cβ or C_2) of acetylene. This proton shuttle results in the formation of vinyl alcohol which subsequently may tautomerize to aldehyde (Scheme 4.7A).

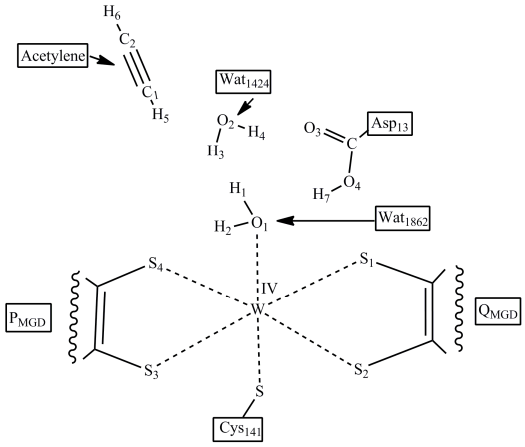

Fig 4.5: The chemical structure of the active site model complexes for the electrophilic pathway derived from the protein X-ray crystal structure of AH.[100]

- *Optimized active site model complex* **SE-E**:

The reduced active site model complex **SE-E** derived from the protein X-ray crystal structure of AH[100] was geometry optimized where oxidation state of tungsten is IV and the overall charge is -1. The optimized geometry of active site model complex **SE-E** is distinctively different in geometrical parameters of the coordination site of the metal center in comparison to the protein X-ray crystal structure of AH.[100] The optimized data shows a reduction in the

S_1-S_2-S_3-S_4 dihedral angle (from -31.4˚ to -20.8˚) and in the bond distances between tungsten (W) and ene-dithiolate sulfur atoms (S) (from ~2.442 Å to ~2.415 Å). The W-O_1 bond distance is increased from 2.041 Å to 2.279 Å (Table 4.1).

- *Optimized educt substrate complex* **SE-ES**:

In the optimizated educt-substrate complex **SE-ES**, the acetylene is loosely bound to the active site where a hydrogen bond is formed between the H_5 of acetylene and the oxygen atom (O_2) of Wat_{1424} (see Fig. 4.2). The optimization data shows no considerable change in the S_1-S_2-S_3-S_4 dihedral angle (from -20.8˚ to -20.4˚) and in the W-S bond distances (from ~2.415 Å to ~2.413 Å) when comparison is made with the optimized **SE-E** geometry. The W-O_1 distance is increased from 2.279 Å to 2.300Å while the O_1-H_1 bond is reduced from 1.142 Å to 1.087 Å. The H_1-O_2 and H_7-O_1 distances are increased from 1.318 Å to 1.430 Å and from 1.392 Å to 1.435 Å, respectively (Table 4.1).

In the optimized **SE-ES** complex, H_5 of acetylene is at a distance of 1.994 Å from the O_2 of Wat_{1424}, forming a hydrogen bond. The H_1-C_1 and the C_1-C_2 distances are 4.994 Å and 1.236 Å, respectively. The H_5-C_1-C_2 and C_1-C_2-H_6 bond angles of acetylene are 179.8˚ and 179.7˚, respectively (Table 4.1).

- *Optimized transition state complex* **SE-TS**:

Geometry optimization of the transition state complex **SE-TS** shows no considerable change in the S_1-S_2-S_3-S_4 dihedral angle (from -20.4˚ to -19.8˚), in the W-S bond distances (from ~2.413 Å to ~2.412 Å) as well as in the W-O_1 (from 2.300 Å to 2.317 Å) and O_1-H_1 (from 1.087 Å to 1.083 Å) bond distances relative to the optimized **SE-ES** geometry (Table 4.1). The H_1-C_1 and C_2-O_2 distances are reduced from 4.994 Å to 1.651 Å and 4.274 Å to 2.110 Å, respectively. The H_5-C_1-C_2 (from 179.8˚ to 139.4˚) and C_1-C_2-H_6 (179.7˚ to 163.8˚) bond angles are reduced. The energy barrier for the transition state is 28.5 kcal/mol in the continuum (30.4 kcal /mol in the gas phase) relative to the educt-substrate (**SE-ES**) complex (Table 4.3).

The educt substrate (**SE-ES**) complex and the alcohol product (**SE-EP1**) complex starting geometries for geometry optimization were generated from the optimized transition state (**SE-TS**) geometry. Slight reduction of W-O_1 bond together with the elongation of the H_1-C_1 and the C_2-O_2 distances generate the starting geometry for the **SE-ES** complex. On the other

hand a slight elongation of the W-O_1 bond and reduction of the H_1-C_1 and C_2-O_2 distances were performed to generate the starting geometry for the **SE-EP1** complex.

- *Optimized alcoholic product complex* **SE-EP1**:

The formation of a vinyl alcohol complex, an initial product of acetylene hydration, is an exothermic reaction with respect to the **SE-ES** complex, -36.2 kcal/mol in the continuum (-33.6 kcal/mol in the gas phase) (Table 4.3). In the optimized alcoholic product (**SE-EP1**) complex, the vinyl alcohol is bound to the active site W metal. Geometry optimization of the **SE-EP1** complex shows a slight change in the S_1-S_2-S_3-S_4 dihedral angle (from -19.8˚ to -22.5˚) and in the W-S bond distances (from ~2.412 Å to ~2.421 Å) (Table 4.1). The W-O_1 bond is reduced from 2.317 Å to 2.118 Å while the O_1-H_1 distance is increased from 1.083 Å to 4.892 Å. The C_1-C_2 distance is increased from 1.269 Å to 1.357 Å indicating the formation of C=C double bond (~1.33 Å). The C_2-O_2 bond is reduced from 2.110 Å to 1.401 Å whereas the O_2-H_4 bond is broken (distance is increased from 1.022 Å to 1.401 Å) resulting in the formation of vinyl alcohol. On the other hand the reduction of the H_4-O_3 distance from 1.597 Å to 1.057 Å and the elongation of O_4-H_7 distance (from 1.070 Å to 1.613 Å) results in the restoration of protonated Asp_{13}. Finally, the reduction of O_1-H_7 (from 1.470 Å to 1.010 Å) indicates the formation of a water ligand attached to the active site metal. The H_5-C_1-C_2 and C_1-C_2-H_6 bond distances are reduced from 139.4˚ to 119.4˚ and from 163.8˚ to 123.2˚, respectively (Table 4.1).

The tautomerized acetaldehyde product complex **SE-EP2** starting geometry for geometry optimization was generated by a slight modification in the vinyl alcohol part of the optimized **SE-EP1** complex geometry. The O_2-H_3 bond was broken together with the reduction of C_1-H_3 and C_2-O_2 distances to generate the starting geometry for the **SE-EP2** complex.

- *Optimized tautomerized product complex* **SE-EP2**:

The computed energy barrier for the tautomerization of vinyl alcohol (C_2H_3OH) to acetaldehyde (CH_3CHO, without the educt complex) with the assistance of two water molecules is 20.7 kcal/mol in the continuum (20.3 kcal/mol in the gas) (see Table 4.12). The computed reaction energy for the tautomerized product complex **SE-EP2** is also exothermic, -10.4 kcal/mol in the continuum (-9.9 kcal/mol in the gas) relative to the **SE-EP1** and -46.6 kcal/mol in continuum (-43.5 kcal/mol) relative to the **SE-ES** complex (Table 4.3). Geometry optimization shows a slight change in the S_1-S_2-S_3-S_4 dihedral angle (from -22.5˚ to -19.3˚). No considerable change is observed in the W-S bond distances (from ~2.421 Å to ~2.423Å).

The elongation of the C_1-C_2 bond (from 1.357 Å to 1.512 Å which is typical for a C-C single bond (~1.53 Å)) and the reduction of the C_2-O_2 bond (1.401 Å to 1.286 Å which shows the C=O bond) indicates the formation of the aldehyde product (Table 4.1).

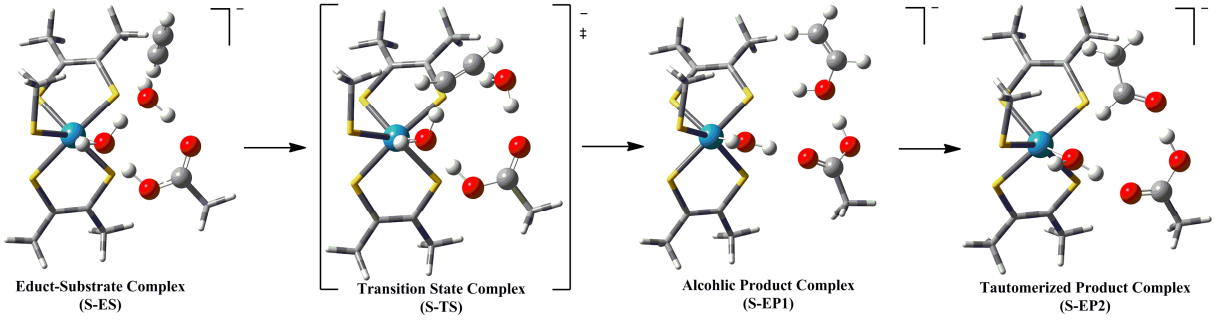

Fig. 4.6: Optimized geometries for the small model complexes involved in the electrophilic pathway of acetylene hydration by AH.

Table 4.1: Geometrical parameters of the optimized model complexes of the electrophilic reaction mechanism for acetylene hydration by the small model complexes of AH.

	X	SE-E	SE-ES	SE-TS	SE-EP1	SE-EP2
W-S_1 (Å)	2.432	2.435	2.434	2.433	2.446	2.443
W-S_2 (Å)	2.489	2.405	2.404	2.414	2.398	2.395
W-S_3 (Å)	2.511	2.401	2.418	2.395	2.419	2.410
W-S_4 (Å)	2.336	2.420	2.397	2.404	2.422	2.444
S_1-S_2-S_3-S_4 (°)	-31.4	-20.8	-20.4	-19.8	-22.5	-19.3
W-O_1 (Å)	2.041	2.279	2.300	2.317	2.118	2.141
O_1-H_1 (Å)	-	1.142	1.087	1.083	4.892	-
H_1-O_2 (Å)	-	1.318	1.430	3.027	-	-
H_1-C_1 (Å)	-	-	4.994	1.651	1.095	-
C_1-C_2 (Å)	-	-	1.236	1.269	1.357	1.512
C_2-O_2 (Å)	-	-	4.274	2.110	1.401	1.286
O_2-H_4 (Å)	-	1.046	1.047	1.022	1.401	-
H_4-O_3 (Å)	-	1.522	1.518	1.597	1.057	1.085
O_4-H_7 (Å)	-	1.109	1.089	1.070	1.613	1.535
H_7-O_1 (Å)	-	1.392	1.435	1.470	1.010	1.028
H_5-C_1-C_2 (°)	-	-	179.8	139.4	119.4	-
C_1-C_2-H_6 (°)	-	-	179.7	163.8	123.2	-

Where, **X** = protein X-ray crystal structure data,[100] **SE-E** = educt complex, **SE-ES** = educt-substrate complex, **SE-TS** = transition state complex, **SE-EP1** = alcoholic product complex, **SE-EP2** = aldehyde product complex

- ***Nucleophilic Pathway* SN*:***

The second mechanism proposed by Seiffert et al.[100] is the nucleophilic attack (Scheme 4.7B) of a W-bound water molecule (Wat_{1862}) on the acetylene substrate. DFT calculations for this reaction mechanism were carried out on small model complexes derived from the protein X-ray crystal structure, where Asp_{13} was considered to be in anionic form. The W center, which acts as a Lewis acid activates water molecule (Wat_{1862}), generates a W-bound hydroxide and protonated Asp_{13}. The transition state for the nucleophilic attack of this W-bound hydroxide at the alpha carbon atom (Cα or C_1) of acetylene also involves the simultaneous transfer of a proton from the Asp_{13} to the second acetylene carbon atom (Cβ or C_2) resulting in the formation of vinyl alcohol which subsequently may tautomerize to aldehyde.

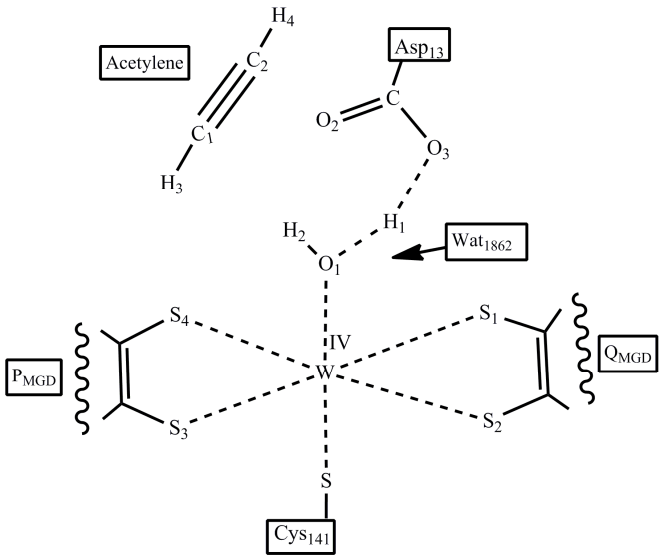

Fig. 4.7: The chemical structure of the active site model complexes for the nucleophilic pathway derived from the protein X-ray crystal structure of AH.[100]

- *Optimized active site model complex* **SN-E**:

The reduced active site model complex **SN-E** derived from the protein X-ray crystal structure of AH[100] was geometry optimized where the oxidation state of tungsten is IV and the overall charge is -2. The optimized geometry of active site model complex **SN-E** is similar in geometrical parameters of the metal coordination site in comparison to the protein X-ray crystal structure of AH.[100] No considerable change is observed in the S_1-S_2-S_3-S_4 dihedral angle (from -31.4˚ to -27.4˚) and in the bond distances between tungsten (W) and

enedithiolene sulfurs (S) (from ~2.442 Å to ~2.443 Å) (Table 4.2). The W-O_1 bond distance is increased from 2.041 Å to 2.257 Å.

- *Optimized educt substrate complex* **SN-ES**:

In the educt substrate complex **SN-ES**, a W-bound water molecule is activated by the W-center generating a W-bound hydroxide (OH) and protonated Asp_{13}. Geometrical optimization of the **SN-ES** complex shows no considerable change in the S_1-S_2-S_3-S_4 dihedral angle (from -27.4˚ to -26.7˚). On the other hand, the W-S bond distances are increased from ~2.443 Å to ~2.467 Å when comparison is made with the optimized **SN-E** geometry. The W-O_1 and H_1-O_3 distances are reduced from 2.257 Å to 2.075 Å and from 1.821 Å to 1.021 Å, respectively while the O_1-H_1 distance is increased from 1.036 Å to 3.736 Å (Table 4.2).

In the optimized **SN-ES** complex geometry, the acetylene is loosely bound to the active site where a hydrogen bond is formed between the H_3 of acetylene and the oxygen atom (O_1) of W-bound hydroxide. The distance between the O_1-C_1 is 2.687 Å, C_1-C_2 is 1.246 Å and C_2-H_1 is 2.078 Å. The H_3-C_1-C_2 and C_1-C_2-H_4 bond angles of acetylene are 172.2˚ and 175.4˚, respectively (Table 4.2).

- *Optimized transition state complex* **SN-TS**:

Geometry optimization of the transition state complex **SN-TS** shows no considerable change in the S_1-S_2-S_3-S_4 dihedral angle (from -26.7˚ to -26.3˚) and in the W-S bond distances (from ~2.467 Å to ~2.469 Å) when compared with the optimized **SN-ES** geometry. The W-O_1 (from 2.075 Å to 2.043 Å), O_1-C_1 (from 2.687 Å to 2.305 Å) and C_2-H_1 (from 2.078 Å to 1.705 Å) distances are reduced while the C_1-C_2 distance is slightly elongated from 1.246 Å to 1.269Å (Table 4.2). The H_3-C_1-C_2 (from 172.2˚ to 161.1˚) and C_1-C_2-H_4 (from 175.4˚ to 143.9˚) bond angles of acetylene are reduced. The energy barrier for the formation of the transition state (**SN-TS**) complex is 17.0 kcal/mol in the continuum (15.7 kcal/mol in the gas phase) relative to the **SN-ES** complex (Table 4.3).

The educt substrate complex **SN-ES** and the alcohol product complex **SN-EP1** starting geometries for geometry optimization were generated from the optimized transition state (**SN-TS**) geometry. Slight reduction of the W-O_1 bond together with the elongation of the O_1-C_1 and C_2-H_1 distances gives the starting geometry for the **SN-ES** complex. On the other hand a slight elongation of the W-O_1 and O_3-H_1 bonds and reduction of the O_1-C_1 and C_2-H_1 distances were performed to generate the starting geometry for the **SN-EP1** complex.

➢ *Optimized alcoholic product complex* **SN-EP1**:

The formation of the initial product of acetylene hydration, a vinyl alcohol, is an exothermic step, -29.3 kcal/mol (-31.3 kcal/mol) relative to the **SN-ES** complex (Table 4.3). In this alcoholic product complex **SN-EP1**, the O_1H_2 part of the vinyl alcohol is bound to the active site W metal. Geometry optimization of the **SN-EP1** complex shows a slight change in the S_1-S_2-S_3-S_4 dihedral angle (from -26.3˚ to -22.0˚) and in the W-S bond distances (from ~2.466 Å to ~2.431 Å) with respect to the optimized **SN-TS** geometry. The W-O_1 and H_1-O_3 distances are increased from 2.043 Å to 2.314 Å and from 1.065 Å to 2.038 Å, respectively. The O_1-C_1 (from 2.305 Å to 1.440 Å) and C_2-H_1 (from 1.705 Å to 1.110 Å) distances are reduced while the C_1-C_2 bond is elongated from 1.269 Å to 1.351 Å. The H_3-C_1-C_2 and C_1-C_2-H_4 bond angles of acetylene are reduced from 161.1˚ to 127.5˚ (a typical H-C=C bond angle is ~121.3˚) and 143.9˚ to 123.8˚, respectively (Table 4.2).

The tautomerized acetaldehyde product (**SN-EP2**) complex starting geometry for geometry optimization was generated by a slight modification in the vinyl alcohol part of the optimized **SN-EP1** complex geometry. The O_2-H_3 bond was broken together with the reduction of C_1-H_3 and C_2-O_2 distances to generate the starting geometry for the **SN-EP2** complex.

➢ *Optimized tautomerized product complex* **SN-EP2**:

The computed reaction energy for the tautomerized product complex is again strongly exothermic, -50.2 kcal/mol (-54.2 kcal/mol) relative to the **SN-ES** complex (Table 4.3). Geometry optimization of the **SN-EP2** complex shows a change in the S_1-S_2-S_3-S_4 dihedral angle (from -22.0˚ to -28.8˚) back to roughly the value of the optimized **SN-E** complex and in the W-S bond distances (from ~2.431 Å to ~2.467 Å) when comparison is made with the optimized **SN-EP1** geometry. The W-O_1 (from 2.314 Å to 2.002 Å) and O_1-C_1 (from 1.440 Å to 1.299 Å) bonds are reduced while C1-C2 bond is elongated from 1.351 Å to 1.496 Å.

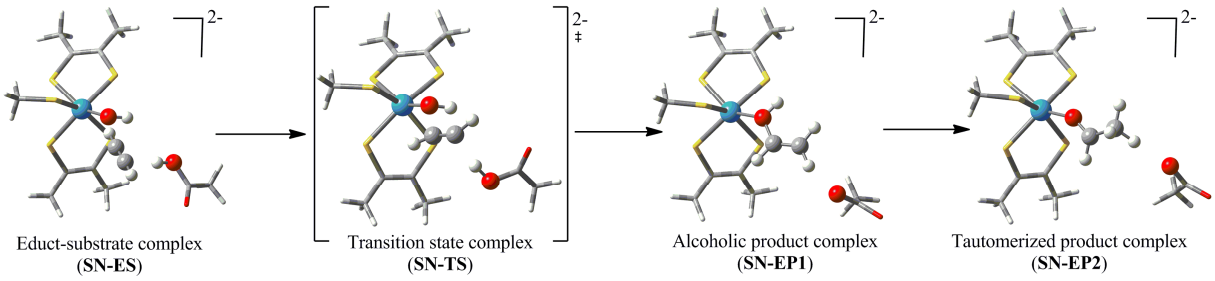

Fig. 4.8: Optimized geometries for the small model complexes involved in the nucleophilic pathway of acetylene hydration by AH.

Table 4.2: Geometrical parameters of the optimized model complexes of the nucleophilic reaction mechanism for acetylene hydration by the small model complexes of AH.

	X	**SN-E**	**SN-ES**	**SN-TS**	**SN-EP1**	**SN-EP2**
W-S_1 (Å)	2.432	2.413	2.490	2.495	2.439	2.486
W-S_2 (Å)	2.489	2.438	2.437	2.452	2.422	2.446
W-S_3 (Å)	2.511	2.505	2.477	2.469	2.427	2.481
W-S_4 (Å)	2.336	2.417	2.463	2.459	2.434	2.455
S_1-S_2-S_3-S_4 (°)	-31.4	-27.4	-26.7	-26.3	-22.0	-28.8
W-O_1 (Å)	2.041	2.257	2.075	2.043	2.314	2.002
O_1-H_1 (Å)	-	1.036	3.736	-	-	-
H_1-O_3 (Å)	-	1.821	1.021	1.065	2.038	-
O_1-C_1 (Å)	-	-	2.687	2.305	1.440	1.299
C_1-C_2 (Å)	-	-	1.246	1.269	1.351	1.496
C_2-H_1 (Å)	-	-	2.078	1.705	1.110	-
H_3-C_1-C_2 (°)	-	-	174.2	161.1	127.5	-
C_1-C_2-H_4 (°)	-	-	175.4	143.9	123.8	

Where, **X** = protein X-ray crystal structure data,[100] **SN-E** = educt complex, **SN-ES** = educt-substrate complex, **SN-TS** = transition state complex, **SN-EP1** = alcoholic product complex, **SN-EP2** = tautomerized product complex

Table 4.3: Computed energies [kcal/mol] relative to the edduct-substrate complex for stationary points relevant in the hydration of acetylene by small model complexes of AH.

	Electrophilic Pathway, SE	**Nucleophilic Pathway, SN**	
ES	0.0	0.0	//BP86[a] SDD[b] COSMO[c]
TS	**30.1** **30.4** **28.5**	**12.9** **15.7** **17.0**	//BP86[a] SDD[b] COSMO[c]
EP1	-27.9 -33.6 -36.2	-27.1 -31.3 -29.3	//BP86[a] SDD[b] COSMO[c]
EP2	-34.0 -43.5 -46.6	-53.8 -54.2 -50.2	//BP86[a] SDD[b] COSMO[c]

Where, **ES** = educt-substrate complex, **TS** = transition state complex,
EP1 = alcohol product complex, **EP2** = tautomerized product complex.
a) BP86/Lanl2DZ(p), b) B3LYP/SDDp// BP86/Lanl2DZ (p),
c) COSMO-B3LYP/SDDp// BP86/Lanl2DZ(p) (see Computational details)

4.2. Large model complexes:

Computed relative energies for the small model complexes indicate that the nucleophilic reaction pathway is more favorable relative to the electrophilic pathway. Now in order to identify the most probable reaction mechanism for the hydration of acetylene large AH model complexes were analyzed considering the surrounding amino acid residues, Trp_{179}, Trp_{293} and Trp_{472}, that may take part in the reaction.

- ***Electrophilic pathway* LE**:

➢ *Optimized active site model complex* **LE-E**:

The reduced active site large model complex **LE-E** of AH was geometry optimized where the oxidation state of tungsten is IV and the overall charge is -1. The optimized geometry of the active site model complex **LE-E** is distinctively different in geometrical parameters of the metal coordination site in comparison to the protein X-ray crystal structure of AH[100] as well as to the optimized **SE-E** geometry (see Table 4.1 and 4.4). The optimized data shows a reduction in the S_1-S_2-S_3-S_4 dihedral angle (from -31.4˚ to -17.4˚) and in the bond distance between tungsten (W) and dithiolate sulfur atoms (S) (from ~2.442 Å to ~2.388 Å) (Table 4.4) when comparison is made to the protein X-ray crystal structure of AH. The W-O_1 bond distance is increased from 2.041 Å to 2.182 Å.

➢ *Optimized educt substrate complex* **LE-ES**:

Geometry optimization of educt-substrate complex **LE-ES** shows that Wat_{1862} is detached from the W center. The W-O_1 bond distance is increased from 2.182 Å to 4.229 Å while no considerable change is observed in the O_1-H_1 bond of Wat_{1862} (from 0.976 Å to 0.979 Å). A reduction in the S_1-S_2-S_3-S_4 dihedral angle (from -17.4˚ to -2.3˚) and in the W-S bond distances (from ~2.388 Å to ~2.364 Å) is observed when comparison is made with the optimized **LE-E** geometry (Table 4.4).

In the optimized **LE-ES** complex, H_5 of acetylene is at a distance of 2.041 Å from the O_2 of Wat_{1424}, forming a hydrogen bond. The H_1-C_1 and the C_1-C_2 distances are 2.385 Å and 1.225 Å, respectively. The H_5-C_1-C_2 and C_1-C_2-H_6 bond angles of acetylene are 178.9˚ and 178.7˚, respectively (Table 4.4).

- *Optimized transition state complex* **LE-TS**:

In the optimized transition state complex **LE-TS** geometry, a hydronium ion (H_3O^+) is formed with the transfer of a proton (H_7) from the Asp_{13} to the O_1 of Wat_{1862} leaving Asp_{13} an anion (see Fig 4.9). The optimized data shows a change in the S_1-S_2-S_3-S_4 dihedral angle (from -2.3˚ to -12.6˚), in the W-S bond distances (from ~2.364 Å to ~2.350 Å) and in the W-O_1 (from 4.229 Å to 4.134 Å) relative to the optimized **LE-ES** geometry (Table 4.4). The O_1-H_1 bond of Wat_{1862} is elongated from 0.797 Å to 1.097 Å while the H_1-C_1 and the C_2-O_2 distances are reduced from 2.385 Å to 1.540 Å and 3.104 Å to 1.930 Å, respectively. The H_5-C_1-C_2 and the C_1-C_2-H_6 bond angles of acetylene are reduced from 178.9˚ to 125.6˚ and from 178.7˚ to 155.0˚, respectively. The energy barrier for the formation of this transition state is 54.6 kcal/mol in the polarizable continuum (50.8 kcal /mol in the gas phase) relative to the educt-substrate (**LE-ES**) complex (Table 4.6).

The optimized transition state complex **LE-TS** geometry is slightly modified to generate the starting geometries for the geometry optimization of the educt substrate complex **LE-ES** and the alcohol product complex **LE-EP1**. A slight reduction of W-O_1, O_1-H_1, O_4-H_7 and O_2-H_4 bonds together with the elongation of the H_1-C_1, C_2-O_2, O_3-H_4 and O_1-H_7 distances generate the starting geometry for the **LE-ES** complex. On the other hand a slight elongation of the W-O_1, O_1-H_1, O_4-H_7 and O_2-H_4 bonds and reduction of the H_1-C_1, C_2-O_2, O_3-H_4 and O_1-H_7 distances were performed to generate the starting geometry for the **LE-EP1** complex.

- *Optimized alcoholic product complex* **LE-EP1**:

Geometry optimization of vinyl alcohol complex **LE-EP** shows a change in the S_1-S_2-S_3-S_4 dihedral angle (from -12.6˚ to 6.5˚) and in the W-S bond distances (from ~2.350 Å to ~2.365 Å) (Table 4.4). The W-O_1 and the O_1-H_1 distances are increased from 4.134 Å to 4.688 Å and from 1.097 Å to 3.303 Å, respectively. The C_1-C_2 distance is increased from 1.278 Å to 1.346 Å and the C_2-O_2 bond is reduced from 1.930 Å to 1.406 Å whereas the O_2-H_4 bond is broken (distance is increased from 1.045 Å to 5.021 Å) resulting in the formation of vinyl alcohol. On the other hand the reduction of the H_4-O_3 distance from 1.477 Å to 1.014 Å and the elongation of the O_4-H_7 distance from 1.314 Å to 1.859 Å results in the restoration of protonated Asp_{13}. The H_5-C_1-C_2 and C_1-C_2-H_6 bond angles of acetylene are further reduced from 125.6˚ to 120.3˚ and from 155.0˚ to 123.6˚ (Table 4.4).

The formation of vinyl alcohol complex is an exothermic reaction with respect to the **LE-ES** complex, -32.5 kcal/mol in the polarizable continuum (-28.9 kcal/mol in the gas phase) (Table

4.6). Although the formation of vinyl alcohol is an exothermic step, this mechanism was not pursued further due to the high energy barrier of the transition state **LE-TS**.

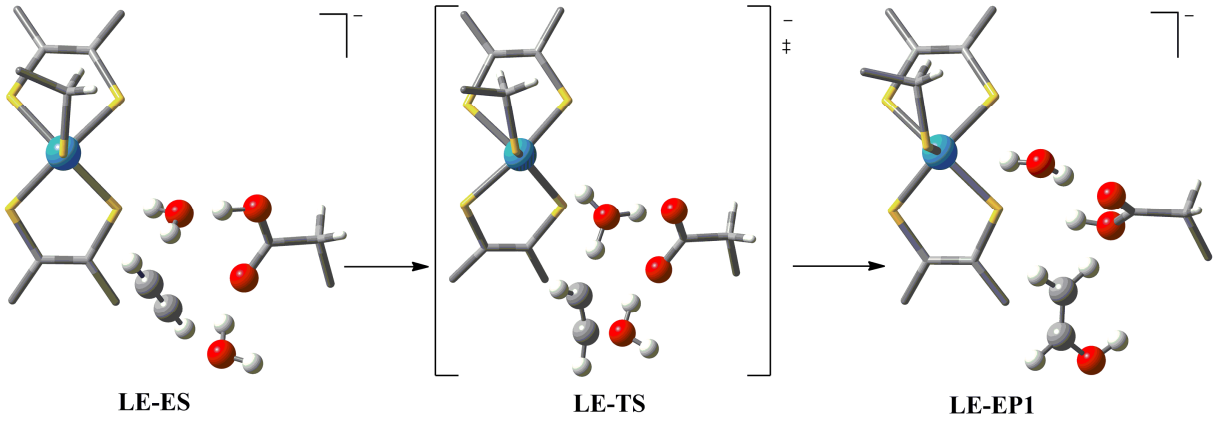

Fig. 4.9: Optimized geometries for the large model complexes involved in the electrophilic pathway of acetylene hydration by AH.

Table 4.4: Geometrical parameters of the optimized model complexes of the electrophilic reaction mechanism for acetylene hydration by the large model complexes of AH.

	X	**LE-E**	**LE-ES**	**LE-TS**	**LE-EP1**
W-S_1 (Å)	2.432	2.429	2.374	2.359	2.380
W-S_2 (Å)	2.489	2.366	2.362	2.358	2.367
W-S_3 (Å)	2.511	2.356	2.357	2.333	2.355
W-S_4 (Å)	2.336	2.400	2.362	2.348	2.359
S_1-S_2-S_3-S_4 (°)	-31.4	-17.4	-2.3	-12.6	6.5
W-O_1 (Å)	2.041	2.182	4.229	4.134	4.688
O_1-H_1 (Å)	-	0.976	0.979	1.097	3.303
H_1-C_1 (Å)	-	-	2.385	1.540	1.086
C_1-C_2 (Å)	-	-	1.225	1.278	1.346
C_2-O_2 (Å)	-	-	3.104	1.930	1.406
O_2-H_4 (Å)	-	0.987	0.999	1.045	5.021
H_4-O_3 (Å)	-	1.788	1.683	1.477	1.014
O_4-H_7 (Å)	-	1.068	1.097	1.314	1.859
H_7-O_1 (Å)	-	2.729	1.341	1.113	0.982
H_5-C_1-C_2 (°)	-	-	178.9	125.6	120.3
C_1-C_2-H_6 (°)	-	-	178.7	155.0	123.6

Where, **X** = protein X-ray crystal structure data,[100] **LE-E** = educt complex, **LE-ES** = educt-substrate complex, **LE-TS** = transition state complex, **LE-EP1** = alcoholic product complex.

- ***Nucleophilic pathway* LN*:***

  - *Optimized active site model complex* **LN-E**:

The reduced active site model complex **LN-E** of AH was geometry optimized where the oxidation state of tungsten is IV and the overall charge is -2. Unlike **SN-E** optimized geometry, the optimized active site model complex **LN-E** geometry is distinctively different in geometrical parameters of the metal coordination site in comparison to the protein X-ray crystal structure of AH.[100] The optimized data shows a slight reduction in the S_1-S_2-S_3-S_4 dihedral angle (from -31.4˚ to -22.1˚) and in the bond distances between tungsten (W) and dithiolate sulfur atoms (S) (from ~2.442 Å to ~2.386 Å) (Table 4.5). The W-O_1 bond distance is increased from 2.041 Å to 2.203 Å.

  - *Optimized educt substrate complex* **LN-ES**:

Geometry optimization of the **LN-ES** complex shows a slight change in the S_1-S_2-S_3-S_4 dihedral angle (from -22.1˚ to -26.6˚) and in the W-S bond distances (from ~2.386 Å to ~2.365 Å) when comparison is made with the optimized **LN-E** geometry. The W-O_1 and H_1-O_3 distances are slightly reduced from 2.203 Å to 2.196 Å and from 1.559 Å to 1.544 Å, respectively (Table 4.5).

In the optimized **LN-ES** complex geometry, the distance between the O_1-C_1 is 3.779 Å, C_1-C_2 is 1.223 Å and C_2-H_1 is 4.483 Å. The H_3-C_1-C_2 and C_1-C_2-H_4 bond angles of acetylene are 179.6˚ and 177.8˚, respectively (Table 4.5).

  - *Optimized transition state complex* **LN-TS**:

Geometry optimization of the transition state complex **LN-TS** shows a slight change in the S_1-S_2-S_3-S_4 dihedral angle (from -26.6˚ to -24.0˚) and in the W-S bond distances (from ~2.365 Å to ~2.384 Å) when compared with the optimized **LN-ES** geometry. The W-O_1 (from 2.196 Å to 2.067 Å), O_1-C_1 (from 3.779 Å to 2.212 Å) and C_2-H_1 (from 4.483 Å to 1.433 Å) distances are reduced while the C_1-C_2 distance is slightly elongated from 1.223 Å to 1.266Å (Table 4.5). The H_3-C_1-C_2 and C_1-C_2-H_4 bond angles of acetylene are reduced from 179.6˚ to 117.8˚ and from 177.8˚ to 138.1˚, respectively. The energy barrier for the formation of the transition state complex **LN-TS** is 35.2 kcal/mol in the continuum (44.6 kcal/mol in the gas phase) relative to the **LN-ES** complex (Table 4.6).

➢ *Optimized alcoholic product complex* **LN-EP1**:

The formation of the vinyl alcohol product complex **LN-EP1** is an exothermic step, -27.8 kcal/mol (-26.8 kcal/mol) relative to the **LN-ES** complex (Table 4.6). In this alcoholic product (**LN-EP1**) complex, the O_1H_2 part of the vinyl alcohol is bound to the active site W metal. Geometry optimization of the **LN-EP1** complex shows no considerable change in the S_1-S_2-S_3-S_4 dihedral angle (from -24.0˚ to -24.4˚). The W-S bond distances are slightly decreased from ~2.384 Å to ~2.375 Å with respect to the optimized **LN-TS** geometry. The W-O_1 and H_1-O_4 distances are increased from 2.067 Å to 2.306 Å and from 1.158 Å to 2.676 Å, respectively. The O_1-C_1 (from 2.212 Å to 1.381 Å) and C_2-H_1 (from 1.433 Å to 1.086 Å) distances are reduced while C_1-C_2 bond is elongated from 1.266 Å to 1.353 Å. The H_3-C_1-C_2 bond angle of acetylene is slightly increased from 117.8˚ to 122.5˚ while the C_1-C_2-H_4 bond angle is reduced from 138.1˚ to 119.1˚, respectively (Table 4.5).

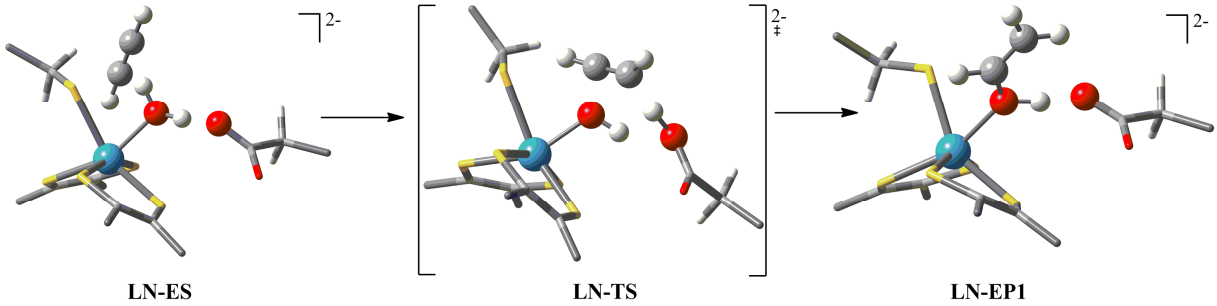

Fig. 4.10: Optimized geometries for the large model complexes involved in the nucleophilic pathway of acetylene hydration by AH.

Table 4.5: Geometrical parameters of the optimized model complexes of the nucleophilic reaction mechanism for acetylene hydration by the large model complexes of AH.

	X	**LN-E**	**LN-ES**	**LN-TS**	**LN-EP1**
W-S_1 (Ù)	2.432	2.405	2.379	2.411	2.403
W-S_2 (Ù)	2.489	2.367	2.340	2.346	2.353
W-S_3 (Ù)	2.511	2.383	2.369	2.391	2.346
W-S_4 (Ù)	2.336	2.388	2.373	2.387	2.397
S_1-S_2-S_3-S_4 (ę)	-31.4	-22.1	-26.6	-24.0	-24.4
W-O_1 (Ù)	2.041	2.203	2.196	2.067	2.306
O_1-H_1 (Ù)	-	1.022	1.022	-	-
H_1-O_3 (Ù)	-	1.559	1.544	1.158	2.676
O_1-C_1 (Ù)	-	-	3.779	2.212	1.381
C_1-C_2 (Ù)	-	-	1.223	1.266	1.353
C_2-H_1 (Ù)	-	-	4.483	1.433	1.086
H_3-C_1-C_2 (ę)	-	-	179.6	117.8	122.5
C_1-C_2-H_4 (ę)	-	-	177.8	138.1	119.1

Where, **X** = protein X-ray crystal structure data,[100] **LN-E** = educt complex, **LN-ES** = educt-substrate complex, **LN-TS** = transition state complex, **LN-EP1** = alcoholic product complex.

Table 4.3: Computed energies [kcal/mol] relative to the edduct-substrate complex for stationary points relevant in the hydration of acetylene by small model complexes of AH.

	Electrophilic Pathway, LE	**Nucleophilic Pathway, LN**	
ES	0.0	0.0	//B3LYP[a] SDD[b] COSMO[c]
TS	**47.1** **50.8** **54.6**	**47.2** **44.6** **35.2**	//B3LYP[a] SDD[b] COSMO[c]
EP1	-18.3 -28.9 -32.5	-21.5 -26.8 -27.8	//B3LYP[a] SDD[b] COSMO[c]

Where, **ES** = educt-substrate complex, **TS** = transition state complex, **EP1** = alcohol product complex. a) B3LYP/Lanl2DZ(p), b) B3LYP/SDDp//B3LYP/Lanl2DZ (p),
c) COSMO-B3LYP/SDDp//B3LYP/Lanl2DZ(p) (see Computational details)

4.3. Large model complexes including water molecules:

Computational results from the large model complexes also favour the nucleophilic pathway. Although the relative energies for the formation of vinyl alcohol products are comparable with the results from the small model complexes, the energy barriers are considerably higher for both mechanistic options. The optimized geometry for the transition state following the large model nucleophilic reaction pathway features a cisoid arrangement of hydrogen atoms in acetylene while it is transoid in the small model nucleophilic pathway.

According to the protein X-ray crystal structure,[100] there are at least 16 well defined water molecules in a vestibule directly adjacent to the active site. Considering these water molecules may help for the hydration of acetylene; we have included four water molecules (Wat_{1209}, Wat_{1212}, Wat_{1424}, and Wat_{1432}) which are in the proximity of the W metal center and connected together through hydrogen bonding (Fig 4.7). Ala_{137}, Met_{138}, Ile_{113}, Ile_{142}, and Phe_{611} residues were also included to keep these water molecules at their location, as they may be involved in hydrogen bonds to these water molecules. DFT studies were carried out on these water containing large model complexes to check the possible assistance of additional water molecules in the active site.

- ***Electrophilic reaction pathway* (XE):**

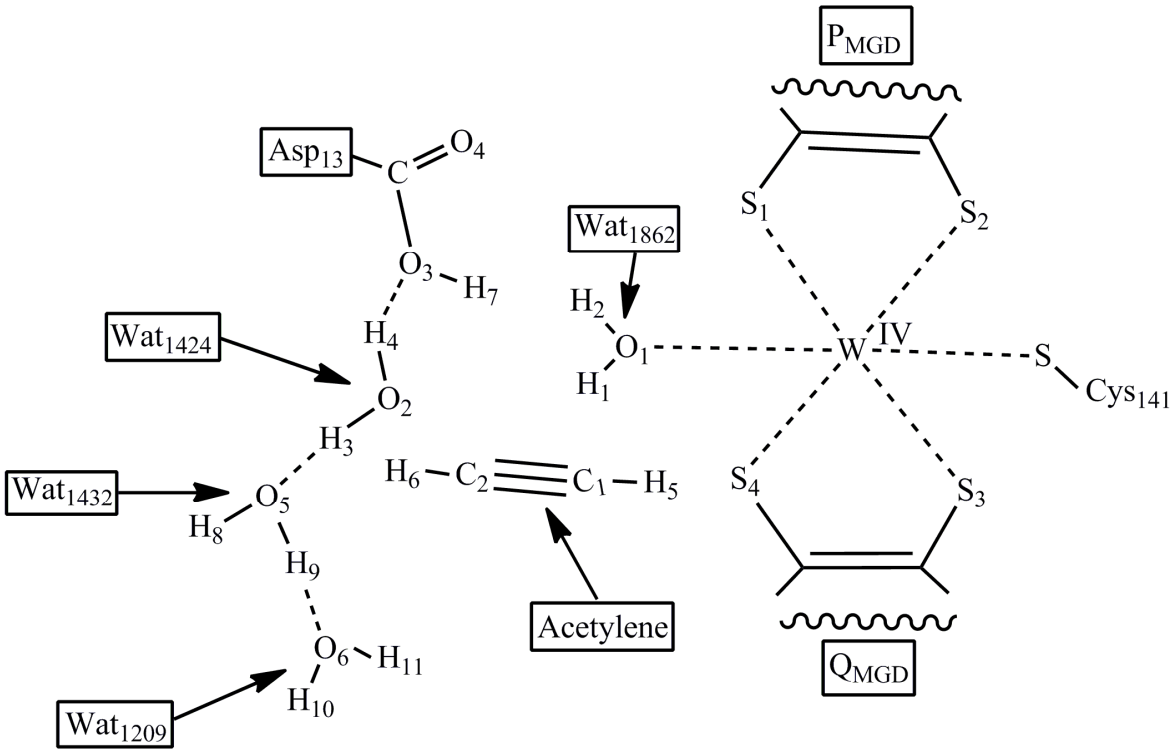

Fig. 4.11: The chemical structure of the large active site model (water containing) complexes for the electrophilic pathway derived from the protein X-ray crystal structure of AH.[100]

- *Optimized active site model complex* **XE-E**:

The reduced active site large model (water containing) complex **XE-E** of AH was geometry optimized where oxidation state of tungsten is IV and the overall charge is -1. The optimized geometry of active site model complex **XE-E** is distinctively different in geometrical parameters of the metal coordination site in comparison to the protein X-ray crystal structure of AH[100] as well as to the optimized **SE-E** and **LE-E** geometries (see Table 4.1, 4.4 and 4.7). The optimized data shows a reduction in the S_1-S_2-S_3-S_4 dihedral angle (from -31.4˚ to -24.9˚) and in the bond distance between tungsten (W) and dihtiolate sulfur atoms (S) (from ~2.442 Å to ~2.377 Å) when comparison is made with the protein X-ray crystal structure of AH (Table 4.7). The W-O_1 bond distance is increased from 2.041 Å to 2.326 Å as H_1 is forming hydrogen bond with the O_2 (see Fig 4.11). The O_1-H_1 bond distance is 1.107 Å. The O_2-H_3 and H_3-O_5 (hydrogen bond) distances are 1.001 Å and 1.727Å, respectively.

- *Optimized educt substrate complex* **XE-ES**:

In the optimizated educt-substrate complex **XE-ES** geometry, the acetylene is loosely bound to the active site pocket. The hydrogen bonding is present between all the water molecules as well as between the H_4 of Wat_{1424} and the O_3 of Asp_{13} (see Fig 4.11). Geometry optimization of **XE-ES** complex shows a slight change in the S_1-S_2-S_3-S_4 dihedral angle (from -24.9˚ to -26.6˚) and in the W-S bond distances (from ~2.377 Å to ~2.379 Å) when comparison is made with the optimized **XE-E** geometry. The W-O_1 and O_1-H_1 bond distances are reduced from 2.326 Å to 2.192Å and from 1.107 Å to 0.982 Å, respectively. The H_4-O_3 and H_7-O_1 distances are increased from 1.714 Å to 2.033 Å and from 1.545 Å to 2.477 Å, respectively. The O_3-H_7 bond is reduced from 1.042 Å to 1.016 Å (Table 4.1). No considerable change is observed in the O_2-H_3 bond (from 1.001 Å to 0.995 Å) while H_3-O_5 (H-bond) distance is increased from 1.727 Å to 1.809 Å.

In the optimized **XE-ES** complex geometry, the H_1-C_1, C_1-C_2 and C_2-O_2 distances are 2.357 Å, 1.226 Å and 2.979 Å, respectively. The H_5-C_1-C_2 and C_1-C_2-H_6 bond angles of acetylene are 176.2˚ and 175.3˚, respectively (Table 4.7).

- *Optimized transition state complex* **XE-TS**:

In the optimized transition state complex **XE-TS** geometry, the water molecules, Wat_{1432}, and Wat_{1209} are also involved in the process of vinyl alcohol formation. The O_2-H_3 bond of Wat_{1424} (distance increased from 0.995 Å to 1.438 Å) is broken and H_3 is transferred from

Wat_{1424} to the O_5 of Wat_{1432} making it a hydronium ion while the electron donating part (-OH) of Wat_{1424} is transferred to the substrate (see Fig. 4.12). The energy barrier for the formation of this transition state is 23.1 kcal/mol in the continuum (29.2 kcal /mol in the gas phase) relative to the educt-substrate (**XE-ES**) complex (Table 4.9).

Geometry optimization of the transition state **XE-TS** complex shows no considerable change in the S_1-S_2-S_3-S_4 dihedral angle (from -26.6˚ to -26.2˚) and in the W-S bond distances (from ~2.379 Å to ~2.384 Å). The W-O_1 bond is slightly reduced from 2.192 Å to 2.122 Å and the O_1-H_1 bond is elongated from 0.982 Å to 1.162 Å) relative to the optimized **XE-ES** geometry (Table 4.7). The H_1-C_1 and C_2-O_2 distances are reduced from 2.357 Å to 1.471 Å and 2.979 Å to 1.477 Å, respectively. The C_1-C_2 bond is elongated from 1.226 Å to 1.349 Å. The H_4-O_3 distance is reduced from 2.033 Å to 1.695 Å. The O_3-H_7 and H_7-O_1 distances are elongated from 1.016 Å to 1.023 Å and from 2.477 Å to 2.730 Å, respectively. The O_2-H_3 distance is increased from 0.995 Å to 1.438 Å while the H_3-O_5 distance is reduced from 1.809 Å to 1.063 Å. The H_5-C_1-C_2 and C_1-C_2-H_6 bond angles of acetylene are reduced from 176.2˚ to 110.8˚ and from 175.3˚ to 128.7˚, respectively.

The educt substrate complex **XE-ES** and the alcohol product complex **XE-EP1** starting geometries for the geometry optimization were generated from the optimized transition state complex **XE-TS** geometry. Slight reduction of W-O_1 and O_2-H_3 bonds together with the elongation of the H_1-C_1 and C_2-O_2 distances gave the starting geometry for the **XE-ES** complex. On the other hand a slight elongation of the W-O_1 bond and reduction of the O_2-H_3, H_1-C_1 and C_2-O_2 distances were performed to generate the starting geometry for the **XE-EP1** complex.

- *Optimized alcoholic product complex* **XE-EP1**:

The formation of vinyl alcohol complex **XE-EP1** is an exothermic reaction with respect to the **XE-ES** complex, -29.8 kcal/mol in continuum (-28.7 kcal/mol in the gas phase) (Table 4.9). Geometry optimization result shows a slight change in the S_1-S_2-S_3-S_4 dihedral angle (from -26.2˚ to -23.5˚) and in the W-S bond distances (from ~2.384 Å to ~2.373 Å) (Table 4.7). The W-O_1 and O_1-H_1 distances are increased from 2.122 Å to 2.252 Å and from 1.162 Å to 3.156 Å, respectively. The C_1-C_2 distance is increased from 1.349 Å to 1.358 Å. The H_1-C_1 and C_2-O_2 bond distances are reduced from 1.471 Å to 1.087 Å and from 1.477 Å to 1.378 Å, respectively, whereas the O_2-H_4 distance is increased from 0.998 Å to 1.048 Å. The reduction of H_4-O_3 distance from 1.695 Å to 0.994 Å and the elongation of O_3-H_7 distance (from 1.023

Å to 2.649 Å) results in the restoration of protonated Asp_{13}. Finally, the reduction of O_1-H_7 (from 2.730 Å to 0.983 Å) results in the formation of a water ligand attached to the active site metal. The O_2-H_3 distance is reduced from 1.438 Å to 1.048 Å while the H_3-O_5 distance is increased from 1.063 Å to 1.463 Å. The H_5-C_1-C_2 bond angle of acetylene is slightly increased from 110.8˚ to 118.5˚ while the C_1-C_2-H_6 is slightly reduced from 128.7˚ to 120.9˚ (Table 4.7).

The tautomerized acetaldehyde product (**XE-EP2**) complex starting geometry for geometry optimization was generated by a slight modification in the vinyl alcohol part of the optimized **XE-EP1** complex geometry. The O_2-H_3 bond was broken together with the reduction of C_1-H_3 and C_2-O_2 distances to generate the starting geometry for the **XE-EP2** complex.

- *Optimized tautomerized product complex* **XE-EP2**:

The computed reaction energy for the tautomerized product complex **XE-EP2** is exothermic relative to the **XE-ES** complex, -35.2 kcal/mol in continuum (-32.9 kcal/mol) (Table 4.9). Geometry optimization shows no considerable change in the S_1-S_2-S_3-S_4 dihedral angle (from -23.5˚ to -23.1˚) and in the W-S bond distances (from ~2.373 Å to ~2.379Å). The W-O_1 bond is reduced from 2.252 Å to 2.181 Å. The elongation of C_1-C_2 bond (from 1.358 Å to 1.494 Å) and the reduction of C_2-O_2 bond (from 1.048 Å to 1.256 Å) indicate the formation of the acetaldehyde product complex (Table 4.7).

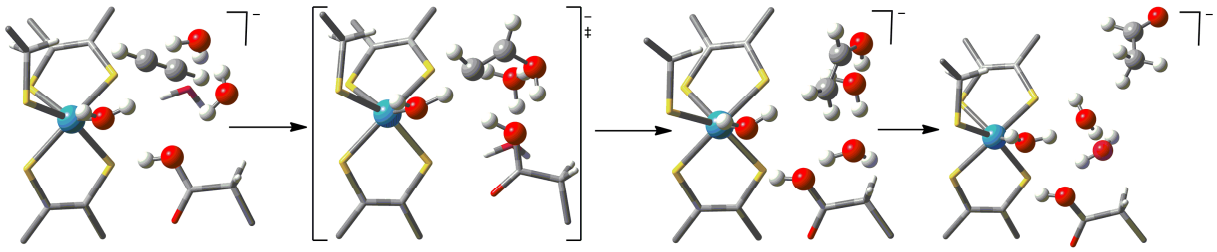

Fig. 4.12: Optimized geometries for the large model (water containing) complexes involved in the electrophilic pathway of acetylene hydration by AH.

Table 4.7: Geometrical parameters of the optimized model complexes of the electrophilic reaction mechanism for acetylene hydration by the large model complexes (containing water molecules) of AH.

	X	**XE-E**	**XE-ES**	**XE-TS**	**XE-EP1**	**XE-EP2**
W-S_1 (Å)	2.432	2.412	2.421	2.417	2.400	2.399
W-S_2 (Å)	2.489	2.396	2.394	2.381	2.390	2.395
W-S_3 (Å)	2.511	2.348	2.339	2.369	2.351	2.359
W-S_4 (Å)	2.336	2.350	2.362	2.367	2.348	2.363
S_1-S_2-S_3-S_4 (°)	-31.4	-24.9	-26.6	-26.2	-23.5	-23.1
W-O_1 (Å)	2.041	2.326	2.192	2.122	2.252	2.181
O_1-H_1 (Å)	-	1.107	0.980	1.162	3.156	-
H_1-C_1 (Å)	-	-	2.357	1.471	1.087	-
C_1-C_2 (Å)	-	-	1.226	1.349	1.358	1.494
C_2-O_2 (Å)	-	-	2.979	1.477	1.378	1.256
O_2-H_4 (Å)	-	0.997	0.983	0.998	-	-
O_2-H_3 (Å)		1.001	0.995	1.438	1.048	-
H_3-O_5 (Å)		1.727	1.809	1.063	1.463	-
H_4-O_3 (Å)	-	1.714	2.033	1.695	0.994	-
O_3-H_7 (Å)	-	1.042	1.016	1.023	-	-
H_7-O_1 (Å)	-	1.545	2.477	2.730	0.983	-
H_5-C_1-C_2 (°)	-	-	176.2	110.8	118.5	-
C_1-C_2-H_6 (°)	-	-	175.3	128.7	120.9	-

Where, **X** = protein X-ray crystal structure data,[100] **XE-E** = educt complex, **XE-ES** = educt-substrate complex, **XE-TS** = transition state complex, **XE-EP1** = alcoholic product complex, **XE-EP2** = aldehyde product complex

- ***Nucleophilic reaction pathway* XN*:***

➢ *Optimized active site model complex* **XN-E**:

The reduced active site large (water containing) model complex **XN-E** of AH is geometry optimized where the oxidation state of tungsten is IV and the overall charge is -2. The optimized geometry of **XN-E** is distinctively different in geometrical parameters of the metal coordination site in comparison to the protein X-ray crystal structure of AH[100] as well as to the optimized **SN-E** and **LN-E** geometries (see Table 4.2, 4.5 and 4.8). The optimized data shows a change in the S_1-S_2-S_3-S_4 dihedral angle (from -31.4˚ to -26.3˚) and in the bond distances between tungsten (W) and dithiolate sulfur atoms (S) (from ~2.442 Å to ~2.383 Å) relative to the protein X-ray crystal structure of AH. The W-O_1 bond distance is increased from 2.041 Å to 2.167 Å. The O_1-H_1 and H_1-O_3 distances are 1.013 Å and 3.633 Å, respectively (Table 4.8).

➢ *Optimized educt substrate complex* **XN-ES**:

Geometry optimization of the **XN-ES** complex shows a change in the S_1-S_2-S_3-S_4 dihedral angle (from -26.3˚ to -29.4˚) and in the W-S bond distances (from ~2.383 Å to ~2.414 Å) when comparison is made with the optimized **XN-E** geometry. The W-O_1 and H_1-O_3 distances are reduced from 2.167 Å to 2.024 Å and from 3.633 Å to 1.014 Å, respectively (Table 4.8).

In the optimized **XN-ES** complex geometry, the distance between the O_1-C_1 is 2.727 Å, C_1-C_2 is 1.232 Å and C_2-H_1 is 2.057 Å. The H_3-C_1-C_2 and C_1-C_2-H_4 bond angles of acetylene are 173.2˚ and 172.2˚, respectively (Table 4.8).

➢ *Optimized transition state complex* **XN-TS**:

Geometry optimization of the transition state complex **XN-TS** shows no considerable change in the the S_1-S_2-S_3-S_4 dihedral angle (from -29.4˚ to -27.6˚) and in the W-S bond distances (from ~2.414 Å to ~2.416 Å) when compared with the optimized **XN-ES** geometry. The W-O_1 (from 2.024 Å to 2.009 Å), O_1-C_1 (from 1.014 Å to 1.051 Å) and C_2-H_1 (from 2.057 Å to 1.733 Å) distances are reduced while the C_1-C_2 distance is slightly elongated from 1.232 Å to 1.246Å (Table 4.8). The H_3-C_1-C_2 and C_1-C_2-H_4 bond angles of acetylene are reduced from 173.2˚ to 163.0˚ and from 172.2˚ to 154.7˚, respectively. The energy barrier for the formation of this transition state complex **XN-TS** is 14.4 kcal/mol in the continuum (13.4 kcal/mol in the gas phase) relative to the **XN-ES** complex (Table 4.10).

The educt substrate complex **XN-ES** and the alcohol product complex **XN-EP1** starting geometries for geometry optimization were generated from the optimized transition state (**XN-TS**) geometry. Slight reduction of W-O_1 bond together with the elongation of the O_1-C_1 and C_2-H_1 distances gave the starting geometry for the **XN-ES** complex. On the other hand a slight elongation of the W-O_1 and O_3-H_1 bonds and reduction of the O_1-C_1 and C_2-H_1 distances were performed to generate the starting geometry for the **XN-EP1** complex.

- *Optimized alcoholic product complex* **XN-EP1**:

The formation of initial product of acetylene hydration, a vinyl alcohol, is an exothermic step, -38.3 kcal/mol in the polarizable continuum (-47.3 kcal/mol) relative to the **XN-ES** complex (Table 4.10). In this alcoholic product complex **XN-EP1**, the O_1H_2 part of the vinyl alcohol is bound to the active site W metal. Geometry optimization of the **XN-EP1** complex shows a change in the S_1-S_2-S_3-S_4 dihedral angle (from -27.6˚ to -25.1˚) and in the W-S bond distances (from ~2.416 Å to ~2.380 Å) with respect to the optimized **XN-TS** geometry. The W-O_1 (from 2.009 Å to 2.202 Å) and the H_1-O_3 (from 1.051 Å to 3.327 Å) distances are increased. The O_1-C_1 (from 2.262 Å to 1.414 Å) and C_2-H_1 (from 1.733 Å to 1.086 Å) distances are reduced while the C_1-C_2 bond is elongated from 1.246 Å to 1.342 Å. The H_3-C_1-C_2 and C_1-C_2-H_4 bond angles of acetylene are reduced from 163.0˚ to 124.5˚ and from 154.7˚ to 122.7˚, respectively (Table 4.8).

The tautomerized acetaldehyde product (**XN-EP2**) complex starting geometry for geometry optimization was generated by a slight modification in the vinyl alcohol part of the optimized **XN-EP1** complex geometry. The O_2-H_3 bond was broken together with the reduction of C_1-H_3 and C_2-O_2 distances to generate the starting geometry for the **XN-EP2** complex.

- *Optimized tautomerized product complex* **XN-EP2**:

The computed reaction energy for the formation of tautomerized product complex **XN-EP2** is again strongly exothermic, -51.4 kcal/mol in the continuum (-61.4 kcal/mol) relative to the **XN-ES** complex (Table 4.10). Geometry optimization result shows only minor changes in the S_1-S_2-S_3-S_4 dihedral angle (from -25.1˚ to -27.7˚) and in the W-S bond distances (from ~2.380 Å to ~2.406 Å) when comparison is made with the optimized **XN-EP1** geometry. No change is observed in the W-O_1 bond distance. The O_1-C_1 bond is reduced from 1.414 Å to 1.272 Å while the C_1-C_2 bond is elongated from 1.342 Å to 1.498 Å.

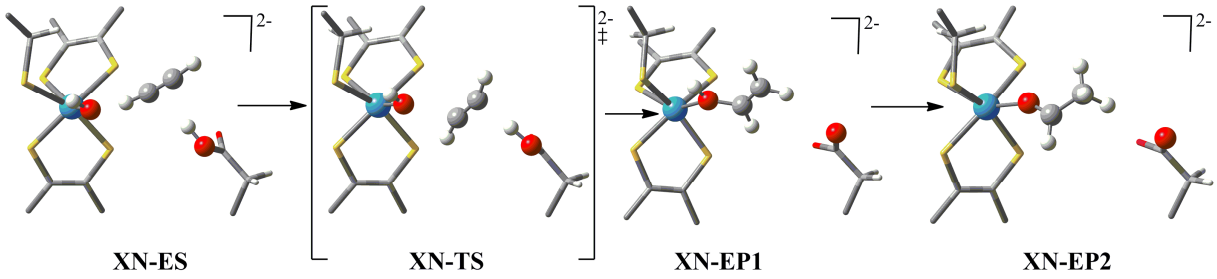

Fig. 4.13: Optimized geometries for the large model (water containing) complexes involved in the nucleophilic pathway of acetylene hydration by W containing AH.

Table 4.8: Geometrical parameters of the optimized model complexes of the nucleophilic reaction mechanism for acetylene hydration by the large model (water containing) complexes of AH.

	X	XN-E	XN-ES	XN-TS	XN-EP1	XN-EP2
W-S_1 (Å)	2.432	2.402	2.413	2.425	2.387	2.399
W-S_2 (Å)	2.489	2.388	2.362	2.373	2.361	2.383
W-S_3 (Å)	2.511	2.367	2.410	2.403	2.369	2.412
W-S_4 (Å)	2.336	2.376	2.469	2.464	2.404	2.428
S_1-S_2-S_3-S_4 (°)	-31.4	-26.3	-29.4	-27.6	-25.1	-27.7
W-O_1 (Å)	2.041	2.167	2.024	2.009	2.202	2.202
O_1-H_1 (Å)	-	1.013	-	-	-	-
H_1-O_3 (Å)	-	3.633	1.014	1.051	3.327	-
O_1-C_1 (Å)	-	-	2.727	2.262	1.414	1.272
C_1-C_2 (Å)	-	-	1.232	1.246	1.342	1.498
C_2-H_1 (Å)	-	-	2.057	1.733	1.086	-
H_3-C_1-C_2 (°)	-	-	173.2	163.0	124.5	-
C_1-C_2-H_4 (°)	-	-	172.2	154.7	122.7	-

Where, **X** = protein X-ray crystal structure data,[100] **XN-E** = educt complex, **XN-ES** = educt-substrate complex, **XN-TS** = transition state complex, **XN-EP1** = alcoholic product complex, **XN-EP2** = aldehyde product complex

- ***Nucleophilic reaction pathway for acetylene hydration by Mo-containing AH* (Mo)*:***

Molybdenum dependent active acetylene hydratase enzyme was purified from *P.acetylenicus* cells which had been grown in the absence of tungsten.[179] The activity of Mo-dependent AH for acetylene hydration was believed to be similar to the W-dependent AH. In order to check the influence of the nature of metal on the acetylene hydration, we have computed the same, water molecules containing, large active site model complexes (**XN**) derived from the protein X-ray crystal structure of AH[100] for acetylene hydration (via nucleophilic pathway) where only the W is replaced by Mo atom at the active site.

- *Optimized active site model complex* **Mo-E**:

The reduced active site large (water containing) model complex **Mo-E** of AH is geometry optimized where the oxidation state of tungsten is IV and the overall charge is -2. The optimized geometry of **Mo-E** is distinctively different in geometrical parameters of the metal coordination site in comparison to the optimized **XN-E** geometry. Although, the optimized data shows no considerable change in the S_1-S_2-S_3-S_4 dihedral angle (from -26.3˚ to -29.5˚), the bond distances between molybdenum (Mo) and dithiolate sulfur atoms (S) increases from ~2.383 Å to ~2.394 Å (Table 4.9). The M-O_1 bond distance is increased from 2.167 Å (W-O_1) to 2.242 Å (Mo-O_1). A slight change is observed in the O_1-H_1 bond distance from 1.013 Å to 1.000 Å while the H_1-O_3 distance is decreased from 3.633 Å to 1.923 Å.

- *Optimized educt substrate complex* **Mo-ES**:

Geometry optimization of the **Mo-ES** complex shows no change in the S_1-S_2-S_3-S_4 dihedral angle (from -29.5˚ to -29.0˚) but the Mo-S bond distances are increased from ~2.394 Å to ~2.425 Å when comparison is made with the optimized **Mo-E** geometry. The Mo-O_1 and H_1-O_3 distances are reduced from 2.242 Å to 2.047 Å and from 1.923 Å to 1.015 Å, respectively (Table 4.9).

In the optimized **Mo-ES** complex geometry, the distance between the O_1-C_1 is 2.700 Å, C_1-C_2 is 1.233 Å and C_2-H_1 is 2.052 Å. The H_3-C_1-C_2 and C_1-C_2-H_4 bond angles of acetylene are 172.6˚ and 172.0˚, respectively (Table 4.9).

- *Optimized transition state complex* **Mo-TS**:

Geometry optimization of the transition state complex **Mo-TS** shows no considerable change in the the S_1-S_2-S_3-S_4 dihedral angle (from -29.0˚ to -27.7˚) and in the Mo-S bond distances

(from ~2.425 Å to ~2.428 Å) when compared with the optimized **Mo-ES** geometry. The Mo-O_1 (from 2.047 Å to 2.029 Å), O_1-C_1 (from 2.700 Å to 2.262 Å) and C_2-H_1 (from 2.052 Å to 1.725 Å) distances are reduced while C_1-C_2 distance is slightly elongated from 1.233 Å to 1.247Å (Table 4.9). The H_3-C_1-C_2 and C_1-C_2-H_4 bond angles of acetylene are reduced from 172.6˚ to 162.7˚ and from 172.0˚ to 155.3˚, respectively. The energy barrier for the formation of this transition state complex **Mo-TS** is 13.3 kcal/mol in the continuum (13.1 kcal/mol in the gas phase) relative to the **Mo-ES** complex (Table 4.10). The energy barrier for **Mo-TS** is similar to the energy barrier for the tungsten containing complex **XN-TS** (14.4 kcal/mol in the polarizable continuum).

The educt substrate complex **Mo-ES** and the alcohol product complex **Mo-EP1** starting geometries for geometry optimization were generated from the optimized transition state complex **Mo-TS** geometry. Slight reduction of the Mo-O_1 bond together with the elongation of the O_1-C_1 and C_2-H_1 distances gave the starting geometry for the **Mo-ES** complex. On the other hand a slight elongation of the Mo-O_1 and O_3-H_1 bonds and reduction of the O_1-C_1 and C_2-H_1 distances were performed to generate the starting geometry for the **Mo-EP1** complex.

- *Optimized alcoholic product complex* **Mo-EP1**:

The formation of initial product of acetylene hydration, a vinyl alcohol, is an exothermic step, -42.7 kcal/mol in the polarizable continuum (-51.3 kcal/mol) relative to the **Mo-ES** complex (Table 4.10). The formation of **Mo-EP1** is ~4 kcal/mol lower in energy than the formation of **XN-EP1**. In this alcoholic product (**Mo-EP1**) complex, the O_1H_2 part of the vinyl alcohol is bound to the active site Mo metal. Geometry optimization of the **Mo-EP1** complex shows no considerable change in the S_1-S_2-S_3-S_4 dihedral angle (from -27.7˚ to -25.7˚) but the Mo-S bond distances are decreased from ~2.428 Å to ~2.389 Å relative to the optimized **Mo-TS** geometry. The Mo-O_1 (from 2.029 Å to 2.235 Å) and the H_1-O_3 (from 1.052 Å to 2.606 Å) distances are increased. The O_1-C_1 (from 2.262 Å to 1.409 Å) and C_2-H_1 (from 1.725 Å to 1.086 Å) distances are reduced while the C_1-C_2 bond is elongated from 1.247 Å to 1.343 Å (a typical C=C bond length). The H_3-C_1-C_2 and C_1-C_2-H_4 bond angles of acetylene are further reduced from 162.7˚ to 124.1˚ and from 155.3˚ to 122.7˚, respectively (Table 4.9).

The tautomerized acetaldehyde product complex **Mo-EP2** starting geometry for geometry optimization was generated by a slight modification in the vinyl alcohol part of the optimized **Mo-EP1** complex geometry. The O_2-H_3 bond was broken together with the reduction of C_1-H_3 and C_2-O_2 distances to generate the starting geometry for the **Mo-EP2** complex.

- *Optimized tautomerized product complex* **Mo-EP2**:

The computed reaction energy for the formation of tautomerized product complex **Mo-EP2** is again strongly exothermic, -55.5 kcal/mol in the continuum and -63.7 kcal/mol in the gas phase (again ~4 kcal/mol lower in energy than **XN-EP2**) relative to the **Mo-ES** complex (Table 4.10). Geometry optimization shows no change in the S_1-S_2-S_3-S_4 dihedral angle (from -25.7˚ to -25.6˚) while the Mo-S bond distances are increased from ~2.389 Å to ~2.404 Å when comparison is made with the optimized **Mo-EP1** geometry. The Mo-O_1 bond distance is reduced from 2.235 Å to 2.129 Å. The O_1-C_1 bond is reduced from 1.409 Å to 1.260 Å while the C_1-C_2 bond is elongated from 1.343 Å to 1.497 Å (a typical C-C bond).

Table 4.9: Geometrical parameters of the optimized model complexes of the nucleophilic reaction mechanism for acetylene hydration by the large model (water containing) complexes of AH.

	XN-E	**Mo-E**	**Mo-ES**	**Mo-TS**	**Mo-EP1**	**Mo-EP2**
Mo-S_1 (Ù)	2.402	2.405	2.427	2.439	2.394	2.402
Mo-S_2 (Ù)	2.388	2.376	2.368	2.383	2.366	2.380
Mo-S_3 (Ù)	2.367	2.391	2.416	2.408	2.382	2.410
Mo-S_4 (Ù)	2.376	2.402	2.488	2.482	2.415	2.425
S_1-S_2-S_3-S_4 (ę)	-26.3	-29.5	-29.0	-27.7	-25.7	-25.6
Mo-O_1 (Ù)	2.167	2.242	2.047	2.029	2.235	2.129
O_1-H_1 (Ù)	1.013	1.0	4.176	-	-	-
H_1-O_3 (Ù)	3.633	1.923	1.015	1.052	2.606	-
O_1-C_1 (Ù)	-	-	2.700	2.262	1.409	1.260
C_1-C_2 (Ù)	-	-	1.233	1.247	1.343	1.497
C_2-H_1 (Ù)	-	-	2.052	1.725	1.086	-
H_3-C_1-C_2 (ę)	-	-	172.6	162.7	124.1	-
C_1-C_2-H_4 (ę)	-	-	172.0	155.3	122.7	-

Where, **XN-E** = educt complex of the nucleophilic reaction mechanism for acetylene hydration by the large model (water contining) complex of W-AH. **Mo-E** = educt complex, **Mo-ES** = educt-substrate complex, **Mo-TS** = transition state complex, **Mo-EP1** = alcoholic product complex, **Mo-EP2** = aldehyde product complex

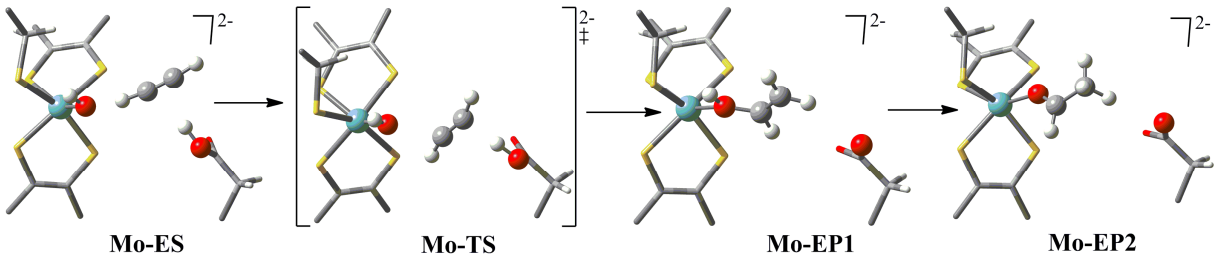

Fig 4.14: Optimized geometries for the large model (water containing) complexes involved in nucleophilic pathway of acetylene hydration by Mo containing AH.

Table 4.10: Computed energy barriers [kcal/mol] relative to the edduct-substrate complex for hydration of acetylene by the large model (water containing) complexes of AH.

	Electrophilic Pathway, XE	**Nucleophilic Pathway, XN**	**Nucleophilic Pathway, Mo**	
ES	0.0	0.0	0.0	//B3LYP[a] SDD[b] COSMO[c]
TS	**26.5** **29.2** **23.1**	**14.3** **13.4** **14.4**	**14.3** **13.1** **13.3**	//B3LYP[a] SDD[b] COSMO[c]
EP1	-36.1 -28.7 -29.8	-47.1 -47.3 -38.3	-50.7 -51.3 -42.7	//B3LYP[a] SDD[b] COSMO[c]
EP2	-34.0 -32.9 -35.2	-56.7 -61.4 -51.4	-57.3 -63.7 -55.5	//B3LYP[a] SDD[b] COSMO[c]
EP3	-	-56.5 -62.5 -58.6	-58.9 -65.4 -61.6	//B3LYP[a] SDD[b] COSMO[c]

Where, **ES** = educt-substrate complex, **TS** = transition state complex, **EP1** = alcohol product complex, **EP2** = tautomerized product complex, **EP3** = product complex, where acetaldehyde is replaced by surrounding water molecule but acetaldehyde is also present in the structure.

a) B3LYP/Lanl2DZ(p), b) B3LYP/SDDp//B3LYP/Lanl2DZ (p),

c) COSMO-B3LYP/SDDp//B3LYP/Lanl2DZ(p) (see Computational details).

- ***Optimized energy barriers for the tautomerization of vinyl alcohol to acetaldehyde*:**

In the absence of the educt complex, the energy barriers for the tautomerization of vinyl alcohol (**VA**) to the acetaldehyde (**AA**) were computed with (intermolecular) and without (intramolecular) the assistance of water molecules using the density functional theory (DFT) calculations.

➢ *Intramolecular* **1A**:

The computed energy barrier for the intramolecular conversion of **1A-VA** to **1A-AA** is 58.8 kcal/mol in the continuum (57.7 kcal/mol in the gas phase) relative to the vinyl alcohol molecule **1A-VA** (Table 4.12). In the optimized transition state **1A-TS**, the C_3-O_5 (form 1.395 Å to 1.324 Å) and C_1-H_6 (from 2.578 Å to 1.542 Å) distances are reduced while the O_5-H_6 distance is increased from 0.980 Å to 1.324 Å when comparison is made with the optimized **1A-VA** geometry (Table 4.11). An imaginary frequency of 2168i cm^{-1} corresponds to the stretching vibration modes of O_5-H_6 and C_1-H_6 in **1A-TS** and confirmed the saddle point character between the **1A-VA** and **1A-AA**.

The computed relative energy for the acetaldehyde formation **1A-AA** is exothermic, -13.8 kcal/mol in the continuum (-14.4) relative to the **1A-VA** (Table 4.12). In the optimized **1A-VA**, the C_3-O_5 (form 1.324 Å to 1.244 Å) and C_1-H_6 (from 1.542 Å to 1.093 Å) distances are further reduced while the O_5-H_6 distance is increased from 1.324 Å to 2.615 Å when comparison is made with the optimized **1A-TS** geometry (Table 4.11).

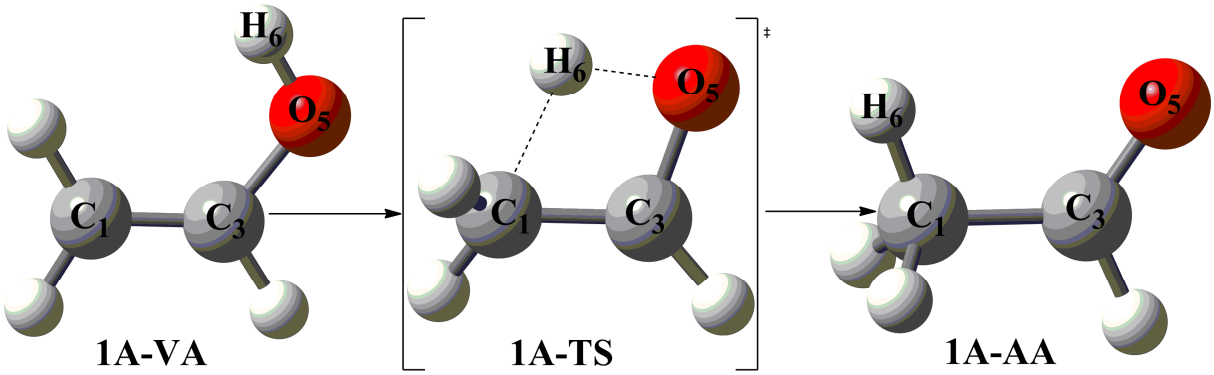

Fig. 4.15: Optimized geometries for the intramolecular tautomerization of vinyl alcohol to acetaldehyde.

➢ *Intermolecular - Single water molecule catalyzed reaction* **2A** :

Suenobu et al.[173] suggest that the energy barrier for the conversion of **VA** to **AA** decreases with the assistance of a water molecule (intermolecular). The computed energy barrier for the water catalyzed conversion of **2A-VA** to **2A-AA** is 30.7 kcal/mol in the continuum (27.8 kcal/mol) relative to the **2A-VA** (Table 4.12). An imaginary frequency of 1711ί cm^{-1} corresponds to the stretching vibration modes of O_5-H_6, O_7-H_9 and C_1-H_9 in **2A-TS** and confirmed the saddle point character between the **2A-VA** and **2A-AA**. In the optimized transition state **2A-TS**, the C_3-O_5 (form 1.381 Å to 1.313 Å), H_6-O_7 (form 1.679 Å to 1.187 Å), and C_1-H_9 (from 4.228 Å to 1.463 Å) distances are reduced while the O_5-H_6 (from 0.999 Å to 1.263 Å) and O_7-H_9 (from 0.975 Å to 1.223 Å) distances are increased when comparison is made with the optimized **2A-VA** geometry (Table 4.11).

The computed relative energy for the acetaldehyde **2A-AA** formation in the water catalyzed reaction is also exothermic, -11.5 kcal/mol in the continuum (-12.9 kcal/mol in the gas) relative to the **2A-VA**. The computed relative energy for the formation of **2A-AA** is similar to the formation of **1A-AA** (see Table 4.12). In the optimized **2A-AA**, the H_6 is transferred from the O_5 of **2A-VA** to the O_7 of water molecule while the H_9 from the water molecule is transferred to the C_1 of **2A-VA** (see Fig. 4.16). The C_3-O_5 (form 1.313 Å to 1.251 Å), H_6-O_7 (form 1.187 Å to 0.988 Å), and C_1-H_9 (from 1.463 Å to 1.093 Å) distances are further reduced while the O_5-H_6 (from 1.263 Å to 1.841 Å) and O_7-H_9 (from 1.223 Å to 2.326 Å) distances are increased when comparison is made with the optimized **2A-TS** geometry (Table 4.11).

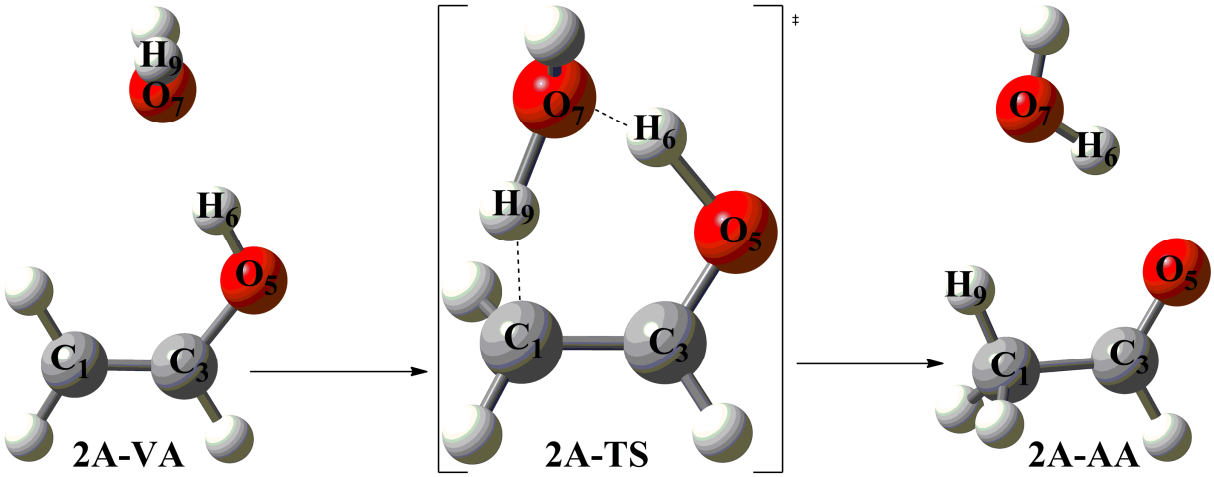

Fig. 4.16: Optimized geometries for the single water molecule catalyzed, intermolecular tautomerization of vinyl alcohol to acetaldehyde.

➢ *Intermolecular ï reaction catalyzed by two water molecules* **3A**:

Lledós et al.[174] suggest that the intervention of a chain of two water molecules reduces dramatically the potential energy barrier. The computed energy barrier for the conversion of **3A-VA** to **3A-AA** catalyzed by two water molecules is 20.7 kcal/mol in the continuum (20.3 kcal/mol) relative to the **3A-VA** (Table 4.12). An imaginary frequency of 1318í cm^{-1} corresponds to the stretching vibration modes of O_5-H_6, O_7-H_6, O_7-H_9, O_{11}-H_9, O_{11}-H_{13} and C_1-H_{13} in **3A-TS** and confirmed the saddle point character between the **3A-VA** and **3A-AA**. In the optimized transition state **3A-TS**, the C_3-O_5 (from 1.364 Å to 1.304 Å), H_6-O_7 (from 1.562 Å to 1.125 Å), H_9-O_{11} (from 1.625 Å to 1.186 Å), and C_1-H_{13} (from 2.172 Å to 1.467 Å) distances are reduced while the O_5-H_6 (from 1.020 Å to 1.306 Å), O_7-H_9 (from 1.005 Å to 1.216 Å) and O_{11}-H_{13} (from 0.991 Å to 1.188 Å) distances are increased when comparison is made with the optimized **3A-VA** geometry (Table 4.11).

The computed relative energy for the acetaldehyde **3A-AA** formation is also exothermic, -12.0 kcal/mol in the continuum (-11.0 kcal/mol) relative to the **3A-VA**. The computed relative energy for the formation of **3A-AA** is similar to the formation of **1A-AA** and **2A-AA** (see Table 4.12). In the optimized **3A-AA**, the H_6 is transferred from the O_5 of **3A-VA** to the O_7 of one water molecule. The H_9 from O_7 of water molecule is transferred to the O_{11} of the second water molecule while the H_{13} is transferred from the O_{11} to the C_1 of **3A-VA** (see Fig. 4.17). The C_3-O_5 (form 1.304 Å to 1.252 Å), H_6-O_7 (form 1.125 Å to 0.995 Å), H_9-O_{11} (form 1.186 Å to 1.002 Å), and C_1-H_{13} (from 1.467 Å to 1.098 Å) distances are further reduced while the O_5-H_6 (from 1.306 Å to 1.712 Å), O_7-H_9 (from 1.216 Å to 1.643 Å) and O_{11}-H_{13} (from 1.188 Å to 2.129 Å) distances are increased when comparison is made to the optimized **3A-TS** geometry (Table 4.11).

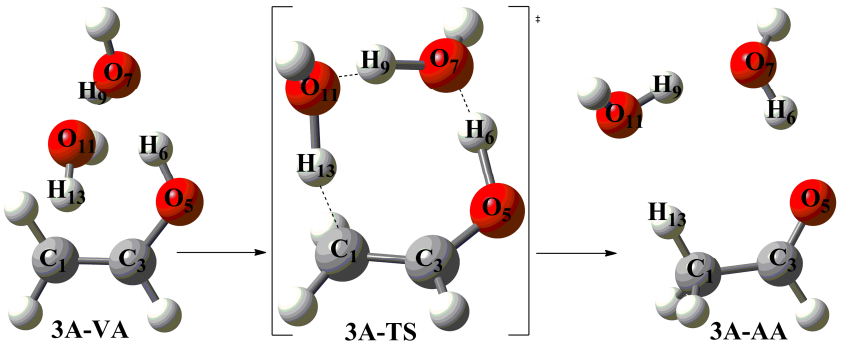

Fig. 4.17: Optimized geometries for the intermolecular tautomerization of vinyl alcohol to acetaldehyde catalyzed by two water molecules.

➢ *Tautomerization of vinyl alcohol to acetaldehyde in the educt complex* **WN**:

According to the computational results for the tautomerization of vinyl alcohol (**VA**) to acetaldehyde (**AA**) (without educt complex), the energy barrier decreases when the reaction is catalyzed by the chain of two water molecules. Therefore, we have computed the vinyl alcohol to acetaldehyde tautomerization in the educt complex **WN**. **WN-TS** complex geometry for the transition state search was generated by the addition of two water molecules in the optimized **SN-EP1** geometry. The **WN-VA** and **WN-AA** geometries for the geometry optimization were generated by the slight modifications in the optimized **WN-TS** geometry.

In the optimized **WN-VA** geometry, a water molecule forms the hydrogen bond with the Asp_{13} as well as with the other water molecule (Fig. 4.18). The computed energy barrier for the **WN-TS** is 18.9 kcal/mol in the continuum (28.5 kcal/mol) relative to the **WN-VA** complex (Table 4.12). In the optimized transition state **WN-TS** geometry, the C_3-O_5 bond is reduced from 1.410 Å to 1.351 Å. The O_5-H_6, O_7-H_9 and O_{11}-H_{13} bond distances are 1.5324 Å, 1.214 Å and 1.171 Å, respectively. The H_6-O_7, H_9-O_{11} and C_1-H_{13} distances are 1.062 Å, 1.226 Å and 1.505 Å, respectively (Table 4.11).

The computed relative energy for the formation of acetaldehyde containing product complex **WN-AA** is also exothermic, -13.0 kcal/mol in the continuum (-9.7 kcal/mol) relative to the **WN-VA** complex (Table 4.12). The C_3-O_5 (from 1.351 Å to 1.299 Å), H_6-O_7 (form 1.062 Å to 1.003 Å), H_9-O_{11} (form 1.226 Å to 1.023 Å), and C_1-H_{13} (from 1.505 Å to 1.103 Å) distances are reduced while the O_5-H_6 (from 1.534 Å to 3.572 Å), O_7-H_9 (from 1.214 Å to 1.613 Å) and O_{11}-H_{13} (from 1.171 Å to 6.303 Å) distances are increased when comparison is made with the optimized **WN-VA** geometry (Table 4.11).

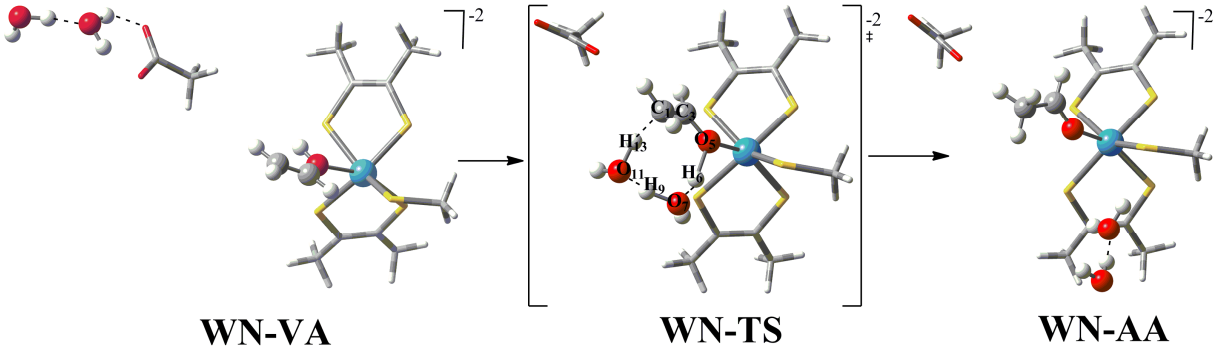

Fig. 4.18: Optimized geometries for the intermolecular tautomerization of vinyl alcohol to acetaldehyde catalyzed by two water molecules in the educt complex, **WN**. (Labelling of the atoms are according to the reaction **3A** (Fig 4.17)).

Table 4.11: Geometrical parameters of the optimized model complexes for the tautomerization of vinyl alcohol (**VA**) to acetaldehyde (**AA**).

	C_3-O_5 (Ù)	**O_5-H_6 (Ù)**	**C_1-H_6 (Ù)**	**H_6-O_7 (Ù)**	**O_7-H_9 (Ù)**	**C_1-H_9 (Ù)**	**H_9-O_{11} (Ù)**	**O_{11}-H_{13} (Ù)**	**C_1-H_{13} (Ù)**
1A-VA	1.395	0.980	2.578	-	-	-	-	-	-
1A-TS	1.324	1.324	1.542	-	-	-	-	-	-
1A-AA	1.244	2.615	1.093	-	-	-	-	-	-
2A-VA	1.381	0.999	-	1.679	0.975	4.228	-	-	-
2A-TS	1.313	1.263	-	1.187	1.223	1.463	-	-	-
2A-AA	1.251	1.841	-	0.988	2.326	1.093	-	-	-
3A-VA	1.364	1.020	-	1.562	1.005	-	1.625	0.991	2.172
3A-TS	1.304	1.306	-	1.125	1.216	-	1.186	1.188	1.467
3A-AA	1.252	1.712	-	0.995	1.643	-	1.002	2.129	1.098
WN-VA	1.410	1.00	-	-	-	-	-	-	-
WN-TS	1.351	1.534	-	1.062	1.214	-	1.226	1.171	1.505
WN-AA	1.299	3.572	-	1.003	1.613	-	1.023	6.303	1.103

Where, **1A** = intramolecular reaction, **2A** = single water molecule catalyzed reaction, **3A** = reaction catalyzed by two water molecules, **WN** = small model complex (**SN-EP1**) with two additional water molecules, **VA** = vinyl alcohol, **TS** = transition state, **AA** = acetaldehyde.

(see Fig 4.15, 4.16, 4.17 and 4.18).

Table 4.12: Computed energy barriers (kcal/mol) for the tautomerization of vinyl alcohol to the acetaldehyde.

	VA	TS	AA	
1A	0.0	**62.6**	-9.6	//B3LYP[a]
		57.7	-14.4	SDD[b]
		58.8	-13.8	COSMO[c]
2A	0.0	**26.4**	-7.3	//B3LYP[a]
		27.8	-12.9	SDD[b]
		30.7	-11.5	COSMO[c]
3A	0.0	**13.3**	-5.3	//B3LYP[a]
		20.3	-11.0	SDD[b]
		20.7	-12.0	COSMO[c]
WN	0.0	**18.3**	-8.6	//BP86[d]
		28.5	-9.7	SDD[e]
		18.9	-13.0	COSMO[f]

Where, **1A** = intramolecular reaction, **2A** = single water molecule catalyzed reaction, **3A** = reaction catalyzed by two water molecules, **WN** = small model complex (**SN-EP1**) with two additional water molecules, **VA** = vinyl alcohol, **TS** = transition state, **AA** = acetaldehyde.

a) B3LYP/Lanl2DZ(p), b) B3LYP/SDDp//B3LYP/Lanl2DZ (p),

c) COSMO-B3LYP/SDDp//B3LYP/Lanl2DZ(p), d) BP86/Lanl2DZ(p),

e) B3LYP/SDDp//BP86/Lanl2DZ(p), f) COSMO-B3LYP/SDDp//BP86/Lanl2DZ(p)

(see Computational details).

Scheme 4.8: Graphical representation of the computed energy barriers (kcal/mol) for the tautomerization of vinyl alcohol to acetaldehyde.

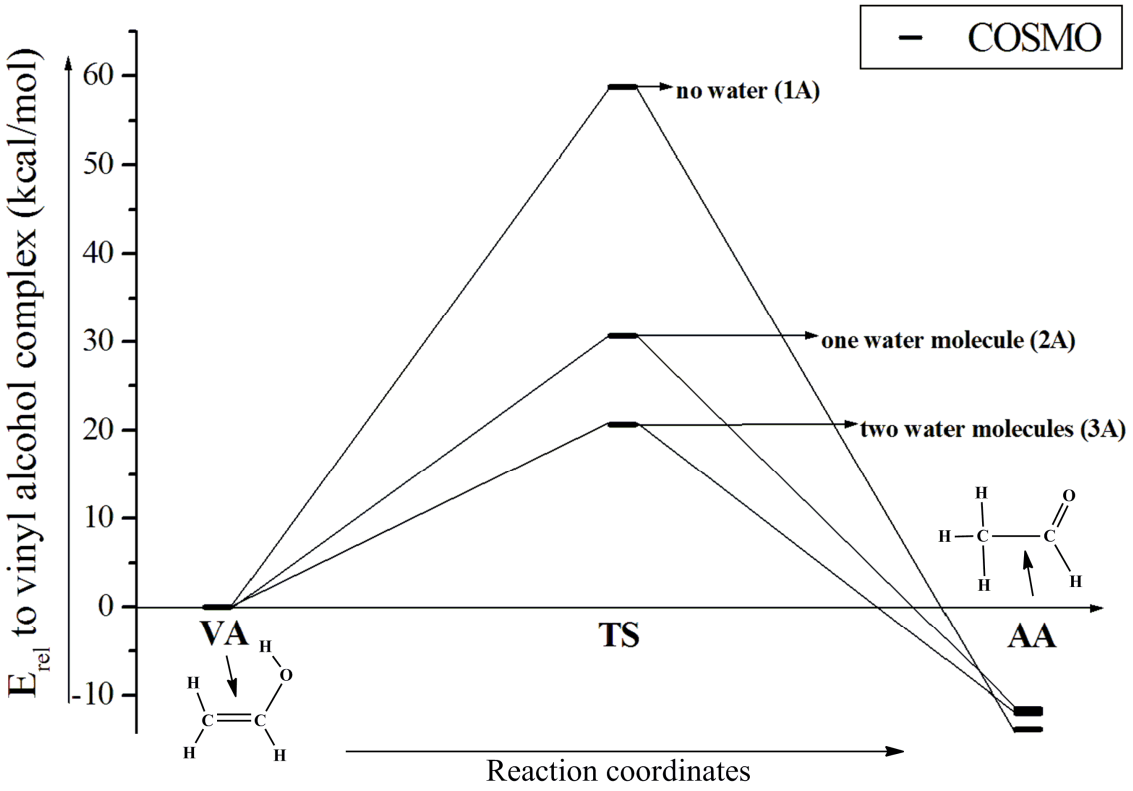

Where, **VA** = vinyl alcohol, **TS** = transition state, **AA** = acetaldehyde.

5. Discussion

Acetylene hydratase (AH) is a unique tungsten-containing enzyme as it does not appear to catalyze a redox reaction. The protein X-ray crystal structure of AH[100] provides important clues on the catalytic mechanism and the role of the W center. For catalysis, the enzyme is activated by the reduction of W center from W^{VI} to W^{IV}, as only W^{IV} participates in the catalysis of acetylene hydration, and the [4Fe-4S] cluster facilitates this step. The reactive species in AH is either a hydroxo or a water molecule coordinated to the W center. Considering the nature of the oxo-ligand attached to the W, we have computed two pathways (as suggested by Seiffert et al.[100]): an electrophilic pathway, where the coordinated water molecule would act as an electrophile and a nucleophilic pathway, where the hydroxide would act as a nucleophile.

In the electrophilic pathway, Asp_{13} was considered to be protonated. The W-bound water molecule (Wat_{1862}) is activated by the nearby protonated Asp_{13} residue and a second water molecule (Wat_{1424}). The transition state involves the electrophilic attack of activated Wat_{1862} molecule on the triple bond of acetylene with the simultaneous transfer of protons among

Asp_{13}, Wat_{1862}, Wat_{1424} and acetylene. The proton from the Asp_{13} residue (-COOH) is transferred to the Wat_{1862} molecule and one proton of the Wat_{1862} molecule is transferred to the alpha carbon atom (Cα or C_1) of acetylene. From the Wat_{1424}, one proton is transferred to Asp_{13} while its electron donating part (-OH) is transferred to the second carbon atom (Cβ or C_2) of acetylene. This proton shuttle results in the formation of vinyl alcohol which subsequently may tautomerize to aldehyde (Scheme 4.7A).

In the nucleophilic pathway, Asp_{13} was considered to be in the anionic form. The W center, which acts as a Lewis acid activates water molecule Wat_{1862}, generates a W-bound hydroxide and protonated Asp_{13}. The transition state involves the nucleophilic attack of this W-bound hydroxide at the alpha carbon atom (Cα or C_1) of acetylene together with the simultaneous transfer of a proton from the Asp_{13} to the second acetylene carbon atom (Cβ or C_2) resulting in the formation of vinyl alcohol which subsequently may tautomerize to aldehyde (Scheme 4.7B).

The density functional theory (DFT) computations were, first, performed on the small model complexes derived from the protein X-ray crystal structure of AH.[100] For the small model complexes W metal center coordinated with two molybdopterin ligands (MGD), a metal bound water (Wat_{1862}) molecule, a cysteinate (Cys_{141}) ligand and an additional aspartate (Asp_{13}) residue was considered. The water molecule (Wat_{1424}), present near Asp_{13} and water molecule Wat_{1862}, were also considered in case of the electrophilic reaction mechanism (Scheme 4.7 A). The computational results for the small model complexes show that the nucleophilic pathway is energetically more favorable than the electrophilc pathway. The energy barrier for the electrophilic pathway transition state **SE-TS** (28.5 kcal/mol in the continuum) is higher than the energy barrier for the nucleophilic pathway transition state **SN-TS** (17.0 kcal/mol). The vinyl alcohol product **SE-EP1** formation is ~7 kcal/mol lower in energy than the **SN-EP1**. The final step may involve the tautomerization of vinyl alcohol intermediate to the acetaldehyde. The formation of acetaldehyde product **SN-EP2** is ~4 kcal/mol lower in energy than the formation of **SE-EP2** (Table 4.3).

The energy barrier for the tautomerization of vinyl alcohol (**VA**) to acetaldehyde (**AA**) was computed (without educt complex) without the assistance of a water molecule and with the assistance of one or two water molecules (Table 4.12 and Scheme 4.8). The computed energy barrier for the intramolecular conversion of **VA** to **AA** was 58.8 kcal/mol in the polarizable continuum. This energy barrier decreases to 30.7 kcal/mol when the reaction is catalysed by a water molecule. The same effect was explained by the Suenobou et al.[173] where the energy

barrier (in the gas phase) decreases from 55.8 kcal/mol to 29.6 kcal/mol when the reaction is catalysed by a water molecule. As the energy barrier drops dramatically with the assistance of two water molecules as suggested by Lledós et al.,[174] we then computed the energy barrier of 20.7 kcal/mol in the continuum for the tautomerization of **3A-VA** to **3A-AA** in the presence of two water molecules (Table 4. 12 and Scheme 4.8).

The tautomerization of **VA** to **AA** is then computed in the educt complex, **WN**, which was generated by the introduction of two water molecules in the optimized small model **SN-EP1** complex. The computed energy barrier for this conversion of **VA** to **AA** in **WN-TS** is 18.9 kcal/mol in the continuum (Table 4.12). Now, when we compare this energy barrier of **WN-TS** with the energy barrier for alcohol formation in the electrophilic (**SE-TS** = 28.5 kcal/mol) and nucleophilic (**SN-TS** = 17.0 kcal/mol) pathways, the tautomerization of **VA** to **AA** seems to be the rate limiting step in the nucleophilic pathway.

The large model complexes were then analyzed to identify the most probable reaction mechanism. In the large model complexes some surrounding amino acid residues, Trp_{179}, Trp_{293} and Trp_{472}, which may take part in the reaction were also considered. The computational results for the large model complexes also favors the nucleophilic pathway for the formation of vinyl alcohol as the energy barrier for **LN-TS** is ~20 kcal/mol lower than the energy barrier for **LE-TS** (Table 4.6). The formation of vinyl alcohol complexes **LE-EP1** and **LN-EP1** are exothermic for both pathways; however, **LN-EP1** is ~4 kcal/mol lower in energy than **LN-EP1**. Although the relative energies for the vinyl alcohol formation were comparable with the results from the small model complexes, the energy barriers are considerably higher for **LN-TS** and **LE-TS** to continue the mechanism (see Table 4.3 and 4.6).

Now, according to the protein X-ray crystal structure of AH, there are at least 16 well defined water molecules adjacent to the active site. These water molecules may help in the hydration of acetylene. So, in the large model complex we included four water molecules (Wat_{1209}, Wat_{1212}, Wat_{1424}, and Wat_{1432}) which are in the proximity of W metal center and connected together through the hydrogen bonding (Fig 4.7). To keep these water molecules at their location, some surrounding residues, Ala_{137}, Met_{138}, Ile_{113}, Ile_{142}, and Phe_{611}, were also included. The computational results for the water molecules containing large model complexes also favor the nucleophilic pathway for vinyl alcohol formation. The energy barrier for the nucleophilic pathway transition state complex **XN-TS** (14.4 kcal/mol) is ~9 kcal/mol lower than the energy barrier for the electrophilic pathway transition state complex **XE-TS** (23.1 kcal/mol). In the small model and the large model computational results, the

vinyl alcohol containing electrophilic pathway **EP1** complexes (**SE-EP1** and **LE-EP1**) were lower in energy than the nucleophilic pathway **EP1** complexes (**SN-EP1** and **LN-EP1**). However, in the water molecules containing large model complexes, the energy for the formation of vinyl alcohol product **XN-EP1** is ~8 kcal/mol lower than the **XE-EP1**. The relative energies for the acetaldehyde product complexes **XN-EP2** and **XE-EP2** are also exothermic but the **XN-EP2** is ~16 kcal/mol lower in energy than the **XE-EP2**. In the nucleophilic pathway, the W-center is regenerated by the replacement of acetaldehyde with one of the surrounding water molecule. The reaction energy for this step (**XN-EP3**) is also exothermic, -7.2 kcal/mol in the polarizable continuum and -1.1 kcal/mol in the gas phase, relative to the **XN-EP2** complex (Table 4.10).

In 1997, Rosner et al.[179] purified a molybdenum dependent active acetylene hydratase enzyme *P.acetylenicus* cells which had been grown in the absence of tungsten. The molecular mass and the first 10 amino acids of the N-terminus of Mo-dependent AH was identical to the W-dependent AH enzyme. Now, to find the influence of metal on the acetylene hydration we have computed the same, water molecules containing, large active site model complexes (nucleophilic reaction pathway) only differing in the metal (W is replaced by Mo) at the active site center. The computational results shows that the energy barrier for **Mo-TS** (13.3 kcal/mol) is similar to the W containing transition state model complex **XN-TS** (14.4 kcal/mol) (Table 4.10). The relative energies for the formation of vinyl alcohol (**Mo-EP1**= -55.5 kcal/mol, **XN-EP1** = -51.4 kcal/mol in the continuum) and acetaldehyde (**Mo-EP2**= -61.6 kcal/mol, **XN-EP2** = -58.6 kcal/mol) are also similar (Table 4.10). So, no decisive influence of the metal on the hydration of acetylene was observed when W is replaced with Mo.

Based on the computational results we here present the most likely mechanism for the hydration of acetylene by the acetylene hydratase (AH) enzyme which is essentially the nucleophilic reaction pathway proposed by Seiffert et al.[100] DFT studies were carried out on the active site model complexes derived from the protein X-ray crystal structure of AH (PDB-ID: 2E7Z)[100] relevant along this mechanistic pathway. In this mechanism, the water (Wat_{1424}) molecule is coordinated to the W center and Asp_{13} is assumed to be in anionic form. The role of W is to activate the Wat_{1424} molecule making it a Lewis acid. This activated Wat_{1424} then donates one of its proton to the anionic Asp_{13} forming the W-bound hydroxide and protonated Asp_{13}. The W-bound hydroxide then attacks the Cα or C_1 atom of acetylene together with the transfer of proton from the Asp_{13} to its Cβ or C_2 atom, resulting in the formation of a vinyl

alcohol intermediate complex. The energy barrier for this step is 14.4 kcal/mol in the polarizable continuum. The final step corresponds to the tautomerization of vinyl alcohol intermediate to the acetaldehyde via intermolecular assistance of two water molecules. The energy barrier for this step is 18.9 kcal/mol in the polarizable continuum (calculated only for the small model complexes, **SN**). This step should be the rate-limiting step in the nucleophilic pathway (see Table 4.10 and 4.12). However, the energy associated with the rate limiting step is higher in the acetylene hydration reaction mechanisms proposed in the literature: the mechanism proposed by Vincent et al.[171] has a maximum energy barrier as high as 34.0 kcal/mol while the mechanism proposed by the Himo et al.[172] has an energy barrier of 23.9 kcal/mol. The mechanism presented here is more favorable by 5 kcal/mol.

Selenate Reductase

1. Introduction

The chalcogen elements (i.e., elements of group 16 of the periodic table) oxygen (O), sulfur (S) and selenium (Se) fulfill a wide range of essential biological functions. All three elements are constituents of functional groups in biomolecules that participate in redox reactions.[180,181] There are close similarities but also striking differences between sulfur and selenium in terms of their chemistry and biochemistry. Both S and Se are present in proteins as constituents of the natural amino acids cysteine, methionine, selenocysteine and selenomethionine[182] and also occur as substrates e.g., for the sulfite oxidase and selenate reductase enzymes, respectively. These are mononuclear molybdenum enzymes. All mononuclear molybdoenzymes contain a molybdenum cofactor, Moco, which consists of either one or two organic moieties of metalopterin (MPT) or some of its nucleotide variants, coordinated to Mo through an enedithiolate motif. Based on the active site composition, i.e., the number of MPT and type of additional ligands, these enzymes are generally grouped into three families (Fig. 1.2); the xanthine oxidase (XO) family,[9,40-42,47] the sulfite oxidase (SO) family[9,53-55] and the dimethylsulfoxide reductase (DMSOR) family.[9,59-61]

Selenate reductase (SeR) from *Thauera selenatis*[149,183] is a soluble periplasmic molybdoenzyme that catalyzes the two electron reduction of selenate (SeO_4^{2-}) to selenite (SeO_3^{2-}).

$$SeO_4^{2-} + 2H^+ + 2e^- \rightleftharpoons SeO_3^{2-} + H_2O \quad (5.1)$$

This reduction is associated with the respiratory electron transfer chains that generates an electro-chemical gradient across the cytoplasmic membrane of bacteria.[184,149] Selenate is the oxidized form of selenium which is highly soluble and can present significant hazards to health and the environment. Selenate detoxification can be done by the reduction of selenate to selenite catalyzed by the microbial reductase. The microbes that can reduce selenate are not restricted to any particular group/subgroup of prokaryotes and examples are found throughout the bacterial domain.[185]

Physiologically, SeR is the terminal reductase supporting anaerobic growth on acetate in the presence of selenate. It shows substrate specificity and does not reduce nitrate, arsenate or sulfate, but does reduce chlorate.[186] It is the only dissimilatory selenate reductase known and is of considerable interest as a novel member of the molybdenum enzymes. SeR contains an

active site that is characteristic of the prokayrotic oxotransferase (DMSO reductase) family of molybdenum enzymes.[187] Periplasmic SeR from *Thauera selenatis* is a heterotrimeric enzyme. It comprises three subunits, SeR-A, SeR-B and SeR-C. (Fig.5.1) SeR-A is the catalytic subunit containing the molybdenum active site coordinated with the two molybdopterin guanine dinucleotide (*bis*-MGD) ligands and a hydroxide group in the reduced form. SeR-B contains a number of cysteine rich motifs that coordinate a [3Fe-4S] and three [4Fe-4S] iron sulfur clusters. SeR-C contains *b*-type cytochrome that is rarely found in periplasmic proteins.[187,187,188,189,190]

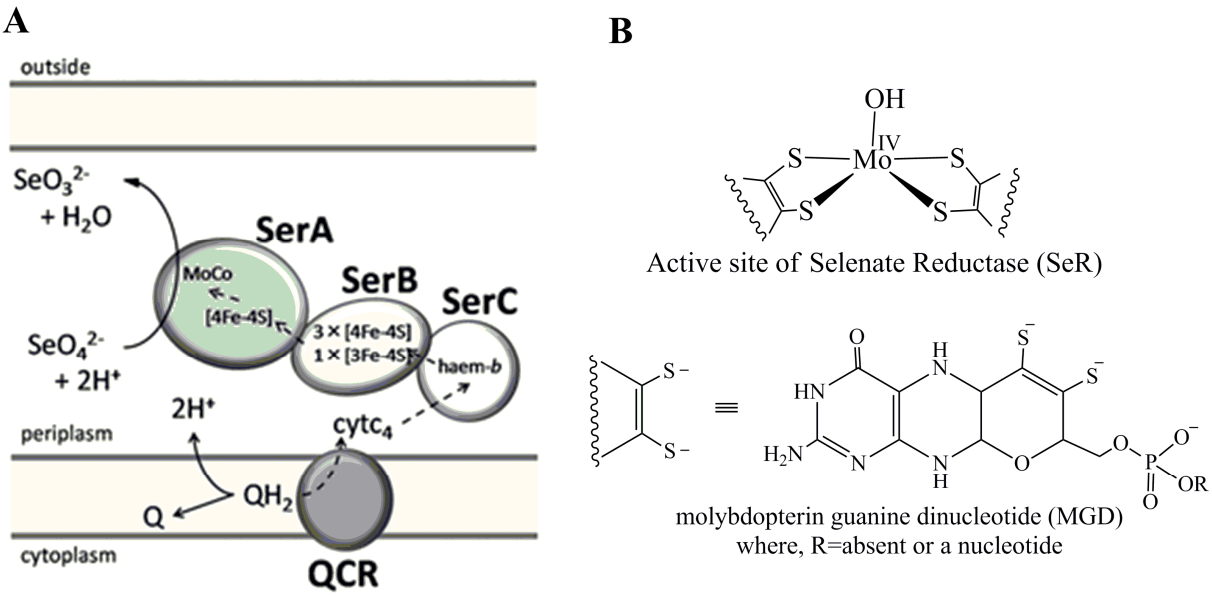

Fig. 5.1: (**A**) Schematic representations of selenate reduction SerABC from *Thauera selenatis*.[186] SerABC receives electrons from cytochrome c_4, which is reduced by quinol-cytochrome *c* (QCR) oxidoreductase coupled with quinol oxidation. The dashed arrows represent electron flow; Q, quinones; QH_2, quinols; $cytc_4$, cytochrome c_4; [4Fe-4S], iron-sulfur cluster; [3Fe-4S], iron-sulfur cluster; MoCo, molybdenum cofactor; SeO_4^{2-}, selenate; SeO_3^{2-}, selenite.[191] (**B**) Active site of selenate reductase depicted from the X-ray absorption spectroscopy.[187]

The SeR enzyme is stable and active upon incubation at temperatures upto 60˚C with an optimum activity recorded at 65˚C. The SeR-C component appears to be least stable once above 60˚C and perhaps the loss of this contributes to the overall instability of the SeR complex.[186,192] The location as a soluble protein in the periplasm and thermostability of SeR is consistent with the other molybdoenzymes from mesophilic bacteria e.g. TMAO reductase from *E.coli.*[102]

Analogue reaction systems for the reduction of selenate to selenite using *bis*(dithiolene) complexes of Mo^{IV} and W^{IV} demonstrate that chemically both metals can function as a catalyst for the selenate reduction. However, to date no evidence has been presented regarding the effect of tungsten on selenate reduction in an enzyme system.[184] Recently it has been observed that *T. selenatis* can grow readily on a tungsten rich medium and SeR isolated under such conditions show 20-fold reduction in the selenate reductase activity, and 23-fold increased affinity for selenate. The tungsten substitution may have enhanced the bond strengths of the W-substrate complexes leading to the observed higher substrate affinity which in turns makes the complex kinetically slower that the equivalent Mo-substrate complexes, when measured at the mesophilic range of temperatures.[191]

Sulfite oxidase (SO) is the name giving member of the sulfite oxidase family of mononuclear molybdenum enzymes. It catalyzes the oxidation of sulfite to sulfate through an oxygen atom transfer (OAT) reaction.[31]

$$SO_3^{2-} + H_2O \rightleftharpoons SO_4^{2-} + 2H^+ + 2e^- \quad (5.2)$$

In the active site of reduced SO the central Mo atom is five-fold coordinated in a square pyramidal fashion by one metalopterin (MPT) ligand, one terminal oxygen atom, one sulfur atom of cysteine and one water or hydroxide. In the oxidized form of the enzyme the water/hydroxyl is probably replaced by a second oxo group. The MPT forms a tricylic ring system with a pyran ring fused to the pyrazine ring of the pterin and is not conjugated by an additional nucleotide (Fig. 5.2).[31] The cysteine and dithiolene moieties have been implicated in the tuning of the flexibility of the equatorial oxo group towards the OAT reaction.

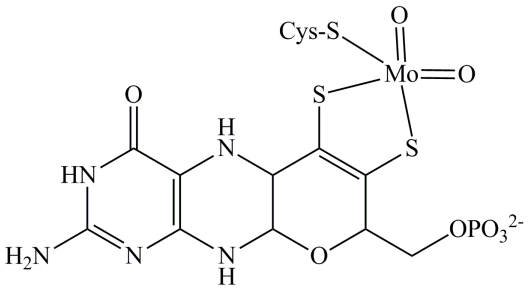

Fig. 5.2: Schematic representation of the active site of oxidized sulfite oxidase (SO)[193]

The mode of sulfite attack to the Mo center could be oxoanionic as suggested or sulfur lone pair attack.[194] Detailed theoretical studies were carried out by Sarkar et al,[195] using DFT calculations. The author investigated the reaction of the substrate (HSO_3^-) with the computational model complex $[Mo^{VI}O_2(mpt)(Cys)]^-$ (**1**) of Moco, derived from the X-ray

crystal structure of native SO,[31] and with the experimental model complex[196] $[Mo^{VI}O_2(mnt)_2]^{2-}$ (**2**) (Scheme 5.1). The calculations show that the initial step in the oxygen atom transfer reaction of **1** and **2** with HSO_3^{1-} is the oxoanionic binding of the substrate to the Mo^{VI} resulting in the formation of an intermediate complex (Scheme 5.1). This intermediate complex participates in product formation through a six-membered $\{MoO_{eq}SOHO_{ax}\}$ transition state involving breaking of the Mo-O_{eq} bond and formation of the $S_{sulfite}$-O_{eq} bond (Scheme 5.1).

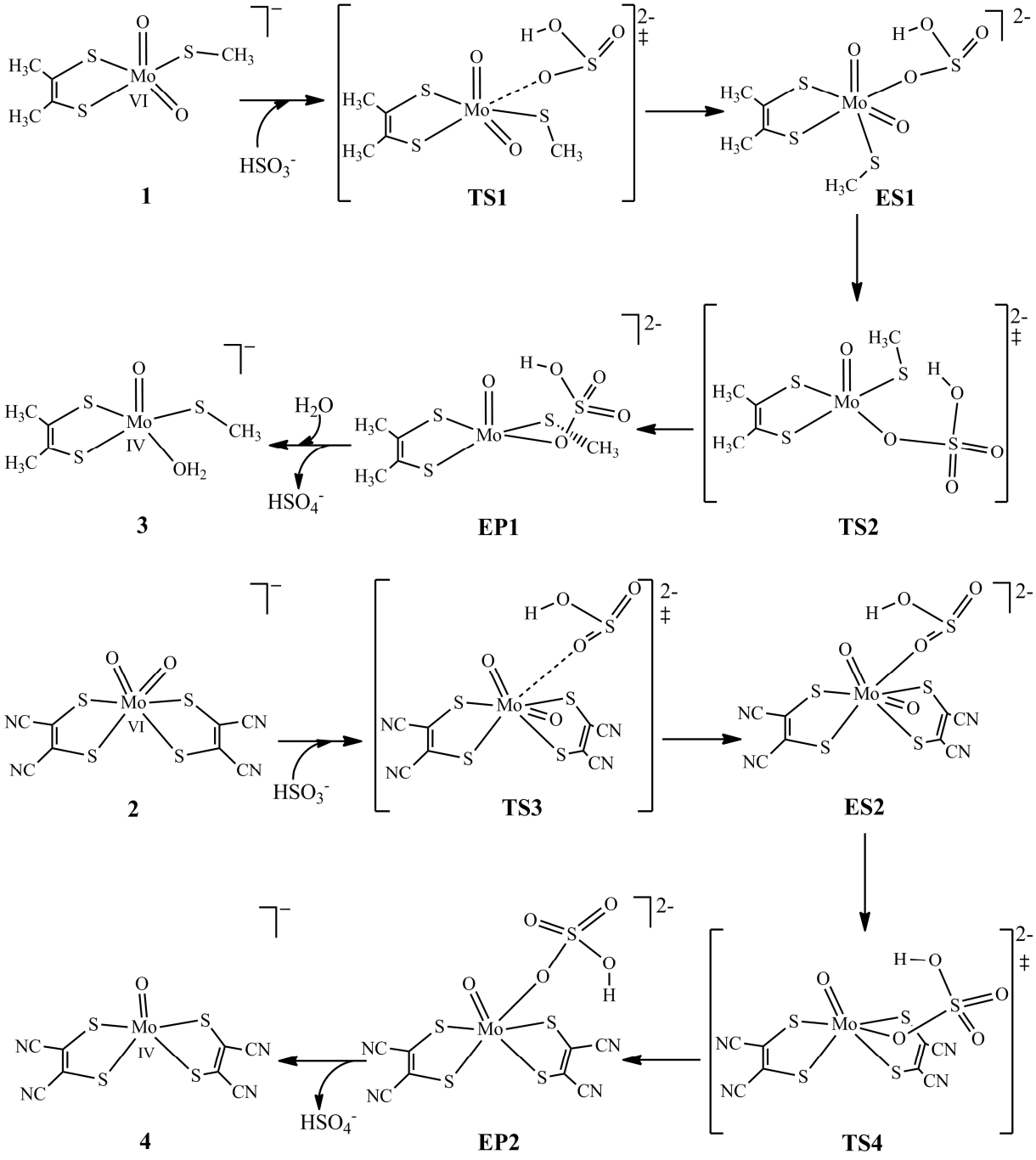

Scheme 5.1: Reaction scheme of sulfite oxidation to sulfate suggested by Sarkar et al.[195]

Nitrate reductases (NRs) play key roles in the first step of biological nitrogen cycles[197,198,199] i.e., assimilatory ammonification (to incorporate nitrogen into biomolecules), denitrification (to generate energy for cellular function) and dissimilatory ammonification (to dissipate extra energy by respiration). NRs have been classified into three groups, assimilatory nitrate reductases (Nas), respiratory nitrate reductases (Nar) and periplasmic nitrate reductases (Nap) (Fig. 5.3). Nas belongs to the sulfite oxidase family and is located in the cytoplasm.[200] Dissimilatory nitrate reductases, Nar and Nap belong to the DMSO reductase family of mononuclear MPT containing molybdo-enzymes. They are linked to respiratory electron transport systems and are located in the membrane and periplasm, respectively. Although Nas, Nap and Nar are different at their active site composition (Fig. 5.3) and belong to two different families of mononuclear molybdoenzymes, they all catalyze the same reaction; reduction of nitrate to nitrite.

$$NO_3^- + 2H^+ + 2e^- \rightleftharpoons NO_2^- + H_2O \quad (5.3)$$

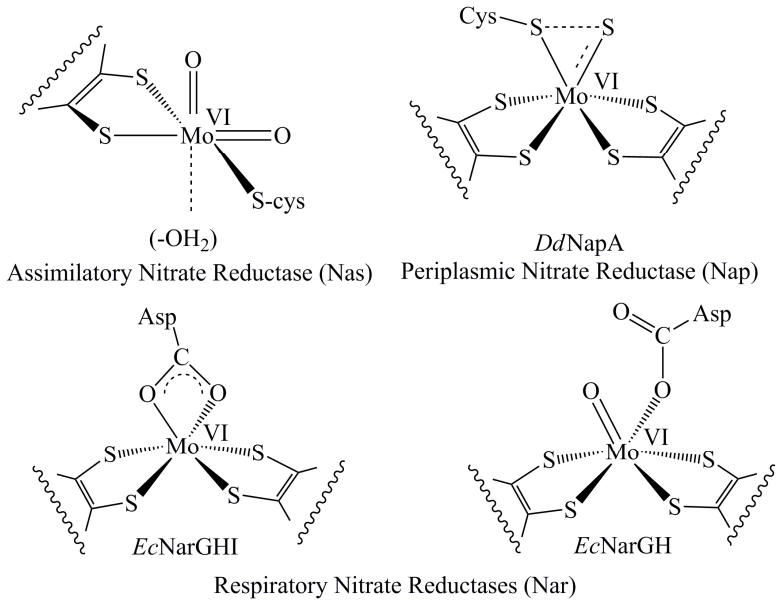

Fig. 5.3: Active site composition of nitrate reductases.

2. Project: I

When we compare the active site composition of SO, SeR and NRs we find that SO has one MPT ligand and it oxidizes sulfite to sulfate, SeR has two MPT ligands and it reduces selenate to selenite, while NRs reduce nitrate to nitrite and is able to do this with either one or with two MPT's coordinated to Mo. Now, the question arises whether the active site itself is special in some way for the oxidation/reduction process or it is the substrates or the different active sites behave the same way and it is the role of the protein to make it specific.

To answer these questions, we have performed the DFT calculations for the reaction of HSO_3^- and $HSeO_3^-$ with the computational model complex, $[Mo^{VI}O_2(S_2C_2Me_2)SMe]^-$ (**A**) of Moco, derived from the X-ray crystal structure of native SO,[31] and with the experimental model complex[196] $[Mo^{VI}O_2(mnt)_2]^{2-}$ (**B**) through oxoanionic binding of substrate at the Mo center.

2.1. Computational Details

All calculations were performed with the Gaussian 03[175] program package using B3LYP[123] hybrid functional of density functional theory (DFT). For the geometry optimizations, the LANL2DZ basis set[124,125,126,127] augmented by polarization functions on all atoms except Mo and H (ζ =0.600, 1.154, 0.864, 0.421, 0.338 for C, O, N, S and Se, respectively)[128] was employed. The optimized minima and transition-state structures were characterized by frequency calculations with the same method and basis set to verify that all minima have no imaginary frequency and each transition state has exactly one. Single point energies were computed with the B3LYP functional and the Stuttgart-Dresden effective core potential basis set (SDD)[129,130] augmented by polarization functions for all atoms except Mo, and H (ζ =0.600, 1.154, 0.864, 0.421, 0.338 for C, O, N, S and Se, respectively).[128] The self-consistent reaction field (SCRF) computations were performed on the optimized geometries by a conductor like polarizable continuum method (CPCM)[131] with a dielectric constant of 4 and solvent radius of 1.4Å.

2.2. Active Site Models

Model complexes studied here were the same used by Sarkar et al.[195] where the initial active site geometry for $[Mo^{VI}O_2(S_2C_2Me_2)SMe]^-$ (**A**) was derived from the protein X-ray crystal structure of the native SO enzyme[31] while the initial geometry of $[Mo^{VI}O_2(mnt)_2]^{2-}$ (**B**) was obtained from the crystal structure (Fig. 5.4) reported for this compound.[196] The complex **B** is similar to the active site composition of SeR[190,191] as both contain two MPT ligands.

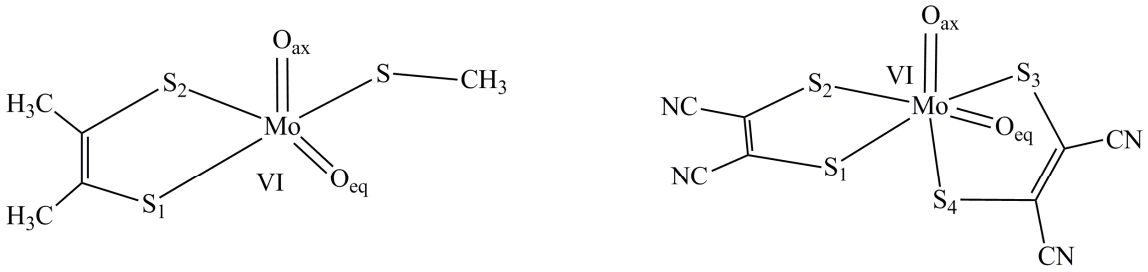

A = $[Mo^{VI}O_2(S_2C_2Me_2)SMe]^-$ **B** = $[Mo^{VI}O_2(mnt)_2]^{2-}$

Fig. 5.4: Active site composition of initial active site model geometries **A** and **B**.

2.3. Results

- **Molybdenum (VI) dithiolene complex $[Mo^{VI}O_2(S_2C_2Me_2)SMe]^-$ with $HSeO_3^-$ A1:**
  - *Optimized educt* $[Mo^{VI}O_2(S_2C_2Me_2)SMe]^-$ *complex* **A1-E**:

The molybdenum dithiolene complex **A1-E**, derived from the protein X-ray crystal structure of the native SO enzyme,[31] was geometry optimized where the oxidation state of the molybdenum is VI and overall charge on the complex is -1. The optimized data shows that the Mo-O_{ax} and Mo-O_{eq} bond lengths are 1.724 Å and 1.736 Å, respectively. The dithiolene Mo-S bond distances are ~2.510 Å and the Mo-S_{CH3} bond distance is 2.452 Å (Table 5.1).

  - *Optimized transition state complex for educt-substrate complex formation* **A1-TS1**:

Oxygen atom transfer (OAT), from square pyramidal complex $[Mo^{VI}O_2(S_2C_2Me_2)SMe]^{1-}$ (**A1-E**) to $HSeO_3^-$ is initiated by a transition state $[Mo^{VI}O_2(S_2C_2Me_2)SMe(HSeO_3)]^{2-}$ (**A1-TS1**). The energy barrier for **A1-TS1** is 10.0 kcal/mol in the polarizable continuum (47.3 kcal/mol in the gas phase) relative to the separate substrate, $HSeO_3^-$, and educt (**A1-E)** complex (Table 5.3). One imaginary frequency of 49i cm^{-1} corresponds predominantly to the stretching vibration mode of Mo-O_{Se}.

The optimized **A1-TS1** has a distorted square pyramidal geometry. The optimized data shows a slight decrease in the Mo-O_{ax} bond distance from 1.724 Å to 1.719 Å when comparison is made with the optimized **A1-E** geometry. The dithiolene Mo-S bond distances are increased from ~2.510 Å to ~2.543 Å. Because of the oxoanionic approach of selenite, the -SCH_3 group moves from an equatorial to an axial position and the Mo-S_{CH3} bond distance is increased from 2.452 Å to 2.474 Å. At this stage, the $HSeO_3^-$ is loosely bound to the Mo center. The distance between Mo-O_{Se} is 3.159Å (Table 5.1).

  - *Optimized educt-substrate intermediate complex* **A1-ES**:

The computed reaction energy for the formation of intermediate complex $[Mo^{VI}O_2(S_2C_2Me_2)SMe(HSeO_3)]^{2-}$ (**A1-ES**) is endothermic, 9.7 kcal/mol in the polarizable continuum (40.0 kcal/mol) relative to the separate substrate, $HSeO_3^-$, and educt (**A1-E**) complex (Table 5.3). Geometry optimization of **A1-ES** shows a decrease in the Mo-O_{Se} distance from 3.159 Å to 2.231 Å while the dithiolene Mo-S bond distances are further increased from ~2.543 Å to 2.600 Å. The Mo-O_{ax} bond distance is also increased from 1.719 Å to 1.754 Å whereas the Mo-O_{eq} bond length remains unchanged. The Mo-S_{CH3} bond

distance is increased from 2.474 Å to 2.570 Å as compared to the optimized **A1-TS1** geometry. The O_{eq}-Se distance is 3.372 Å (Table 5.1).

- *Optimized transition state complex for oxygen atom transfer* (OAT) **A1-TS2**:

Oxygen atom transfer occurs through a transition state **A1-TS2** of distorted square pyramidal geometry with a relative energy of 37.4 kcal/mol in the polarizable continuum (68.0 kcal/mol in the gas phase) (Table 5.3). Geometry optimization of **A1-TS2** shows that the Mo-O_{eq} bond length is elongated from 1.738 Å to 1.945 Å and the O_{eq}-Se distance is decreased from 3.372 Å to 1.969 Å while the Mo-O_{Se} distance is increased from 2.231 Å to 4.675 Å when comparison is made with the optimized **A1-ES** geometry. The Mo-O_{ax} bond distance is decreased from 1.754 Å to 1.721 Å. At this stage, the dithiolene Mo-S bond distances, elongated in the previous step, are decreased from ~2.600 to ~2.476 Å. The -SCH_3 group is moved back to an equatorial position (Mo-S_{CH3} = 2.439 Å). An imaginary frequency of 339i cm^{-1} corresponds to the stretching vibration modes of Mo-O_{eq} and O_{eq}-Se ($HSeO_3^-$) and confirms the saddle point character between the selenite and selenate complexes (Table 5.1).

- *Optimized product bound complex* **A1-EP**:

To complete OAT reaction, a product bound complex $[Mo^{IV}O(S_2C_2Me_2)SMe(HSeO_4)]^{2-}$ (**A1-EP**) is formed as a result of breaking of Mo-O_{eq} bond and formation of O_{eq}-Se bond in the optimized **A1-TS2** geometry. The computed reaction energy for the formation of **A1-EP** is endothermic, 35.9 kcal/mol and 62.8 kcal/mol are computed with and without a continuum model, respectively, relative to the separate substrate, $HSeO_3^-$ and educt (**A1-E**) complex (Table 5.3). The **A1-EP** is higher in energy than **A1-ES** by 27.7 kcal/mol in the continuum (22.8 kcal/mol in the gas phase). At this stage, the OAT reaction is complete and $HSeO_4^-$ is loosely bound to the Mo^{IV} centre via one oxo group in **A1-EP**.

The optimized data shows that the Mo-O_{eq} bond and Mo-O_{ax} bond distances are elongated from 1.945 Å to 2.296 Å and from 1.721 Å to 1.731 Å, respectively. The O_{eq}-Se ($HSeO_3^-$) bond length is decreased from 1.969 Å to 1.669 Å as compared to the optimized **A1-TS2** geometry. The dithiolene Mo-S bond distances are further decreased from ~2.476 Å to ~2.410 Å (Table 5.1).

- *Optimized reduced complexes* **A1-P** *and* **A1-P**:

Loss of the oxidized substrate $HSeO_4^-$ from **A1-EP** gives the reduced complex $[Mo^{IV}O(S_2C_2Me_2)SMe]^{1-}$ (**A1-P**) with tetrahedral geometry in an endothermic reaction, 34.7

kcal/mol in the continuum (33.8 kcal/mol in gas phase) relative to the separate substrate, $HSeO_3^-$ and educt (**A1-E**) complex (Table 5.3). Complex **A1-P** is slightly exothermic (-1.2 kcal/mol in the continuum) relative to the **A1-EP** complex. The optimized data shows the reduction in the Mo-O_{ax} bond length (from 1.731 Å to 1.713 Å) and in the Mo-S bond distances (from ~2.410 Å to ~2.350 Å) when comparison is made with the optimized **A1-EP** geometry. The Mo-S_{CH3} bond is also reduced from 2.434 Å to 2.421 Å when comparison is made with the optimized **A1-EP** geometry (Table 5.1).

Direct replacement of $HSeO_4^-$ in **A1-EP** by a water molecule leads to $[Mo^{IV}O(S_2C_2Me_2)SMe(H_2O)]^{1-}$, **A1-Pô** which has also square pyramidal geometry as **A1-EP**. This ligand exchange is computed to be endothermic by 28.7 kcal/mol (26.9 kcal/mol when no continuum model is applied) relative to the separate substrate, $HSeO_3^-$ and educt (**A1-E**) complex (Table 5.3). The optimized data shows a reduction in the Mo-O_{ax} bond length (from 1.731 Å to 1.713 Å) and in the Mo-S bond distances (from ~2.410 Å to ~2.391 Å) as compared to the optimized **A1-EP** geometry. The Mo-S_{CH3} bond is slightly elongated from 2.434 Å to 2.442 Å when comparison is made with the optimized **A1-EP** geometry (Table 5.1). The Mo-O_{H2O} bond length is 2.383 Å.

Table 5.1: Selected bond lengths [Å] of optimized stationary points along the reaction path for oxygen atom transfer from $[Mo^{VI}O_2(S_2C_2Me_2)SMe]^{1-}$ to $HSeO_3^-$.

	A1-E	**A1-TS1**	**A1-ES**	**A1-TS2**	**A1-EP**	**A1-P**	**A1-Pô**
Mo-O_{ax} (Ù)	1.724	1.719	1.754	1.721	1.731	1.713	1.713
Mo-O_{eq} (Ù)	1.736	1.736	1.738	1.945	2.296	-	-
Mo-O_{H2O} (Ù)	-	-	-	-	-	-	2.383
Mo-O_{Se} (Ù)	-	3.159	2.231	4.675	-	-	-
O_{eq}-Se (Ù)	-	-	3.372	1.969	1.669	-	-
Mo-S_1 (Ù)	2.562	2.605	2.700	2.484	2.410	2.350	2.375
Mo-S_2 (Ù)	2.457	2.481	2.499	2.468	2.409	2.350	2.406
Mo-S_{CH3} (Ù)	2.452	2.474	2.570	2.439	2.434	2.421	2.442

Where, **A1-E** = Mo-dithiolene educt complex, **A1-TS1** =transition state complex for educt-substrate complex formation, **A1-ES** = educt-substrate complex, **A1-TS2** = transition state complex for oxygen atom transfer, **A1-EP** = product bound complex, **A1-P** = reduced product complex without water molecule, **A1-Pô** = reduced product complex with water molecule.

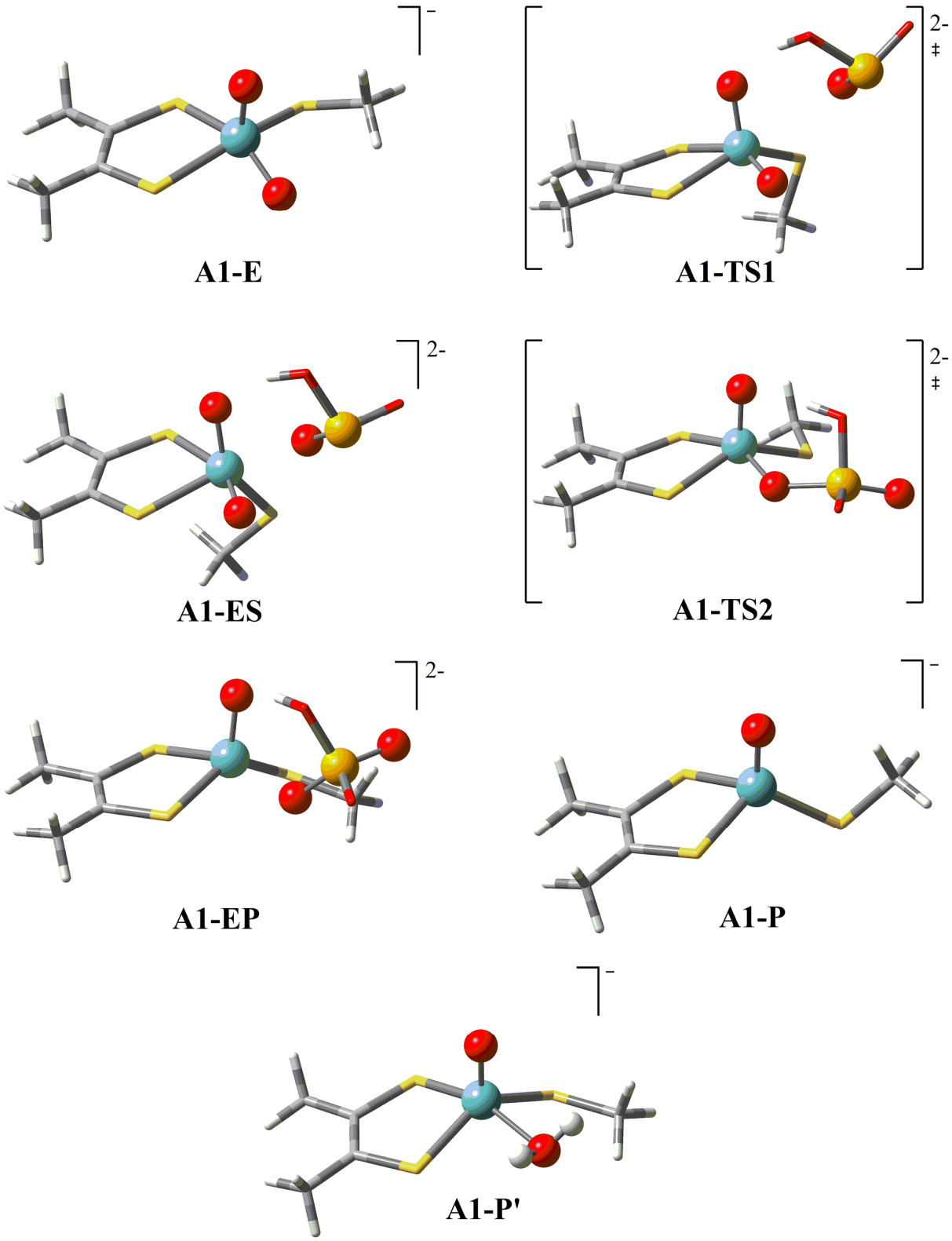

Fig. 5.5: Optimized geometries along the reaction pathway for the oxygen atom transfer from $[Mo^{VI}O_2(S_2C_2Me_2)SMe]^{1-}$ to $HSeO_3^-$.

- **Molybdenum (VI) dithiolene complex $[Mo^{VI}O_2(S_2C_2Me_2)SMe]^-$ with HSO_3^- A2:**
  - *Optimized educt* $[Mo^{VI}O_2(S_2C_2Me_2)SMe]^-$ *complex* **A2-E**:

The molybdenum dithiolene complex **A2-E** is identical to the optimized educt complex **A1-E**, derived from the protein X-ray crystal structure of the native SO enzyme[31] (Table 5.2).

  - *Optimized transition state complex for educt-substrate complex formation* **A2-TS1**:

Oxygen atom transfer (OAT), from square pyramidal $[Mo^{VI}O_2(S_2C_2Me_2)SMe]^{1-}$ (**A2-E**) to HSO_3^- is initiated by a transition state $[Mo^{VI}O_2(S_2C_2Me_2)SMe(HSO_3)]^{2-}$ (**A2-TS1**). The energy barrier for **A2-TS1** is 25.4 kcal/mol in the polarizable continuum (58.0 kcal/mol in the gas phase) relative to the separate substrate, HSO_3^-, and educt (**A2-E**) complex (Table 5.3). This energy barrier is 15.4 kcal/mol (in the continuum) higher than the energy barrier for the **A1-TS2**. One imaginary frequency of 55í cm^{-1} corresponds predominantly to the stretching vibration mode of $Mo\text{-}O_{Sulfite}$.

The optimized **A2-TS1** has a distorted square pyramidal geometry. The optimized data shows no considerable change in the $Mo\text{-}O_{ax}$ bond distance (from 1.724 Å to 1.721 Å) while the dithiolene Mo-S bond distances are increased from ~2.510 Å to ~5.548 Å when comparison is made with the optimized **A2-E** geometry. Like in **A1-TS1**, the $-SCH_3$ group moves from an equatorial to an axial position because of the oxoanionic approach of sulfite and the $Mo\text{-}S_{CH3}$ bond distance is increased from 2.452 Å to 2.482 Å. At this stage, the HSO_3^- is loosely bound to the Mo center. The distance between $Mo\text{-}O_{Sulfite}$ is 3.012Å (Table 5.2).

  - *Optimized educt-substrate intermediate complex* **A2-ES**:

The computed relative energy for the formation of intermediate complex $[Mo^{VI}O_2(S_2C_2Me_2)SMe(HSO_3)]^{2-}$ (**A2-ES**) is endothermic, 25.9 kcal/mol in the continuum (55.7 kcal/mol) (Table 5.3). The relative energy for the formation of **A2-ES** is similar to the relative energy for the **A2-TS1** (**A2-TS1** is 0.5 kcal/mol higher in energy). Geometry optimization of **A2-ES** shows a decrease in the $Mo\text{-}O_{Sulfite}$ distance from 3.012 Å to 2.244 Å while the dithiolene Mo-S bond distances are increased from ~2.548 Å to ~2.597 Å relative to the optimized **A2-TS1** geometry. The $Mo\text{-}O_{ax}$ bond distance is increased from 1.721 Å to 1.757 Å whereas the $Mo\text{-}O_{eq}$ bond length remains unchanged. The $Mo\text{-}S_{CH3}$ bond distance is increased from 2.482 Å to 2.577Å (Table 5.2). The $O_{eq}\text{-}S_{Sulfite}$ distance is 3.522 Å.

- *Optimized transition state complex for oxygen atom transfer* (OAT) **A2-TS2**:

The energy barrier for the formation of distorted square pyramidal transition state **A2-TS2** is 48.8 kcal/mol in the polarizable continuum (79.4 kcal/mol in the gas) relative to the separate substrate, HSO_3^- and educt (**A2-E**) complex (Table 5.3). Geometry optimization of **A2-TS2** shows that the Mo-O_{eq} bond length is elongated from 1.735 Å to 1.908 Å and the O_{eq}-$S_{Sulfite}$ distance is decreased from 3.552 Å to 1.979 Å whle the Mo-$O_{Sulfite}$ distance is increased from 2.244 Å to 4.494 Å as compared to the optimized **A2-ES** geometry. The Mo-O_{ax} bond distance is decreased from 1.757 Å to 1.722 Å. At this stage, the dithiolene Mo-S bond distances, elongated in the previous step, are decreased from ~2.597 to ~2.490 Å. The -SCH_3 group is moved back to an equatorial position (Mo-S_{CH3} = 2.448 Å) (Table 5.2). An imaginary frequency of 380í cm^{-1} corresponds to the stretching vibration modes of Mo-O_{eq} and O_{eq}-$S_{Sulfite}$ (HSO_3^-) and confirms the saddle point character between the sulfite and sulfate complexes.

- *Optimized product bound complex* **A2-EP**:

The computed relative energy for the formation of product bound complex $[Mo^{IV}O(S_2C_2Me_2)SMe(HSO_4)]^{2-}$ (**A2-EP**) is endothermic, 33.2 kcal/mol in the continuum (61.1 kcal/mol in the gas) (Table 5.3). The **A2-EP** is higher in energy than **A2-ES** by only 7.3 kcal/mol in the continuum (5.4 kcal/mol in the gas phase). At this stage, the OAT reaction is complete and HSO_4^- is loosely bound to a Mo^{IV} centre in **A2-EP**.

The optimized data shows that the Mo-O_{eq} bond and Mo-O_{ax} bond distances are elongated from 1.908 Å to 2.340 Å and from 1.722 Å to 1.728 Å, respectively when comparison is made with the optimized **A2-TS2** geometry. The O_{eq}-$S_{Sulfite}$ (HSO_3^-) bond distance is decreased from 1.979 Å to 1.542 Å. The dithiolene Mo-S bond distances are further decreased from ~2.491 Å to ~2.411 Å (Table 5.2).

- *Optimized reduced complexes* **A2-P** *and* **A2-P**ô:

Loss of the oxidized substrate $HSeO_4^-$ from **A2-EP** gives the reduced complex $[Mo^{IV}O(S_2C_2Me_2)SMe]^{1-}$ (**A2-P**) with tetrahedral geometry in an endothermic reaction, 30.5 kcal/mol in the continuum (31.0 kcal/mol in gas phase) relative to the separate substrate, HSO_3^-, and educt (**A2-E**) complex (Table 5.3). Complex **A2-P** is slightly exothermic (-2.7 kcal/mol in the continuum) relative to the **A2-EP** complex. The optimized data shows the reduction in the Mo-O_{ax} bond length (from 1.728 Å to 1.713 Å) and in the Mo-S bond

distances (from ~2.411 Å to ~2.350 Å). The Mo-S_{CH3} bond is also reduced from 2.436 Å to 2.421 Å when comparison is made with the optimized **A2-EP** geometry (Table 5.2).

Direct replacement of HSO_4^- in **A2-EP** by a water molecule leads to the formation of $[Mo^{IV}O(S_2C_2Me_2)SMe(H_2O)]^{1-}$, **A2-Pô** which has also square pyramidal geometry as **A2-EP**. This ligand exchange is computed to be endothermic by 24.4 kcal/mol in the polarizable continuum (24.2 kcal/mol in the gas phase) relative to the separate substrate, HSO_3^- and educt (**A2-E)** complex (Table 5.3). The optimized data shows the reduction in the Mo-O_{ax} bond distance (from 1.728 Å to 1.713 Å) and in the Mo-S bond distances (from ~2.411 Å to ~2.391 Å). The Mo-S_{CH3} bond is slightly elongated from 2.436 Å to 2.442 Å when comparison is made with the optimized **A2-EP** geometry (Table 5.2). The Mo-O_{H2O} bond length is 2.383 Å.

Table 5.2: Selected bond lengths [Å] of optimized geometries along the reaction pathway for oxygen atom transfer from $[Mo^{VI}O_2(S_2C_2Me_2)SMe]^{1-}$ to HSO_3^-.

	A2-E	**A2-TS1**	**A2-ES**	**A2-TS2**	**A2-EP**	**A2-P**	**A2-Pô**
Mo-O_{ax} (Ù)	1.724	1.721	1.757	1.722	1.728	1.713	1.713
Mo-O_{eq} (Ù)	1.736	1.736	1.735	1.908	2.340	-	-
Mo-O_{H2O} (Ù)	-	-	-	-	-	-	2.383
Mo-$O_{Sulfite}$ (Ù)	-	3.012	2.244	4.494	-	-	-
O_{eq}-$S_{Sulfite}$ (Ù)	-	-	3.522	1.979	1.542	-	-
Mo-S_1 (Ù)	2.562	2.615	2.702	2.503	2.411	2.350	2.375
Mo-S_2 (Ù)	2.457	2.480	2.491	2.478	2.410	2.350	2.406
Mo-S_{CH3} (Ù)	2.452	2.482	2.577	2.448	2.436	2.421	2.442

Where, **A2-E** = Mo-dithiolene educt complex, **A2-TS1** =transition state complex for educt-substrate complex formation, **A2-ES** = educt-substrate complex, **A2-TS2** = transition state complex for oxygen atom transfer, **A2-EP** = product bound complex, **A2-P** = reduced product complex without water molecule, **A2-Pô** = reduced product complex with water molecule.

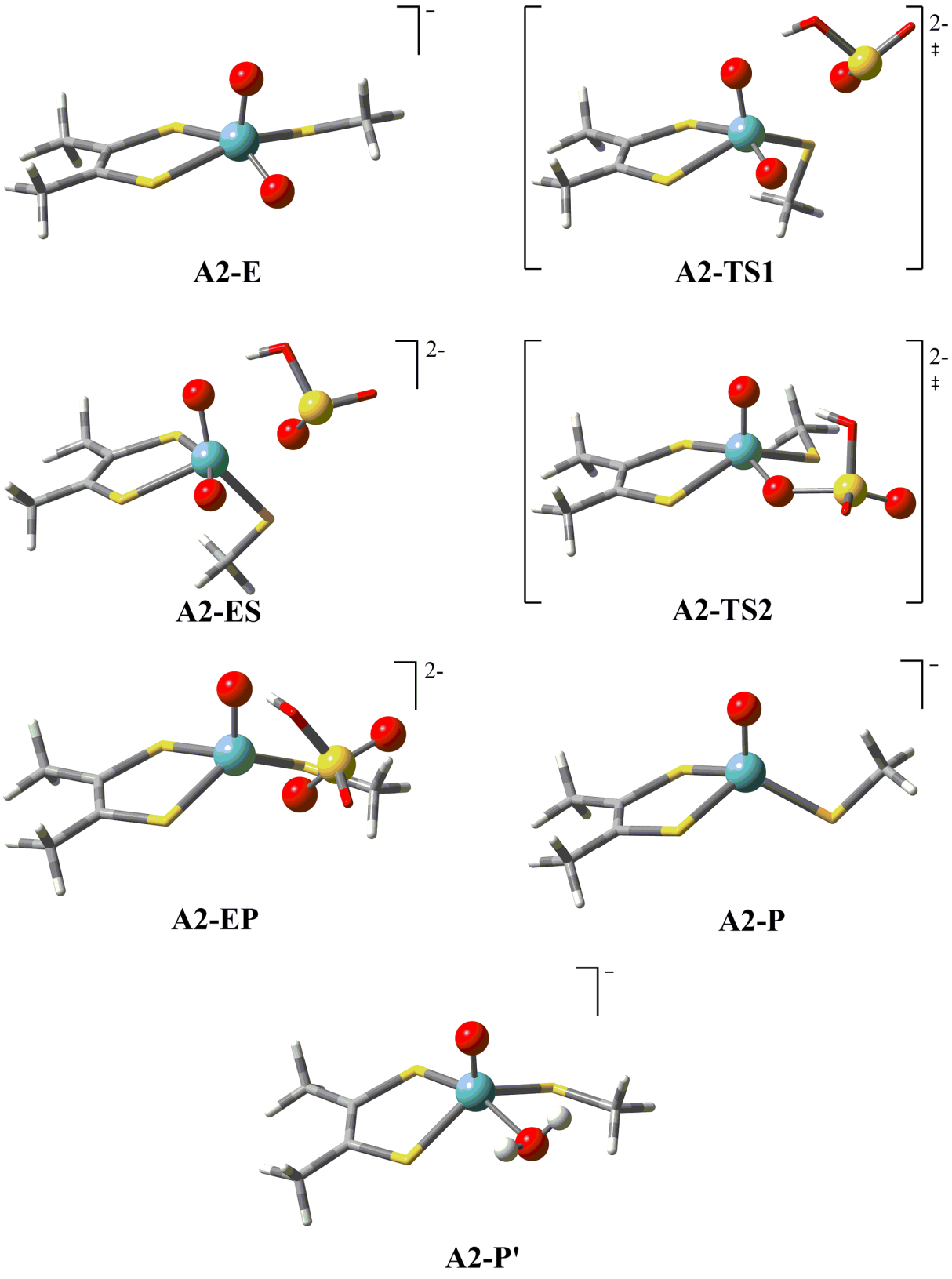

Fig. 5.6: Optimized geometries along the reaction pathway for oxygen atom transfer from $[Mo^{VI}O_2(S_2C_2Me_2)SMe]^{1-}$ to HSO_3^-.

Table 5.3: Relative energies (kcal/mol) computed for stationary points along the OAT from $[Mo^{VI}O_2(S_2C_2Me_2)SMe]^{1-}$ to $HSeO_3^-$ (**A1**) and HSO_3^- (**A2**)

	A1	**A2**	
E	0.0	0.0	//B3LYP[a] SDD[b] COSMO[c]
TS1	**43.3** **47.3** **10.0**	**58.5** **58.0** **25.4**	//B3LYP[a] SDD[b] COSMO[c]
ES	39.4 40.0 9.7	56.3 55.7 25.9	//B3LYP[a] SDD[b] COSMO[c]
TS2	**59.3** **68.0** **37.4**	**74.3** **79.4** **48.8**	//B3LYP[a] SDD[b] COSMO[c]
EP	47.7 62.8 35.9	51.0 61.1 33.2	//B3LYP[a] SDD[b] COSMO[c]
P	17.1 33.8 34.7	18.6 31.0 30.5	//B3LYP[a] SDD[b] COSMO[c]
Pô	11.8 26.9 28.7	13.3 24.2 24.4	//B3LYP[a] SDD[b] COSMO[c]

Where, **E** = educt complex, **TS1** =transition state complex for educt-substrate complex formation, **ES** = educt-substrate complex, **TS2** = transition state complex for oxygen atom transfer, **EP** = product bound complex, **P** = reduced product complex without water molecule, **Pô**= reduced product complex with water molecule.

A1 = Mo(VI)dithiolene complex $[Mo^{VI}O_2(S_2C_2Me_2)SMe]^-$ with $HSeO_3^-$,

A2 = Mo(VI)dithiolene complex $[Mo^{VI}O_2(S_2C_2Me_2)SMe]^-$ with HSO_3^-, a) B3LYP/Lanl2DZ(p), b) B3LYP/SDDp//B3LYP/Lanl2DZ(p), c) COSMO-B3LYP/SDDp//B3LYP/Lanl2DZ(p) (see Computational details).

- **Molybdenum (VI) maleonitriledithiolate (mnt) complex with $HSeO_3^-$ B1:**
  - *Optimized educt* $[Mo^{VI}O_2(mnt)_2]^{2-}$ *complex* **B1-E**:

The $[Mo^{VI}O_2(mnt)_2]^{2-}$ complex, **B1-E** (distorted octahedral geometry) obtained from the reported crystal structure,[196] was geometry optimized where the oxidation state of the molybdenum is VI and the overall charge on the complex is -2. The optimized data shows that both the Mo-O_{ax} and Mo-O_{eq} bonds are of equal length, i.e., 1.732 Å. The dithiolate Mo-S bond distances are ~2.622 Å where the dithiolate Mo-S_2 and Mo-S_4 bonds are trans to O_{eq} and trans to O_{ax}, respectively, and are of equal length (2.742 Å). The Mo-S_1 and Mo-S_3 bonds are also equal in length (2.502 Å) but shorter than the Mo-S_2 and Mo-S_4 bonds (Table 5.4).

  - *Optimized transition state complex for educt-substrate complex formation* **B1-TS1**:

Oxygen atom transfer (OAT), from distorted octahedral $[Mo^{VI}O_2(mnt)_2]^{2-}$ (**B1-E**) to $HSeO_3^-$ is initiated by a transition state $[Mo^{VI}O_2(mnt)_2(HSeO_3)]^{3-}$ (**B1-TS1**). The energy barrier for **B1-TS1** is 27.2 kcal/mol in the polarizable continuum (89.2 kcal/mol in the gas phase) relative to the separate substrate, $HSeO_3^-$, and educt (**B1-E**) complex (Table 5.6). An imaginary frequency of 59í cm^{-1} corresponds to the Mo-O_{Se} stretching mode.

The optimized data shows no considerable change in the Mo-O_{ax} and Mo-O_{eq} bond distances while the dithiolate Mo-S bond distances are increased from ~2.622 Å to ~2.687 Å when comparison is made with the optimized **B1-E** geometry. The two dithiolate Mo-S bonds (trans to oxo), Mo-S_2 and Mo-S_4 are elongated from 2.742 Å to 2.781 Å and from 2.742 Å to 2.898 Å, respectively. At this stage, the $HSeO_3^-$ is loosely bound to the Mo^{VI} center and the Mo-O_{Se} distance is 2.794 Å (Table 5.4).

  - *Optimized educt-substrate intermediate complex* **B1-ES**:

The computed relative energy for the formation of intermediate complex $[Mo^{VI}O_2(mnt)_2(HSeO_3)]^{3-}$ (**B1-ES**) is endothermic, 26.0 kcal/mol in the continuum (89.2 kcal/mol) (Table 5.6). Geometry optimization of **B1-ES** shows a decrease in the Mo-O_{Se} distance from 2.794 Å to 2.359 Å while the dithiolate Mo-S bond distances are increased from ~2.687 Å to 2.718 Å. The dithiolate Mo-S_2 bond is decreased from 2.781 Å to 2.771 Å while no considerable change is observed in the Mo-S_4 bond (from 2.898 Å to 2.901 Å). The Mo-O_{ax} and the Mo-O_{eq} bond distances are increased from 1.728 Å to 1.741 Å and from 1.728 Å to 1.734 Å, respectively, when comparison is made with the optimized **B1-TS1** geometry. The O_{eq}-Se distance is 3.147 Å (Table 5.4).

- *Optimized transition state complex for oxygen atom transfer* (OAT) **B1-TS2**:

The energy barrier for the transition state **B1-TS2** is endothermic, 53.8 kcal/mol in the polarizable continuum (114.0 kcal/mol in the gas phase) relative to the separate substrate, $HSeO_3^-$ and the educt (**A1-E**) complex (Table 5.6). An imaginary frequency of 386í cm^{-1} corresponds to the stretching vibration modes of Mo-O_{eq} and O_{eq}-Se ($HSeO_3^-$) and confirms the saddle point character between the selenite and selenate complexes.

Geometry optimization of **B1-TS2** shows an increase in the Mo-O_{eq} bond length from 1.734 Å to 1.947 Å and in the Mo-O_{Se} distance from 2.359 Å to 4.689 Å while the O_{eq}-Se distance is decreased from 3.147 Å to 1.965 Å. The Mo-O_{ax} (from 1.741 Å to 1.728 Å) and the dithiolate Mo-S (from ~2.718 Å to ~2.603 Å) bond distances are decreased as compared to the optimized **B1-ES** geometry (Table 5.4). The dithiolate Mo-S bonds (trans to oxo), Mo-S_2 and Mo-S_4 are decreased from 2.771 Å to 2.585 Å and from 2.901 Å to 2.779 Å, respectively

- *Optimized product bound complex* **B1-EP**:

To complete OAT reaction, a product bound intermediate complex $[Mo^{IV}O(mnt)_2(HSeO_4)]^{3-}$ (**B1-EP**) is formed as a result of breaking of the Mo-O_{eq} bond and formation of the O_{eq}-Se bond in the optimized **B1-TS2** geometry. **B1-EP** has a distorted octahedral geometry. The computed relative energy for the formation of **B1-EP** (distorted square pyramidal geometry) is endothermic, 35.9 kcal/mol in the polarizable continuum (62.8 kcal/mol in the gas) (Table 5.6). At this stage, the OAT reaction is complete and $HSeO_4^-$ is loosely bound to a Mo^{IV} centre.

The optimized data shows a decrease in the Mo-O_{ax} bond distance from 1.728 Å to 1.702 Å while the Mo-O_{eq} bond is elongated from 1.947 Å to 2.349 Å relative to the optimized **B1-TS2** geometry. The O_{eq}-Se ($HSeO_3^-$) bond distance is decreased from 1.965 Å to 1.663 Å. The dithiolate Mo-S bond distances are further decreased from ~2.603 Å to ~2.568 Å (Table 5.4). The dithiolate Mo-S_2 bond is decreased from 2.585 Å to 2.472 Å while the Mo-S_4 bond is increased from 2.779 Å to 2.799 Å.

- *Optimized reduced complex* **B1-P**:

The loss of the oxidized substrate, $HSeO_4^-$ gives the reduced complex $[Mo^{IV}O(mnt)_2]^{2-}$ (**B1-P**) with square pyramidal geometry in an endothermic reaction, 7.1 kcal/mol in the polarizable continuum (7.7 kcal/mol in gas phase) relative to the separate substrate, $HSeO_3^-$, and educt (**B1-E**) complex (Table 5.6). The optimized data shows no considerable change in the Mo-O_{ax}

bond distance (from 1.702 Å to 1.701 Å) while the dithiolate Mo-S bond distances are decreased from ~2.568 Å to ~2.458 Å where all Mo-S bonds are of equal length when comparison is made with the optimized **B1-EP** geometry (Table 5.4).

Table 5.4: Selected bond lengths [Å] of optimized geometries along the reaction pathway for oxygen atom transfer from $[Mo^{VI}O_2(mnt)_2]^{2-}$ to $HSeO_3^-$.

	B1-E	**B1-TS1**	**B1-ES**	**B1-TS2**	**B1-EP**	**B1-P**
Mo-O_{ax} (Å)	1.732	1.728	1.741	1.728	1.702	1.701
Mo-O_{eq} (Å)	1.732	1.728	1.734	1.947	2.349	-
Mo-O_{Se} (Å)	-	2.794	2.359	4.689	-	-
O_{eq}-Se (Å)	-	-	3.147	1.965	1.663	-
Mo-S_1 (Å)	2.502	2.561	2.638	2.482	2.447	2.458
Mo-S_2 (Å)	2.742	2.781	2.771	2.585	2.472	2.458
Mo-S_3 (Å)	2.502	2.508	2.561	2.565	2.554	2.458
Mo-S_a (Å)	2.742	2.898	2.901	2.779	2.799	2.458

Where, **B1-E** = Mo-mnt educt complex, **B1-TS1** =transition state complex for educt-substrate complex formation, **B1-ES** = educt-substrate complex, **B1-TS2** = transition state complex for oxygen atom transfer, **B1-EP** = product bound complex, **B1-P** = reduced product complex.

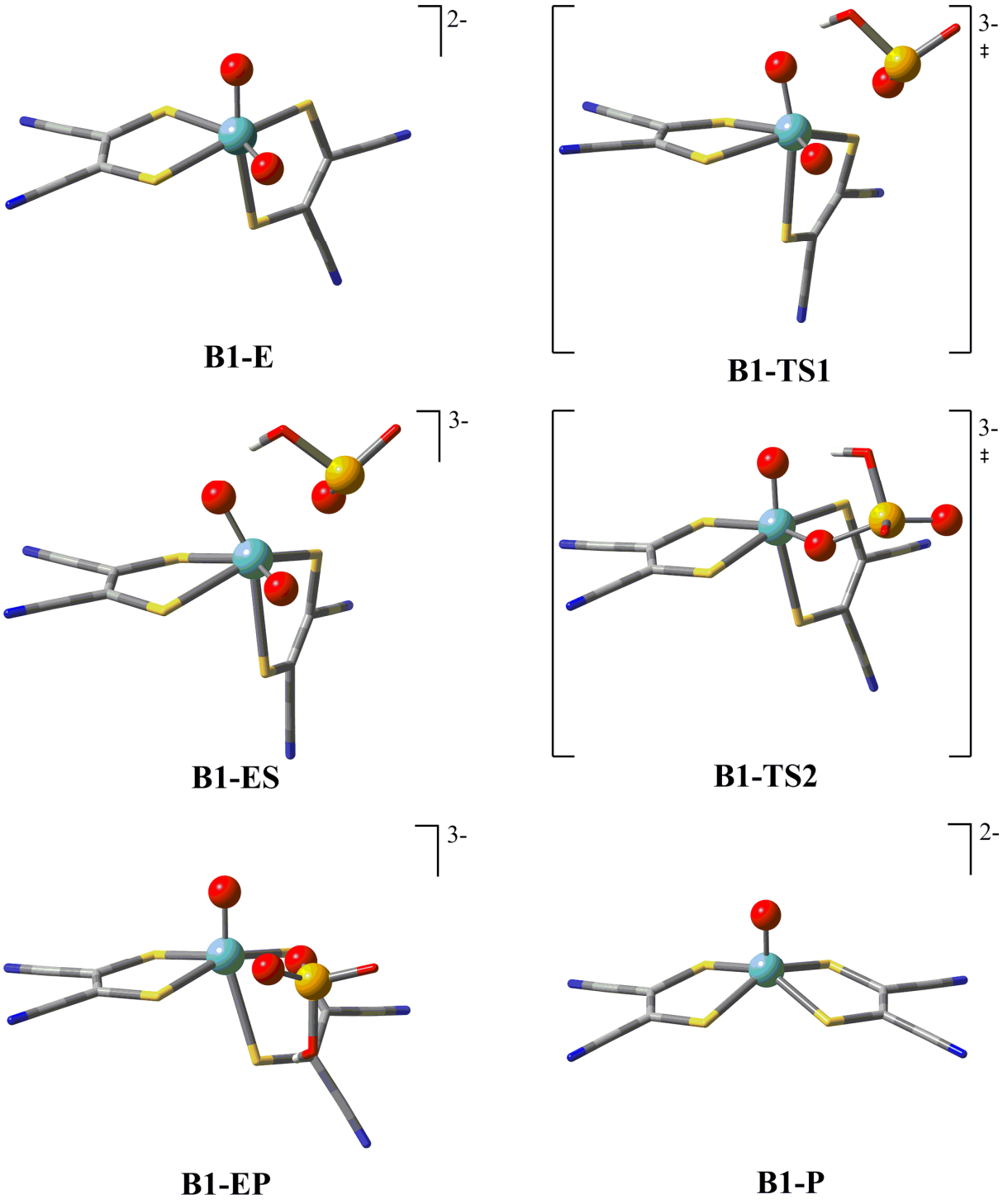

Fig. 5.7: Optimized geometries along the reaction pathway for oxygen atom transfer from $[Mo^{VI}O_2(mnt)_2]^{2-}$ to $HSeO_3^-$.

- **Molybdenum (VI) maleonitriledithiolate (mnt) complex with HSO_3^- B2:**
  - *Optimized educt* $[Mo^{VI}O_2(mnt)_2]^{2-}$ *complex* **B2-E**:

The $[Mo^{VI}O_2(mnt)_2]^{2-}$ complex, **B2-E** is identical to the optimized educt complex **B1-E** obtained from the reported crystal structure[196] (Table 5.5).

  - *Optimized transition state complex for educt-substrate complex formation* **B2-TS1**:

The energy barrier for the transition state $[Mo^{VI}O_2(mnt)_2(HSO_3)]^{3-}$ (**B2-TS1**) associated with the formation of educt substrate complex is 37.0 kcal/mol in the polarizable continuum (93.6 kcal/mol in the gas phase) (Table 5.6). An imaginary frequency of 27ί cm^{-1} corresponds to the $Mo\text{-}O_{Sulfite}$ stretching mode.

The optimized data shows no considerable change in the $Mo\text{-}O_{ax}$ (from 1.732 Å to 1.734 Å) and $Mo\text{-}O_{eq}$ (from 1.732 Å to 1.728 Å) bond distances when comparison is made with the optimized **B2-E** geometry (Table 5.5). The ditholate $Mo\text{-}S_2$ and $Mo\text{-}S_4$ bonds are elongated from 2.742 Å to 2.784 Å and from 2.742 Å to 2.903 Å, respectively. At this stage, the HSO_3^- is loosely bound to the Mo^{VI} center and the $Mo\text{-}O_{Se}$ distance is 2.575 Å (Table 5.5).

  - *Optimized educt-substrate intermediate complex* **B2-ES**:

The computed reaction energy for the formation of intermediate complex $[Mo^{VI}O_2(mnt)_2(HSO_3)]^{3-}$ (**B2-ES**) is endothermic, 20.5 kcal/mol in the polarizable continuum (93.0 kcal/mol) relative to the separate substrate, HSO_3^-, and educt (**B2-E**) complex (Table 5.6). **B2-ES** complex is ~6 kcal/mol lower in energy than **B1-ES**. Geometry optimization of **B2-ES** shows a decrease in the $Mo\text{-}O_{Sulfite}$ distance from 2.575 Å to 2.500 Å. No considerable change is observed in the dithiolate $Mo\text{-}S_2$ and the $Mo\text{-}S_4$ bond distances as well as in the $Mo\text{-}O_{ax}$ and the $Mo\text{-}O_{eq}$ bond distances when comparison is made to the optimized **B2-TS1** geometry. The $O_{eq}\text{-}S_{Sulfite}$ distance is 3.256 Å (Table 5.5).

  - *Optimized transition state complex for oxygen atom transfer* (OAT) **B2-TS2**:

The energy barrier for the transition state **B2-TS2**, associated with the oxygen atom transfer, is endothermic, 53.7 kcal/mol in the polarizable continuum (114.1 kcal/mol in the gas phase) relative to the substrate, HSO_3^-, and the educt (**B2-E**) complex (Table 5.6). This energy barrier of **B2-TS2** is similar to the energy barrier for **B1-TS2** (see Table 5.6). An imaginary frequency of 434ί cm^{-1} corresponds to the stretching vibration modes of $Mo\text{-}O_{eq}$ and

O_{eq}-$S_{Sulfite}$ (HSO_3^-) and confirms the saddle point character between the sulfite and sulfate complexes.

Geometry optimization of **B2-TS2** shows an increase in the Mo-O_{eq} bond length from 1.729 Å to 1.905 Å and Mo-$O_{Sulfite}$ distance from 2.509 Å to 4.470 Å while the O_{eq}-$S_{Sulfite}$ distance is reduced from 3.256 Å to 1.974 Å. No considerable change is observed in the Mo-O_{ax} (from 1.737 Å to 1.734 Å) bond distance. The dithiolate Mo-S_2 and Mo-S_4 bond distances are decreased from 2.782 Å to 2.622 Å and from 2.903 Å to 2.779 Å as compared to the optimized **B2-ES** geometry (Table 5.5).

- *Optimized product bound complex* **B2-EP**:

The computed relative energy for the formation of product bound intermediate complex $[Mo^{IV}O(mnt)_2(HSO_4)]^{3-}$ (**B2-EP**) is also endothermic, 31.0 kcal/mol in the polarizable continuum (93.8 kcal/mol in the gas) (Table 5.6).

The optimized data shows a decrease in the Mo-O_{ax} bond distance from 1.734 Å to 1.702 Å while the Mo-O_{eq} bond is elongated from 1.905 Å to 2.345 Å relative to the optimized **B2-TS2** geometry. The O_{eq}-$S_{Sulfite}$ (HSO_3^-) bond distance is decreased from 1.974 Å to 1.537 Å and the dithiolate Mo-S_2 bond is decreased from 2.622 Å to 2.472 Å while the Mo-S_4 bond is increased from 2.779 Å to 2.806 Å (Table 5.5).

- *Optimized reduced complex* **B2-P**:

The loss of oxidized substrate, HSO_4^- gives the reduced complex $[Mo^{IV}O(mnt)_2]^{2-}$ (**B2-P**) with square pyramidal geometry in an exothermic reaction, -10.6 kcal/mol in the polarizable continuum (-7.6 kcal/mol in gas phase) relative to the separate substrate, HSO_3^-, and educt (**B2-E**) complex (Table 5.6). The optimized data shows no considerable change in the Mo-O_{ax} bond distance (from 1.702 Å to 1.701 Å) while the Mo-S bond distances are decreased from ~2.571 Å to ~2.458 Å where all Mo-S bonds are of equal length when comparison is made with the optimized **B2-EP** geometry (Table 5.5).

Table 5.5: Selected bond lengths [Å] of optimized geometries along the reaction pathway for oxygen atom transfer from $[Mo^{VI}O_2(mnt)_2]^{2-}$ to HSO_3^-.

	B2-E	**B2-TS1**	**B2-ES**	**B2-TS2**	**B2-EP**	**B2-P**
Mo-O_{ax} (Ù)	1.732	1.734	1.737	1.734	1.702	1.701
Mo-O_{eq} (Ù)	1.732	1.728	1.729	1.905	2.345	-
Mo-$O_{Sulfite}$ (Ù)	-	2.575	2.509	4.470	-	-
O_{eq}-$S_{Sulfite}$ (Ù)	-	-	3.256	1.974	1.537	-
Mo-S_1 (Ù)	2.502	2.588	2.600	2.488	2.446	2.458
Mo-S_2 (Ù)	2.742	2.784	2.782	2.622	2.472	2.458
Mo-S_3 (Ù)	2.502	2.534	2.543	2.572	2.561	2.458
Mo-S_a (Ù)	2.742	2.903	2.903	2.779	2.806	2.458

Where, **B2-E** = Mo-mnt educt complex, **B2-TS1** =transition state complex for educt-substrate complex formation, **B2-ES** = educt-substrate complex, **B2-TS2** = transition state complex for oxygen atom transfer, **B2-EP** = product bound complex, **B2-P** = reduced product complex.

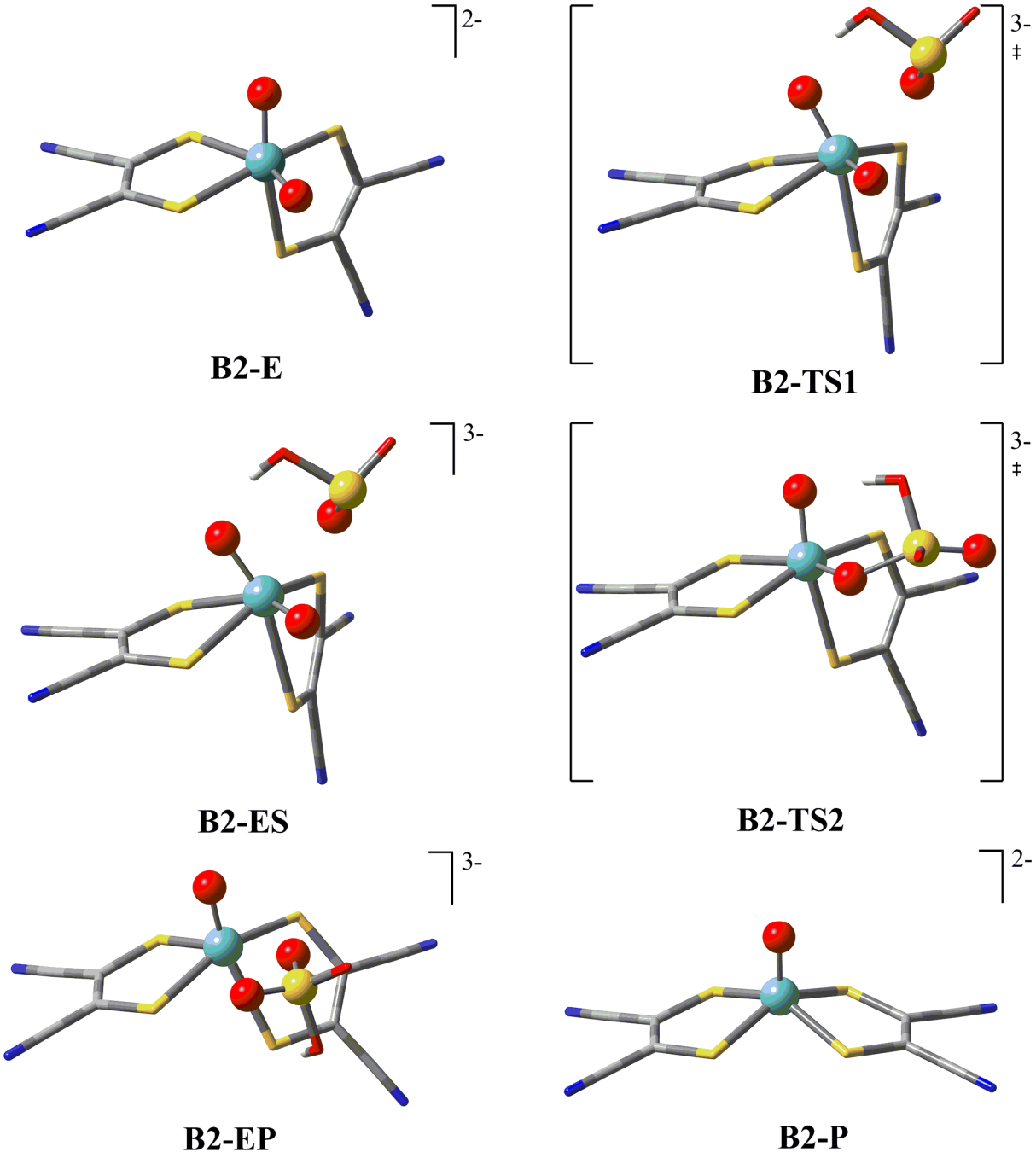

Fig. 5.8: Optimized geometries along the reaction pathway for oxygen atom transfer from $[Mo^{VI}O_2(mnt)_2]^{2-}$ to HSO_3^-.

Table 5.6: Relative energies (kcal/mol) computed for stationary points along the OAT from $[Mo^{VI}O_2(mnt)_2]^{2-}$ to $HSeO_3^-$ (**B1**) and HSO_3^- (**B2**)

	B1	**B2**	
E	0.0	0.0	//B3LYP[a] SDD[b] COSMO[c]
TS1	**89.8** **89.2** **27.2**	**92.7** **93.6** **37.0**	//B3LYP[a] SDD[b] COSMO[c]
ES	89.4 89.2 26.0	92.8 93.0 20.5	//B3LYP[a] SDD[b] COSMO[c]
TS2	**106.6** **114.0** **53.8**	**109.1** **114.1** **53.7**	//B3LYP[a] SDD[b] COSMO[c]
EP	94.2 106.7 46.4	84.0 93.8 31.0	//B3LYP[a] SDD[b] COSMO[c]
P	-5.8 7.7 7.1	-17.6 -7.6 -10.6	//B3LYP[a] SDD[b] COSMO[c]

Where, **E** = educt complex, **TS1** =transition state complex for educt-substrate complex formation, **ES** = educt-substrate complex, **TS2** = transition state complex for oxygen atom transfer, **EP** = product bound complex, **P** = product complex. **B1** = Mo (VI) maleonitriledithiolate complex with $HSeO_3^-$, **B2** = Mo (VI) maleonitriledithiolate complex with HSO_3^-. a) B3LYP/Lanl2DZ(p), b) B3LYP/SDDp//B3LYP/Lanl2DZ(p), c) COSMO-B3LYP/SDDp//B3LYP/Lanl2DZ(p) (see Computational details).

2.4. Discussion

Sulfite oxidase (SO), selenate reductase (SeR) and nitrate reductases (NRs) are among the mononuclear molybdenum enzymes involved in the catalysis of redox reactions in biological activities. The active site composition of SO has one MPT ligand and it oxidizes the sulfite to sulfate, SeR has two MPT ligands and it reduces the selenate to selenite, while NRs reduces nitrate to nitrite by either one or with two MPT's. In this context the question arises whether the active site itself is special in some way for the oxidation/reduction process of the one or the other substrate or the different active sites behave the same way and it is the role of the protein to make it specific. In order to address these questions, density functional theory (DFT) studies have been performed on the computational model complex, $[Mo^{VI}O_2(S_2C_2Me_2)SMe]^-$ (**A**) derived from the X-ray crystal structure of native SO,[31] and on the experimental model complex[196] $[Mo^{VI}O_2(mnt)_2]^{2-}$ (**B**, coordination geometry similar to the active site of SeR) for the oxidation of selenite and sulfite. For both the computational and experimental model complexes, two transition states (**TS1** and **TS2**) are involved in the oxygen atom transfer (OAT) reaction from the Mo^{VI} to the substrate.

Three different levels of computation (**OPT**, **SDD** and **COSMO**) were considered for all the geometries involved in the OAT reaction mechanisms. The relative energies show a slight change between the level of optimization (**OPT**) and the single point energy calculations in the gas phase (**SDD**) but a major difference is evident between the **SDD** and the polarizable continuum (**COSMO**) results where the relative energy decreases in the presence of continuum models (see Table 5.3 and 5.6). This may be because both the reactant and the substrate molecules are negatively charged and the association of two negatively charged ions increases the overall energy of the reaction pathway in the gas phase due to the repulsive interaction between two similar charged species. This repulsive interaction is stabilized in the continuum model resulting in the decrease of energies (see Table 5.3 and 5.6).

In the computed reaction pathway for the OAT from model complex **A** to $HSeO_3^-$ (**A1**), the energy barrier associated with **A1-TS1**, required for the formation of educt substrate complex, is 10.0 kcal/mol in the polarizable continuum. The educt-substrate **A1-ES** complex is only 0.3 kcal/mol lower in energy than **A1-TS1**. The energy barrier associated with the OAT from Mo to $HSeO_3^-$ (**A1-TS2**) is 37.4 kcal/mol in the polarizable continuum, the rate limiting step. The relative energy for the formation of $HSeO_4^-$ bound product complex **A1-EP** is 35.9 kcal/mol in the polarizable continuum. **A1-EP** is 1.5 kcal/mol lower in energy than the **A1-TS2**. The relative energy for the formation of reduced complex **A1-P** (starting geometry is generated by

the removal of oxidized substrate $HSeO_4^-$ from **A1-EP)** is 34.7 kcal/mol while relative energy for the direct replacement of $HSeO_4^-$ with water molecule (**A1-Pô**) in **A1-EP** is 28.7 kcal/mol in the continuum. **A1-Pô** is ~6 kcal/mol lower in energy than **A1-P** (Table 5.3).

In the computed reaction pathway for the OAT from model complex **A** to HSO_3^- (**A2**), the energy barrier associated with **A2-TS1** is 25.4 kcal/mol in the polarizable continuum i.e. much higher then for $HSeO_3^-$ (10.0 kcal/mol). The computed relative energy for the formation of educt-substrate complex **A2-ES** (25.9 kcal/mol) is similar to the relative energy for **A2-TS1**. The energy barrier associated with OAT reaction (**A2-TS2**, the rate limiting step) is 48.8 kcal/mol in the polarizable continuum relative to separate substrate and educt complex **A2-E**. The barrier for OAT in the substrate complex, however (i.e. **A2-TS2** vs **A2-ES**) is 22.9 kcal/mol. The activation energy for OAT in the $HSeO_3^-$ complex is 27.7 kcal/mol (**A1-TS2** vs **A1-ES**) and hence larger by 4.8 kcal/mol. The formation of HSO_4^- bound product complex **A2-EP** is endothermic, 33.2 kcal/mol in the polarizable continuum relative to **A2-E** and HSO_3^-. The energy relative to the substrate complex is only 7.3 kcal/mol (26.2 kcal/mol for $HSeO_3^-$ as substrate i.e. **A1-EP** vs **A1-E**). With the involvement of one water molecule to replace the oxidized substrate the OAT reaction starting from the substrate complex becomes slightly exothermic (-1.5 kcal/mol) for HSO_3^- but is computed to be considerably endothermic for $HSeO_3^-$ as substrate (+19.0 kcal/mol) (compare Table 5.3).

In summary, when the active site with one enedithiolato ligand (**A**) should **oxidize** a substrate it is a much better catalyst for HSO_3^- than for $HSeO_3^-$ (lower barrier, reaction energy close to thermoneutral). In a reduction reaction $HSeO_4^-$ requires a smaller activation energy (8.7 kcal/mol, **A1-Pô** vs **A1-TS2**) than HSO_4^- (24.4 kcal/mol, **A2-Pô** vs **A2-TS2**) but shows considerable exothermicity (-19.0 kcal/mol) (Scheme 5.1).

Scheme 5.1: Plot of computed reaction energies (kcal/mol) relative to separate substrate and educt complex vs steps involved in the OAT from educt complex **A** to $HSeO_3^-$ and HSO_3^-.

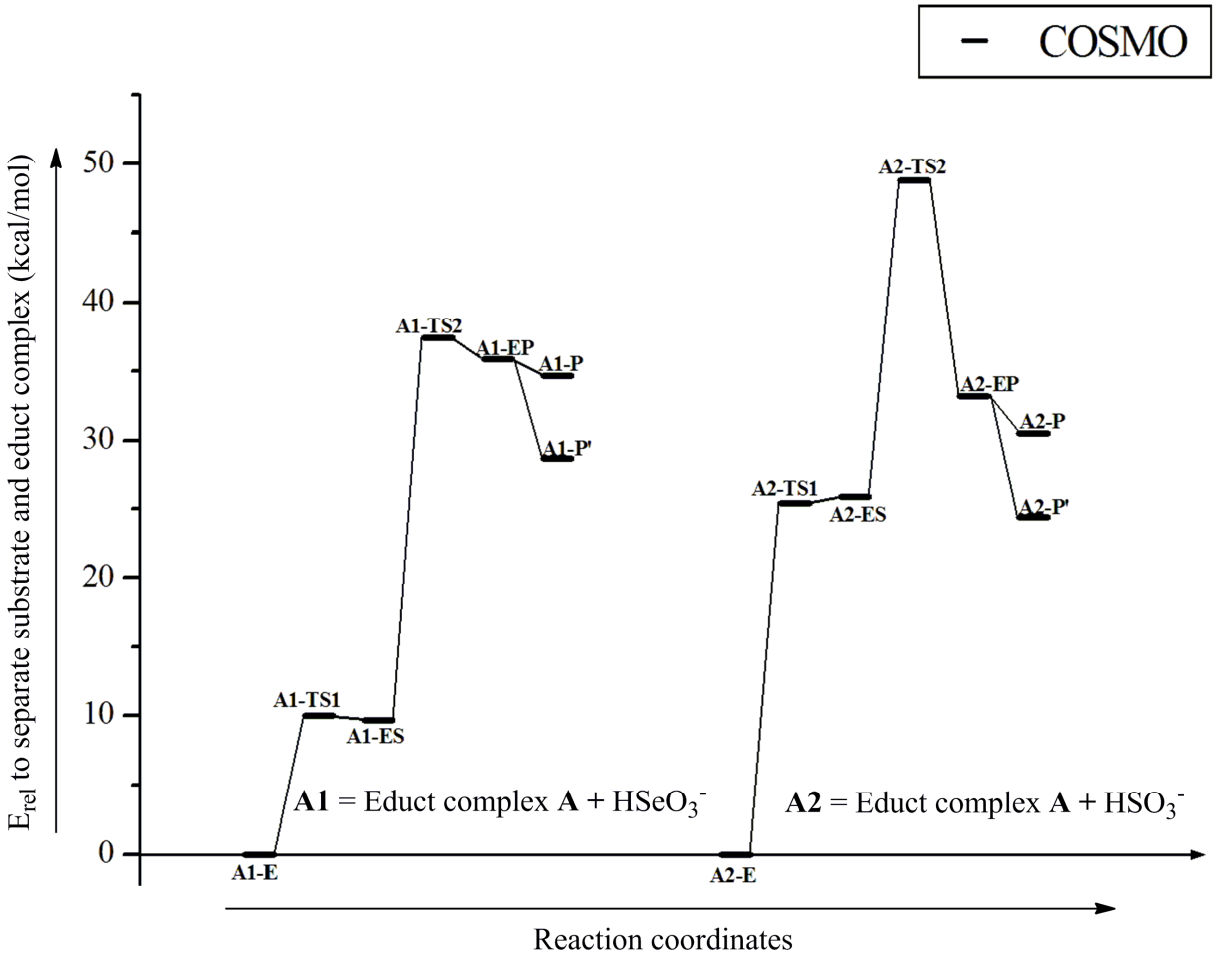

In the computed reaction pathway for the OAT from model complex **B** to $HSeO_3^-$ (**B1**), the energy barrier associated with **B1-TS1** is 27.2 kcal/mol in the polarizable continuum. The relative energy for the formation of educt substrate **B1-ES** complex is 26.0 kcal/mol in the polarizable continuum. **B1-ES** is 1.2 kcal/mol lower in energy than the **B1-TS1**. The energy barrier associated with **B1-TS2**, the rate limiting step, is 53.8 kcal/mol in the polarizable continuum. This results in an energy barrier of 27.8 kcal/mol for OAT in the substrate complex (**B1-TS2** vs **B1-ES**), which is almost identical to the value computed for model **A1** (27.7 kcal/mol). The relative energy for the formation of the $HSeO_4^-$ bound product complex **B1-EP** is 46.4 kcal/mol in the polarizable continuum. The loss of $HSeO_4^-$ from the **B1-EP** complex gives a **B1-P** complex in an exothermic reaction, -39.3 kcal/mol in the polarizable continuum (Table 5.6).

In the computed reaction pathway for the OAT from model complex **B** to HSO_3^- (**B2**), the energy barrier for the formation of educt-substrate complex (**B2-TS1**) is 37.0 kcal/mol in the

polarizable continuum. The relative energy for the formation of **B2-ES** is 20.5 kcal/mol in the polarizable continuum. **B2-ES** is 16.5 kcal/mol lower in energy than **B2-TS1**. The **B2-ES** intermediate is therefore in a much deeper dip on the potential energy surface than both the $HSeO_3^-$ intermediate complex and the **A2-ES** HSO_3^- intermediate complex. The energy barrier associated with the **B2-TS2** is 53.7 kcal/mol in the polarizable continuum. The barrier for OAT in the substrate complex **B2-ES** is therefore 33.2 kcal/mol. This value is significantly higher than for the $HSeO_3^-$ oxidation (27.8 kcal/mol) and also higher than for the HSO_3^- oxidation with the **A2** model (22.9 kcal/mol). The relative energy for the HSO_4^- bound product complex **B2-EP** is 31.0 kcal/mol in the polarizable continuum. The loss of HSO_4^- from the **B2-EP** gives a reduced complex **B2-P** in an exothermic reaction, -41.6 kcal/mol in the polarizable continuum (Table 5.6). The overall reaction from separate educt complex **E** and substrate to separate product complex **P** and oxidized substrate is computed to be exothermic for HSO_3^- (**B2**, -10.6 kcal/mol) but endothermic for $HSeO_3^-$ as substrate (**B1**, 7.1 kcal/mol).

In both cases (**B1** and **B2**) the release of the product, $HSeO_4^-$ and HSO_4^-, respectively, is computed to be strongly exothermic. However, this will probably not be the case for the enzyme. Fivefold coordinate product complex **P** adopts a square pyramidal geometry, which is not possible in the presence of the protein framework which restricts the flexibility of the large molybdopterin ligands. More meaningful are therefore the reaction energies leading to the product complexes **P** or the water complex **Pô** and released product. However, distorted octahedral starting geometries for the geometry optimization of $[MoO(OH_2)(mnt)_2]^{2-}$ lead to square pyramidal $[MoO(mnt)_2]^{2-}$ with the water molecule only bound through hydrogen bonds without coordination to Mo (Scheme 5.2, Table 5.6).

Considering all computational results one can state that model **A** with one enedithiolate ligand is well suited for the oxidation of sulfite. It has a lower barrier than for the selenite oxidation and also than model complex **B** with two chelating ligands.

The reduction is always easier for selenate than for sulfate (lower activation, stronger exothermicity). The hydrogen sulfate complex needs less activation for OAT with model A than with model **B**. However, the reduction is much more exothermic with **A** than with **B**.

Of course the energy profile obtained here for small model complexes may be significantly modeifoed in the presence of the protein part of the enzyme.

Scheme 5.2: Plot of computed reaction energies (kcal/mol) relative to separate substrate and educt complex vs steps involved in the OAT from educt complex **B** to $HSeO_3^-$ and HSO_3^-.

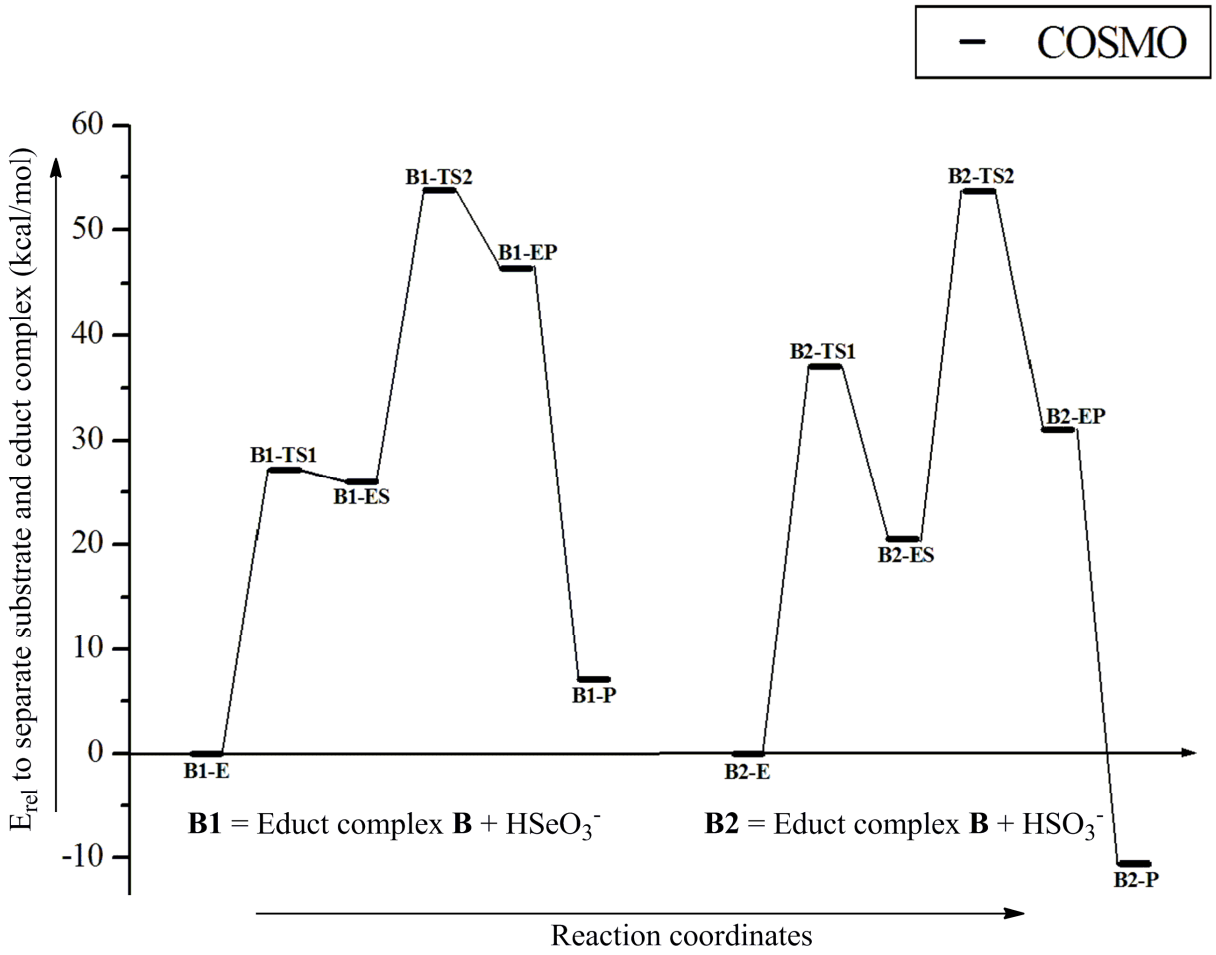

3. Project: II

Wang et al.[184] depicted a reaction pathway for the reduction of selenate to selenite, (Fig. 5.9) where the oxidation state of metal changes from +IV to +VI. Two electrons and two protons are required for the reductive half reaction, resulting in the formation of a water molecule and a selenite ion (Eq 5.1).

$$SeO_4^{2-} + 2H^+ + 2e^- \rightleftharpoons SeO_3^{2-} + H_2O \quad (5.1)$$

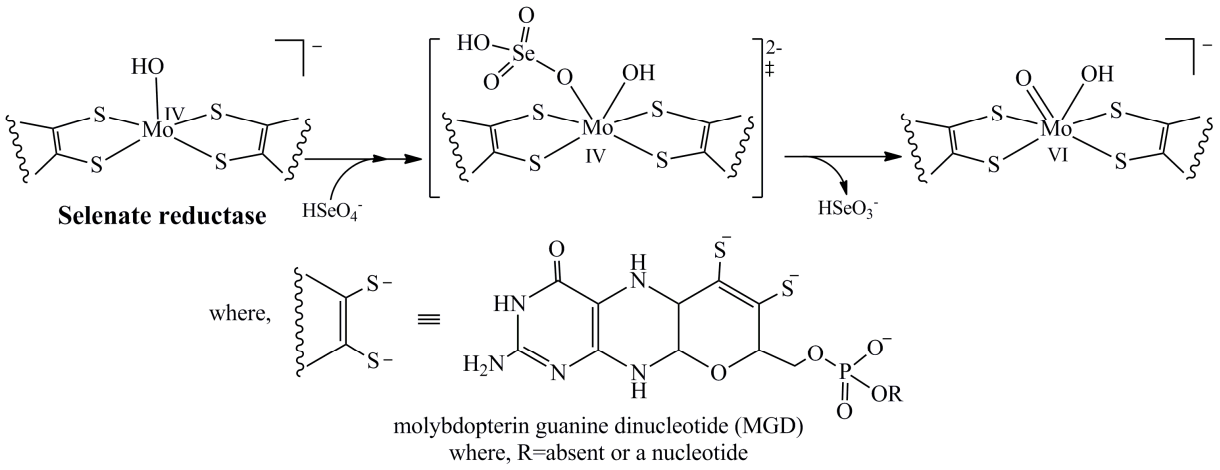

Fig. 5.9: Selenate reduction reaction based on the active site structures postulated from X-ray absorption spectroscopy depicted by Wang et al.[184]

Here, we have investigated additional ways of binding the substrate with the active site besides the reported analogous way (Fig. 5.9) by using the density functional theory (DFT). Experimental model complex $[Mo^{IV}(OH)(mnt)_2]^{1-}$ (**1**) obtained from the reported crystal structure[196] was used as an initial geometry.

3.1. Computational Details

All calculations were performed with the Gaussian 03[175] program package using B3LYP[123] hybrid functional of density functional theory (DFT). For the geometry optimizations, the LANL2DZ basis set[124,125,126,127] augmented by polarization functions on all atoms except Mo and H (ζ =0.600, 1.154, 0.864, 0.421, 0.338 for C, O, N, S and Se, respectively)[128], was employed. The optimized minima and transition-state structures were characterized by frequency calculations with the same method and basis set to verify that all minima have no imaginary frequency and each transition state has exactly one. Single point energies were computed with the B3LYP functional and the Stuttgart-Dresden effective core potential basis set (SDD)[129,130] augmented by polarization functions for all atoms except Mo, and H.[128] The self-consistent reaction field (SCRF) computations were performed on the optimized geometries by a conductor like polarizable continuum method (CPCM)[131] with a dielectric constant of 4 and solvent radius of 1.4Å.

3.2. Active Site Models

The initial active site geometry for the model complex $[Mo^{IV}(OH)(mnt)_2]^{1-}$ (**1**) studied here were obtained from the reported crystal structure.[196]

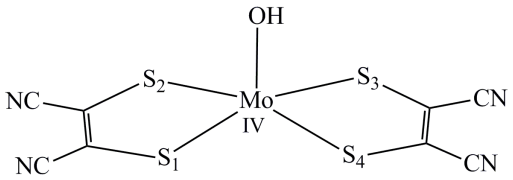

$[Mo^{IV}OH(mnt)_2]^-$

Fig. 5.10: Active site composition of initial active site geometry for selenate reductase obtained from the reported crystal structure.[196]

3.3. Results

For the oxygen atom transfer (OAT) reaction, in which $HSeO_4^-$ reacts with the *bis*-dithiolene Mo-OH complex $[Mo^{IV}(OH)(mnt)_2]^-$ (**1**) having square pyramidal geometry, different coordination modes between the two molecules were considered:

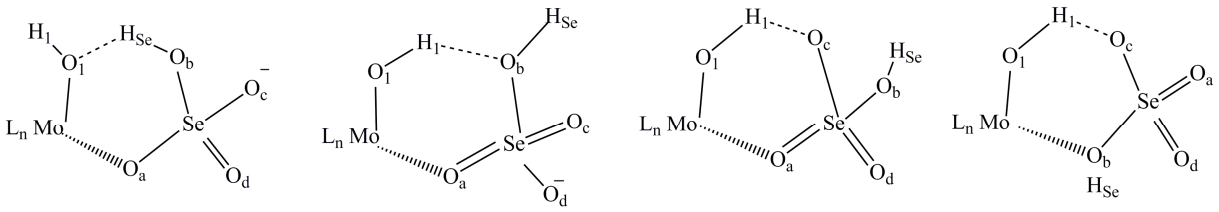

Fig. 5.11: Different ways of binding the substrate to the active site,
where, L_n = *bis*-maleonitriledithiolate (mnt) ligand.

- *Optimized educt* $[Mo^{IV}(OH)(mnt)_2]^-$ *complex* **1**:

The $[Mo^{IV}O(mnt)_2]^-$ complex, **1** obtained from the reported crystal structure,[196] was geometry optimized where the oxidation state of the molybdenum is IV and the overall charge on the complex is -1. The optimized data shows that the dithiolenes are not twisted against each other as the S_1-S_2-S_3-S_4 dihedral angle is 0.0° and the Mo-S bond distances are ~2.381 Å. The Mo-O_1 and O_1-H_1 bond distances are 1.882 Å and 0.971 Å, respectively (Table 5.11).

- **1A:**

In this case, the interaction between the two molecules is complemented by the attachment of selenate by its oxygen atom O_a to the Mo center as well as by a bond between the hydrogen atom of selenate (H_{Se}) and the hydroxo oxygen (O_1) attached to the Mo centre (Fig. 5.11).

- *Optimized educt-substrate complex,* **1A-ES**:

The computed reaction energy for the formation of educt-substrate complex, **1A-ES** is endothermic, 7.2 kcal/mol in the polarizable continuum (20.1 kcal/mol in the gas phase) relative to the separate substrate and educt (**1**) complex (Table 5.11). The optimized data shows an increase in the dithiolene S_1-S_2-S_3-S_4 dihedral angle (from 0.0˚ to 20.3˚) and in the Mo-S bond distances (from ~2.381 Å to ~2.411 Å) when comparison is made with the optimized **1** geometry. The Mo-O_1 bond distance is increased from 1.882 Å to 2.034 Å. The O_1-H_{Se} distance (hydrogen bond distance) is 1.552 Å and the H_{Se}-O_b bond distance is 1.015 Å. The Mo-O_a and O_a-Se bond distances are 2.116 Å and 1.708 Å, respectively (Table 5.7).

- *Optimized transition state complex,* **1A-TS**:

The energy barrier for the oxygen atom transfer from substrate to the Mo center (**1A-TS**) is 13.1 kcal/mol in the polarizable continuum (27.5 kcal/mol in the gas phase) relative to the separate substrate and educt (**1**) complex (Table 5.11). An imaginary frequency of 157*i* cm^{-1} corresponds to the stretching vibration modes of Mo-O_a and O_a-Se ($HSeO_4^-$) and confirms the saddle point character between the selenate and selenite complexes.

Geometry optimization of **1A-TS** shows an increase in the dithiolene S_1-S_2-S_3-S_4 dihedral angle (from 20.3˚ to 37.7˚) and in the Mo-S bond distances (from ~2.411 Å to ~2.489 Å) when comparison is made with the optimized **1A-ES** geometry. The Mo-O_1 (from 2.034 Å to 2.015 Å), H_{Se}-O_b (from 1.015 Å to 0.992 Å) and Mo-O_a (from 2.116 Å to 1.826 Å) bond distances are decreased while O_1-H_{Se} and O_a-Se bond distances are increased from 1.552 Å to 1.715 Å and from 1.708 Å to 2.217 Å, respectively (Table 5.7).

- *Optimized product bound complex,* **1A-EP**:

During the geometry optimization of **1A-EP**, the hydrogen H_1 from the hydroxo group of Mo complex is shifted to the selenite complex resulting in the formation of di-oxo Mo^{VI} complex and the selenous acid H_2SeO_3 which are not the desired products. The relative energy for the

formation of **1A-EP** complex is exothermic, -26.0 kcal/mol in the polarizable continuum (-16.7 kcal/mol in the gas phase) (Table 5.11).

The optimized data shows an increase in the dithiolene S_1-S_2-S_3-S_4 dihedral angle (from 37.7˚ to 54.0˚) and in the Mo-S bond distances (from ~2.489 Å to ~2.589 Å) when comparison is made with the optimized **1A-TS** geometry. A decrease in the Mo-O_1 (from 2.015 Å to 1.723 Å) and Mo-O_a (from 1.826 Å to 1.783 Å) bond distances are observed. The O_a-Se distance is increased from 2.217 Å to 3.391 Å (Table 5.7).

- *Optimized oxidized product complex,* **1A-P**:

The removal of selenous acid H_2SeO_3 leads to the formation of dioxo Mo complex $[Mo^{VI}O_2(mnt)_2]^{2-}$ (**1A-P**). The computed reaction energy for the formation **1A-P** is exothermic (-17.0 kcal/mol) in the polarizable continuum while it is endothermic (9.0 kcal/mol) in the gas phase relative to the separate substrate and educt (**1**) complex (Table 5.11).

The optimized data shows no change in the dithiolene S_1-S_2-S_3-S_4 dihedral angle while the Mo-S bond distances are increased from ~2.589 Å to ~2.622 Å when comparison is made with the optimized **1A-EP** geometry. The Mo-O_a bond distance is decreased from 1.783 Å to 1.732 Å (Table 5.7).

Table 5.7: Selected bond lengths [Å] of optimized geometries along the reaction pathway for oxygen atom transfer from $HSeO_4^-$ to $[Mo^{IV}OH(mnt)_2]^-$ in the **1A** coordination mode of substrate binding.

A	1	1A-ES	1A-TS	1A-EP	1A-P
Mo-O_1 (Å)	1.882	2.034	2.015	1.723	1.732
O_1-H_1 (Å)	0.971	0.966	0.968	-	-
O_1-H_{Se} (Å)	-	1.552	1.715	-	-
H_{Se}-O_b(Å)	-	1.015	0.992	0.995	-
Mo-O_a (Å)	-	2.116	1.826	1.783	1.732
O_a-Se (Å)	-	1.708	2.217	3.391	-
Mo-S_1 (Å)	2.385	2.402	2.454	2.491	2.502
Mo-S_2 (Å)	2.386	2.432	2.517	2.662	2.742
Mo-S_3 (Å)	2.377	2.411	2.475	2.475	2.502
Mo-S_4 (Å)	2.377	2.400	2.509	2.726	2.742
S_1-S_2-S_3-S_4 (e)	0.0	20.3	37.7	54.0	54.1

Where, **1** = Mo(IV) bis-maleonitriledithiolate complex, **1A-ES** = educt-substrate complex, **1A-TS** = transition state complex, **1A-EP** = product bound complex, **1A-P** = oxidized product complex.

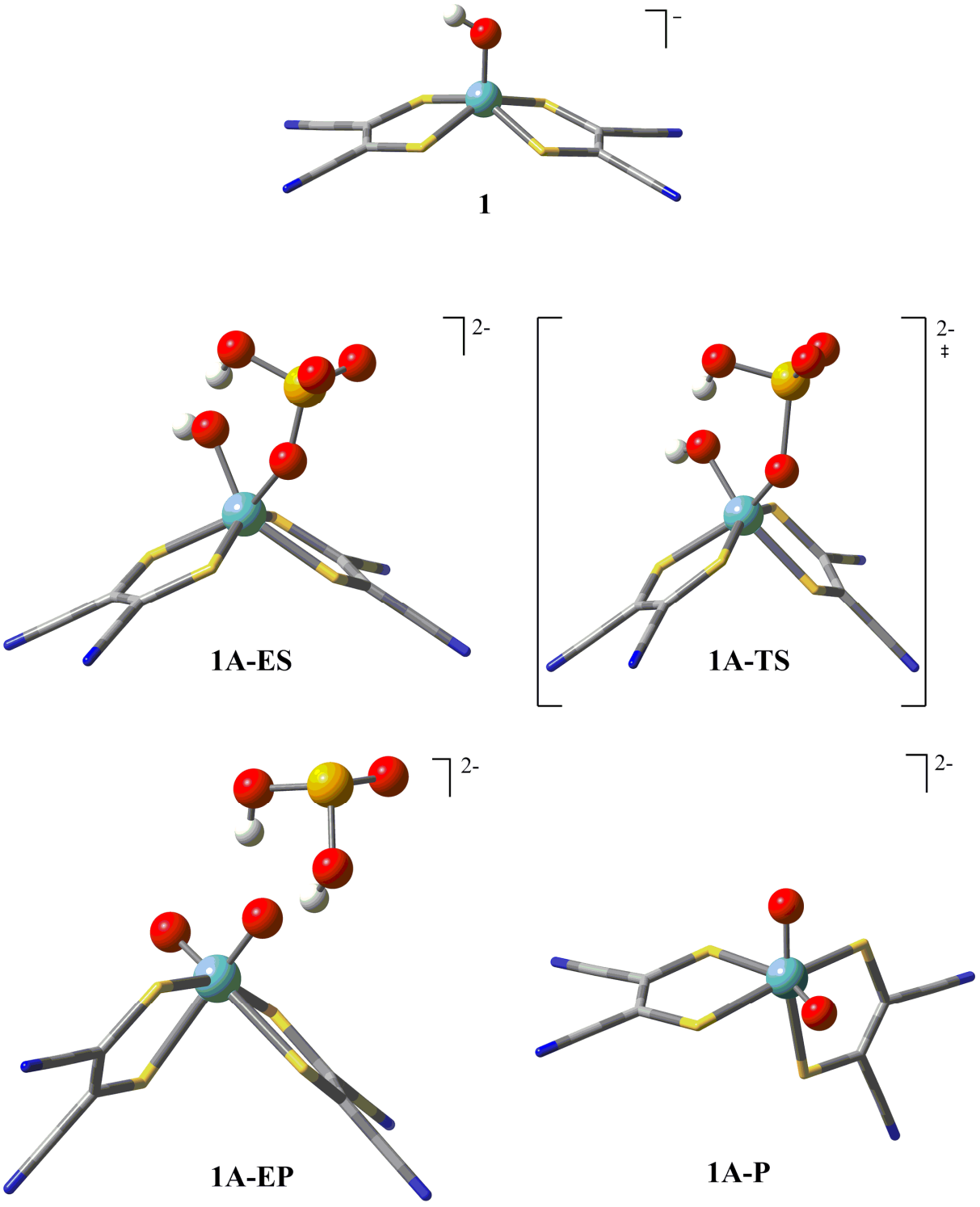

Fig. 5.12: Optimized geometries along the reaction pathway for oxygen atom transfer from $HSeO_4^-$ to $[Mo^{IV}OH(mnt)_2]^-$ in the **1A** coordination mode of substrate binding.

- **1B:**

In this case, the interaction between the educt (**1**) and substrate molecule is complemented by the attachment of selenate by its oxygen atom O_3 to the Mo center as well as by a bond between the hydroxo hydrogen atom of Mo (H_1) and the hydroxo oxygen atom (O_b) of selenate (Fig. 5.11).

- *Optimized educt-substrate complex,* **1B-ES**:

The computed reaction energy for the formation of educt-substrate complex **1B-ES** is endothermic, 15.3 kcal/mol in the polarizable continuum (26.2 kcal/mol in the gas phase) relative to the separate substrate and educt (**1**) complex (Table 5.11). The optimized data shows a slight increase in the Mo-O_1 and O_1-H_1 bond distances from 1.882 Å to 1.891 Å and from 0.971 Å to 0.980 Å, respectively, when comparison is made with the optimized **1** geometry. The H_1-O_b, Mo-O_a and O_a-Se bond distances are 1.968 Å, 2.365 Å and 1.664 Å, respectively. The dithiolene S_1-S_2-S_3-S_4 dihedral angle (from 0.0˚ to 33.0˚) and the Mo-S bond distances (from ~2.381 Å to ~2.418 Å) are increased (Table 5.8).

- *Optimized transition state complex,* **1B-TS**:

The energy barrier for the oxygen atom transfer from substrate to the Mo center (**1B-TS**) is 20.1 kcal/mol in the polarizable continuum (39.1 kcal/mol in the gas phase) relative to the separate substrate and educt (**1**) complex (Table 5.11). This energy barrier associated with **1B-TS** is 7 kcal/mol higher than for **1A-TS**. An imaginary frequency of 376í cm^{-1} corresponds to the stretching vibration modes of Mo-O_a and O_a-Se ($HSeO_4^-$) and confirms the saddle point character between the selenate and selenite complexes.

Geometry optimization of **1B-TS** shows an increase in the Mo-O_1 (from 1.891 Å to 1.954 Å), H_1-O_b (from 1.968 Å to 1.994 Å) and O_a-Se (from 1.664 Å to 2.028 Å) bond distances when comparison is made with the optimized **1B-ES** geometry. No change is observed in the O_1-H_1 bond distance while the Mo-O_a distance is decreased from 2.365 Å to 1.902 Å. An increase is observed in the dithiolene S_1-S_2-S_3-S_4 dihedral angle (from 33.0˚ to 43.7˚) and in the Mo-S bond distances (from ~2.418 Å to ~2.485 Å) (Table 5.8).

- *Optimized product bound complex,* **1B-EP**:

During the geometry optimization of **1B-EP**, the hydrogen H_1 from the hydroxo group of Mo complex is shifted to the hydroxo oxygen atom O_b of selenite complex resulting in the

formation of SeO_2, H_2O and di-oxo Mo^{VI} complex which are not the desired products. The computed reaction energy for the formation of **1B-EP** complex is exothermic, -19.5 kcal/mol in the polarizable continuum (-11.5 kcal/mol in the gas phase) relative to the separate substrate and educt (**1**) complex (Table 5.11).

The optimized data shows a decrease in the Mo-O_1 (from 1.954 Å to 1.763 Å), H_1-O_b (from 1.994 Å to 0.999 Å) and Mo-O_a (from 1.902 Å to 1.731 Å) bond distances when comparison is made with the optimized **1B-TS** geometry. The O_1-H_1 and the O_a-Se bond distances are increased from 0.980 Å to 1.679 Å and from 2.028 Å to 3.511 Å, respectively. An increase is observed in the dithiolene S_1-S_2-S_3-S_4 dihedral angle (from 43.7˚ to 52.3˚) and in the Mo-S bond distances (from ~2.485 Å to ~2.593 Å) (Table 5.8).

- *Optimized oxidized product complex*, **1B-P**:

The removal of SeO_2 and H_2O molecules from **1B-EP** leads to the formation of dioxo Mo complex $[Mo^{VI}O_2(mnt)_2]^{2-}$ (**1B-P**) which has the computed relative energy of -3.5 kcal/mol in the polarizable continuum while it is endothermic (26.4 kcal/mol) in the gas phase (Table 5.11).

The optimized data shows a decrease in the Mo-O_1 bond distance from 1.763 Å to 1.732 Å while no change is observed in the Mo-O_a bond distance when comparison is made with the optimized **1B-EP** geometry. No considerable change is observed in the dithiolene S_1-S_2-S_3-S_4 dihedral angle (from 52.3˚ to 54.1˚) while the Mo-S bond distances are increased from ~2.593 Å to ~2.622 Å (Table 5.8).

Table 5.8: Selected bond lengths [Å] of optimized geometries along the reaction pathway for oxygen atom transfer from $HSeO_4^-$ to $[Mo^{IV}OH(mnt)_2]^-$ in the **1B** coordination mode of substrate binding.

B	**1**	**1B-ES**	**1B-TS**	**1B-EP**	**1B-P**
Mo-O_1 (Å)	1.882	1.891	1.954	1.763	1.732
O_1-H_1 (Å)	0.971	0.980	0.980	1.679	-
H_1- O_b (Å)	-	1.968	1.994	0.999	-
Mo-O_a (Å)	-	2.365	1.902	1.731	1.732
O_a-Se (Å)	-	1.664	2.028	3.511	-
Mo-S_1 (Å)	2.385	2.339	2.435	2.480	2.502
Mo-S_2 (Å)	2.386	2.368	2.480	2.713	2.742
Mo-S_3 (Å)	2.377	2.485	2.520	2.505	2.502
Mo-S_4 (Å)	2.377	2.481	2.506	2.675	2.742
S_1-S_2-S_3-S_4 (φ)	0.0	33.0	43.7	52.3	54.1

Where, **1** = Mo(IV) bis-maleonitriledithiolate complex, **1B-ES** = educt-substrate complex, **1B-TS** = transition state complex, **1B-EP** = product bound complex, **1B-P** = oxidized product complex.

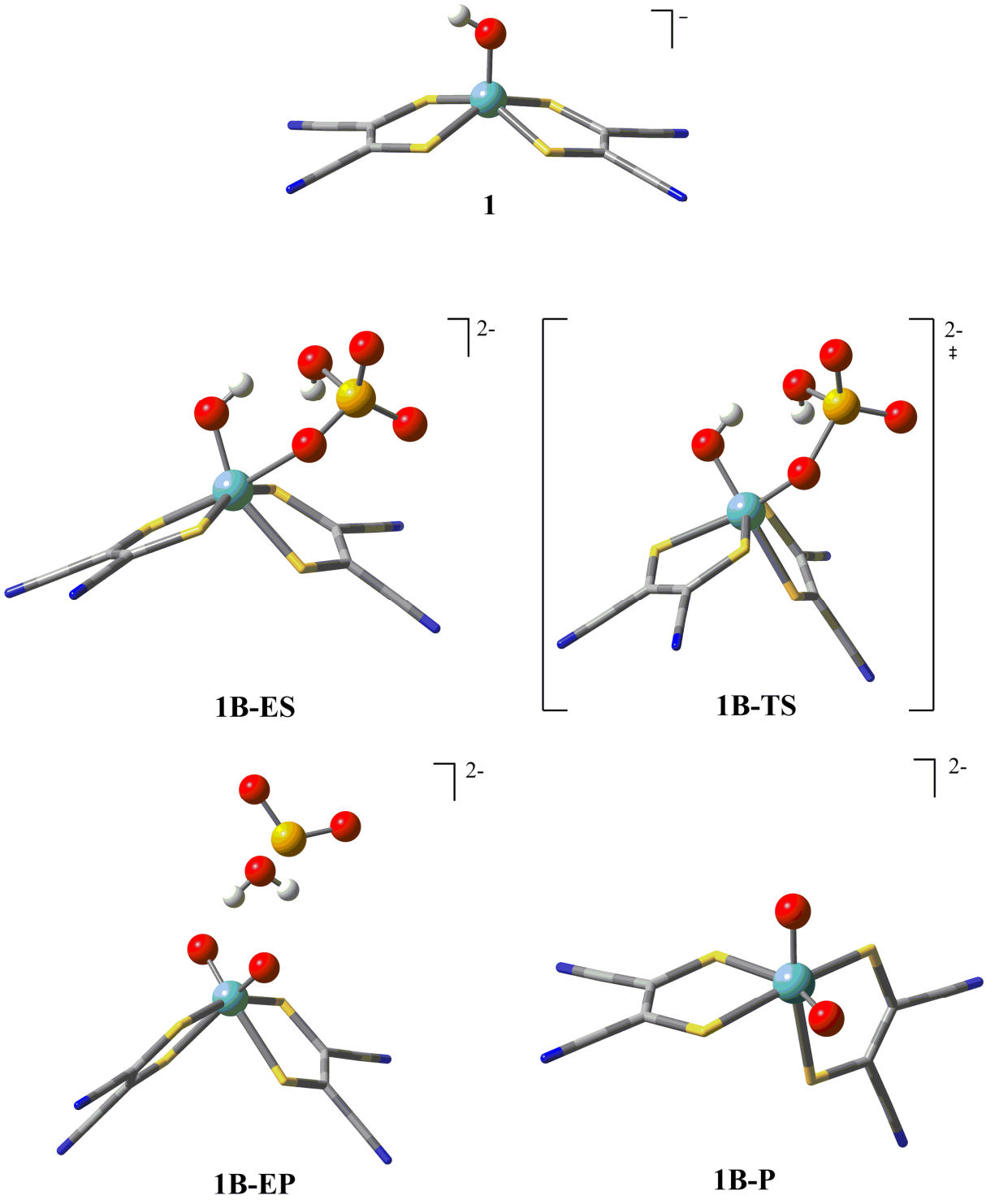

Fig. 5.13: Optimized geometries along the reaction pathway for oxygen atom transfer from $HSeO_4^-$ to $[Mo^{IV}OH(mnt)_2]^-$ in the **1B** coordination mode of substrate binding.

- **1C:**

In this case, the interaction among the two reactants is complemented by the attachment of selenate by its oxygen atom O_a to the Mo center as well as by the hydrogen bond between hydroxo hydrogen atom of Mo (H_1) and the oxygen atom (O_c) of selenate (Fig. 5.11).

➢ *Optimized educt-substrate complex,* **1C-ES**:

The computed reaction energy for the formation of educt-substrate complex **1C-ES** is endothermic, 9.7 kcal/mol in the polarizable continuum (20.1 kcal/mol in the gas phase) relative to the separate substrate and educt (**1**) complex (Table 5.11). The optimized data shows a decrease in the Mo-O_1 bond distance from 1.882 Å to 1.848 Å while the O_1-H_1 bond distance is increased from 0.971 Å to 1.016 Å when comparison is made with the optimized **1** geometry. The H_1-O_c, Mo-O_a and O_a-Se bond distances are 1.593 Å, 2.468 Å and 1.657 Å, respectively. The dithiolene S_1-S_2-S_3-S_4 dihedral angle (from 0.0˚ to 32.4˚) and the Mo-S bond distances (from ~2.381 Å to ~2.442 Å) are increased (Table 5.9).

➢ *Optimized transition state complex,* **1C-TS**:

The energy barrier for the oxygen atom transfer from substrate to the Mo (**1C-TS**) is 17.7 kcal/mol in the polarizable continuum (28.9 kcal/mol in the gas phase) relative to the separate substrate and educt (**1**) complex (Table 5.11). This energy barrier associated with **1C-TS** is 4.6 kcal/mol higher in energy than the **1A-TS** while 2.4 kcal/mol lower in energy than the **1B-TS**. An imaginary frequency of 398í cm^{-1} corresponds to the stretching vibration modes of Mo-O_a and O_a-Se ($HSeO_4^-$) and confirms the saddle point character between the selenate and selenite complexes.

Geometry optimization of **1C-TS** shows an increase in the Mo-O_1 (from 1.848 Å to 1.922 Å), H_1-O_c (from 1.593 Å to 1.758 Å) and O_a-Se (from 1.657 Å to 2.023 Å) bond distances when comparison is made with the optimized **1C-ES** geometry. The O_1-H_1 and Mo-O_a bond distances are decreased from 1.016 Å to 0.995 Å and from 2.468 Å to 1.910 Å, respectively. An increase is observed in the dithiolene S_1-S_2-S_3-S_4 dihedral angle (from 32.4˚ to 45.3˚) and in the Mo-S bond distances (from ~2.442 Å to ~2.496 Å) (Table 5.9).

➢ *Optimized product bound complex,* **1C-EP**:

During the geometry optimization of **1C-EP**, the hydrogen H_1 from the hydroxo group of Mo complex is shifted to the oxygen atom O_c of selenite complex resulting in the formation of

H_2SeO_3 and di-oxo Mo^{VI} complex which are also not the desired products. The computed relative energy for the formation of **1C-EP** complex is exothermic, -27.3 kcal/mol in the polarizable continuum (-18.7 kcal/mol in the gas phase) (Table 5.11).

The optimized data shows a decrease in the Mo-O_1 (from 1.922 Å to 1.758 Å), H_1-O_c (from 1.758 Å to 0.996 Å) and Mo-O_a (from 1.910 Å to 1.731 Å) bond distances as compared to the optimized **1C-TS** geometry. The O_1-H_1 and the O_a-Se distances are increased from 0.995 Å to 1.727 Å and from 2.023 Å to 3.341 Å, respectively. An increase is observed in the dithiolene S_1-S_2-S_3-S_4 dihedral angle (from 45.3˚ to 52.6˚) and in the Mo-S bond distances (from ~2.496 Å to ~2.596 Å) (Table 5.9).

- *Optimized oxidized product complex*, **1C-P**:

The removal of H_2SeO_3 molecule leads to the formation of dioxo Mo complex $[Mo^{VI}O_2(mnt)_2]^{2-}$ (**1C-P**). The computed reaction energy for **1C-P** is exothermic (-17.0 kcal/mol) in the polarizable continuum while it is endothermic (9.0 kcal/mol) in the gas phase relative to the separate substrate and educt (**1**) complex (Table 5.11).

The optimized data shows a decrease in the Mo-O_1 bond distance from 1.758 Å to 1.732 Å while no change is observed in the Mo-O_a bond distance when comparison is made to the optimized **1C-EP** geometry. No considerable change is observed in the dithiolene S_1-S_2-S_3-S_4 dihedral angle (from 52.6˚ to 54.1˚) while the Mo-S bond distances are increased from ~2.596 Å to ~2.622 Å (Table 5.9).

Table 5.9: Selected bond lengths [Å] of optimized geometries along the reaction pathway for oxygen atom transfer from $HSeO_4^-$ to $[Mo^{IV}OH(mnt)_2]^-$ in the **1C** coordination mode of substrate binding.

C	1	1C-ES	1C-TS	1C-EP	1C-P
Mo-O_1 (Å)	1.882	1.848	1.922	1.758	1.732
O_1-H_1 (Å)	0.971	1.016	0.995	1.727	-
H_1- O_c (Å)	-	1.593	1.758	0.996	-
Mo-O_a (Å)	-	2.468	1.910	1.731	1.732
O_a-Se (Å)	-	1.657	2.023	3.341	-
Mo-S_1 (Å)	2.385	2.412	2.427	2.480	2.502
Mo-S_2 (Å)	2.386	2.362	2.494	2.711	2.742
Mo-S_3 (Å)	2.377	2.490	2.533	2.507	2.502
Mo-S_4 (Å)	2.377	2.503	2.529	2.684	2.742
S_1-S_2-S_3-S_4 (deg)	0.0	32.4	45.3	52.6	54.1

Where, **1** = Mo(IV) bis-maleonitriledithiolate complex, **1C-ES** = educt-substrate complex, **1C-TS** = transition state complex, **1C-EP** = product bound complex, **1C-P** = oxidized product complex.

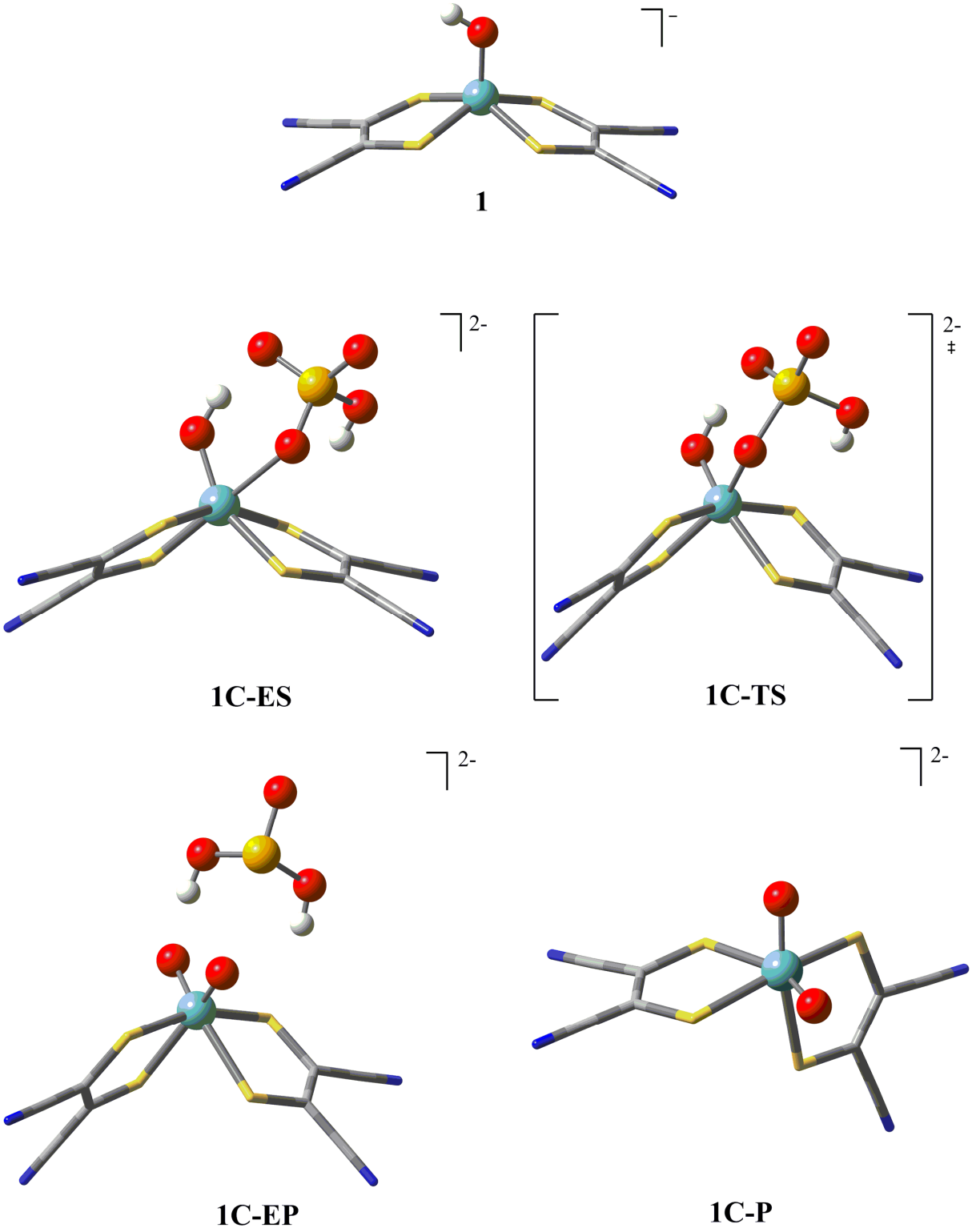

Fig. 5.14: Optimized geometries along the reaction pathway for oxygen atom transfer from $HSeO_4^-$ to $[Mo^{IV}OH(mnt)_2]^-$ in the **1C** coordination mode of substrate binding.

- **1D:**

In this case, the interaction between the two molecules is complemented by the attachment of selenate by its hydroxo oxygen atom O_b to the Mo center as well as by a bond between the hydroxo hydrogen atom of Mo (H_1) and the oxygen atom (O_c) of selenate (Fig. 5.11).

➢ *Optimized educt-substrate complex,* **1D-ES**:

The geometry optimization of **1D-ES** leads to the transfer of hydroxo hydrogen H_1 from the Mo to the selenate resulting in the formation of H_2SeO_4 and reduced mono-oxo complex $[Mo^{IV}O(mnt)_2]^{2-}$. The computed reaction energy for the formation of **1D-ES** is exothermic (-3.2 kcal/mol) in the polarizable continuum while it is endothermic (4.5 kcal/mol) in the gas phase relative to the separate substrate and educt (**1**) complex (Table 5.11). The optimized data shows a decrease in the Mo-O_1 bond distance from 1.882 Å to 1.729 Å while the O_1-H_1 bond distance is increased from 0.971 Å to 1.561 Å when comparison is made with the optimized **1** geometry. The H_1-O_c distance is 1.018Å. No considerable change is observed in the dithiolene S_1-S_2-S_3-S_4 dihedral angle (from 0.0° to -3.3°) while the Mo-S bond distances are increased from ~2.381 Å to ~2.440 Å (Table 5.10).

Table 5.10: Selected bond lengths [Å] of optimized geometries along the reaction pathway for oxygen atom transfer from $HSeO_4^-$ to $[Mo^{IV}OH(mnt)_2]^-$ in the **1D** coordination mode of substrate binding.

D	**1**	**1D-ES**
Mo-O_1 (Å)	1.882	1.729
O_1-H_1 (Å)	0.971	1.561
H_1- O_c (Å)	-	1.018
Mo-O_b (Å)	-	-
O_b-Se (Å)	-	-
Mo-S_1 (Å)	2.385	2.430
Mo-S_2 (Å)	2.386	2.435
Mo-S_3 (Å)	2.377	2.440
Mo-S_4 (Å)	2.377	2.454
S_1-S_2-S_3-S_4 (φ)	0.0	-3.3

Where, **1** = Mo(IV) bis-maleonitriledithiolate complex, **1D-ES** = educt-substrate complex.

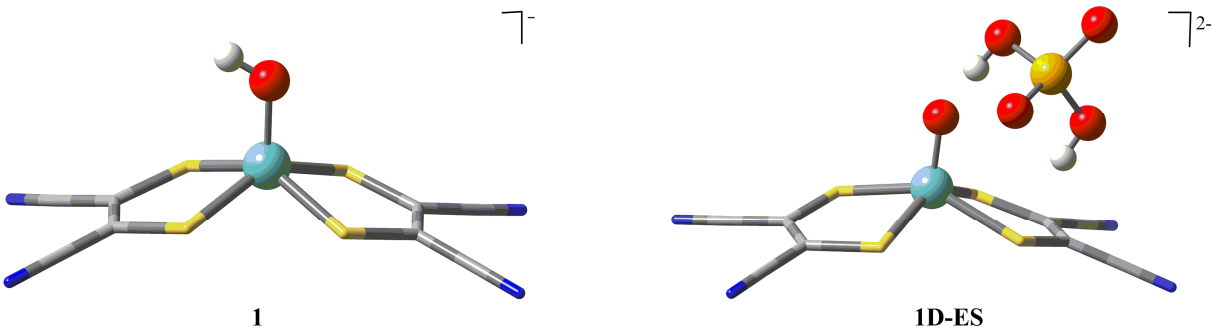

Fig. 5.15: Optimized geometries along the reaction pathway for oxygen atom transfer from $HSeO_4^-$ to $[Mo^{IV}OH(mnt)_2]^-$ in the **1D** coordination mode of substrate binding.

Table 5.11: Relative energies (kcal/mol) computed for stationary points along the OAT from $HSeO_4^-$ to $[Mo^{IV}OH(mnt)_2]^-$ (**1**) in the four different coordination modes of substrate binding.

	1A	**1B**	**1C**	**1D**	
E	0.0	0.0	0.0	0.0	//B3LYP[a] SDD[b] COSMO[c]
ES	19.6 20.1 7.2	25.3 26.2 15.3	18.5 20.1 9.7	4.7 4.5 -3.2	//B3LYP[a] SDD[b] COSMO[c]
TS	35.9 27.5 13.1	38.9 39.1 20.1	35.2 28.9 17.7	-	//B3LYP[a] SDD[b] COSMO[c]
EP	-6.4 -16.7 -26.0	3.3 -11.5 -19.5	-6.1 -18.7 -27.3	-	//B3LYP[a] SDD[b] COSMO[c]
P	56.3 9.0 -17.0	38.2 26.4 -3.5	56.3 9.0 -17.0	-	//B3LYP[a] SDD[b] COSMO[c]

Where, **E** = Mo(IV) bis-maleonitriledithiolate complex (**1**), **ES** = educt-substrate complex, **TS** =transition state complex, **EP** = product bound complex, **P** = oxidized product complex. **1A, 1B, 1C, 1D** are the different modes of substrate coordination to the educt complex (**1**).

a) B3LYP/Lanl2DZ(p), b) B3LYP/SDDp//B3LYP/Lanl2DZ (p),

c) COSMO-B3LYP/SDDp//B3LYP/Lanl2DZ(p) (see Computational details).

Discussion:

Density functional theory (DFT) studies have been performed to investigate various ways of binding the substrate with the active site including but not limited to the reported way (Fig. 5.9). For the oxygen atom transfer, (OAT) in which $HSeO_4^-$ reacts with the *bis*-dithiolene Mo-OH complex $[Mo^{IV}(OH)(mnt)_2]^-$ (**1**), different coordination modes between the two molecules have been considered (Fig. 5.11):

In structures **1A-1C** $HSeO_4^-$ coordinates to Mo through an oxygen atom (O_a), while in **1D** it coordinates through the hydroxo oxygen (O_b) atom of the substrate.

In case of **1A**, the interaction is complemented by a bond between the hydrogen atom (H_{Se}) of selenate and the hydroxo oxygen atom (O_1) attached to the Mo centre. The computed reaction energy for this complex **1A-ES** is 7.2 kcal/mol in the continuum (20.1 kcal/mol in the gas phase) relative to the separate substrate, $HSeO_4^-$ and educt (**1**) complex. Transition state **1A-TS**, has a distorted octahedral geometry and energy barrier of 13.1 kcal/mol in the continuum (27.5 kcal/mol in the gas phase). It is characterized by one imaginary frequency of 157í cm^{-1} and a transition vector that shows mainly stretching mode of Mo-O_a. Its computed barrier is the lowest we could find. Geometry optimization of $[Mo^{VI}O(OH)(mnt)_2HSeO_3]^{2-}$ leads to the formation of complex **1A-EP** containing the dioxo Mo complex $[Mo^{VI}O_2(mnt)_2]^{2-}$ and selenous acid (H_2SeO_3), where both hydrogen atoms of selenous acid form hydrogen bonds with one oxo group (O_a) of the Mo complex. The complex **1A-EP** was not the expected result from OAT reaction from selenate to the reduced Mo^{IV} complex. In the gas phase this complex, however, is probably more stable than the expected hydroxo-oxo-complex with $HSeO_3^-$. The relative energy for the formation of this product bound complex (**1A-EP**) is -26.0 kcal/mol in the polarizable continuum (-16.7 kcal/mol in the gas phase). The loss of H_2SeO_3 from the **1A-EP** gives the dioxo Mo complex $[Mo^{VI}O_2(mnt)_2]^{2-}$ (**1A-P**) in an exothermic step (-17.0 kcal/mol) in the polarizable continuum while in an endothermic step (9.0 kcal/mol) without the continuum relative to the separate substrate, $HSeO_4^-$ and educt (**1**) complex .

In case of **1B**, there is an additional hydrogen bond between the hydroxo hydrogen (H_1) of the Mo complex and the hydroxo oxygen atom (O_b) of the $HSeO_4^-$. The computed relative energy for such a Mo^{IV} starting complex **1B-ES** is 15.3 kcal/mol in the continuum (26.2 kcal/mol in the gas phase). An OAT transition state **1B-TS** with a distorted octahedral geometry and an energy barrier of 20.1 kcal/mol in the polarizable continuum (39.2 kcal/mol in the gas phase)

could be found. It is characterized by an imaginary frequency of 376í cm^{-1} and a transition vector that shows the stretching mode of Mo-O_a. However, geometry optimization of $[Mo^{VI}O(OH)(mnt)_2HSeO_3]^{2-}$ did not lead to the expected $HSeO_3^-$ complex, but the complex **1B-EP**, in which SeO_2 and H_2O are loosely bound to $[Mo^{VI}O_2(mnt)_2]^{2-}$. **1B-EP** has a computed relative energy of -19.5 kcal/mol in the polarizable continuum (-11.5 kcal/mol in the gas phase). This structure may be rationalized as a result of a proton being transferred from the hydroxo group at Mo to the hydroxo group of the reduced substrate rearranging to water, selenium dioxide and a dioxo Mo complex. Loss of water and selenium dioxide from **1B-EP** gives the Mo complex, $[Mo^{VI}O_2(mnt)_2]^{2-}$ (**1B-P**), which has a relative energy of -3.5 kcal/mol in the polarizable continuum (26.4 kcal/mol in the gas phase).

In case of **1C**, the hydrogen bond is formed between the Mo bound hydroxo hydrogen (H_1) and an oxo group (O_c) of selenate. The relative energy for such a reduced complex **1C-ES** is 9.7 kcal/mol in the polarizable continuum (20.1 kcal/mol in the gas phase). The distorted octahedral transition state **1C-TS** has an energy barrier of 17.7 kcal/mol (28.9 kcal/mol in the gas phase). **1C-TS** is characterized by an imaginary frequency of 398í cm^{-1} and a transition vector that shows the stretching mode of Mo-O_a. The H_2SeO_3 bound complex $[Mo^{VI}O_2(mnt)_2(H_2SeO_3)]^{2-}$ (**1C-EP**) formed as a result of geometry optimization, has a relative energy of -27.3 kcal/mol in the polarizable continuum (-18.7 kcal/mol in the gas phase). **1C-EP** is not the desired complex as hydrogen (H_1) from the hydoxo group of Mo complex is shifted to the selenite complex forming selenous acid and dioxo Mo complex. Loss of selenous acid gives the Mo complex, $[Mo^{VI}O_2(mnt)_2]^{2-}$ (**1C-P**), which has the relative energy of -17.0 kcal/mol in the polarizable continuum (9.0 kcal/mol in the gas phase).

In case of **1D**, we tried to explore the possibility of the hydoxo (O_bH_{Se}) transfer from the selenate to the Mo complex **1**. However, during the optimization of a starting geometry (**1D-ES**) the hydrogen atom (H_1) is shifted from the Mo complex to the selenate forming selenic acid (H_2SeO_4) and the mono oxo Mo^{IV} complex. It has a relative energy of -3.2 kcal/mol in the polarizable continuum (4.5 kcal/mol in the gas phase).

Scheme 5.3: Plot of computed reaction energies (kcal/mol) relative to separate substrate and educt complex vs steps involved in the OAT from $HSeO_4^-$ to educt complex **1** in the four different coordination modes of substrate binding.

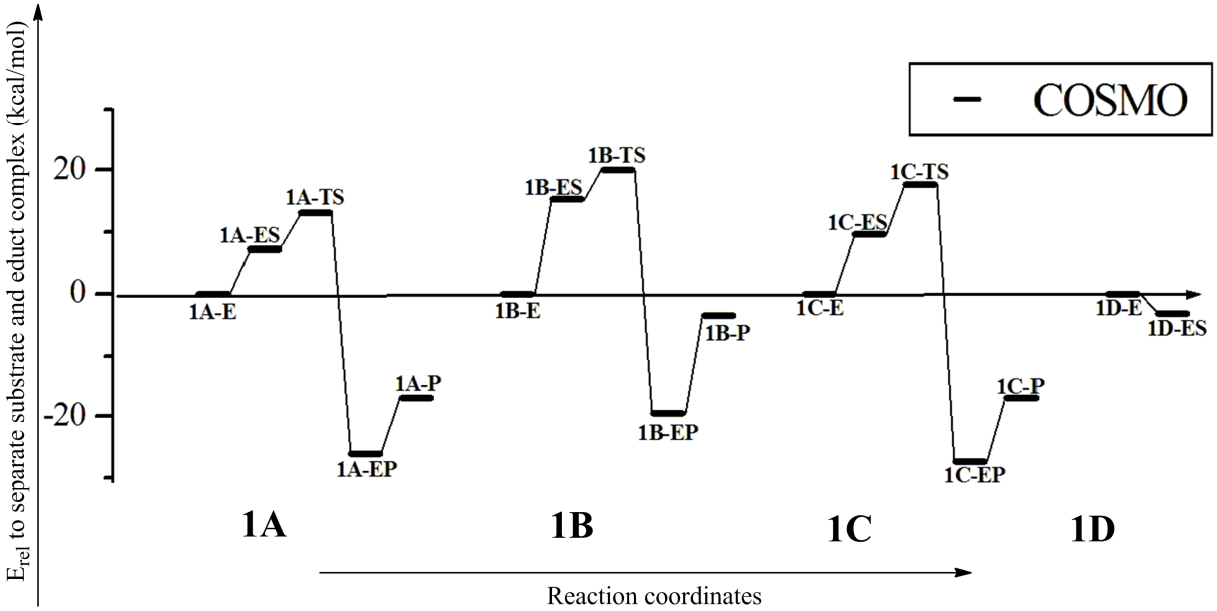

The best way for selenate reduction by the chosen model complex corresponds to **1A**. While an oxygen atom is transferred from the selenate to Mo the substrate OH group forms a hydrogen bond with the hydroxyl oxygen atom coordinated to Mo. Barriers computed for alternative arrangements are higher by only a few kcal/mol. The difficulties in locationg the expected product complexes where the $HSeO_3^-$ product is attached to a Mo complex demonstrate the necessity to investigate this reaction by a larger model system representing the enzyme active site more realistically, i.e. including part of the neighbouring amino acids of the protein part.

Conclusion

Different mononuclear Mo/W containing active site model complexes derived from the protein X-ray crystal structure of their native enzymes were computed to elucidate mechanistic details.

Nitrate reductase is an enzyme that catalyzes the reduction of nitrate to nitrite. The first W-containing nitrate reductase (Nar) isolated from *Pyrobaculum aerophilum* was computed for nitrate reduction where both Mo and W model complexes were considered. The energy barrier for OAT transfer in W-Nar is lower than the Mo-Nar; however, Mo-Nar is the best choice for the reduction of nitrate (oxidation of educt complex is less exothermic than W-Nar). The computed results indicate that although the reduction of nitrate is stimulated when W replaces Mo in the active site of Nar the catalytic cycle breaks after the reduction of nitrate to nitrite when the biochemical reducer is not strong enough to reduce the metal center.

Ethylbenzene dehydrogenase (EBDH) is an enzyme that catalyzes the oxygen-independent, stereospecific hydroxylation of ethylbenzene to (*S*)-1-phenylethanol. EBDH active site models were computed to find the most probable mechanism, ionic or radical pathway. Models with protonation of His_{192}, Lys_{450}, Asp_{223} and a model without protonation were investigated for comparison. Computed relative energies indicate that the overall lowest energy barrier pathway results when ionic and radical pathways are mixed and the Lys_{450} protonated EBDH model shows the energetically best pathway for the hydroxylation of ethylbenzene.

Acetylene hydratase (AH) of *Pelobacter acetylenicus* is a W containing iron-sulfur enzyme that catalyzes the transformation of acetylene to acetaldehyde. Based on the computational results for AH active site models the most likely *nucleophilic* mechanism for the hydration of acetylene by the acetylene hydratase (AH) enzyme is the one where the water (Wat_{1424}) molecule is coordinated to the W center and Asp_{13} is assumed to be in anionic form. For the AH, first small model complexes were computed but we have more reliable results when the surrounding amino acid residues were included.

Sulfite oxidase (SO), selenate reductase (SeR) and nitrate reductases (NRs) are among the mononuclear molybdenum enzymes involved in the catalysis of metabolic redox reactions. SeR is an enzyme that catalyzes the *reduction* of selenate to selenite and has two molybdopterin (MPT) ligands, SO *oxidizes* the sulfite to sulfate and has one MPT ligand, while NRs reduces nitrate to nitrite by either one or with two MPT ligands at the active site.

The sulfite model **A** (the computational model complex, $[Mo^{VI}O_2(S_2C_2Me_2)SMe]^-$), which resembles the SO active site is clearly the best choice (lowest energy barrier, minor exothermicity) for sulfite oxidation. For the reduction of selenate, however, a smaller activation is computed for model **A**, but the reaction is less exothermic with model **B** ($[Mo^{VI}O_2(mnt)_2]^{2-}$, resembling SeR), which resembles the SeR active site.

The simple active site model complexes of SeR were computed to investigate different ways of binding the substrate and the OAT reaction. Unfortunately, the results are little conclusive. Larger models might be needed to obtain more meaningful computational results as the active site environment may have the influence on the reactions catalyzed by the enzyme.

References

[1] The Catalytic Site Atlas at *The European Bioinformatics Institute*. Retrieved 4 April **2007**

[2] Holm, R. H., Kennepohl, P., and Solomon, E. I., *Chem. Rev.,* **1996**, *96*, 2239-2314.

[3] Kletzin, A., and Adams, M. W., *FEMS Microbiol Rev.,* **1996**, *18*, 5-63.

[4] Greenwood, N. N., and Earnshaw, A., *The Chemistry of the Elements,* Pergamon Press, Oxford, UK, **1984**, p.1170.

[5] Lawson, D. M., Williams, C. E., White, D. J., Choay, A. P., Mitchenhall, L. A., and Pau, R. N., *J. Chem. Soc., Dalton Trans.,* **1997**, 3981-3984.

[6] Lawson, D. M., Williams, C. E., Mitchenhall, L. A., and Pau, R. N., *Structure.,* **1998**, *6*, 1529-1539.

[7] Sigel, A., Sigel, H., *Metal Ions in Biological Systems 39*; Marcel Dekker: New York, **2002**.

[8] Hille, R., *Trends Biochem. Sci.,* **2002**, *27*, 360.

[9] Hille, R., *Chem. Rev.,* **1996,** *96,* 2575-2816.

[10] Holm, R. H. *Chem. Rev.,* **1987**, *87*, 1401.

[11] Young, C. G., and Wedd, A. G., in *Molybdenum. Molybdopterin Containing Enzymes, Encyclopedia of Inorganic Chemistry,* Vol. *4* (R. B. King, ed.), John Wiley & Sons, New York, **1994**, pp. 2330-2346.

[12] Garner, C. D., Banham, R., Cooper, S. J., Davies, E. S., and Stewart, L. J., in *Enzymes and Proteins Containing Molybdenum or Tungsten* (I. Bertini, A. Sigel, and H. Sigel, eds.), *Handbook on Metalloproteins*, Marcel Dekker, New York, **2001**, pp. 1023-1090.

[13] Howard, J. B., Rees, D. C., *Chem. Rev.,* **1996**, *96*, 2965.

[14] Burgess, B. K., Lowe, D. J., *Chem. Rev.,* **1996**, *96*, 2983.

[15] Campbell, W. H., *Annu. Rev. Plant Physiol.*, **1999**, *50*, 277-303.

[16] Sekimoto, H., Seo, M., Dohmae, N., Takio, K., Kamiya, Y., and Koshiba, T., *J. Biol. Chem.,* **1997**, *272*, 15280-15285.

[17] Gladyshev, V. N., Khangulov, S. V., and Stadtman, T. C., *Biochemistry.,* **1996**, *35*, 212-223.

[18] Lehmann, M., Tshisuaka, B., Fetzner, S., and Lingens, F., *J. Biol. Chem.,* **1995**, *270,* 14420-14429.

[19] Bläse, M., Bruntner, C., Tshisuaka, B., Fetzner, S., and Lingens, F., *J. Biol. Chem.,* **1996**, *271*, 23068-23079.

[20] Canne, C., Stephan, I., Finsterbusch, J., Lingens, F., Kappl, R., Fetzner, S., and Hüttermann, J., *Biochemistry.*, **1997**, *36*, 9780-9790.

[21] Weiner, J. H., Rothery, R. A., Sambasivarao, D., and Trieber, C. A., *Biochim. Biophys. Acta.,* **1992**, *1102*, 1-18.

[22] Massey, V., Komai, H., Palmer, G., and Elion, G. B., *J. Bio. Chem.*, **1970**, *245*, 2837-2844.

[23] Huang, D.Y., Furukawa, A., and Ichikawa, Y., *Arc. Biochem. Biophys.,* **1999**, *364,* 264-272.

[24] Rajagopalan, K. V., in *Molybdenum and Molybdenum Containing Enzymes* (M. P. Coughlan, ed.), Pergamon Press, New York, **1980**, pp. 241-272.

[25] Ljungdahl, L. G., *Trends Biochem. Sci.,* **1976**, *1*, 63-65.

[26] Ljungdahl, L. G., and Andreesen, J. R., *Meth. Enzymol.,* **1978**, *53*, 360-372.

[27] Andreesen, J. R., and Ljungdahl, L. G., *J. Bacteriol.,* **1973**, *116*, 867-873.

[28] Andreesen, J. R., and El Ghazzawi, E., *Arch. Microbiol.,* **1974**, *96*, 103-110.

[29] Yamamoto, I., Saiki, T., Liu, S.-M., and Ljungdahl, L. G., *J. Biol. Chem.*, **1983**,*258*, 1826-1832.

[30] Johnson, M. K., Rees, D. C., and Adams, M. W. W., *Chem. Rev.*, **1996**, *96*, 2817-2840.

[31] Kisker, C., Schindelin, H., Pacheco, A., Wehbi, W. A., Garrett, R. M., Rajagopalan, K. V., Enemark, J. H., and Rees, D. C., *Cell.,* **1997**, *91*, 973-983.

[32] Kisker, C., Schindelin, H., and Rees, D. C., *Annu. Rev. Biochem.,* **1997**, *66*, 233-267.

[33] Fischer, K., Barbier, G. G., Hecht, H. J., Mendel, R. R., Campbell, W. H., Schwarz, G., *Plant. Cell.,* **2005**, *17*, 1167-1179.

[34] Kisker, C., Schindelin, H., Baas, D., Retey, J., Meckenstock, R. U., and Kroneck, P. M., *FEMS Microbiol Rev.,* **1998**, *22*, 503-521.

[35] Stiefel, E. I., *J Chem Soc Dalton Trans.,* **1997**, 3915- 3923.

[36] Ellis, P. J., Conrads, T., Hille, R., and Kuhn, P., *Structure.,* **2001**, *9*, 125-132.

[37] Hille R., *European Journal of Inorganic Chemistry.,* **2006,** *10*, 1905–2095.

[38] Hille, R., and Sprecher, H., *J. Biol. Chem.*, **1987**, *262*, 10914–10917.

[39] Wootton, J. C., Nicolson, R. E., Cock, J. M., Walters, D. E., Burke, J.F., Doyle, W.A., et al.

Biochim Biophys Acta., **1991**, *1057*, 157–185.

[40] Beedham, C., *Prog. Med. Chem*., **1987**, *24*, 85–121.

[41] Turner, N. A., Doyle, W. A., Ventom, A. M. and Bray, R. C., *Eur. J. Biochem*., **1995**, *232*, 646–657.

[42] Hille, R., *Arch. Biochem. Biophys.,* **2005**, *433*, 107–116.

[43] Krenitsky, T. A., Neil, S. M., Elion, G. B. and Hitchings, G. H., *Arch. Biochem. Biophys*., **1972**, *150*, 585–599.

[44] Bray, R. C. In *The Enzymes,* Boyer, P. D., Ed., **1975**, *12*, 299.

[45] Romao, M. J., Archer, M., Moura, I., Moura, J. J. G., LeGall, J., Engh, R., Schneider, M., Hof, P., and Huber, R., *Science.*, **1995**, *270*, 1170-1176.

[46] Huber, R., Hof, P., Duarte, R. O., Moura, J. J. G., Moura, I., LeGall, J., Hille, R., Archer, M., and Romao, M. J., *Proc. Natl. Acad. Sci. USA.,* **1996**, *93*, 8846-8851.

[47] Harrison, R., *Free Radic. Biol. Med.,* **2002**, *33*, 774–797.

[48] Murray, K. N., Watson, J. G., Chaykin, S., *J. Biol. Chem.,* **1966**, *241*, 4798.

[49] Komai, H., Massey, V., Palmer, G., *J. Biol. Chem.,* **1969**, *244*, 1692.

[50] Olson, J. S., Ballou, D. P., Palmer, G., Massey, V., *J. Biol. Chem.,* **1974**, *249*, 4350-4362.

[51] Hille, R., Massey, V., *J. Biol. Chem.,* **1981**, *256*, 9090.

[52] Porras, A. G., Olson, J. S., Palmer, G., *J. Biol. Chem.,* **1981**, *256*, 9096.

[53] Rajagopalan, K.V., *Bio Chem Elem.,* **1984**, *3*, 149.

[54] Kessler, D. L., Rajagopalan, K. V., *J. Biol. Chem.,* **1972**, *247*, 6566.

[55] MacLeod, R. M., Farkas, W., Fridovich, I., Handler, P., *J. Biol. Chem.,* **1961**, *236*, 1841.

[56] Campbell, W.H., *Structure and synthesis of higher plant nitrate reductase*, **1989**, See ref. 102a, pp. 123-154.

[57] Campbell, W.H., *Plant Physiol.,* **1992**, *99*, 693-699.

[58] Campbell, W.H., *Annu. Rev. Plant Physiol.,* **1999**, *50*, 277-303.

[59] Barrett, E. L., and Kwan, H. S., *Annu. Rev. Microbiol.,* **1985**, *39*, 131-149.

[60] Sigel, A., Sigel, H., *Metal Ions in Biological Systems 39*; Marcel Dekker: New York, **2002**, p. 202-204.

[61] McAlpine, A. S., McEwan, A. G., and Bailey, S., *J. Mol. Biol.,* **1998**, *275*, 613-623.

[62] Santos, J. P. D., Lobbi-Nivol, C., Giordano, C. C. G., and MeÂjean, V., *J. Mol. Biol.,* **1998**, *284*, 421-433.

[63] Richardson, D. J., Berks, B. C., Russell, D. A., Spiro, S., Taylor, C. J., *Cell. Mol. Life Sci.,* **2001**, *58*, 165-178.

[64] Campbell, W. H., *Cell. Mol. Life Sci.,* **2001**, *58*, 194-204.

[65] Richardson, D. J., and Watmough, N. J., *Curr. Opin. Chem. Biol.,* **1999**, *3*, 207-219.

[66] Hofmann. M., *J. Biol. Inorg. Chem.,* **2009**, *14*, 1023-1035.

[67] Blasco, F., Iobbi, C., Giordano, G., Chippaux, M., and Bonnefoy, V., *Mol. Gen. Genet.,* **1989**, 249-256.

[68] Lin, J. T., Stewart, V., *Adv. Microb. Physiol.,* **1998**, *39*, 1-30.

[69] Majumdar, A., Sarkar, S., *Coord. Chem. Rev.,* **2011**, *255*, 1039-1054.

[70] Boyington J. C., Gladyshev, V. N., Khangulov, S. V., Stadman, T. C., Sun, P. D., *Science.,* **1997**, *275*, 1305-1308.

[71] Jormakka, M., Tornroth, S., Byrne, B., Iwata, S., *Science.,* **2002**, *295*, 1863-1868.

[72] Costa, C., Teixeira, M., LeGall, J., Moura, J.J.G., Moura, I., *J. Biol. Inorg. Chem.,* **1997**, *2*, 198–208.

[73] George, G.N., Costa, C., Moura, J.J.G., Moura, I., *J. Am. Chem. Soc.,* **1999**, *121*, 2625–2626.

[74] Brondino, C. D., Passeggi, M.C.G., Caldeira, J., Almendra, M.J., Feio, M.J., Moura, J.J.G., Moura, I., *J. Biol. Inorg. Chem.,* **2004**, *9,* 145-151.

[75] Messerschmidt, A., Niessen, H., Abt, D., Einsle, O., Schink, B., and Kroneck, P. M. H., *Proc. Natl. Acad. Sci. U. S. A.,* **2004**, *101 (2),* 11571-11576.

[76] Ellis, P. J., Conrads, T., Hille, R., and Kuhn, P., *Structure,* **2001**, *9*, 125-132.

[77] Almendra, M. J., Brondino, C. D., Gavel, O., Pereira, A. S., Tavares, P., Bursakov, S., Duarte, R., Caldeira, J., Moura, J. J. G., Moura, I., *Biochemistry.,* **1999**, *38*, 16366–16372.

[78] de Bok, F. A. M., Hagedoorn, P. L., Silva, P. J., Hagen, W. R., Schiltz, E., Fritsche, K., Stams, A. J. M., *Eur. J..Biochem.,* **2003**, *270*, 2476–2485.

[79] Bevers, L. E., Hagedoorn, P. –L., Hagen, W. R., Coord. Chem. Rev., 2009, 253, 269-290.

[80] Sigel, A., Sigel, H., *Metal Ions in Biological Systems 39*; Marcel Dekker: New York, **2002**, p. 677-680.

[81] Mukund, S., and Adams, M. W. W., *J. Biol. Chem.,* **1991**, *266*, 14208-14216.

[82] Ma, K., Hutchins, A., Sung, S. –H. S., and Adams, M. W. W., *PNAS*, **1997**, *94*, 9608-9613.

[83] Heider, J., Ma, K., and Adams, M. W. W., *J. Bacteriol.,* **1995**, *177*, 4757-4764.

[84] Sigel, A., Sigel, H., *Metal Ions in Biological Systems 39*; Marcel Dekker: New York, **2002**, p. 680-684.

[85] Chan, M. K., Mukund, S., Kletzin, A., Adams, M. W. W., Rees, D. C., *Science.,* **1995**, *267 (5203),* 1463-1469.

[86] Mukund, S., and Adams, M. W. W., *J. Biol. Chem.,* **1993**, *268*, 13592-13600.

[87] Roy. R., Mukund, S., Schut, G. J., Dunn, D. M., Weiss, R., and Adams, M. W. W., *J. Bacteriol.,* **1999**, *181*, 1171-1180.

[88] Sigel, A., Sigel, H., *Metal Ions in Biological Systems 39*; Marcel Dekker: New York, **2002**, p. 687-688.

[89] Mukund, S., and Adams, M. W. W., *J. Biol. Chem.,* **1995**, *270*, 8389-8392.

[90] Sigel, A., Sigel, H., *Metal Ions in Biological Systems 39*; Marcel Dekker: New York, **2002**, p. 690-691.

[91] White, H., Strobl, G., Feicht, R., and Simon, H., *Eur. J. Biochem.,* **1989**, *184,* 89-96.

[92] Sigel, A., Sigel, H., *Metal Ions in Biological Systems 39*; Marcel Dekker: New York, **2002**, p. 685-686.

[93] Hensgens, C. M. H., Hagen, W. R., and Hansen, T. H., *J. Bacteriol.,* **1995**, *177*, 6195-6200.

[94] Zellner, G., Jargon, A., *Arch. Microbiol.,* **1997**, *168*, 480-485.

[95] Yamamoto, I., Saiki, T., Liu, S. –M., and Ljungdahl, L. G., *J. Biol. Chem.,* **1983**, *258*, 1826-1832.

[96] Almendra, M. J., Brondino, C. D., Gavel, O., Pereira, S., Tavares, P., Bursakov, S., Duarte, R., Caldeira, J., Moura, J. J. G., and Moura, I., *Biochemistry.,* **1999**, *38*, 16366-16372.

[97] Schmitz, R. A., Linder, D., Stetter, K. O., and Thauer, R. K., *Arch. Microbiol.,* **1991**, *156*, 427-434.

[98] Rosner, B., and Schink, B., *J. Bacteriol.,* **1995**, *177*, 5767-5772.

[99] Meckenstock, R. U., Kreiger, R., Ensign, S., Kroneck, P. M. H., and Schink, B., *Eur. J. Biochem.,* **1999**, *264*, 176-182.

[100] Seiffert, G. B., Ullmann, G. M., Messerschmidt, A., Schink, B., Kroneck, P. M. H., and Einsle, O., *Proc. Natl. Acad. Sci. USA.,* **2007**, *104*, 3073-3077.

[101] Johnson, J. L., Rajagopalan, K. V., and Cohan. H. J., *J. Biol. Chem.*, **1974**, *249*, 5046-5055.

[102] Buc, J., Santini, C. –L., Giordano, R., Czjek, M., Wu, L. –F., and Giordano, G., *Mol. Microbiol.,* **1999**, *32*, 159-168.

[103] Stewat, L. J., Bailey, S., Bennett, B., Charnock, J. M., Garner, C. D., and McAlpine, A. S., *J. Mol. Biol.,* **2000**, *299*, 593-600.

[104] Sung, K. –M., and Holm, R. H., *J. Am. Chem. Soc.,* **2001**, *123*, 1931-1943.

[105] Jormakka, M., Richardson, D., Byrne, B., and Iwata, S., *Structure.,* **2004**, *12*, 95-104.

[106] Afshar, S., Johnson, E., de Vries, D., and Schröder, I., *J. Bacteriol.,* **2001**, *183*, 5491-5495.

[107] Kisker, C., Schindelin, H., Baas, D., Rétey, J., Meckenstock, R. U., Kriger, R., and Kroneck, P. M. H., *FEMS Microbiol. Rev*., **1999**, *178*, 163-167.

[108] Stolz, J. F., and Basu, P., *Chem. Bio. Chem.,* **2002**, *3*, 198-206.

[109] Kroneck, P. M. H., Abt, D. J., *Met. Ions. Biol. Syst.,* **2002**, *39*, 369-403.

[110] Cabello, P., Roldan, M. D., Moreno-vivian, C., *Microbiology.,* **2004**, *150*, 3527-3546.

[111] Richardson, D. J., and Watmough, N. J., *Curr. Opin. Chem. Biol.,* **1999**, *3*, 207-219.

[112] Campbell, W. H., *Annu. Rev. Plant Physiol. Plant Mol.Biol.,* **1999**, *50*, 277-303.

[113] Lin, J. T., Stewart, V., *Adv. Microb. Physiol.,* **1998**, *39*, 1-30.

[114] De Vries, S., Momcilovic, M., Strampraad, M. J. F., Whitelegge, J. P., Baghai, A., and Schröder, I., *Biochemistry.,* **2010**, *49*, 9911-9921.

[115] Zumft, W. G., *Microbiol. Mol. Biol. Rev.,* **1997**, *61*, 533-616.

[116] Enoch, H. G., and Lester, R. L., *J. Bacteriol.,* **1972**, *110*, 1032-1040.

[117] Brondino, C. D., Passeggi, M. C., Caldeira, J., Almendra, M. J., Feio, M. J., Moura, J. J., and Moura, I., *J. Biol. Inorg. Chem.,* **2004**, *9*, 145–151.

[118] Stewart, L. J., Bailey, S., Bennett, B., Charnock, J. M., Garner, C. D., and McAlpine, A. S., *J. Mol. Biol.,* **2000**, *299*, 593–600.

[119] Afshar, S., Kim, C., Monbouquette, H. G., and Schröder, I., *Applied And Environmental Microbiology.,* **1998**, *64* (8), 3004-3008.

[120] Chaudhry, G. R., and MacGregor, C. H., *J. Biol. Chem.,* **1983**, *258*, 5819–5827.

[121] Holm, R. H., *Chem. Rev*., **1987**, *87*, 1401-1449.

[122] Jiang, J., and Holm, R. H., *Inorg. Chem.,* **2005**, *44*, 1068-1072.

[123] Lee, C., Yang, W., Parr, R. G., *Phys Rev B.,* **1988**, *37*, 785-789.

[124] Hay, P. J., Wadt, W. R., *J. Chem. Phys.,* **1985**, *82*, 270-283.

[125] Wadt, W. R., Hay, P. J., *J. Chem. Phys.,* **1985**, *82*, 284-293.

[126] Hay, P. J., Wadt, W. R., *J. Chem. Phys.,* **1985**, *82*, 299-310.

[127] Dunning, T. H., Hay, P. J., *In Schaefer HF III (ed) Modern theoretical chemistry,* **1976**, *vol 3*. Plenum, New York.

[128] Huzinaga, S., Andzelm, J., Klobukowski, M., Radzio-Andzelm, E., Sakai, Y., Tatewaki, H., *Gaussian basis sets for molecular orbital calculations, Elesevier,* **1984**, Amsterdam

[129] Andrae, D., Haeussermann, U., Dolg, M., Preuss, H., *Theor Chim Acta.,* **1990**, *77*, 123-141.

[130] Andrae, D., Haeussermann, U., Dolg, M., Preuss, H., *Theor Chim Acta.,* **1991**, *78*, 247-266.

[131] Klamt, A., Jonas, V., Buerger, T., Lohrenz, J.C.W., *J. Phys. Chem.,* **1998**, *102*, 5074-5085.

[132] Barone, V., Cossi, M., *J. Phys Chem A.,* **1998**, *102*, 1995.

[133] Cossi, M., Rega, N., Scalmani, G., Barone, V., *J. Comp. Chem.,* **2003**, *24*, 669-681.

[134] Florsi, F., and Tomasi, J., *J. Comp. Chem.*, **1989**, *10,* 616.

[135] Florsi, F., and Tomasi, J., and Pascual-Ahuir, J. L., *J. Comp. Chem.*, **1991**, *12,* 784.

[136] Cammi, R., Cappelli, C., Corni, S., and Tomasi, J., *J. Phys. Chem. A.*, **2000**, *104,* 9874-9879.

[137] Pascual-Ahuir, J. L., Silla, E., and Tuñón, I., *J. Comp. Chem.*, **1994**, *15*, 1127-1138.

[138] George, G. N., Turner, N. A., Bray, R. C., Morpeth, F. F., Boxer, D. H., and Cramer, S. P., *Biochem. J.,* **1989**, *259*, 693-700.

[139] McAlpine, A. S., McEwan, A. G., and Bailey, S., *J. Mol. Biol.,* **1998**, *275*, 613-623.

[140] Cotton, F. A., Wing, R. M., *Inorg. Chem.,* **1965**, *4*, 867-873.

[141] Yoshimatsu, K., Iwasaki, T., and Fujiwara, T., *FEBS Lett.,* **2002**, *516*, 145-150.

[142] Yoshimatsu, K., Sakurai, T., and Fujiwara, T., *FEBS Lett.,* **2000**, *470*, 216-220.

[143] Martinez-Espinosa, R. M., Richardson, D. J., Butt, J. N., and Bonete, M. J., *Biochem. Soc. Trans.,* **2006**, *34*, 115-117.

[144] Klenitz, A., and Adams, M. W. W., *FEMS Microbiol. Rev.,* **1996**, *18*, 5-63.

[145] Sigel, A., Sigel, H., *Metal Ions in Biological Systems 39*; Marcel Dekker: New York, **2002**.

[146] De Vries, S., Momcilovic, M., Strampraad, M. J. F., Whitelegge, J. P., Baghai, A., and Schröder, I., *Biochemistry.,* **2010**, *49*, 9911-9921.

[147] Stewart, L. J., Bailey, S., Bennett, B., Charnock, J. M., Garner, C. D., and McAlpine, A. S., *J. Mol. Biol.,* **2000**, *299*, 593–600.

[148] Szaleniec, M., Hagel, C., Menke, M., Nowak, P., Witko, M., and Heider, J., *Biochemistry.,* **2007**, *46*, 7637-7646.

[149] Schröder, I., Rech, S., Macy, J. M., *J. Biol. Chem*., **1997**, *272*, 23765-23768.

[150] McDevitt, C. A., Hugenholtz, P., Hanson, G. R., and MsEwan, A. G., *Mol. Microbiol.,* **2002**, *44*, 1575-1587.

[151] Liedo, B., Martinez-Espinosa, R. M., Marhuenda-Egea, F. C., and Bonete, M. J., *Biochim Biophys. Acta.,* **2004**, *1674*, 50-59.

[152] Yoshimatsu, K., Iwasaki, T., and Fujiwara, T., *FEBS Lett.,* **2002**, *516*, 145-150.

[153] Kniemeyer, O., and Heider, J., *J. Biol. Chem.,* **2001**, *276*, 21381-21386.

[154] Johnson, H. A., Pelletier, D. A., and Spormann, A. M., *J. Bacteriol.,* **2001**, *183*, 4536-4542.

[155] Kloer, D. P., Hagel, C., Heider, J., and Schulz, G. E., *Structure.,* **2006**, *14*, 1377-1388.

[156] Ball, A. A., Johnson, H. A., Reinhard, M., and Spormann, A. M., *J. Bacteriol.,* **1996**, *178*, 5755-5761.

[157] Rabus, R., and Widdel, F., *Arch. Microbiol.,* **1995**, *163*, 96-103.

[158] Fischer, B., Enemark, J. H., and Basu, P., *J. Inorg. Bio. Chem.,* **1998**, *72*, 13-21.

[159] Szaleniec, M., Witko, M., and Heider, J., *J. Mol. Catal. A: Chem.,* **2008**, *286*, 128-136.

[160] Schlegel, H. B., and McDouall, J. J., in *Computational Advances in Organic Chemistry*, Ed. Ögretir, C., and Csizmadia, I. G., (Kluwer Academic, The Netherlands, **1991**) 167-185.

[161] Bacskay, G. B., *Chem. Phys.*, **1981**, *61***,** 385-404.

[162] Szaleniec, M., Borowski, T., Schühle, K., Witko, M., and Heider, J., *J. Am. Chem. Soc.,* **2010**, *132*, 6014-6024.

[163] Szaleniec, M., Salwiński, A., Borowski, T., Heider, J., and Witko, M., *J. Quantum. Chem.,* **2011**, *000*, 000.

[164] Schink, B., *Arch. Microbiol.,* **1985**, *142*, 295-301.

[165] Burgess, B. K., and Lowe, D. L. *Chem. Rev.,* **1996**, *96*, 2983-3012.

[166] Yadav, J., Das, S. K., and Sakar, S., *J. Am. Chem. Soc.,* **1997**, *119*, 4315-4316.

[167] Einsle, O., Niessen, H., Abt, D. J., Seiffert, G., Schink, B., Huber, R., Messeschmidt, A., and Kroneck, P. M. H., *Acta Crystallogr. Sect. F: Struct. Biol. Cryst. Commun.,* **2005**, *61*, 299-301.

[168] Bevers, L. E., Hagedoorn, P. L., Hagen, W. R., *Coord. Chem. Rev.,* **2009**, *253*, 269-290.

[169] Johnson, M. K., Rees, D. C., and Adams, M. W. W., *Chem. Rev*., **1996**, *96*, 2817-2859.

[170] Antony, A., and Bayse, C. A., *Organometallics.,* **2009**, *28*, 4938-4944.

[171] Vincent, M. A., Hillier, I. H., Periyasamy, G., and Burton, N. A., *Dalton. Trans.,* **2010**, *39*, 3816-3822.

[172] Liao, R. Z., Yu, J. G., and Himo. F., *PNAS.,* **2010**, *107*, 22523-22527.

[173] Suenobu, K., Nagaoka, M., and Yamabe, T., *Journal of Molecular Structure (Theochem)*., **1999**, *461-462*, 581-588.

[174] LLedós, A., Bertrán, J., and ventura, O. N., *International Journal of Quantum Chemistry*., **1986**, *xxx*, 467-477.

[175] Richardson, D. J., and Watmough, N. J., *Curr. Opin. Chem. Biol.,* **1999**, *3*, 207-219.

[176] Slater, J. C. *Quantum Theory of Molecules and Solids, Vol. 4: The Self-Consistent Field for Molecules and Solids*. McGraw-Hill: New York, **1974**.

[177] Perdew, J. P., *Phys. Rev. B.,* **1986**, *34*, 7406.

[178] Perdew, J. P., *Phys. Rev. B.*, **1986**, *33*, 8822-8824.

[179] Rosner, B. M., Rainey, F. A., Kroppenstedt, R. M., and Schink, B., *FEMS Microbiology Letters*., **1997**, *148*, 175-180.

[180] *Protein Sensors and Reactive Oxygen Species, Part A: Selenoproteins and Thioredoxin* (Eds.: Sies, H., Packer, L), Academic Press, San Diego, **2002**, pp. 1-461.

[181] *Protein Sensors and Reactive Oxygen Species, Part B: Thiol Enzymes and Proteins* (Eds.: Sies, H., Packer, L), Academic Press, San Diego, **2002**, pp. 1-364.

[182] Jacob, C., Giles, G. I., Giles, N. M., and Sies, H., *Angew. Chem. Int. Ed.,* **2003**, *42*, 4742-4758.

[183] Kraft, T., Bowen, A., Theis, F., Macy, J. M., *DNA Sequence*, **2000**, *10*, 365-377.

[184] Wang, J. –J., Tessier, C., and Holm, R. H., *Inorg. Chem.,* **2006**, *45*, 2979-2988.

[185] Watts, C. A., Ridley, H., Dridge, E. J., Leaver, J. T., Reilly, A. J., Richardson, D. J., and Butler, C. S., *10th Nitrogen Cycle meeting 2004*, 173-174.

[186] Dridge, E. J., Watts, C. A., Jepson, B. J. N., Line, K., Santini, J. M., Richardson, D. J., and Butler, C. S., *Biochem. J.,* **2007**, *408*, 19-28.

[187] Maher, M. J., Santini, J., Pickering, I. J., Prince, R. C., Macy, J. M., and George, G. N., *Inorg. Chem.,* **2004**, *43*, 402-404.

[188] Krafft, T., Bowen, A., Theis, F., and Macy, J. M., *DNA Seq.,* **2000**, *10*, 365-377.

[189] Maher, M. J., and Macy, J. M., *Acta Cryst*., **2002**, *D58*, 706-708.

[190] Schröder, I., Rech, S., Kraft, T., and Macy, J. M., *The Journal Of Biological Chemistry*., **1997**, *272*, 23765-23768.

[191] Kuroda, M., Yamashita, M., Miwa, E., Imao, K., Fujimoto, N., Ono, H., Nagano, K., Sei, K., ans Ike, M., *Journal of Bacteriology*., **2011**, *193*, 2141-2148.

[192] Dridge, E. J., and Butler, C. S., *Biochimie.,* **2010**, *92*, 1268-1273.

[193] Kappler, U., *Biochimica et Biophysica Acta*., **2011**, *1807*, 1-10.

[194] George, G. N., Garrett, R. M., Graf, T., Prince, R. C., Rajagopalan, K. V., *J. Am. Chem. Soc.,* **1998**, *120*, 4522-4523.

[195] Pal, K., Chaudhury, P. K., and Sarkar, S., *Chem. Asian. J*., **2007**, *2*, 956-964.

[196] Das, S. K., Chaudhury, P. K., Biswas, D., and Sarkar, S., *J. Am. Chem. Soc*., **1994**, *116*, 9061-9070.

[197] Stolz, J. F., and Basu, P., *Chem. Bio. Chem.,* **2002**, *3*, 198-206.

[198] Kroneck, P. M. H., Abt, D. J., *Met. Ions. Biol. Syst.,* **2002**, *39*, 369-403.

[199] Cabello, P., Roldan, M. D., Moreno-vivian, C., *Microbiology.,* **2004**, *150*, 3527-3546.

[200] Richardson, D. J., and Watmough, N. J., *Curr. Opin. Chem. Biol.,* **1999**, *3*, 207-219.